

Design Optimisation for Stent Manufacture



The University of
Nottingham

UNITED KINGDOM • CHINA • MALAYSIA

Muhammad Farhan Khan

**Department of Mechanical, Materials &
Manufacturing Engineering**

Thesis submitted to the University of Nottingham for the degree of
Doctor of Philosophy

April 2018

© Muhammad Farhan Khan 2018

This thesis is dedicated to my parents and family

Abstract

Intravascular stents of various designs are currently used to prop open diseased arteries and there is evidence that different stent geometries have different in-stent restenosis rates. The majority of commercially available stents are designed generically to fit all individuals. Recent advances in imaging and catheter technologies, however, allow measurement of lesion shape and stiffness. Incorporating patient specific data into the stent design process could enable the development of customised stents. Considering the variety of lesion types, it is envisaged that better outcomes will be achieved if a stent is custom designed in such a way that it has variable radial stiffness longitudinally to hold the varying pressure of plaque and healthy artery at the same time while maintaining an acceptable lumen diameter. This type of operation is suitable for topology optimisation potentially allowing for optimal material distribution of a stent. The primary aim of this research is to develop new stent designs for a set of plaque types and investigate the final radius of the lumen after stent implantation. Stent geometries were obtained by topology optimisation for minimised compliance under different stenosis levels and plaque materials. Three types of stenosis levels by area, i.e. 30%, 40% and 50% with each type having three different plaque material properties i.e. calcified, cellular and hypocellular were studied. The optimisation results were transformed to clear design concepts and their performance was evaluated by implanting them in their respective

stenosed artery types using finite element analysis. The results were compared with a generic stent in similar arteries, which showed that the new designs showed less recoil. In the hardest (calcified) of plaques studied, topology optimised designs overall resulted in 2%, 2% and 6% residual area stenosis compared to 10%, 29% and 35% from the generic design in arteries with 30%, 40% and 50% stenosis respectively. It was shown that higher material distribution resulted in the central region of the stent in order to resist implantation recoil due to higher plaque compressive loads. Additive manufacturing (AM) was utilised to validate the computational approach used in this thesis. This work provides a proof of concept for stents tailored to specific lesions in order to minimise recoil and maintain a patent lumen in stenotic arteries.

Publications

Journal publication

- **Muhammad Khan**, David Brackett, Ian Ashcroft, Christopher Tuck, Ricky Wildman. A novel approach to design lesion-specific stents for minimum recoil, 2016, ASME Journal of Medical Devices doi:10.1115/1.4034880

Oral presentation

- **Muhammad Khan**, Ricky Wildman, Ian Ashcroft, Christopher Tuck. Design optimisation for stent manufacture. Research student conference, Wolfson School of mechanical and manufacturing engineering, Loughborough University, UK. (2011)

Poster presentation

- **Muhammad Khan**, Ricky Wildman, Ian Ashcroft, Christopher Tuck. Design optimisation for stent manufacture. 1st Annual Research Student Conference, Health and Life Sciences Research School, Loughborough University, UK. (2011)

Acknowledgements

All praise is due to Allah, the One, the most Merciful and Beneficent, the only Creator, the Controller and the Sustainer. I thank Him for His countless blessings He has showered upon me and for giving me the opportunity and strength to carry out this research work.

I express my deepest indebtedness to my parents who put forth their best effort to support, educate and provide me with the best. To my father, a civil engineer, who has been the main source of inspiration for me. His mentoring has been instrumental in dealing with every stage of my life. To my mother, whose prayers and unconditional love contributed to all my achievements.

I would like to show my deepest gratitude to my supervisors Prof. Ricky Wildman, Prof. Ian Ashcroft, Prof. Chris Tuck and Dr. David Brackett. Their invaluable guidance and constructive criticism was key to accomplish this work. To Prof. Ricky Wildman, whose advice, patience and continuous support helped me navigate through the hard times. A special thanks to Dr. David Brackett for his help and valuable suggestions in the latter stages of my research. I am also grateful to Prof. Richard Hague and Prof. Adam Clare for their inputs during annual assessments of my research.

Many thanks to my siblings with whom I share many happy memories. To my brother Salman, a PhD from Loughborough University, who has inspired me and was always there to provide motivation and support. I

thank my friends and colleagues Faisal, Waseem, Qadir, Jaya, Ehab, Ajit, Meisam, Amir, Yinfeng, Martin, Vikrant, Deji, Tho, Emrah, Himayat, Riaz, Jiaming, Darryl for their company and support. Thanks to all staff and members of the Additive Manufacturing and 3D Printing Research Group at the University of Nottingham who provided me with a friendly environment to work in and were always happy to answer questions.

I thank my parents for bringing into my life, my wife – most probably my better half. I know how difficult it was for you to watch me struggle with my PhD. You helped me through incredibly difficult times and brightened up the final years of my PhD with your patience, support and understanding.

To our two wonderful children, Saad and Hania for filling my mornings with smiles.

I would also like to acknowledge the support from Charles Wallace Trust towards my maintenance costs in my thesis writing up period.

Finally, I would like to thank the University of Nottingham, Loughborough University and Engineering and Physical Sciences Research Council (EPSRC), UK for funding this research.

Contents

Abstract.....	ii
Publications	iv
Acknowledgements.....	v
List of Figures	x
List of Tables	xvii
Abbreviations and Acronyms	xviii
Glossary.....	xix
Nomenclature	xx
1. Introduction.....	1
1.1 Background	1
1.2 Research Motivation.....	3
1.3 Thesis Outline	4
2. Literature Review.....	6
2.1 Introduction	6
2.2 Physiology of Coronary Arteries	7
2.3 Pathology of Atherosclerosis	8
2.4 Treatment	10
2.5 Cardiovascular Stents and its Complications.....	11
2.6 Impact of Stent Design on Restenosis (Clinical Evidence)	17
2.6.1 Materials	20
2.6.2 Fabrication Methods.....	26
2.6.3 Geometry.....	28
2.7 Finite Element Analysis in Stent Design.....	31
2.8 Structural Optimisation	34
2.8.1 Sizing Optimisation	38
2.8.2 Shape Optimisation	39
2.8.3 Topology Optimisation	39
2.9 Solid Isotropic Material with Penalisation.....	43
2.10 Optimisation of Stent Design and Lesion-Specificity	45
2.11 Using additive manufacturing for design customisation	55

2.12	Summary.....	57
3.	Description of Research Novelty	59
3.1	Introduction	59
3.2	Gaps in the Research	59
3.3	State of the Art & Limitations of the Current Literature	60
3.4	Research Novelty	63
3.5	Aim and Objectives of Current Research.....	65
4.	Methodology: Finite Element Analysis and Lesion-Specific Optimisation	67
4.1	Introduction	67
4.2	Selection of Element Types and Solution Methods.....	69
4.2.1	Introduction to MSC Patran & Marc Mentat.....	72
4.2.2	Treatment of Contact in MSC Marc.....	75
4.3	Diseased Artery Selection and Analysis Steps	75
4.4	Artery-Cylinder Model Creation	78
4.5	Selection of Material Model	79
4.6	Meshing and Boundary Conditions.....	80
4.7	Lesion-Specific Stent Topology Optimisation	84
4.7.1	Model setup and initial exploration	87
4.7.2	Optimisation parameters.....	92
4.7.3	Complications in topology optimisation method	95
4.7.4	Post processing	97
4.8	Comparison with generic stent.....	98
4.9	Summary.....	99
5.	Experimental Validation of the Numerical Methods.....	101
5.1	Introduction	101
5.2	Methods.....	102
5.3	Experimental test rig setup.....	102
5.4	Additive Manufacturing of stents.....	104
5.5	Silicone tensile tests	108
5.6	Experimental procedure	110
5.7	Image analysis.....	114
5.8	FE Analysis	115
5.9	Summary.....	116
6.	Results and Discussion.....	117
6.1	Introduction	117

6.2	Investigation of initial load case scenarios	117
6.3	Assessment of stent-artery contact analysis	123
6.4	Lesion-specific stent topology optimisation results	127
6.5	Assessment of radial displacement	133
6.6	Experimental validation results	147
6.7	Summary	156
7.	Conclusions & future work	158
7.1	Conclusions	158
7.2	Limitations and Future Work	161
	References	164
	Appendix A	182
	Appendix B.....	187
	Appendix C.....	196
	Appendix D	198

List of Figures

Figure 2-1: Structure of literature review.....	6
Figure 2-2: Schematic overview of the main coronary arteries (RCA = right coronary artery, LCA = left coronary artery, LM = left main artery, LCX = left circumex artery, LAD = left anterior descending artery) [6].....	7
Figure 2-3: Structure and composition of the arterial wall [7].....	8
Figure 2-4: Progression of atherosclerosis in coronary arteries: from normal artery (left panel) to severe atherosclerosis (rightmost panel) [11].....	9
Figure 2-5: Main causes of Atherosclerosis [12].....	10
Figure 2-6 : Diagram showing (a) angioplasty procedure and (b) stenting procedure. [12].....	12
Figure 2-7: In-stent restenosis. Open source image [17].	14
Figure 2-8: Some of the factors affecting in-stent restenosis.	16
Figure 2-9: Scanning electron photomicrographs of stents of different configurations: Slotted tube stent before (a) and after (b) expansion; corrugated ring stent before (c) and after (d) expansion. Original magnification x100. [32]	18
Figure 2-10: Bar graph shows vascular injury score per arterial cross section 14 days after balloon injury and implantation of steel stents or after balloon injury alone. Statistical analysis showed a main effect of stent configuration but not of stent coating [32].....	18
Figure 2-11: Examples of balloon-expandable stents. A: Endeavor (Medtronic), B: Taxus Liberte (Boston Scientific), C: Promus (Boston Scientific), D: PRO-Kinetic (Biotronik) [14].....	20
Figure 2-12: Examples of self-expandable stents. A: Wallstent (Boston Scientific), B: RX Acculink (Abbott Vascular), C: Xact (Abbott Vascular), D: SelfX (Abbott Vascular).	21
Figure 2-13: Characteristics of an ideal stent [15].....	21
Figure 2-14: (A) The NEVO cobalt chromium stent, which has an open-cell design and unique reservoirs that contain a biodegradable polymer and sirolimus mix that (B) completely biodegrades within 90 days [16].....	23
Figure 2-15: A variety of metallic (AMS1, DREAMS 1) and polymeric biodegradable stents currently used in clinical practice [49].....	26
Figure 2-16: Esophacojl. Coil stent fabricated from nitinol ribbon [41].....	28
Figure 2-17: Crossflex. A minimally connected helical spiral stent fabricated from stainless steel wire [41].	29
Figure 2-18: Self-expanding knitted Nitinol wire design [41].....	29
Figure 2-19: Strut configuration: open cell (a), closed cell: Non-flex connectors (b), flex-connectors (c), combined flex/non-flex connectors (d).	30
Figure 2-20: Palmaz-Schatz slotted tube type stent [41].	30
Figure 2-21: NIR stent with 'V' type flex connectors [41].....	31
Figure 2-22: Design parameters. Generic stent showing the three parameters of interest: h is the connector bar length (or strut spacing), ρ is the radius of curvature at the crown junctions, and f is the axial amplitude. These three parameters were varied to test their effects on artery wall stress [68].	33

Figure 2-23: Local and global optima.....	35
Figure 2-24: MSC Nastran implementation of structural optimisation [75].	37
Figure 2-25: Size optimisation of a truss structure [77].	38
Figure 2-26: Shape optimisation of a truss structure [77].....	39
Figure 2-27: Topology optimisation of a truss structure [77].....	40
Figure 2-28: General scheme of topology optimisation.	40
Figure 2-29: General process flow of topology optimisation using SIMP. Adapted from Lee 2011 [87].	45
Figure 2-30: Two generic stent designs. Stent 1Z1 as stiff, Stent 2B3 as less stiff with un-deformed plaque geometry [65].....	49
Figure 2-31: Uniaxial tensile stress–strain data represented by the strain energy density functions for the three different plaque types in the finite element models. Source: [64].....	50
Figure 2-32: Progression of atherosclerosis leading to plaque morphology change. Copyright Medmovie, reproduced with permission from Medmovie [100].	50
Figure 2-33: (a) Illustration of the Conor stent with the opened configuration, which is composed of honeycombed strut units joined by flexible links. (b) One strut isolated from the stent unit. (c) The strut model meshed in OptiStruct without holes, yellow part being the design domain for optimisation. (d) The element density distribution with MMS of 0.042mm at the iteration number of 30 [109].	52
Figure 2-34: The stented artery with calcified plaque [111].	53
Figure 2-35: Variable radial force stent with struts thinned in sections C1 on either side [103].	54
Figure 2-36: Steps commonly involved in an additive manufacturing process.....	56
Figure 2-37: Schematics of the selective laser sintering process.	57
Figure 4-1: Methodology of the current work showing three steps: (A) Initial exploration, (B) lesion-specific stent optimisation and (C) experimental validation. .	68
Figure 4-2: A complete design process for customised stents, with step 1 simulated using FEA before carrying out steps 2 and 3.	76
Figure 4-3: Contact analysis steps.	77
Figure 4-4: Artery models with plaque types used for the analyses (XY plane cut view).	79
Figure 4-5: Generic stent, 15mm in length, selected for comparison with optimised stents of the same size.	79
Figure 4-6: Maximum radial displacement of plaque tip in the artery with five different meshes.....	81
Figure 4-7: Graphical representation of the application of boundary conditions for the artery with internal pressure and axial constraints on both ends.	82
Figure 4-8: Hex-meshed model of 50% stenotic artery for contact analysis with cylinder (XZ cut view).....	82
Figure 4-9: Relative position of cylinder and 40% stenotic artery before contact (artery sliced for illustration purpose).....	83
Figure 4-10: Analysis steps for lesion-specific stent optimisation.....	86
Figure 4-11: Proposed approach to design lesion-specific stents.	87

Figure 4-12: Load case 1: Uniform inward radial load distribution representing healthy artery compressive pressure on cylinder (coarse mesh used for illustration purpose).....	88
Figure 4-13: RBE3 elements connecting end nodes at one end of the cylinder for unconstrained compression. Note the three dependent nodes with free in-plane dof forming a triangle for best numerical conditioning while the central dependent node being fixed in all dofs (coarse mesh used for illustration purpose).	89
Figure 4-14: Demonstration of unconstrained uniform compression due to external pressure using RBE3 elements. Note the Poisson effect shortening (coarse mesh used for illustration purpose).....	89
Figure 4-15: Load case 2: Radial compressive force application at centre top and bottom (coarse mesh used for illustration purpose).....	90
Figure 4-16: Load case 3: Torsional load application using RBE2 elements at both ends of the cylinder (coarse mesh used for illustration purpose).	90
Figure 4-17: Varying radial force on one of the stent design domains obtained from contact analysis with 40% stenosis with calcified plaque for TO. Central node at one end of the cylinder is allowed to expand/contract using RBE3 elements. Note higher forces in the middle due to peak plaque thickness.	91
Figure 4-18: Illustration of diseased artery section with cylinder implanted for force extraction showing expected higher compressive forces from stenotic region.	92
Figure 4-19: Checkerboard pattern in an arbitrary optimum [171].	95
Figure 4-20: Patran FEM smooth option with image (b) showing smoothed elements.	98
Figure 5-1: Schematic diagram of the experimental test rig.	103
Figure 5-2: Image showing experimental setup used for mock artery inflation and stent deployment.	104
Figure 5-3: A close-up image of stent delivery mechanism showing transparent stent housing for orientation before insertion into the inflated tube.	104
Figure 5-4: Stent model used for additive manufacturing and testing.	105
Figure 5-5: Manufacturing defects: Struts at stent ends distorted due to being too thin.....	107
Figure 5-6: Scaled up optimised stent made using SLS used for the experiments....	107
Figure 5-7: Instron tensile test machine used for tensile tests.	108
Figure 5-8: Silicone dumb-bell specimen (a) dimensions and (b) samples cut from tube for tensile tests with die according to BS ISO 37:2017	109
Figure 5-9: Stress vs strain curves of dumb-bell samples.....	110
Figure 5-10: Insertion of optimised stent in the hose connector before tube attachment.	111
Figure 5-11: Stent inserted in to the inflated artery.	112
Figure 5-12: Stent deployment after reducing the gauge pressure to zero.	112
Figure 5-13: Scaled quarter model plaque with dimensions used for experimental observation.....	113
Figure 5-14: 40% simulated plaque made of the same material as the silicone mock artery, initial shape (a), cut to size (b).	113

Figure 5-15: Simulated plaque added to the mock artery with the thickest part at the bottom.....	113
Figure 5-16: Stent implantation in artery with 40% simulated stenosis.	114
Figure 5-17: FEA model of 40% stenotic silicone mock artery and nylon 12 stent. ..	115
Figure 6-1: Mesh 1 (6804 elements) with uniform loading: (a) element density distribution, ρ , representing material densities between 0-1 (b) threshold 0.3 for element filtering and (c) FEM smoothing of the filtered elements.....	119
Figure 6-2: FEM option allowing smooth transition of elements and threshold control for enhancing member connectivity (a) before and (b) after applying element smoothing.....	120
Figure 6-3: Mesh 1 (6804 elements) with crush loading: (a) element density distribution, ρ , representing material densities between 0-1 (b) threshold 0.3 for element filtering and (c) FEM smoothing of the filtered elements.....	120
Figure 6-4: Mesh 1 (6804 elements) with torsional loading: (a) element density distribution, ρ , representing material densities between 0-1 (b) threshold 0.3 for element filtering and (c) FEM smoothing of the filtered elements.....	121
Figure 6-5: Mesh 3 (47507 elements) density distribution, ρ , with central crush loading and MMS 0.3 during different iteration cycles. Note the minimal difference between design cycles 80 through 247.	122
Figure 6-6: Topology of a cylindrical structure resulting from pure torsion [184]. ...	123
Figure 6-7: Contour plot showing radially inward nodal load (N) variation on the design space for stent topology optimisation based on cylinder-artery contact with 30% calcified (a) hypocellular (b) and cellular plaques (c) along with unwrapped versions from cylindrical shape for illustration purpose.	124
Figure 6-8: Contour plot showing radially inward nodal load (N) variation on the design space for stent topology optimisation based on cylinder-artery contact with 40% calcified (a) hypocellular (b) and cellular plaques (c) along with unwrapped versions from cylindrical shape for illustration purpose.	125
Figure 6-9: Contour plot showing radially inward nodal load (N) variation on the design space for stent topology optimisation based on cylinder-artery contact with 50% calcified (a) hypocellular (b) and cellular plaques (c) along with unwrapped versions from cylindrical shape for illustration purpose.	126
Figure 6-10: Stent topology optimisation convergence plots: compliance (Nmm) with respect to design iterations for 30% stenosis for: (a) calcified, (b) cellular and (c) hypocellular plaque types respectively.	128
Figure 6-11: Stent topology optimisation convergence plots: compliance (Nmm) with respect to design iterations for 40% stenosis for: (a) calcified, (b) cellular and (c) hypocellular plaque types respectively.	129
Figure 6-12: Stent topology optimisation convergence plots: compliance (Nmm) with respect to design iterations for 50% stenosis for: (a) calcified, (b) cellular and (c) hypocellular plaque types respectively.	130
Figure 6-13: Stent topology optimisation density distribution results for (a-c) 30%, (d-f) 40% and (g-i) 50% stenosis for calcified, cellular and hypocellular plaque types respectively (results of axial-stent-half unwrapped from cylindrical shape for illustration purposes).....	131

Figure 6-14: Stent topologies for (a-c) 30%, (d-f) 40% and (g-i) 50% for calcified, cellular and hypocellular plaque types respectively, (results unwrapped from cylindrical shape for illustration purpose).....	132
Figure 6-15: Deformation plot (mm) showing contact of optimised stents with their respective stenotic arteries having 30% calcified (a) cellular (b) and hypocellular plaques (c).....	135
Figure 6-16: Deformation plot (mm) showing contact of optimised stents with their respective stenotic arteries having 40% calcified (a) cellular (b) and hypocellular plaques (c).....	136
Figure 6-17: Deformation plot (mm) showing contact of optimised stents with their respective stenotic arteries having 50% calcified (a) cellular (b) and hypocellular plaques (c).....	137
Figure 6-18: Deformation plot (mm) showing contact of a generic stent with stenotic arteries having 30% calcified (a) cellular (b) and hypocellular plaques (c).	138
Figure 6-19: Deformation plot (mm) showing contact of generic stent with stenotic arteries having 40% calcified (a) cellular (b) and hypocellular plaques (c).	139
Figure 6-20: Deformation plot (mm) showing contact of generic stent with stenotic arteries having 50% calcified (a) cellular (b) and hypocellular plaques (c).	140
Figure 6-21: Stress plots (MPa) for calcified 30% (a-c), cellular (d-f) and hypocellular (g-i) representing compressive principal stress.....	142
Figure 6-22: Stress plots (MPa) for calcified 30% (a), cellular (b) and hypocellular (c) representing maximum shear stress.	143
Figure 6-23: Stress plots (MPa) for optimised stents placed in arteries with calcified 30% (a), cellular (b) and hypocellular (c) plaques representing compressive principal stress.....	144
Figure 6-24: Stress plots (MPa) for optimised stents placed in arteries with calcified 30% (a), cellular (b) and hypocellular (c) plaques representing maximum principal shear stress.	145
Figure 6-25: Final lumen radial deformation with a generic stent (a-c) and optimised stents (d-f) for 30, 40 and 50% stenotic arteries respectively with different plaque types based on 11 equally distant points longitudinally along thickest part of plaque, relative to central axis (one half of the stenotic artery deformations illustrated)....	146
Figure 6-26: Post implantation stenosis levels in the remodelled artery due to optimised and generic stents recoil.....	147
Figure 6-27: Image of mock silicone artery (XZ view) before inflation (a) and superimposed image of after inflation showing boundaries using MATLAB.	148
Figure 6-28: Mock silicone artery (XZ view) before (a) and after (b) stent implantation. Both images superimposed in MATLAB showing external tube boundaries (c).	149
Figure 6-29: Mock silicone artery (XZ view) with 40% stenosis before (a) and after (b) stent implantation. Both images superimposed in MATLAB showing external tube boundaries (c).	150
Figure 6-30: Experimental uniaxial tensile data curve fit of silicone NGP60 with Neo-Hookean model in MSC Marc Mentat.	151

Figure 6-31: FEA model of stenotic mock silicone artery with stent: Deformation plot showing radial displacement (mm).	152
Figure 6-32: Deformation plot illustrating radial displacement (mm) in mock artery cross-section with stent implanted.	152
Figure 6-33: Radial displacement plot of arterial external boundary (XZ view) with 40% stenosis before and after stent implantation in FEA.	153
Figure 6-34: Diameter variation resulting from pre and post optimised stent placement in FEA and experimental models (plot showing axial half).	154
Figure 7-1: Mesh 2 (13685 elements) with uniform loading: (a) element density distribution, ρ , representing material densities between 0-1 (b) threshold 0.3 for element filtering and (c) FEM smoothing of the filtered elements.....	199
Figure 7-2: Mesh 2 (13685 elements) with central crush loading: (a) element density distribution, ρ , representing material densities between 0-1 (b) threshold 0.3 for element filtering and (c) FEM smoothing of the filtered elements.....	200
Figure 7-3: Mesh 2 (13685 elements) with torsional loading: (a) element density distribution, ρ , representing material densities between 0-1 (b) threshold 0.3 for element filtering and (c) FEM smoothing of the filtered elements.....	201
Figure 7-4: Mesh 3 (47507 elements) with uniform loading and MMS 0.3: (a) element density distribution, ρ , representing material densities between 0-1 (b) threshold 0.25 for element filtering and (c) FEM smoothing of the filtered elements.	202
Figure 7-5: Mesh 3 (47507 elements) with uniform loading and MMS 0.4: (a) element density distribution, ρ , representing material densities between 0-1 (b) threshold 0.25 for element filtering and (c) FEM smoothing of the filtered elements.	203
Figure 7-6: Mesh 3 (47507 elements) with uniform loading and MMS 0.5: (a) element density distribution, ρ , representing material densities between 0-1 (b) threshold 0.25 for element filtering and (c) FEM smoothing of the filtered elements.	204
Figure 7-7: Mesh 3 (47507 elements) with central crush loading and MMS 0.3: (a) element density distribution, ρ , representing material densities between 0-1 (b) threshold 0.25 for element filtering and (c) FEM smoothing of the filtered elements.	205
Figure 7-8: Mesh 3 (47507 elements) with central crush loading and MMS 0.4: (a) element density distribution, ρ , representing material densities between 0-1 (b) threshold 0.25 for element filtering and (c) FEM smoothing of the filtered elements.	206
Figure 7-9: Mesh 3 (47507 elements) with central crush loading and MMS 0.5: (a) element density distribution, ρ , representing material densities between 0-1 (b) threshold 0.25 for element filtering and (c) FEM smoothing of the filtered elements.	207
Figure 7-10: Mesh 3 (47507 elements) with torsional loading and MMS 0.3: (a) element density distribution, ρ , representing material densities between 0-1 (b) threshold 0.25 for element filtering and (c) FEM smoothing of the filtered elements.	208
Figure 7-11: Mesh 3 (47507 elements) with torsional loading and MMS 0.4: (a) element density distribution, ρ , representing material densities between 0-1 (b)	

threshold 0.25 for element filtering and (c) FEM smoothing of the filtered elements.
..... 209

Figure 7-12: Mesh 3 (47507 elements) with torsional loading and MMS 0.5: (a)
element density distribution, ρ , representing material densities between 0-1 (b)
threshold 0.25 for element filtering and (c) FEM smoothing of the filtered elements.
..... 210

List of Tables

Table 2-1: Selected stent characteristics and their manufacturers [14].	13
Table 2-2: Risk factors of Stent Thrombosis [19].....	15
Table 2-3: Materials with ideal characteristics for coronary stent applications [46]. .	22
Table 2-4: Advantages and disadvantages of stent manufacturing methods [41,57,58].	27
Table 4-1: Commonly used elements for stent systems and arterial tissues.....	70
Table 4-2: Adaptive stepping criteria details used for contact analyses.....	74
Table 4-3: Hyperelastic constants to describe plaque and arterial tissue [64,165]. ...	80
Table 4-4: Optimisation parameters.....	95
Table 6-1: Peak compressive force exerted by stenotic arteries on cylinder after deflation to diastole.....	127
Table 6-2: Post-stenting lumen gain in the generic and optimised designs due to peak plaque radius change.....	134

Abbreviations and Acronyms

AM	-	Additive Manufacturing
BMS	-	Bare Metal Stent(s)
CABG	-	Coronary Artery Bypass Grafting
CAD	-	Coronary Artery Disease
CMR	-	Cardiac Magnetic Resonance
Co-Cr	-	Cobalt Chromium
CT	-	Computer tomography
DES	-	Drug Eluting Stent(s)
FEA	-	Finite Element Analysis
HAZ	-	Heat Affected Zone
ISR	-	In-Stent Restenosis
IVUS	-	Intra-vascular ultrasound
LDL	-	Low Density Lipoprotein
MI	-	Myocardial Infarction
MIS	-	Minimally Invasive Surgery
MRI	-	Magnetic Resonance Imaging
NHS	-	National Health Service
OCT	-	Optical Coherence Tomography
PCI	-	Percutaneous Coronary Intervention
POBA	-	Plain Old Balloon Angioplasty
ST	-	Stent Thrombosis
TO	-	Topology Optimisation
3D	-	Three Dimensional

Glossary

Angioplasty	Procedure involving balloon inflation of an artery
Atherosclerosis	Artery narrowing due to plaque build-up
Coronary	Blood vessels related to the heart
Dogboning	Over expansion of stent ends
Endothelialisation	Smooth muscle cell growth
Foreshortening	Reduction of stent length during expansion
Intima	Inner lining of a blood vessel
In-stent Restenosis	Re-blocking of a stented artery
Lesion	Localised diseased tissue
Lumen	Internal area of a blood vessel
Neointimal Hyperplasia	Abnormal growth of intimal layer cells
Percutaneous	Procedures involving skin puncture
Recoil	Spring-back effect of a stent after expansion
Stenosis	Arterial occlusion
Stenting	Placement of stents
Thrombosis	Blood clot formation
Vascular	Related to blood vessels

Nomenclature

E	elastic modulus
ν	Poisson's ratio
σ_y	yield stress
W	strain energy density function
C	hyperelastic constants
I	strain invariants
C^*	compliance
\mathbf{U}	global displacement vector
\mathbf{F}	global force vector
S	strain energy
\mathbf{K}	stiffness matrix
N	total number of elements
u^i	displacement vector of the nodes
k^i	stiffness matrix after optimisation
k_0	elements initial stiffness
x^i	initial element density
V_0	initial volume
V	volume of the structure after optimisation

V^*	amount of material to be removed
v^i	element volume after optimisation
x_{min}	lower bound of element density
x_{max}	upper bound of element density
p	penalty factor

1. Introduction

1.1 Background

Cardiovascular disease (CVD) is the main cause of death in England. Each year in England and Wales more than 124,000 deaths are caused by CVD among which nearly half are due to Atherosclerosis [1]. Atherosclerosis is the most common type of heart disease, in which plaque is accumulated in coronary arteries restricting oxygen-rich blood supply to a region of heart muscle. This could result in the death of that region and ultimately myocardial infarction (heart attack).

Treatment of blocked arteries can include invasive surgeries such as coronary artery bypass surgery, balloon angioplasty or stent placement. Coronary artery bypass surgery or grafting (CABG) involves the creation of an alternative passage for blood to bypass the obstruction and was performed first in 1960. This procedure is highly invasive for the patient as it requires the opening of the chest to allow access to the heart. In 1977, a less invasive technique was introduced by Dr. Gruentzig called angioplasty [4]. During this minimally invasive surgery (MIS), a balloon catheter is mounted over a guide wire and is advanced to the narrowed section of the vessel through a small skin puncture in the groin or wrist area. Subsequently, the balloon is inflated at high pressure which compresses the plaque against the arterial wall and results in larger

lumen (internal space of an artery) diameter restoring the blood flow through that region.

After deflating the balloon catheter, some of the lumen gain is lost by elastic recoil of the vessel wall. This lumen loss could be limited by placement of a tubular mesh shaped mechanical scaffold called a stent, which in most cases provides a permanent support to the diseased vessel. The first human implantation of a stent was carried out in 1986 [2]. Since then, technological advancements in stent design, materials, deliverability and drug coatings have expanded the application and success rate of the procedure. Presently, the main concern about this treatment is restenosis, or the re-blocking of the stented artery, normally known as in-stent restenosis (ISR).

As the stent is a foreign material to the affected artery, its presence and mechanical stress on the artery lead to a large number of failures due to restenosis. Restenosis typically occurs through a process of neointimal hyperplasia (NH), involving thrombus formation, inflammation and smooth muscle cell proliferation [5]. In the early days of the stenting procedure, approximately one third of patients suffered from in-stent restenosis within 6 months of stent implantation. Subsequently, there has been a tremendous effort devoted to minimising the failures due to restenosis [3].

With the advent of drug-eluting stent (DES) technology, success has been achieved in reducing restenosis rates. These stents are covered with biodegradable polymer coatings consisting of anti-proliferative drugs designed to minimise smooth muscle cell proliferation. Although drug-

eluting stents have decreased restenosis rates in coronary arteries to near 10%, incomplete endothelialisation of stent struts and lack of extensive long-term follow up still limit this technology.

It has been shown that stent design influences treatment outcome and is a major risk factor for restenosis in bare metal stents (BMS). Advances in stent design have reduced the restenosis rates to around 20% in some stents and over 40% in others, with variation depending upon the stent design [3]. Such significant variations show that optimisation of the mechanical and geometrical design parameters could further reduce the incidences of restenosis.

1.2 Research Motivation

Since their first use in 1986 [2], stents have evolved in terms of design, materials and drug coatings to achieve better post-implantation results. Every year, more than 3 million stents are implanted worldwide and around 600,000 implanted in the UK of which nearly 50,000 are coronary stents [3,4]. Presently, the main concern about this treatment is restenosis, or the re-blocking of the stented artery, normally known as in-stent restenosis (ISR). Nowadays, a variety of stent designs is available, differing with regard to material, strut thickness, coating and drug elution. These stent varieties trigger different vascular behaviours. Stenting is not risk free and stent design alone is an independent predictor of re-blocking conditions such as thrombosis and neointimal hyperplasia [5]. These adverse conditions mainly depend upon how the stent geometry interacts with the arterial surface.

Currently stenting (stent deployment) of diseased arteries generally involves the use of only a set of “off-the-shelf” devices. Especially treating diseased arteries with complex geometry and different stiffnesses of plaques can result in unacceptably low lumen area and shape.

Computational modelling coupled with additive manufacturing (AM) offers a cost effective way to design, pre-clinically test and evaluate the performance and effectiveness of stents. Existing studies dealing with numerical modelling of stent-artery interactions have very rarely focused lesion-specific stent with no optimisation studies in this area. Therefore, there is a significant need to analyse and develop lesion-specific stent designs that suits best the challenging vessel geometry and maintain vessel lumen area.

1.3 Thesis Outline

A brief description of the thesis chapters is given below:

Chapter 2 discusses in detail the relevant literature that underpins this thesis. Starting from the physiology of coronary arteries, the pathology of atherosclerosis and its treatment procedures. It explains stent types and the post-implantation complications. A detailed overview is presented about the finite element analysis (FEA) modelling of stents and structural optimisation methods. This chapter also introduces additive manufacturing, which is utilised produce one of the new stent designs to test and validate the computational approach taken in this thesis.

Chapter 3 presents the research novelty of this work by pointing out gaps in the literature along with aims and objectives of the current study.

Chapter 4 describes the methodology followed for the optimisation of lesion-specific stents. It describes the contact analyses between a force evaluating cylinder, a generic stent and different types of plaques. It explains in detail about the geometry creation for the analysis models, material selection, loading and boundary conditions and other analysis parameters. The chapter later details the topology optimisation technique used and the steps taken to develop a new stent design concepts using this method along with initial exploration to demonstrate topology change with loading. It then explains the model setup and the different plaque types used to design lesion-specific stents.

Chapter 5 describes the experimental work done to validate the computational approach used in the thesis. It presents the work carried out to create a test-rig for mock arteries made of silicone tubes and the implantation of scaled models of polymer stents made with additive manufacturing.

Chapter 6 presents the results of all the analyses and optimisation methods used to develop and optimise lesion-specific stent designs along with the findings of proof-of-concept experiments. It also discusses the results achieved in the current work, their benefit and potential solutions for application.

Chapter 7 presents the conclusions of the current work, its limitations and recommendations for future research.

2. Literature Review

2.1 Introduction

This chapter covers the literature that underpins this thesis. As stated in the earlier chapter, the aim of this study is to investigate and develop lesion-specific stents. Before addressing this issue, it is necessary to provide an introduction to coronary heart disease and its treatment types. A detailed account of the impact of stent design on arterial wall mechanics is presented. This is followed by a review of stent design FEA and structural optimisation methods. Finally, a summary of the key decisions made to formulate the research methodology is given. The structure of the literature review is shown in Figure 2-1.

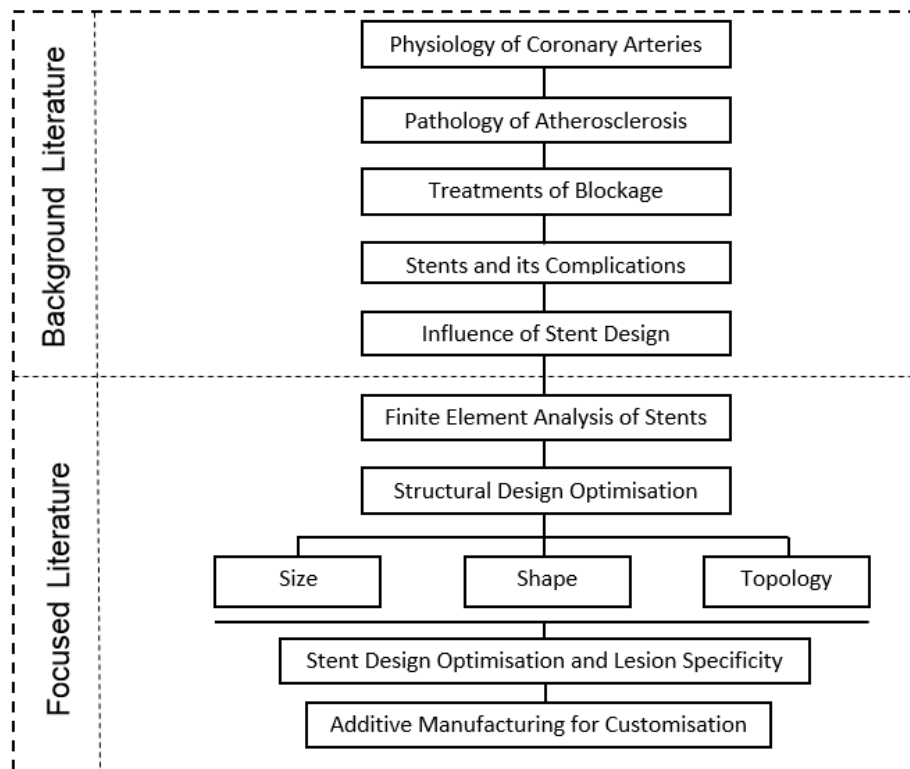


Figure 2-1: Structure of literature review.

2.2 Physiology of Coronary Arteries

The heart muscle is a muscular pump which moves blood around the body. The heart also needs its own blood supply to work properly, and this is done by vessels called coronary arteries. There are two main coronary arteries, the left coronary artery (LCA) and the right coronary artery (RCA), both originating from the base of aorta. The segment of the LCA between the aorta and the first bifurcation is known as the left main artery (LM). The left main bifurcates into the left anterior descending artery (LAD) and the left circumflex artery (LCX). An overview of these coronary arteries is illustrated in Figure 2-2.

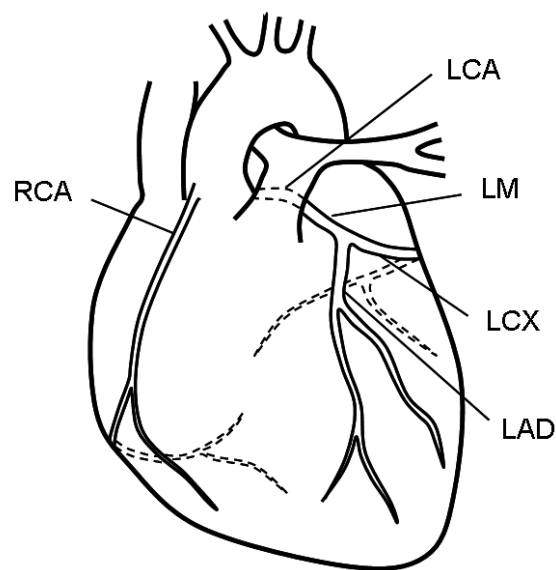


Figure 2-2: Schematic overview of the main coronary arteries (RCA = right coronary artery, LCA = left coronary artery, LM = left main artery, LCX = left circumflex artery, LAD = left anterior descending artery) [6].

Healthy arteries consist of three different layers, the tunica intima, the tunica media and the tunica adventitia as shown in Figure 2-3. The tunica intima is the thin layer closest to the lumen, which consists of a single layer of endothelial cells on a layer of connective tissue. The tunica media is made up of smooth muscle cells surrounded by a matrix of elastin and

collagen fibres, giving strength to the intimal layer. The tunica adventitia, which is the outermost layer, forms a protective layer around the artery.

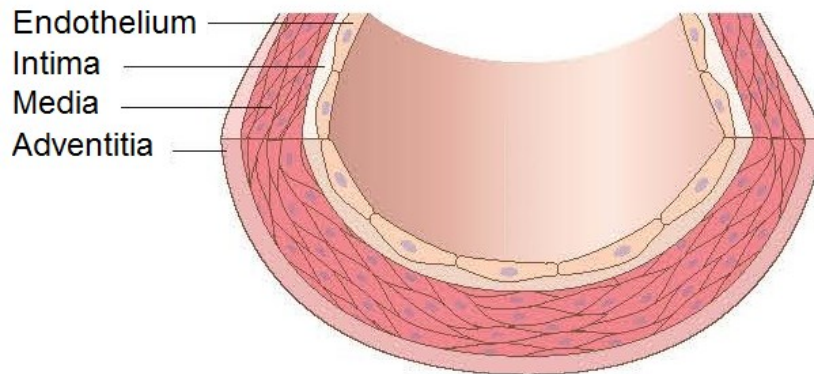


Figure 2-3: Structure and composition of the arterial wall [7].

2.3 Pathology of Atherosclerosis

Atherosclerosis is a disease in which plaque is accumulated in arteries restricting blood supply to a region of heart muscle and could lead to a heart attack. The molecular mechanism involved in atherosclerosis is not yet completely understood. However, it is known that injury of the endothelial layer and inflammatory processes play an important role [8]. The formation of plaque (Figure 2-4) starts with the dysfunction of the endothelial wall [9]. More precisely, the permeability of the endothelial layer changes for the active proteins, such as low density lipoprotein (LDL). LDL acts as a transport medium of cholesterol and it is necessary for the metabolism of the muscle cells in the tunica media.

Things go wrong when the permeability of the endothelial layer increases and causes LDL accumulation between the tunica intima and tunica media. The condition is worsened when part of this LDL oxidises, and the presence of oxidised LDL is directly related to plaque [10]. This situation triggers further complex processes involving smooth muscle cell

migration and vessel growth. In an advanced stage, a considerable reduction in the artery lumen is seen which is known as stenosis.

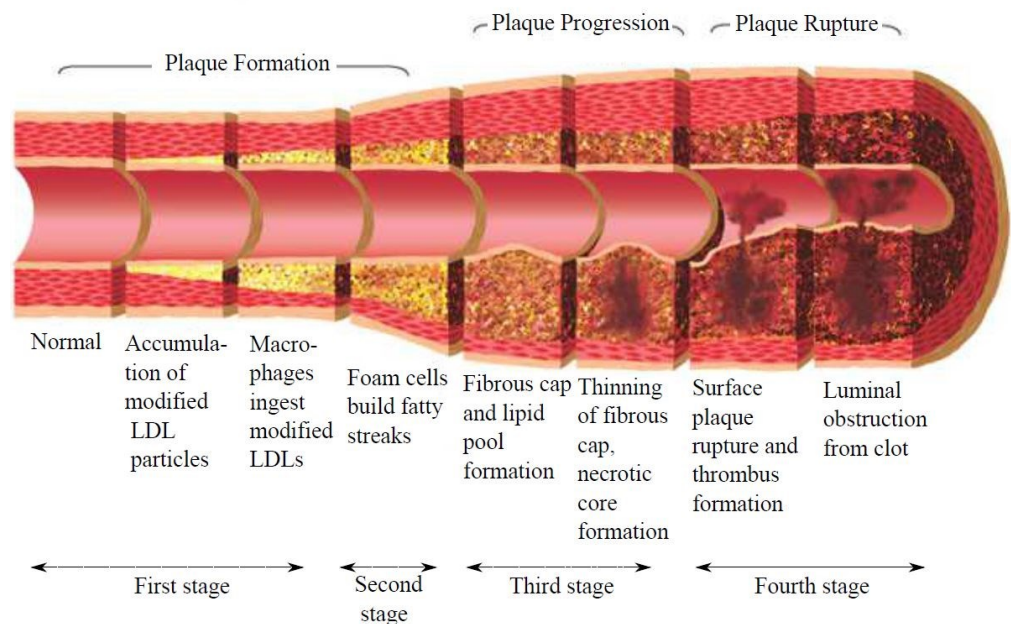


Figure 2-4: Progression of atherosclerosis in coronary arteries: from normal artery (left panel) to severe atherosclerosis (rightmost panel) [11].

A significant narrowing of an artery due to atherosclerosis may induce oxygen deficiency in the downstream regions of the heart and can ultimately lead to heart attack or even death. Major risk factors of atherosclerosis (Figure 2-5) include smoking, obesity, high blood cholesterol, high blood pressure and diabetes [12].



Figure 2-5: Main causes of Atherosclerosis [12].

2.4 Treatment

Treatment of severe stenosis includes bypass surgery, balloon angioplasty and stent placement. With bypass surgery the flow through the blocked artery is given a new pathway through a relocated vessel of the patient placed across the stenosis. This procedure is highly invasive as it requires the opening of the chest to allow access to the heart. In order to reduce the hospital stay, and the risks and costs associated with this high invasive surgery, stenosis can also be treated with less invasive techniques such as angioplasty procedures (with or without stent).

Angioplasty is a much less invasive technique which involves opening the stenosed artery by balloon inflation [13]. This minimally invasive procedure consists of a balloon catheter insertion into the diseased

vessel from a small incision in the femoral or radial artery. The collapsed balloon catheter is positioned in the narrowed segment of the target vessel. Subsequently, the balloon is inflated and when the physician is satisfied with the achieved luminal gain, the balloon is deflated and the catheter removed.

Due to the less invasive nature, the patient recovers faster compared to bypass surgery. However, there are still problems limiting the success of angioplasty. In the short term, elastic recoil from the vessel is seen as soon as the balloon is removed due to the energy released by the elastic fibres in the vessel wall after balloon deflation. In the long term, restenosis of the vessel wall is responsible for re-narrowing of the lumen.

These problems lead to the development of a second revolutionary treatment, the coronary stent, which was first implanted by Sigwart et al. in 1986 [2]. This bare metal, self-expanding stent, known as the “Wall” stent was able to provide a scaffold to the diseased artery and prevented elastic recoil.

2.5 Cardiovascular Stents and its Complications

Cardiovascular stents are tube-like expandable devices used to open narrowed (diseased) arterial segments to restore the blood flow to the heart muscle. The implantation of stents is currently an important part of most interventional procedures for heart treatment. Most commonly, stents are taken to the diseased artery mounted on a delivery system, made of a balloon catheter and guide wire, via a femoral artery in the groin or radial artery in the wrist. Figure 2-6 illustrates the stent treatment

compared to angioplasty procedure for a blocked coronary artery caused by atherosclerosis.

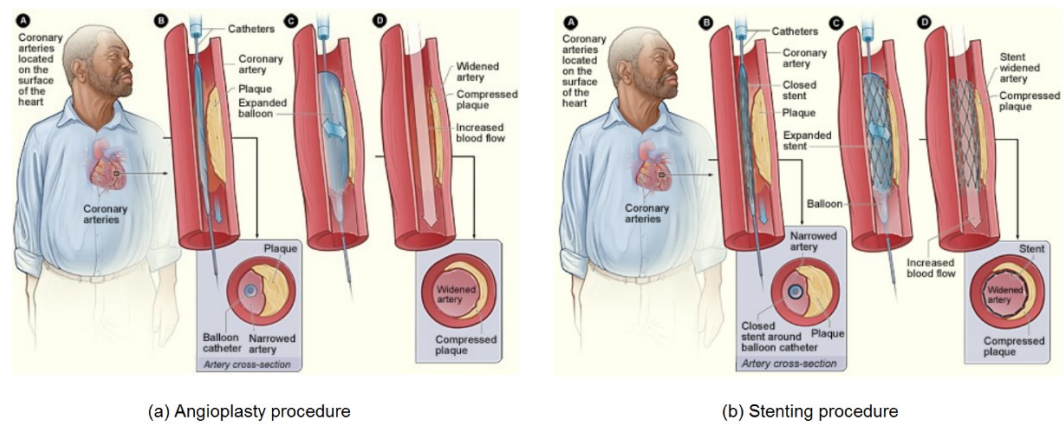


Figure 2-6 : Diagram showing (a) angioplasty procedure and (b) stenting procedure. [12].

A number of different stent types and designs have emerged due to the growing use of stents. Table 2-1 illustrates some of the available stents with their manufacturers and characteristics. Stents can be classified into different categories depending upon their mechanism of expansion i.e. self-expanding or balloon expandable, their material or coating. Although there are many applications for stents (oesophageal, tracheobroncal, biliary, renal etc.), this report mainly focuses on a cardiovascular environment but its findings can be applied to other intravascular applications.

Table 2-1: Selected stent characteristics and their manufacturers [14].

Product	Manufacturer	Structure	Material	Strut (Wire) Thickness (mm)	Metal/Artery (%) [*]	Recoil (%)	Shortening (%)	Radiopacity	Markers	Lengths (mm)	Diameters (mm)
AVE S670	Medtronic	Sinusoidal ring	Stainless steel	0.127	19	3	3	Medium	No	9, 12, 15, 18, 24, 30	3.0, 3.5, 4.0
AVE S7	Medtronic	Sinusoidal ring	Stainless steel	0.102	17-23	2	3	Medium	No	9, 12, 15, 18, 24, 30	3.0, 3.5, 4.0
beStent 2	Medtronic	Slotted tube	Stainless steel	0.085-0.095	12-17	2	0	Low	Yes	9, 12, 15, 18, 24, 30	2.5, 3.0, 3.5, 4.0
Biodivysio AS	Biocompatibles	Slotted tube	Stainless steel	0.091	19-25	2	4	Low	No	11, 15	3.0, 3.5, 4.0
Biodivysio OC	Biocompatibles	Slotted tube	Stainless steel	0.091	9-12	4	4	Low	No	15, 18, 22, 28	3.0, 3.5, 4.0
BxVelocity/Hepaccoat	Cordis, Johnson & Johnson	Slotted tube	Stainless steel	0.14	15	2.5	1.7	Medium	No	8, 13, 18, 23, 28, 32	2.25, 2.5, 2.75, 3.0, 3.5, 4.0, 4.5, 5.0
BxSonic	Cordis, Johnson & Johnson	Slotted tube	Stainless steel	0.14	15	2.4	1.7	Medium	No	8, 13, 18, 23, 28, 33	2.25, 2.5, 2.75, 3.0, 3.5, 4.0
Carbostent Sirius	Sorin	Slotted tube	Stainless steel	0.075	12-17	3-5	0	Low	Yes	9, 12, 15, 19, 25	2.5, 3.0, 3.5, 4.0
Carbostent Syncro	Sorin	Slotted tube	Stainless steel	0.075	12-17	3-5	0	Low	Yes	9, 12, 15, 19, 25	2.5, 3.0, 3.5, 4.0
Cook V-Flex	Cook	Slotted tube	Stainless steel	0.07	15	21	0	Low	No	12, 16, 20, 24	2.5, 3.0, 3.5
Diamond Flex AS	Phytis	Slotted tube	Stainless steel	0.075	10-18	3-5	1	Low	No	9, 12, 16, 20, 25	2.5, 3.0, 3.5, 4.0
JoStent Flex	Jomed	Slotted tube	Stainless steel	0.09	16	4	5	Low	No	9, 16, 26, 32	2.0, 2.5, 3.0, 3.5, 4.0, 4.5
JoStent Plus	Jomed	Slotted tube	Stainless steel	0.09	16	4	5	Low	No	9, 17, 27, 33	2.0, 2.5, 3.0, 3.5, 4.0, 4.5
JoStent Graft	Jomed	Slotted tube	Stainless steel	0.20	100	2	3	High	No	9, 12, 16, 19, 26	2.5, 3.0, 3.5, 4.0, 4.5, 5.0
LP Stent	Boston Scientific	Slotted tube	Stainless steel	0.1	15	2	3-5	Low	No	8, 12, 18, 24	2.5, 3.0, 3.5, 4.0
MAC Carbon Stent	AMG	Slotted tube	Stainless steel	0.085	8-15	3	1	Low	No	9, 13, 17, 22	2.0, 2.5, 3.0, 3.5, 4.0, 4.5
MegaFlex Genus	Eurocor	Slotted tube	Stainless steel	0.12	20	1	1	High	No	9, 12, 13, 15, 16, 17, 19, 23	2.5, 2.75, 3.0, 3.5, 4.0
Multilink Tetra	Guidant	Slotted tube	Stainless steel	0.091-0.124	12-20	2-3	3-4	Medium	No	8, 13, 18, 23, 28	2.5, 2.75, 3.0, 3.5, 4.0
Multilink Penta	Guidant	Slotted tube	Stainless steel	0.091-0.124	12-16	2-3	3-4	Medium	No	8, 13, 15, 18, 23, 28, 33	2.75, 3.0, 3.5, 4.0
Multilink Ultra	Guidant	Slotted tube	Stainless steel	0.127-0.101	15-25	2	5	Medium	No	13, 18, 28, 38	3.5, 4.0, 4.5, 5.0
NIR, 7 cells and 9 cells	Medinol, Boston Scientific	Multicell design	Stainless steel	0.1	11-18	3	3	Low	No	9, 16, 25, 32	2.0, 2.5, 3.0, 3.5, 4.0, 4.5, 5.0
NIR Royal	Medinol, Boston Scientific	Multicell design	Stainless steel, gold	0.1	11-18	5	3	High	No	9, 16, 25, 32	2.0, 2.5, 3.0, 3.5, 4.0, 4.5, 5.0
Express	Boston Scientific	Multicell design	Stainless steel, gold	0.132	11-17	5	5	High	No	8, 12, 16, 20, 24, 28, 32	2.25, 2.5, 2.75, 3.0, 3.5, 4.0, 4.5, 5.0
P-S 153	Cordis, Johnson & Johnson	Slotted tube	Stainless steel	0.062	18	5	8	Medium	No	8, 9, 14, 18	3.0, 3.5, 4.0
PURA-A	Devon	Slotted tube	Stainless steel	0.12	10-15	2	1-5	Low	No	7, 15	3.0, 3.5, 4.0, 4.5, 5.0
PURA Vario AL	Devon	Slotted tube	Stainless steel	0.07	10-18	3	5	Low	No	6, 10, 16, 24, 28	3.5, 4.0
PURA Vario AS	Devon	Slotted tube	Stainless steel	0.07	10-18	3	7	Low	No	6, 10, 16, 24, 28	2.5, 3.0
Teneo Tenax-XR	Biotronik	Slotted tube	Stainless steel	0.08	14-22	5	3	Low	Yes	10, 15, 20, 25, 30	2.5, 3.0, 3.5, 4.0
Tsunami	Terumo	Slotted tube	Stainless steel	0.08	18	5	5	Low	No	10, 15, 20, 30	2.5, 3.0, 3.5, 4.0
Small-vessel stents											
AVE S660	Medtronic AVE	Sinusoidal ring	Stainless steel	0.127	20	2	1.5	Medium	No	9, 12, 15, 18, 24	2.5
beStent (4 crowns)	Medtronic AVE	Slotted tube	Stainless steel	0.085-0.095	12-17	1.6-2.2	0	Low	Yes	9, 12, 15, 18, 24, 30	2.5
Biodivysio SV	Biocompatibles	Slotted tube	Stainless steel	0.05	9	1	4	Low	No	10, 15, 18	2.0, 2.5
BxVelocity	Cordis, Johnson & Johnson	Slotted tube	Stainless steel	0.14	15	2.5	2	Low	No	8, 13, 18, 23, 28, 32	2.25, 2.5, 2.75
Carbostent Sirius, 4 cells	Sorin	Slotted tube	Stainless steel	0.075	12-17	3-5	0	Low	Yes	9, 12, 15, 19, 25	2.5
JoStent Flex	Jomed	Slotted tube	Stainless steel	0.09	16	4	5	Low	No	9, 16, 26, 32	2.0, 2.5
Jostent Plus	Jomed	Slotted tube	Stainless steel	0.09	16	4	5	Low	No	9, 17, 27, 33	2.0, 2.5
Multilink Pixel	Guidant ACS	Slotted tube	Stainless steel	0.099	15	4	11	Medium	No	8, 13, 18, 23, 28	2.25, 2.5
PURA Vario AS	Devon	Slotted tube	Stainless steel	0.07	10-18	3	7	Low	No	6, 10, 16, 24, 28	2.5

^{*}Does not necessarily mean vessel wall coverage.

Compared to balloon angioplasty treatment, the ratio of restenosis after deployment of a stent reduces to 15-20% from 33%-50% [15]. Unfortunately, the major drawback of this stenting procedure is in-stent restenosis, i.e., the reoccurrence of stenosis. This phenomenon is related to both arterial injury and an inflammatory response of the vessel wall against the stent struts (Figure 2-7). The arterial response mainly results in stent thrombosis (ST) and neointimal hyperplasia (NH), which is the abnormal growth of endothelial cells [16].

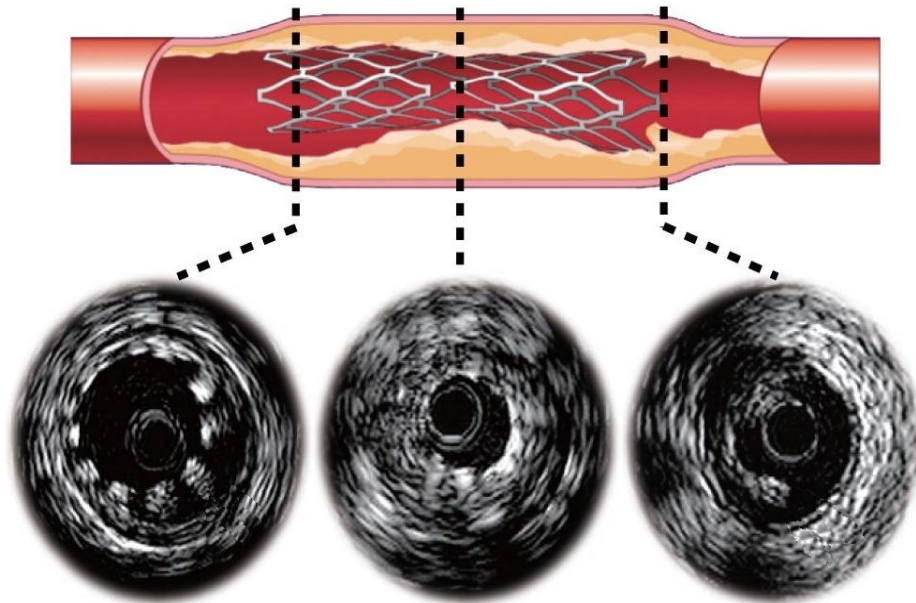


Figure 2-7: In-stent restenosis. Open source image [17].

Zahedmanesh et al. have described in detail the mechanism of in-stent restenosis upon stent implantation [18]. The process starts with disruption of the inner endothelial wall of an artery by stent struts followed by cell growth around the struts.

Table 2-2 summarises some of the risk factors involved in stent thrombosis.

Table 2-2: Risk factors of Stent Thrombosis [19].

Selected Multifactorial Causes of ST		
Stent factors	Hypersensitivity to drug coating or polymer	
	Incomplete endothelialisation	
	Stent design	
	Covered stents	
Patient factors	PCI for acute coronary syndrome/ST-segment elevation MI	
	Diabetes mellitus	
	Renal failure	
	Impaired left ventricular function	
	Premature cessation of dual antiplatelet therapy	
	Aspirin non-responsiveness	
	Clopidogrel non-responsiveness	
	Glycoprotein IIb/IIIa inhibitors	
	Prior brachytherapy	
	Malignancy	
	Saphenous vein graft disease	
	Lesion characteristics	Lesion/stent length
		Vessel/stent diameter
Complex lesions (bifurcation lesions, chronic total occlusions)		
Saphenous vein graft target lesion		
Stasis		
Procedural factors	Inadequate stent expansion/sizing	
	Incomplete stent apposition	
	Stent deployment in necrotic core	
	Residual edge dissection	

MI =myocardial infarction; PCI = percutaneous coronary intervention; ST =stent thrombosis.

In the case of BMS, restenosis occurs in more than 20% of the treated artery sections [20–22]. Figure 2-8 illustrates some of the restenosis risk

factors influenced by stent attributes. This problem of re-narrowing has been significantly reduced to approximately 10% [20,23] by the introduction of DES. But soon after its introduction the results were shadowed by concerns regarding thrombogenicity and long-term outcomes [24]. Therefore, efforts aiming at reducing the arterial injury caused by stent implantations remain crucial.

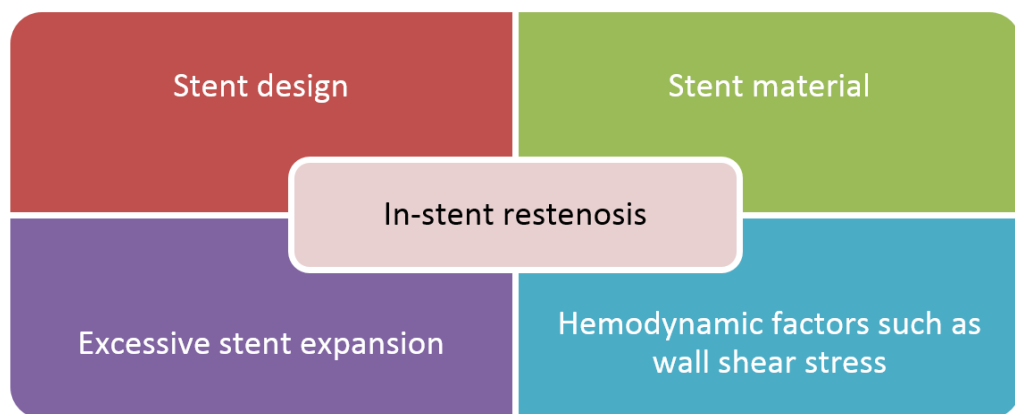


Figure 2-8: Some of the factors affecting in-stent restenosis.

From the literature previously discussed and clinical evidence, it was found that two methods are commonly adopted to reduce in-stent restenosis: stent design alteration and by changing stent materials and coatings to inhibit the abnormal growth of arterial inner wall cells. Therefore, it is believed that with the combination of optimal stent design and drug coating, effective vascular stents may be achieved [25]. This work is focused on the optimisation of stent design for specific lesions. Before going further, it is important first to understand the effect that stent design has on restenosis given by clinical studies as discussed in the next section.

2.6 Impact of Stent Design on Restenosis (Clinical Evidence)

Although a wide variety of stents are currently being used, an 'ideal stent' having no adverse effects still does not exist. As discussed in the preceding section in detail, the two most common problems that may arise after stent implantation are in-stent restenosis, and stent thrombosis which is the formation of blood clot inside the target area.

Several clinical studies [26–29] have concluded that in-stent restenosis is correlated with the vessel injury caused during stent implantation. Hoffman et al. in a clinical study suggested that balloon expansion of a Palmaz-Schatz stent was related to neointimal hyperplasia due to the techniques aggressive nature [30]. Kornowski et al. showed in their study that neointimal formation after stenting was dependent on both arterial injury and inflammatory reaction [31].

Rogers et al. carried out a clinical study of two different types of steel stents deployed in rabbit iliac arteries. They concluded that the stent having 29% less strut-strut intersections than the other, without affecting mass or surface area, reduced vascular injury by 42%, thrombosis by 69% (platelet adhesion), and neointimal hyperplasia by 38% [32]. In their investigation the stent types they used were slotted tube and corrugated ring as shown in Figure 2-9. The corrugated ring type had 29% fewer strut-strut connectors.

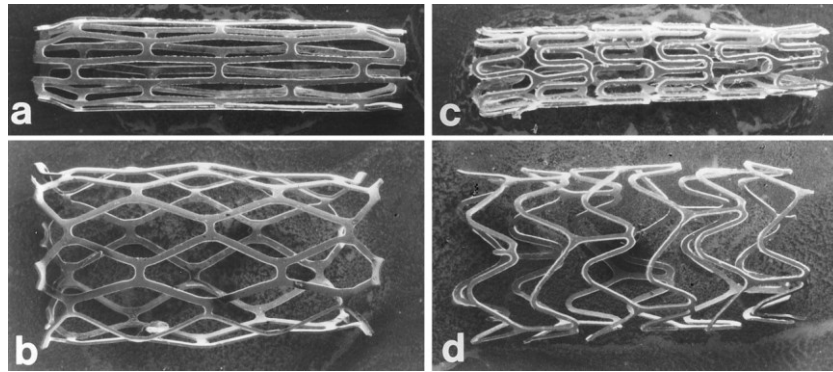


Figure 2-9: Scanning electron photomicrographs of stents of different configurations: Slotted tube stent before (a) and after (b) expansion; corrugated ring stent before (c) and after (d) expansion. Original magnification x100. [32]

The higher incidence of adverse effects associated with the slotted tube stent, as compared to the corrugated ring, was mainly due to vascular injury imposed on the arterial wall by this design. Figure 2-10 shows the difference between the injury score of these two designs under investigation. Polymer coating was also tested for these designs but the stent configuration exhibited the main effect.

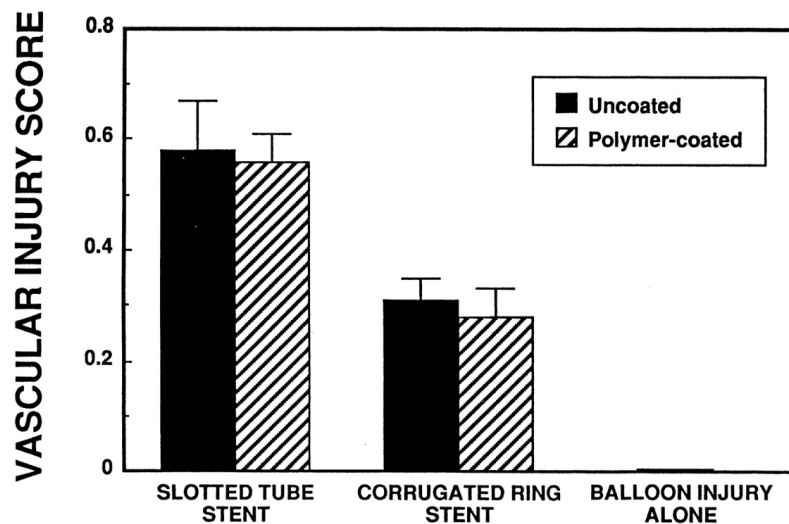


Figure 2-10: Bar graph shows vascular injury score per arterial cross section 14 days after balloon injury and implantation of steel stents or after balloon injury alone. Statistical analysis showed a main effect of stent configuration but not of stent coating [32].

Other clinical studies that focused on stent geometry [5,33] have concluded that the strut thickness especially, is a key indicator of

restenosis rates. In addition to that, a review article by Morton et al., who conducted a series of randomised trials, suggest that stent geometry plays an important role in determining a stent's resistance to restenosis [34].

Rittersma et al. carried out a study including 663 patients, dividing them into two groups. 287 patients were treated with a thin-strut stents (50 μm) and 376 patients with thick-strut stents (>90 μm). The patients treated with thin strut stents had significantly less late luminal loss than those with thick strut stents. Strut thickness was found to be an independent predictor of restenosis in this study [35].

Sommer et al. conducted a study by placing two stent types i.e. crown and wave, in rabbit iliac arteries. In their study they found out that wave stents, where the main axis of struts runs with the blood flow, optimises the flow profile and improves stent endothelialisation which is important for avoiding in-stent thrombosis and subsequent neointimal proliferation. They also suggested that strut thickness also reduces the risk of restenosis [36].

Similar studies in the field of arterial hemodynamics [37–39] and stented-vessel hemodynamic [40] have shown that areas of maximum intimal thickening correlate with areas of low wall shear stress.

The above mentioned clinical studies clearly show that altering stent geometry can potentially lead to both reduction of arterial injury and better hemodynamic response in order to reduce restenosis rates.

2.6.1 Materials

In terms of materials, a variety of stents are available commercially. Materials selected for stents must exhibit corrosion resistance and biocompatibility [41]. Stent materials normally depend upon its biocompatibility and expansion type i.e. self-expanding or balloon expandable. Balloon expandable stents are made from material that can plastically deform when expanded through balloon inflation. They would have ideally low yield strength to make it easily deformed through manageable balloon pressure and high elastic modulus for minimum recoil due to plaque [41]. After expansion, they remain in that position while the catheter is removed. These stents are manufactured in a crimped state (Figure 2-11). The most common materials for balloon expandable stents are stainless steel 316L and nitinol (shape-memory alloy) for self-expanding stents [41].

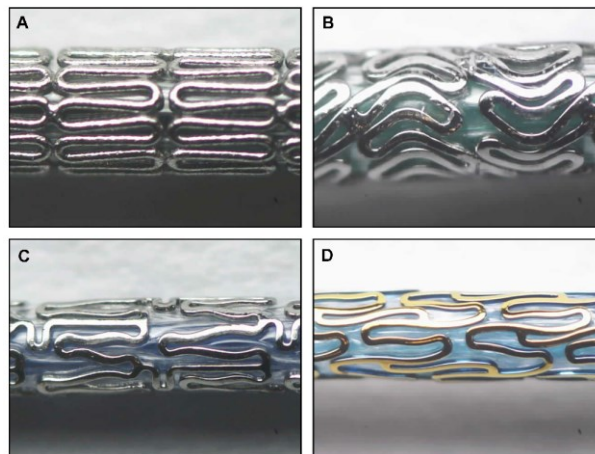


Figure 2-11: Examples of balloon-expandable stents. A: Endeavor (Medtronic), B: Taxus Liberte (Boston Scientific), C: Promus (Boston Scientific), D: PRO-Kinetic (Biotronik) [14].

Self-expanding stents are made from materials that can recover to their final shape by removal of external constraints. These stents are manufactured in their expanded state. Ideally, these stents should have

low elastic modulus and high yield stress for large strains [41]. They are compressed on a delivery system and upon reaching the diseased site, spring-back to the pre-set diameter when released from the delivery system (Figure 2-12).

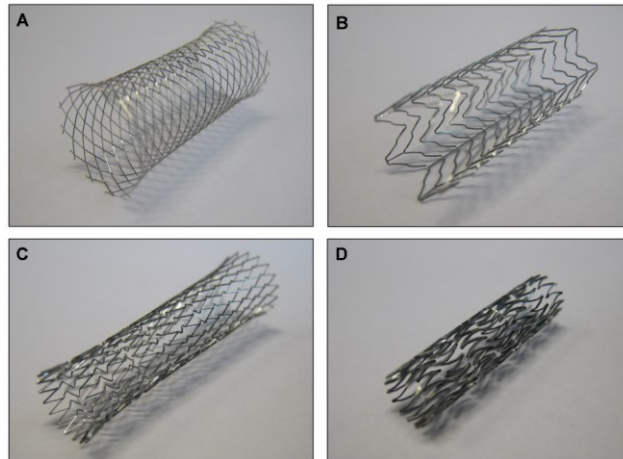


Figure 2-12: Examples of self-expandable stents. A: Wallstent (Boston Scientific), B: RX Acculink (Abbott Vascular), C: Xact (Abbott Vascular), D: SelfX (Abbott Vascular).

The characteristics of an ideal stent have been described (Figure 2-13 & Table 2-3) in numerous reviews [42–45].

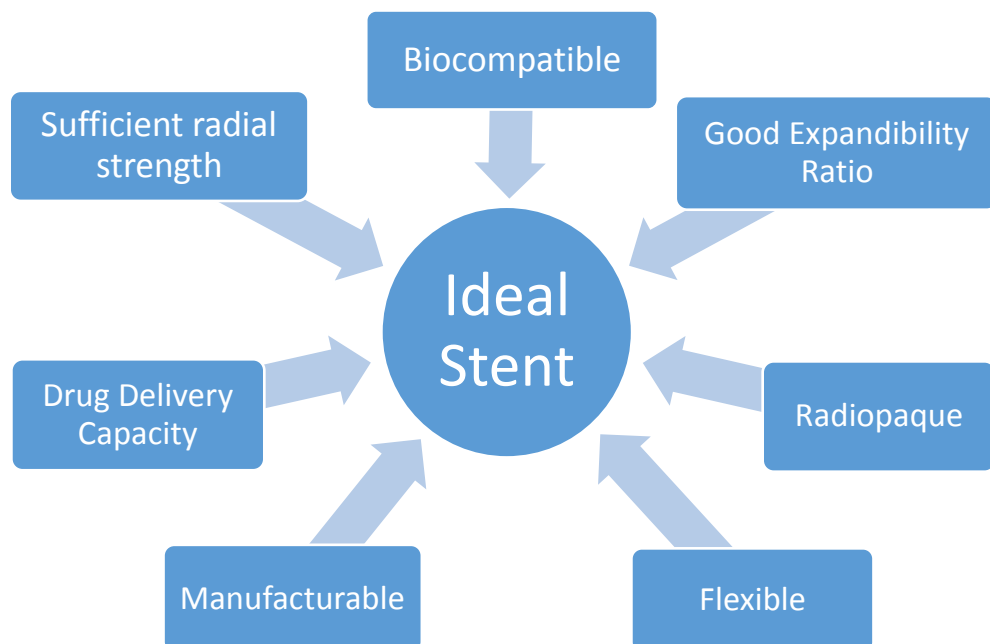


Figure 2-13: Characteristics of an ideal stent [15].

Table 2-3: Materials with ideal characteristics for coronary stent applications [46].

Properties	Material	Rationale
Elongation modulus	316L stainless steel	Optimal value for a balloon expandable stent
Tensile strength	Co–Cr	Higher value
Yield strength	Co–Cr	Much lesser when compared to its own tensile strength
Surface energy	PTFE	Lower value
Biocompatibility	Ti	Extensive literature Presence of stable oxide layer
Surface potential	Ta	Stability of surface oxide layer
Stability of surface oxide layer	Ta/Ti	Excellent stability among the implant materials
Therapeutics	Paclitaxel	Hydrophobicity
Radiopacity	Gold	High density
MRI compatibility	Ta/Ti/Nitinol	No Fe content
Preferred way of drug loading	Polymer based	Amount of drug can be increased to the need just by increasing the thickness of the coating
Preferred way of drug elution	Biodegradable	No polymer material will be present once the process is finished
Preferred category of polymers	Biopolymers	Minimal inflammatory and hypersensitive reactions

2.6.1.1 Metallic Stents

Several metals are being used for coronary stents, the most common being stainless steel 316L, due to its corrosion resistance, suitable

mechanical properties and affordability [41]. However, 316L SS has poor fluoroscopic visibility and is a non-magnetic resonance imaging (MRI) compatible material, due to its ferromagnetic nature. Other metals include platinum-iridium (Pt-Ir) alloy, tantalum (Ta), cobalt-chromium (Co-Cr) alloy, nitinol (Ni-Ti), pure iron (Fe), titanium (Ti) and magnesium alloys [46]. Stents that are made of metals only are known as bare metal stents (BMS). In 2002, a new field of drug-eluting stents (DES) was introduced, having an active drug coating to reduce in-stent restenosis. These DES typically consist of three components: a metallic stent platform, a polymer coating, and the drug itself stored within the coating [47]. After implantation, the coated drug is slowly released from the coating to the injured vessel wall (Figure 2-14).

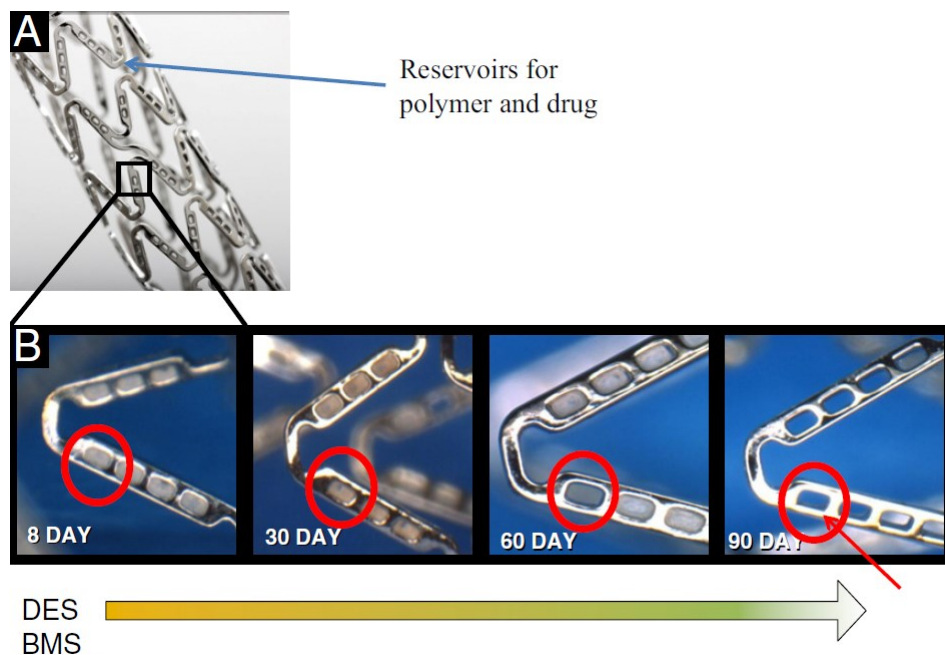


Figure 2-14: (A) The NEVO cobalt chromium stent, which has an open-cell design and unique reservoirs that contain a biodegradable polymer and sirolimus mix that (B) completely biodegrades within 90 days [16].

2.6.1.2 Polymer Stents

Mani et al. [46] have described in their study that polymer stents can be broadly classified into four groups i.e. biodegradable polymers, bio-stable (non-biodegradable) polymers, copolymers and biological polymers. Silicone was the first polymer to be used as a stent; unfortunately it has poor mechanical properties [48]. Other polymers that have already been tested for stents include polyethylene terephthalate (PET), Poly-L-lactic acid (PLLA), and poly-L-glycolic acid (PLGA) [46]. Like metallic stents, polymer stents should also be biocompatible and have sufficient mechanical properties for providing stable support to the diseased vessel.

2.6.1.3 Biodegradable Stents

Permanent metallic or polymer stents including DES have improved the outcomes of coronary angioplasty. However, their permanent presence as a foreign body in the arteries may induce complications in the long run, such as late stent thrombosis and vascular inflammation, although their scaffolding function is only required for a number of weeks [49]. Therefore, a new area of metallic and polymer based biodegradable stents has emerged, which are commonly referred to as scaffolds. These scaffolds can disappear with time after supporting the diseased vessel for a defined period. The other main advantage is that anti-inflammation drugs can be released through these stents in a controllable manner [46].

In metals, pure iron and magnesium alloys have previously been used successfully as biodegradable stents in rabbit and porcine arteries, but

these stents are prone to fracture because their yield strength is close to their tensile strength [50–52]. In polymers, the first biodegradable stent was developed by Stack et al. made of Poly-L-lactic acid (PLLA) and implanted in a canine model. Limited thrombosis and minimal neointimal proliferation was noticed in the short term and also at 18 months [53]. In humans, Igaki-Tamai was the first fully biodegradable stent to be deployed and was made of PLLA without any drug coating. However, it didn't become renowned due to its contrast heating requirement (70-80°C) during deployment to fully cure and shape-form the stent, that could potentially adversely affect the artery [49]. Other polymers, such as Poly-L-glycolic acid (PLGA) and polyurethanes (PU) have been widely used in drug delivery devices, bioresorbable sutures and orthopedic implants and are the most investigated polymers for coronary stents. In terms of drug delivery, the behaviour of PLGA is important due to its controllable degradation [54]. Figure 2-15 shows some of the metallic and polymeric biodegradable stents currently in use [49].

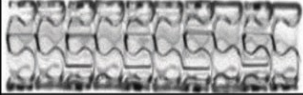









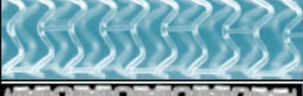

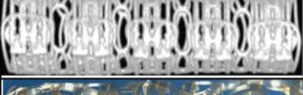


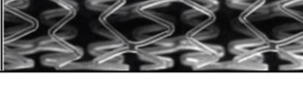
AMS 1		DESolve	
DREAMS 1		ART	
DREAMS 2		ART18Z (ART 2 nd Gen)	
Igaki-Tamai		IDEAL BTI	
BVS 1.0		IDEAL BioStent	
BVS 1.1		Amaranth	
REVA		Xinsorb	
ReZolve		ON-AVS	

Figure 2-15: A variety of metallic (AMS1, DREAMS 1) and polymeric biodegradable stents currently used in clinical practice [49].

2.6.2 Fabrication Methods

Stents are generally made from laser cut hollow tubes and braided or welded wires. Other methods include photochemical etching and knitting [41]. The most preferable production method is laser cutting due to its reliability, ability to cut complex geometries and quicker processing times [55]. Stoeckel et al. have described in their survey that the choice of fabrication method depends mainly on the raw material form used [41]. Coil stents have the simplest geometry and are made from winding wires in the form of a spring. Open and closed cell designs could be made by welding wires at different places to form sinusoidal rings. Similarly, knitting the wires could produce flexible self-expanding or balloon expandable stents. Balloon expandable stents are generally fabricated in

the crimped state and post processed with deburring and surface treatment, mainly electropolishing. On the other hand, self-expanding nitinol stents are normally made in the expanded shape and constrained in the delivery system. Laser cutting also results in a heat affected zone (HAZ) along the cutting edge which is later removed for better outcomes. In comparison to laser cutting, water jet cutting doesn't produce HAZ. A focused water jet is directed at the target metal with some abrasive additives to cut the desired pattern instead of a laser beam. Photochemical etching is another way of producing stents and has been demonstrated to be a suitable method for making magnesium-alloy stents [56]. Some of the advantages and disadvantages of the above manufacturing methods are given in

Table 2-4.

Table 2-4: Advantages and disadvantages of stent manufacturing methods [41,57,58].

Fabrication	Advantages	Disadvantages
Laser Cutting	Intricate patterns, able to process smaller diameter tube, reliable, fast, high precision and low cost. (vastly used)	Heat effects
Welding	Adjustable flexibility and wide range of size and length	Radial strength is usually less than the ones processed with laser cutting
Braiding, Knitting	Simple process, adjustable flexibility	Slow process
Photochemical Etching	Large number parts can be processed in a single run, complex patterns can be produced	Requires extremely clean operating conditions
Additive Manufacturing (AM)	Can potentially make customised stents, multi-material printing, high resolution profile [59] (Not commercialised or tested yet)	Mechanical properties may not be comparable to laser cut, poor surface due to layered fabrication and sintering of particles from the build area [59]

2.6.3 Geometry

Since the introduction of stents more than 30 years ago, a variety of different geometries have evolved to improve mechanical properties such as radial strength and flexibility. Early stents were made in the form of coils or slotted tubes. Slotted tubes designs such as Palmaz-Schatz were known for its strength but lacked flexibility, which is important when it comes to delivery in curved vessels. Later designs consisted of repetitive sinusoidal rings each known as a cell or unit. In a design review, Stoeckel et al. have categorised stent geometries into five different types i.e. Coil, Helical Spiral, Woven, Individual Rings or Sequential Rings, with each having sub-types [41]. Coil stents are usually made for non-vascular applications such as tracheobronchial and prostatic obstructions. They are extremely flexible but have limited radial strength. Figure 2-16 is an example of a coil stent design.



Figure 2-16: Esophacojl. Coil stent fabricated from nitinol ribbon [41].

Helical spiral designs are generally flexible with no or few internal links but lack longitudinal stiffness. Therefore they can be compressed or elongated during implantation, and ultimately result in irregular cell size. Figure 2-17 shows a Crossflex stent having a minimally connected helical spiral design.

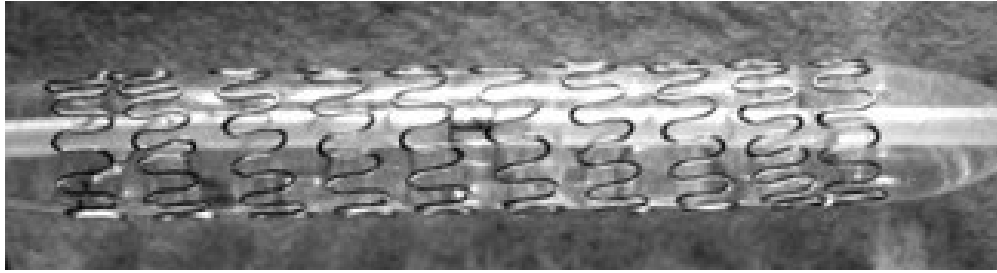


Figure 2-17: Crossflex. A minimally connected helical spiral stent fabricated from stainless steel wire [41].

Woven stent designs are fabricated from one or more strands of wire. Braided wire geometries are often used for self-expanding stents, but the drawback with these designs is that they typically shorten substantially during expansion. The radial strength of these designs mostly depends upon how the ends are fixed. Figure 2-18 illustrates the Cook ZA stent, a self-expanding knitted nitinol wire stent.

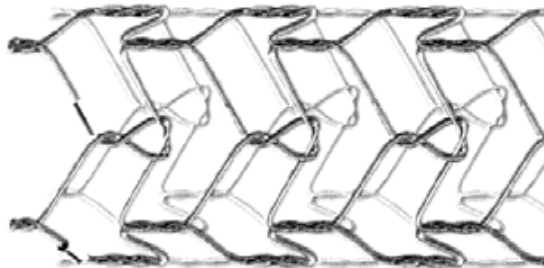


Figure 2-18: Self-expanding knitted Nitinol wire design [41].

Most modern commercially available stents are made up of two main parts: rings and links; the former plays a vital role in providing radial force while the latter mainly is there for flexibility and structural stability [34]. The rings normally have a series of repeated Z-shaped elements known as struts joined by connecting links or bridges. This category of stents could be further divided into two main types i.e. open and closed-cell designs depending upon how the individual rings are linked.

Open-cell designs have minimal links between the rings in a defined pattern compared to closed-cell where all inflection points are connected by links and hence exhibit less flexibility than the closed-cell designs.

Figure 2-19 shows some of the possible strut configurations.

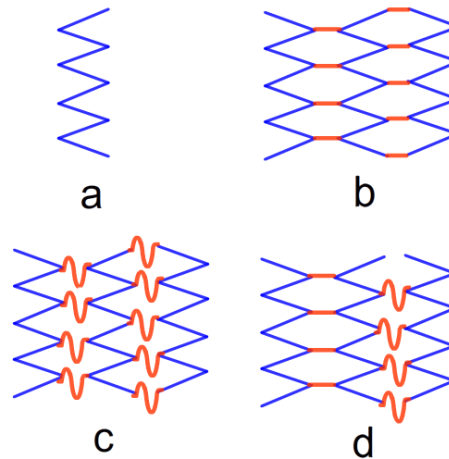


Figure 2-19: Strut configuration: open cell (a), closed cell: Non-flex connectors (b), flex-connectors (c), combined flex/non-flex connectors (d).

A variety of combinations could be formed by introducing links connecting struts at different locations. Peak to peak connection is used to describe rings connected to each other via the outer radius of the inflection points. Similarly in peak to valley connection, the outer radii of ring inflection points are bridged to the inner radii of the adjacent ring inflection points. Other types include mid-strut to mid-strut connections. The shapes of the links also vary; designs have improved flexibility by adding N, S, U and V type flex connectors [41].

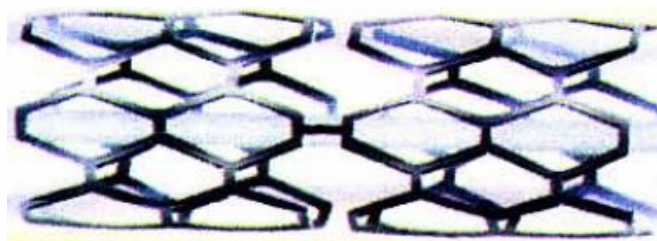


Figure 2-20: Palmaz-Schatz slotted tube type stent [41].

The Palmaz-Schatz stent is an example of closed-cell design, having the main advantage of optimal scaffolding and a uniform surface (Figure 2-20). Later designs such as the NIR stent has improved flexibility due to 'V' type links as shown in Figure 2-21.

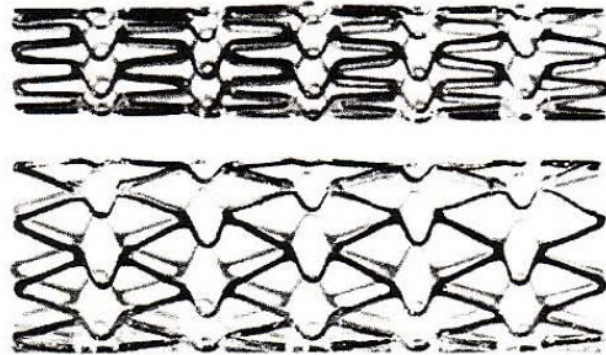


Figure 2-21: NIR stent with 'V' type flex connectors [41].

2.7 Finite Element Analysis in Stent Design

Finite element analyses (FEA) of stent design are very useful tools for evaluating the performance of stents and can be used alongside experimental studies to optimise stent designs. In addition to being cost effective, computational analysis also enables estimation of the arterial wall stresses and behaviour in reaction to stent implantation, therefore providing insights into different aspects of stent geometry that may improve the final outcome.

Numerous studies have employed FEA to look at various stent geometries and determine the patterns of arterial wall stress that they induce. These studies allow us to understand the mechanics of stent-artery interaction [60–62] and the influence of several different stent geometry variables such as stent strut thickness [62,63] and plaque

composition [64,65]. Other studies have investigated and compared commercially available stents [66,67] and generic designs [68].

One of the pioneering studies of stent geometry parameterisation among the above discussed studies was of Migliavacca et al. [60]. In their study they carried out a parametric analysis by varying different features such as strut thickness, slot length and metal/artery index to evaluate the mechanical performance of a slotted tube stent design. They concluded that a stent with lower metal to artery ratio will exhibit higher radial and longitudinal recoil but a lesser degree of 'dog-boning' (excessive expansion of stent ends). Similarly, strut thickness also plays an important role in the expansion profile. They also conducted experiments on stent expansion and observed the deformation under scanning electron microscope, which were in close agreement with the computational model.

Bedoya et al. [68] investigated the interaction of an artery with a parametric stent model. In their study, stents were defined by three geometric parameters: strut spacing (h), radius of curvature (ρ), and axial amplitude (f), illustrated in Figure 2-22. They reported that stent designs having large strut spacing, a non-zero radius of curvature, and large amplitude induced lower stresses on the artery.

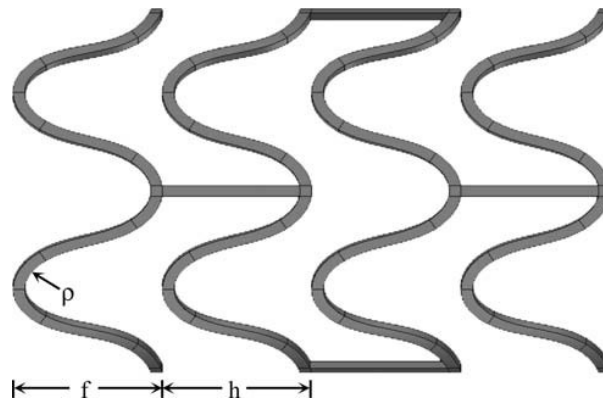


Figure 2-22: Design parameters. Generic stent showing the three parameters of interest: h is the connector bar length (or strut spacing), p is the radius of curvature at the crown junctions, and f is the axial amplitude. These three parameters were varied to test their effects on artery wall stress [68].

Stent expansion during deployment plays a crucial role in the biomechanical environment and significantly influences restenosis. Two-dimensional linear elastic models have been employed by Rogers et al [69] to investigate balloon expansion with stent and artery contact. Results of that study show that high inflation pressures, wide stent-strut spacing and more compliant balloon materials cause larger surface-contact areas and contact stresses between stent struts. It was reported that stent design and deployment methods play a vital role in stenting outcomes. A similar interesting study was carried out by Mortier et al. [70] in which they investigated the effects of balloon folds and placement during stent implantation. Their results showed that the number of balloon folds and position with respect to the stent can greatly reduce the dogboning effect which in turn influences the artery. Chua et al. [71] also looked at a stent design similar to a Palmaz-Shatz stent with five different strut and slot sizes to investigate the stress distribution, deployment pressure, elastic recoil and foreshortening. They found out in their study that increasing slot size is better than strut width to achieve a higher expansion rate without significantly impacting foreshortening.

A number of other studies have focused more on the stresses imposed on the artery wall. Lally et al. [67] modelled the stent-artery interaction of commercially available stents (NIR-Boston Scientific; S7-Medtronic AVE) on an idealised stenosed artery. Their results showed that the modular S7 stent design causes lower stress to an atherosclerotic vessel with a localised stenotic lesion compared to the slotted tube NIR design. These results correlated well with the clinical restenosis rates associated with respective stents. The testing methodology is proposed as a preclinical testing tool, which could be used to compare existing stent designs as well as help in developing novel stent designs. Appendix A presents an overview of selected clinical and FEA stent analysis studies.

2.8 Structural Optimisation

Before describing stent design optimisation studies, this section provides a background and main types of structural optimisation methods. According to Gottfreid and Weisman (1973) optimisation is defined as “*an art of obtaining best policies to satisfy certain objectives at the same time satisfying fixed requirements*”. This definition is found to be applicable in a wide variety of fields such as finance, engineering, biomedical applications and energy [72,73]. In terms of structural engineering, optimisation aims to achieve the best performance for a structure that can sustain service loads while satisfying certain design constraints such as a given amount of material [74]. The ‘best performance’ is normally a measure of mechanical properties of the structure, although other functionalities and aesthetics may also influence the design selection.

From a mathematical point of view, optimisation aims at finding the maximum or minimum of an objective function such that the convergence criteria and all the specified limiting values or constraints are satisfied. That is achieved by changing the values of design variables. The minimum or maximum optimal points of an objective function are called optima. Optima could be local or global depending upon the complexity of the function. Figure 2-23 shows local and global optima for a given function, where it is evaluated in an interval $[x_1, x_5]$ known as the design domain.

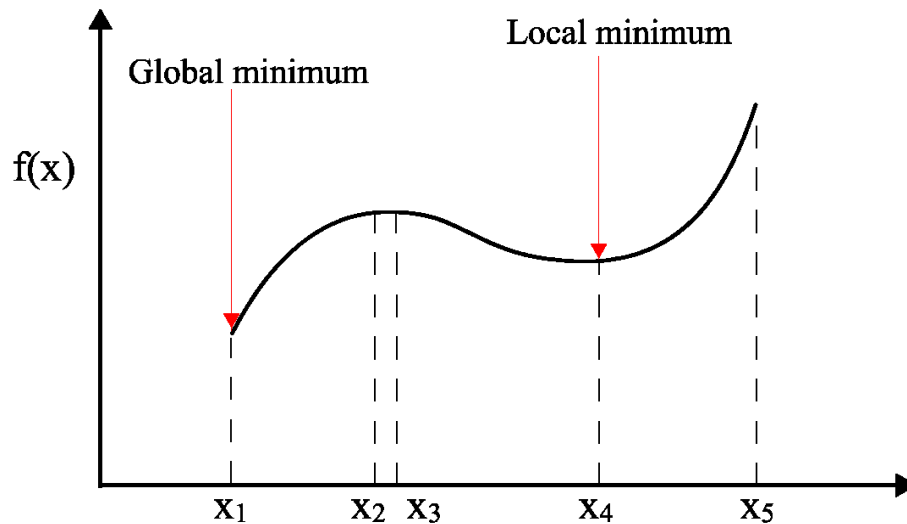


Figure 2-23: Local and global optima.

In most cases, the global optimum is desired but it may be hard to achieve or may not exist especially in nonlinear optimisation. For example gradient-based approaches may struggle to find the global optimum and are likely to get stuck in local optima. Stochastic based algorithms on the other hand aim to increase the probability of finding the global optimum.

Over the past few decades, due to the advancements in computational speeds and algorithms used in design optimisation, a growing number of

engineers and architects have started to experiment with and benefit from design optimisation for a variety of fields including biomedical applications.

The first step towards solving an optimisation problem is to adequately formulate the problem by carefully selecting the desired objective function that needs to be maximised or minimised. Depending upon the requirement, the objective could be a structural response such as displacement, stiffness, force, strain or minimisation of weight of a component etc. The design variables and constraints are then specified. The aim is then to determine the optimal values for the design variables. An example of an optimisation is given below.

$$\text{Objective:} \quad \text{Min } f(x) \quad 5.1$$

$$\text{Design variable:} \quad x = (x_1, x_1, x_1 \dots, x_n)^T \quad 5.2$$

$$x \in X \subset \mathfrak{R}^n \quad 5.3$$

Constraints:

$$g(x) = 0 \quad 5.4$$

$$h(x) \leq 0 \quad 5.5$$

where $f(x)$ is the objective function, x is the design variable which belongs to a subset X of the n -dimensional real space \mathfrak{R}^n . Equations 5.4, 5.5 represent equality and inequality constraints respectively with $g(x)$ and $h(x)$ being the constraint functions.

continuum structures to find optimal design. Topology optimisation (TO) is to find the optimal spatial distribution of material and connectivity of structural elements [74]. In other words, the goal of topology optimisation is to find the best use of material of a structure that is under either single or multiple load scenarios.

Before discussing structural optimisation techniques used for stent applications, an overview of each of these optimisation types is presented as follows [77].

2.8.1 Sizing Optimisation

Sizing optimisation is commonly applied to a truss type structure to obtain the optimal cross-sectional areas of beams. In this case the sizing design variable would be the beam's cross-sectional area, but frequently the material thickness of a plate or sheet is also used. The approach has been successfully applied to the structural design optimisation of wind turbine towers by Negm & Maalawi [78], where the cross-sectional areas of tower segments were used as sizing design variables. A schematic example of sizing optimisation applied to a truss structure can be seen in Figure 2-25.

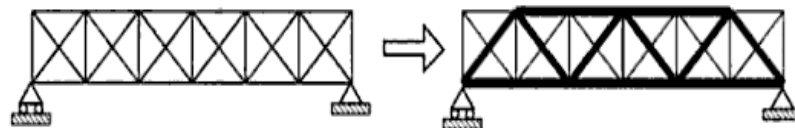


Figure 2-25: Size optimisation of a truss structure [77].

2.8.2 Shape Optimisation

Shape optimisation is more advanced than sizing optimisation in that it determines the optimal boundaries of a structure for a given fixed topology. Design variables are typically geometric parameters, such as spline control points, defining the shape of a structure in either. A shape optimisation technique has been applied by Rispler et al. [79] in the design of adhesive fillets, by Waldmane et al. [80] in the design of shoulder fillets in flat plate plates, and by Jones et al. [81] in the design of holes in plates for the consideration of fracture strength. In each of these cases, spline control points were used as design variables in order to alter each shape boundary. A schematic example of shape optimisation is shown by Figure 2-26.

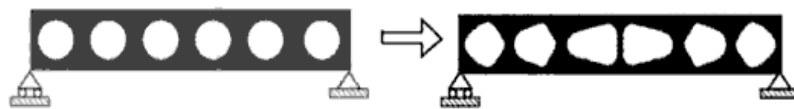


Figure 2-26: Shape optimisation of a truss structure [77].

2.8.3 Topology Optimisation

Both sizing optimisation and shape optimisation, however, has a disadvantage of being completely dependent on the initial structure and are therefore unable to introduce additional holes within the structure for the purpose of reducing weight. Topology optimisation (TO) was developed to overcome this deficiency and is consequently a much more powerful design tool. In theory, topology optimisation is capable of finding the best material distribution within a design space, independent of the initial starting design structure [77]. This allows these methods to be used

earlier in the design process (at the conceptual stage) before the design is heavily constrained, compared to either sizing or shape optimisation. As with shape optimisation, topology optimisation causes changes to the FE model and therefore requires increased computation. A schematic of topology optimisation applied to a simple beam can be seen in Figure 2-27.

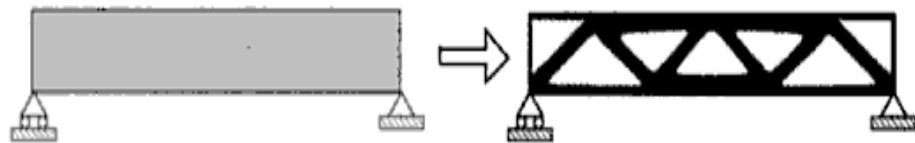


Figure 2-27: Topology optimisation of a truss structure [77].

Typically the given design domain is initially discretised into a mesh of finite elements and is then solved to obtain a structure consisting of solid and void regions based on the optimisation results. Figure 2-28 illustrates the general scheme of TO where a force \mathbf{F} is applied to a structure with a given initial design domain Ω . Ω_v and Ω_s represents the resulting void sub-domain and solid domain respectively.

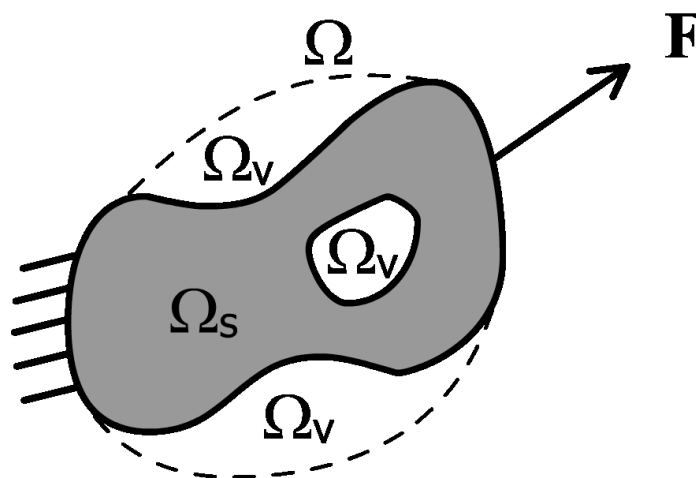


Figure 2-28: General scheme of topology optimisation.

Out of the three structural optimisation sub-categories, topology optimisation offers the greatest opportunity for creating novel designs as a result of it being completely independent of any initial design, unlike both sizing and shape optimisation which rely on an initial design as a starting point. Although topology optimisation has been used rarely for stents, it can be used to produce novel designs.

The finite element method and optimisation are useful tools for designers to analyse different loading conditions and design parameters of stents to improve the outcome of stenting procedure and reduce the adverse effects associated with it. As described earlier, one of the most serious problems with the stenting procedure is the suboptimal deployment of stents which may occur due to high contact forces from different types of diseased arteries. The geometry and stiffness of an atherosclerotic artery varies due to plaque shape and material properties. As a result it applies variable loads longitudinally on an implanted stent. Because of improper stent design, it may recoil due to higher radially compressive force, which leads to unacceptably low lumen area and non-ideal lumen shape. There are no specific rules or guidelines in the literature to design an ideal stent and most commercially available stents are largely developed and experimentally tested using a “trial-and-error” approach. Although many studies have been carried out to improve the typical rings-and-links stent design, TO has not been used to develop a full length stent for lesion-specific environment. TO has the ability to provide stent design concepts with optimal material distribution for different plaque types and is utilised in this work.

TO is often used at conceptual design stage and is usually post-processed to meet the manufacturing requirements. The most commonly used strategies to solve TO problems are the homogenisation method [82,83], the evolutionary structural optimisation (ESO) method [84,85] and the density or solid isotropic material with penalisation (SIMP) method [77]. In the ESO method, an iterative material removal of material is involved which is achieved by either reducing the stiffness of elements or entirely removing them from the design domain. ESO in essence, creates takes the design towards an optimal state by keeping the efficient elements and removing the inefficient elements. In the homogenisation method, each unit cell of a structure is imagined to be made of a composite material with microscale voids or holes to form a porous medium. The optimisation problem is then solved for the optimal porosity of the structure. This is achieved through determining the optimum parameters of holes in each cell such as size and orientation. The porous nature of the method made it difficult to produce it via traditional manufacturing method. This idea was further developed into a simpler approach now commonly known as SIMP where optimal mapping of an isotropic material is determined. The structure is allowed to have a continuous representation of element densities and a single variable is required per element as opposed multiple with the homogenisation method. This method is known as soft-kill compared to the hard-kill method employed by ESO. SIMP is simpler and a powerful TO algorithm and is extensively used in commercial software. It will be used in this

thesis to optimise stent design and is described in the subsequent section.

2.9 Solid Isotropic Material with Penalisation

The SIMP method was first proposed by Bendsøe in 1989, it is also known as the density or power law method. The basic concept of this method is that each variable in a given structure is assigned a density value, which is used as the design variable in the optimisation. Elemental densities are increased in places where the strain energy is higher and decreased in regions where it is lower thereby creating a new stiffness distribution in the structure [86]. The density variable is denoted by ρ , and to penalise the intermediate densities to obtain a discrete solution, a penalty factor is introduced to make elements with intermediate densities less favourable in the optimisation. The penalty factor can increase the efficiency of the results by inhibiting elements with intermediate densities and therefore producing an optimised structure with mostly solid or void elements. No elements are removed in this method. In the SIMP method, the elastic tensor is defined as:

$$\mathbf{E}(x) = x^p E_{ijkl}^0, \quad p > 1 \quad 5.6$$

$$V = \int_{\Omega} x d\Omega \quad 5.7$$

where x is the design variable of each element with volume density ranging $0 \leq x \leq 1$, Ω is the structural design domain for optimisation, p is the penalty factor and the volume V is evaluated as its integral over the design domain. In MSC Nastran, the penalty factor is always greater than

1 and values typically used are 3 for solid elements and 2 for shell elements. Figure 2-29 and the list below illustrates the steps during SIMP topology optimisation for compliance minimisation for a given volume fraction.

- a) All elements of the design domain are assigned a homogenous density distribution initially.
- b) FEA is carried out for the obtained density distribution resulting in nodal displacements. During the iterations, the density variables are updated based on the previous iteration.
- c) Compliance is evaluated and the change in compliance with respect to the objective function is monitored.
- d) The optimisation ends if the change in compliance is small based on the convergence criteria.
- e) The results are post processed by specifying a density threshold.

Upon completion of the optimisation iterations, the output results consist of elements with densities ranging from 0 to 1. MSC Patran allows post processing to produce structures with smoothed boundaries.

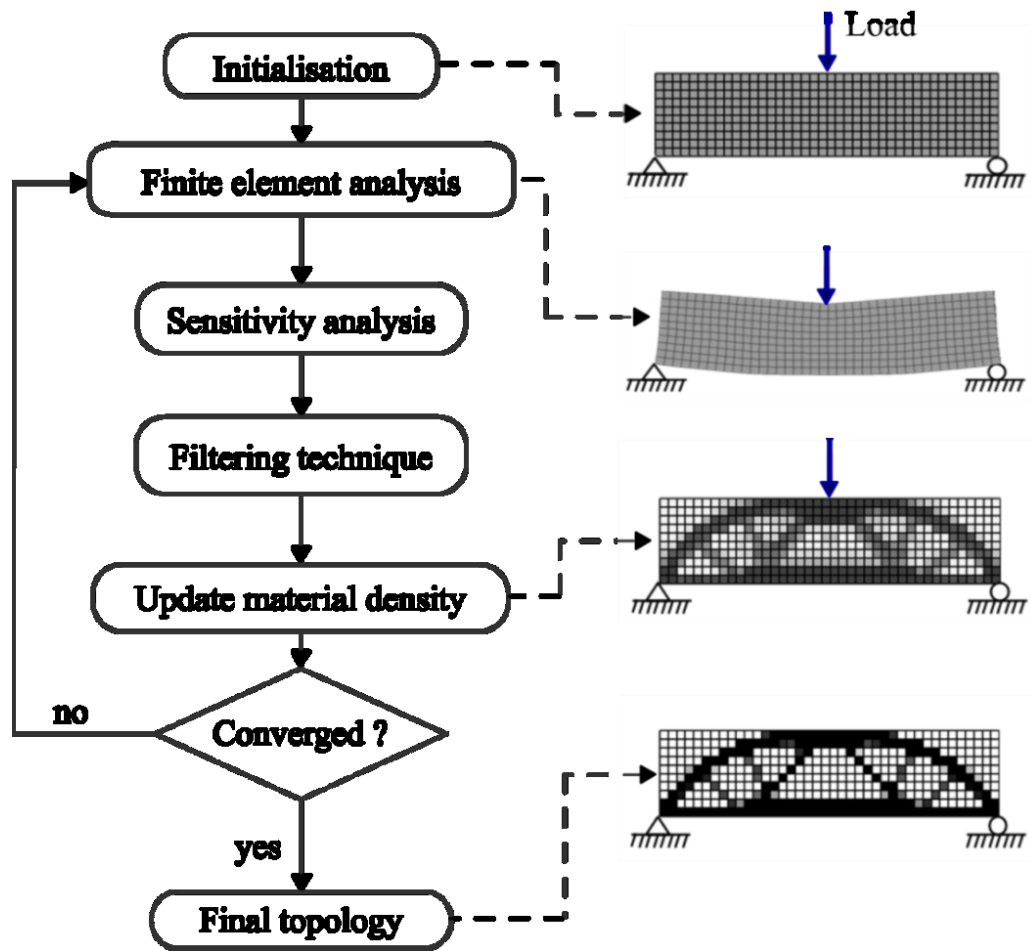


Figure 2-29: General process flow of topology optimisation using SIMP. Adapted from Lee 2011 [87].

2.10 Optimisation of Stent Design and Lesion-Specificity

Although being very limited in the literature, computational models focusing on the optimisation of stent geometry offer effective solutions to address some of the important challenges such as achieving the desirable stent geometry features that reduce the risk of restenosis. Wu et al. [88] conducted a shape optimisation study to increase the scaffolding ability of biodegradable magnesium stents by effectively increasing the strut width, also extending its expected degradation time. Stress concentrations in stent geometry are also crucial to consider in the

design to develop stents with improved fatigue life. Abad et al. [89] used shape optimisation to achieve a design with superior fatigue life.

As explained earlier, expansion of a stent during implantation in an artery is very important with regards to the overall outcome of the treatment. A number of studies have looked at the expansion of stents under different loading conditions. In terms of optimisation, Wang et al. [61] studied the effects of strut cross-section size of two different stent designs on stent expansion and concluded that dog boning and foreshortening could be reduced by altering the strut at the end rings. Beule et al. [90] carried out optimisation of braided wire self-expanding stents and achieved a design with reduced foreshortening by 20% while maintaining radial stiffness but without considering artery or plaque in the investigation. Li et al. [91,92] used a single weighted objective function based on a parametric model in their optimisation to minimise dog-boning, foreshortening and recoil of a commercial stent. They concluded in their investigations that dog boning may be avoided by effectively manipulating strut length of the cells on either sides of the stent, varying from the length of struts in the central part of the stent. Pant et al. [93,94] further extended these studies into multi-objective optimisation of stents incorporating recoil, volume average stress in the arterial tissue, flow index, drug distribution and stent flexibility. They used three geometric parameters (strut thickness, ring amplitude and link height) to optimise these objectives. A non-dominated sorting genetic algorithm (NSGA-II) was used to search for the optimal family of designs and a number of trade-offs between the objectives were identified. Clune et al. [95] used non-uniform rational basis spline

(NURBS) to parameterise stent design to optimise the shape of a single repeating cell of the stent rings in order to achieve better fatigue resistance. Taking a multi-objective optimisation approach, they successfully generated a Pareto front to represent the trade-off between fatigue resistance and flexibility.

Li et al. [96] used an optimisation method combined with kriging surrogate model to develop the approximate relationship between optimisation objectives and design variables for optimal stent expansion. While simulating free expansion of a balloon expandable stent, they kept stent dogboning as the performance factor. They were able to demonstrate improved fatigue life of two selected stent designs (diamond-shaped and sv-shaped) as a test case while eliminating the dogboning phenomenon. Kriging surrogate model, a relatively recent phenomenon, is a semi-parameter interpolation technique and is widely used in multi-disciplinary design optimisation.

In another recent study, Puértolas et al. [97] developed a methodology for patient-specific nitinol colonic stents to alter the behaviour to achieve variable radial stiffness along its longitudinal axis by a parametric analysis of design features such as diameter, slot length, the number of circumferential slots and tube thickness. With their method, they were able to approximate the mechanical behaviour of stents, such as the radial expansion force, in different sections to aid customised designs.

Pant et al. [93] and Amirjani et al. [98] carried out FEA and CFD analyses to generate a range of multi-disciplinary objectives. Amirjani et al. [98]

defined an aggregate objective function which combined mechanobiological response such as arterial wall stress with stent recoil and flow induced shear stress. Generally, with any stent design, objectives such as stent recoil, arterial stress and flexibility are in competition such that improvement in one objective results could result trade-off in others. Pant et al. [93] used stent recoil and flexibility with a drug elution metric in a constrained optimisation study in which optimised designs were obtained for each metric relative to a base line geometry without diminishing any other metric.

The above discussed optimisation studies do not take into account different plaque geometry and composition. A more realistic approach was adopted by Timmins et al. [65] by taking different plaque compositions with two different stent designs to examine the solid mechanical effects of varying stent design and plaque composition on the biomechanical environment in their analysis. In their study they used two generic stents, one stiff and the other less stiff, similarly choosing plaque stiffness as more, less and equally stiff as the artery (Figure 2-30). They concluded that the selection of stent geometry for specific lesions is vital to minimise the injury inducing stresses in the artery. Further investigation is needed to tailor the stent design according to the required realistic loading conditions.

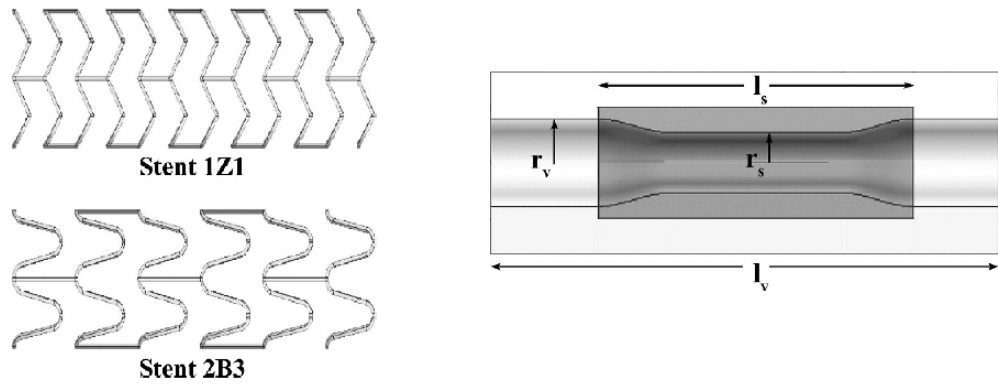


Figure 2-30: Two generic stent designs. Stent 1Z1 as stiff, Stent 2B3 as less stiff with un-deformed plaque geometry [65].

As described in section 2.2, with the progression of atherosclerosis, plaque morphology changes. This means variation in shape, size and composition. Composition also effects the stiffness of the plaque and hence alters the mechano-biological interaction with stents. Stent implantation in arterial environment with different shape and stiffness can likely yield different vascular behaviours. For instance, over-expansion of stent causes arterial injury, which can lead to neointimal hyperplasia [99]. Assessing the nature of the artery and plaque morphology therefore, is crucial in achieving successful stenting procedure. Plaque size and stiffness also vary with the progression of the disease (Figure 2-32). Plaques types could be mainly categorised into three types based on their tensile properties. Figure 2-31 depicts the stress-strain tensile data represented by the strain energy density functions for the three different plaque histological classes averaged from autopsies of 21 patients in a study [64].

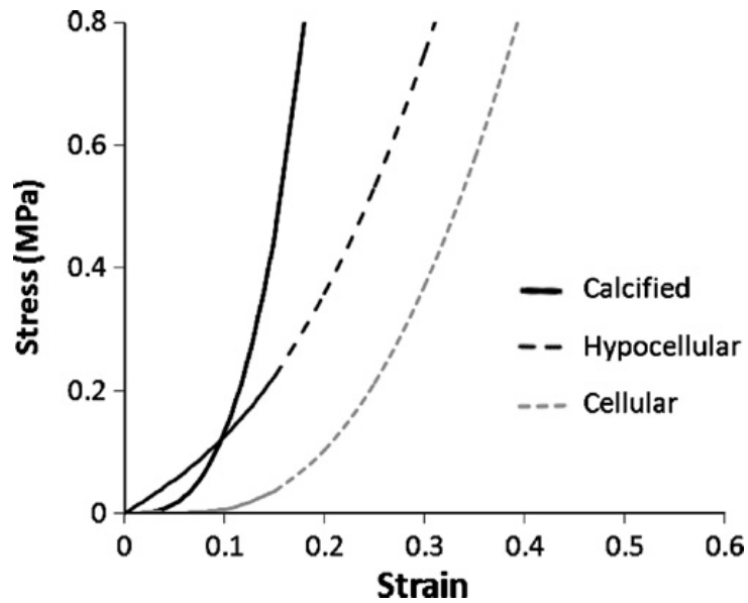


Figure 2-31: Uniaxial tensile stress–strain data represented by the strain energy density functions for the three different plaque types in the finite element models. Source: [64]

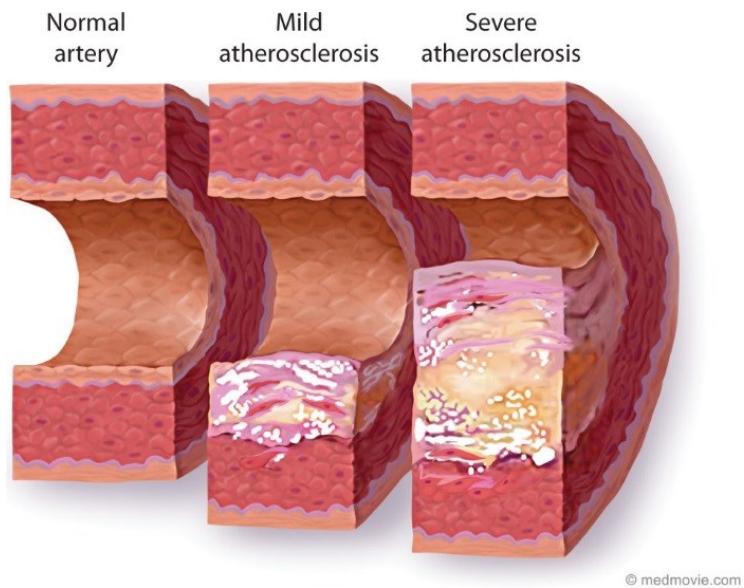


Figure 2-32: Progression of atherosclerosis leading to plaque morphology change. Copyright Medmovie, reproduced with permission from Medmovie [100].

Coronary lesions have been known to be more eccentric [101], this is expected to yield varying compressive pressure on stents and ultimately impact their interaction. Which is one of the reasons that many of the

mentioned FEA studies [62,66,102,103] have chosen asymmetric lesions for their analysis.

In addition to that, it has also been found that male and female coronary arteries differ in morphology. Studies [104–107] have shown that the main coronary arteries in women are smaller in diameter than men. Furthermore, plaques in women also appear less calcified. Hitesh et al. [106] studied gender based differences in coronary arteries of over 700 patients, the difference in diameters was found to be 11.25% to 13.5% larger in males vs females, depending upon the type and location of coronary artery. There was no significant relationship between coronary artery diameter and other clinical factors such as age, race, weight, height, cholesterol, diabetes, hypertension, family history and smoking. As gender significantly influences artery diameters and nature, this warrants gender and patient-specific approaches for stent design and treatments.

Although many groups have researched biomechanical characters of stents using finite element methods [63,65,68,94,108], topology optimisation has been rarely explored in patient-specific stent design fields. Wu et al. [109] conducted a study to topologically optimise the stent struts (Figure 2-33), with a pre-defined overall stent topology, for drug holding capacity while increasing the strut stiffness and keeping in view the manufacturing constraints.

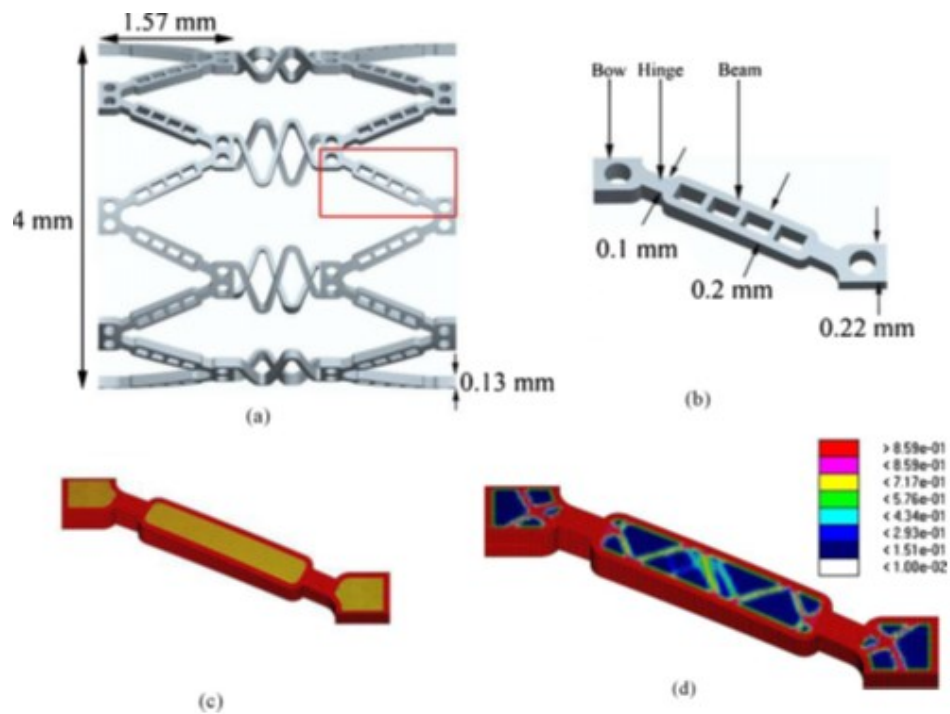


Figure 2-33: (a) Illustration of the Conor stent with the opened configuration, which is composed of honeycombed strut units joined by flexible links. (b) One strut isolated from the stent unit. (c) The strut model meshed in OptiStruct without holes, yellow part being the design domain for optimisation. (d) The element density distribution with MMS of 0.042mm at the iteration number of 30 [109].

Another topology optimisation study looked at creating stent cell design for flexibility and hardening separately [110]. It was demonstrated that it is possible to design stent cells using the topology optimisation technique. Although the resulting topologies were significantly different to the commercial designs, they met the flexibility and hardening criteria.

The final geometry of a diseased artery after stent implantation is of paramount importance. It is shown in another study, involving self-expanding stents [111] that lesion calcification of the arterial wall could lead to a more severe residual stenosis, dog boning effect and corresponding edge stress concentrations after stenting (Figure 2-34).

This ultimately could mean that the stent may not be able to serve its purpose to adequately prop the diseased artery.

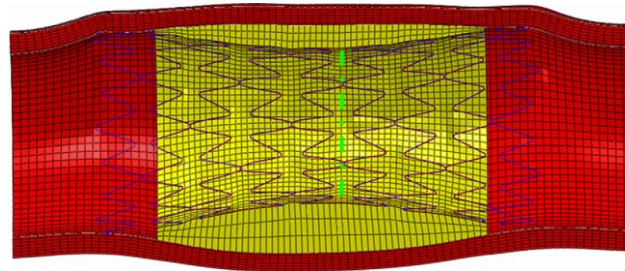


Figure 2-34: The stented artery with calcified plaque [111].

Zhao et al. [112,113], used a soft and a hard plaque both causing a stenosis of 50%. Immediately after stent deployment, 39% residual stenosis still existed in stiffer plaque which does not satisfy the desired residual stenosis standard of 30% or less. It is therefore vital to consider design changes to the stent to achieve acceptable lumen diameter in such calcified arteries.

Garcia et al. [103] investigated the design of a variable radial stiffness self-expanding stent for a carotid artery with calcified plaque. It was emphasised in their study that all desirable features in a stent are hard to achieve at the same time, therefore it is necessary to reach a compromise between tissue stress, stent flexibility and radial force. In their investigation they mainly focused on altering the strut thickness of the stent to achieve minimal contact pressure in the healthy region of the artery during expansion (Figure 2-35).

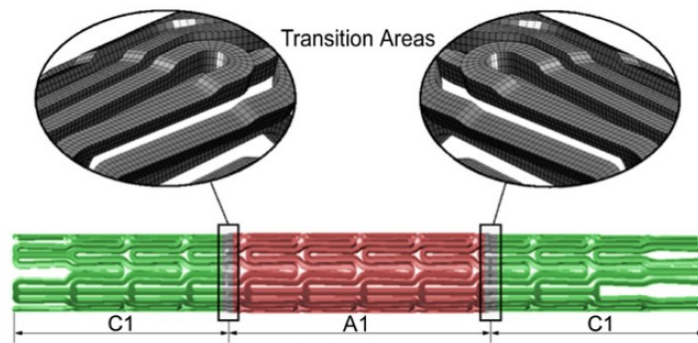


Figure 2-35: Variable radial force stent with struts thinned in sections C1 on either side [103].

This approach by Garcia et al. is a step towards customised stent geometries for specific lesion types. It will be more challenging when it comes to complex lesion geometries and stiff plaques. Therefore topology optimisation based on contact analysis of stent and diseased artery is a novel approach to take into account the accurate loading conditions to tailor the stent design according to specific lesions while maintaining vessel lumen area.

Another important aspect of stent design consideration is its long-term structural integrity and fatigue life. As the heart beats, the arteries pulse at typically 70 times per minute (40 million times per year), which induces cyclic loading on the implanted stent. The US Food and Drug Administration (FDA) recommends that stents must be able to withstand 10 to 15 years of pulsatile loading, which is equivalent of 400-600 million cycles [114]. Coronary stent fracture is relatively a rare complication of stent implantation [115] and can result from a complex interaction of two states of stress i.e. static loading after implantation including higher residual stresses in some regions and the second state being pulsatile loading [116]. It is also envisaged that bioresorbable stents or scaffolds (BRS), which dissolve in the body over time, may resolve this issue of

stent fracture [115]. BRS, also sometimes known as BVS (bioresorbable vascular scaffolds), represent a new era of interventional cardiology and is gaining further attention due to its potential benefits such as disappearing after the healing period and avoiding permanently caging the vessel [117].

2.11 Using additive manufacturing for design customisation

According to the American Society for Testing and Materials (ASTM), additive manufacturing (AM) is the (ASTM 2792-12a):

“process of joining materials to make objects from 3D model data, usually layer upon layer, as opposed to subtractive manufacturing methodologies.”

Another most common term to describe AM is 3D printing. AM technologies can be grouped into seven categories based on the material and process involved (ASTM 2792-12a). These categories include:

- Binder jetting
- Directed energy deposition
- Material extrusion
- Powder bed fusion
- Vat polymerization
- Sheet lamination
- Material jetting

While the above processes differ in certain aspects, common steps involved are illustrated in Figure 2-36:

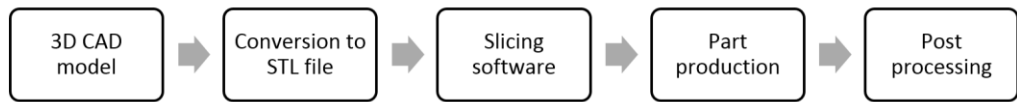


Figure 2-36: Steps commonly involved in an additive manufacturing process.

Manufacturing of truly optimised designs could be limited by traditional methods [118]. This is due to the inherent constraints that forces a design to minimise manufacturing and assembling difficulties [119,120]. AM could potentially achieve optimal geometries utilising the three-dimensional freedom offered by its layered approach.

Traditional methods are generally based on the idea of low cost for large production quantities, for smaller quantities where a customised outcome is required, these techniques can become significantly costly. AM on the other hand can overcome this limitation and allow mass customisation as tool changes are not required and hence the high cost associated is avoided. This benefit could be utilised for creating new customised medical devices and their performance evaluation. Current literature has not explored AM for stent design and fabrication. This method has the potential to create patient-specific stent design and reduce *in vitro* testing cost and time as proposed by the current work [121].

The method used in the current study for validating the performance of one of the new stent designs was selective laser sintering (SLS), which is a powder bed fusion method involving fusion of powder particles with the help of a laser beam [122]. Figure 2-37 shows a schematic diagram of the SLS process.

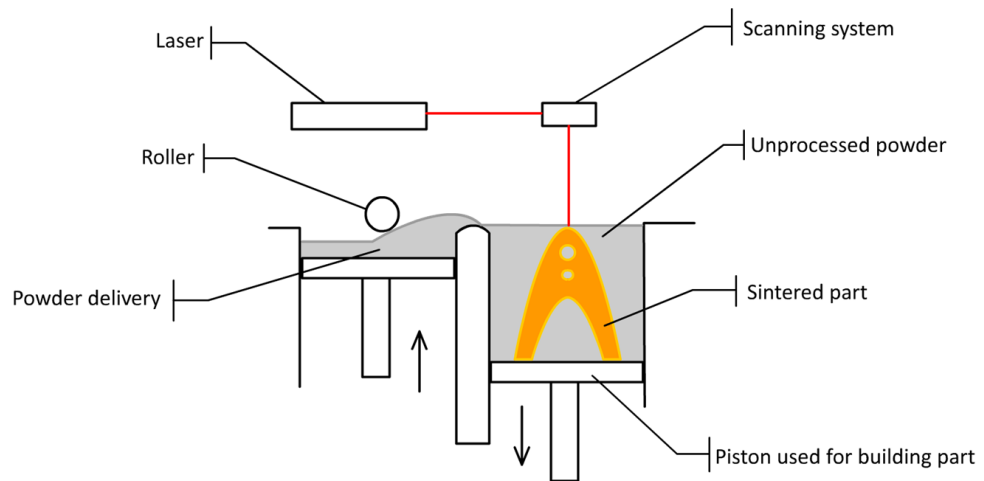


Figure 2-37: Schematics of the selective laser sintering process.

Nylon 12 or polyamide 2200 is most commonly used in SLS. During the SLS process, after each layer of powder is deposited by the roller on the build platform, the laser selectively scans it based on the CAD data of the part. The scanned layer then descends by a distance equal to the next layer height that is to be deposited. This process continues until all layers of the part are scanned. This AM technique can produce more complex topologies without the need of any support structures and is hence used in this research.

2.12 Summary

From the literature review, it can be concluded that limited attempts have been undertaken to date to analyse stents in arteries with specific plaques. Different studies have focused on the parameterisation of stent geometry to find out its influence on the mechanical properties [68,71,90,92,109,110,123–125], but none has optimised stent design for specific disease conditions. There are a variety of stent designs available, each differing with regard to material, strut thickness, coating and drug

elution. It is known that stent varieties trigger different vascular behaviours and a number of desired attributes have been identified in the literature, including biocompatible surface material, thinner struts, modular design, low recoil and low material surface area [32,34,126–128]. Stenting is not risk free and poor stent design can contribute to re-blocking conditions, such as thrombosis and neointimal hyperplasia [5]. These adverse conditions mainly depend upon how the stent geometry interacts with the arterial surface and the resulting effects on blood flow.

Currently stenting (stent deployment) of diseased arteries generally involves the use of only a set of “off-the-shelf” devices. There is a potential risk of suboptimal stent deployment in the some target diseased vessel types. As discussed in section 2.10, stenting arteries with severely calcified plaques can result in unacceptably low lumen area and shape.

It has been noted that a self-expanding stents when deployed in severe calcified arteries could result in immediate residual stenosis [111], therefore design changes are needed to maintain the lumen area to restore the blood flow to acceptable level.

Although many groups have researched biomechanical stent-artery interactions using finite element methods [65,68,103,125,129,130], size and topology optimisation have not been explored in the plaque-specific stent design fields and is the subject of investigation in this research.

3. Description of Research Novelty

3.1 Introduction

This chapter will outline gaps found from the review of the previous literature and present the novelty of the work done in this thesis. The aim and objectives are described at the end.

3.2 Gaps in the Research

Currently, stenting (stent deployment) of diseased arteries involves the use of “off-the-shelf” devices. This lack of personalisation raises the potential risk of suboptimal stent deployment in the target’s diseased vessel. This is particularly the case when treating diseased arteries with severely calcified plaques, which can result in low lumen area and shape.

It is known that with the progression of atherosclerosis, plaque composition and mechanical properties vary considerably and plaque histological types such as cellular, hypocellular and calcified have been found to have statistically different radial compressive stiffness [131]. It is envisaged that lesion properties, such as shape and stiffness will be necessary to create customised stents. As discussed in the previous chapter, it has already been demonstrated [111] that stiff atherosclerotic lesions result in unfavourable stent shape and low lumen area. Stent

design changes are therefore, important to achieve acceptable lumen diameter in such calcified arteries.

Another study [103] produced a variable stiffness self-expanding stent by altering strut thickness at the stent centre to allow more capability to hold stiff plaque, although the study lacked optimisation and relied on manual design of the stent to a single plaque. Pericevic et al. [64] investigated the influence of plaque materials on a selected stent based on balloon-expandable design and concluded that plaque type has a significant effect on the stresses induced within an artery which may alter arterial response. These studies provide the evidence of the impact of lesion types on the outcome of stenting procedure but have not used varied compression in their stent design studies. This demonstrates a need to develop customised stent geometries for specific lesion types.

3.3 State of the Art & Limitations of the Current Literature

As described in detail in section 2.10, a very limited number of studies have explored stent design optimisation. These studies [61,63,88,89,91,109,110,132,133] have investigated the effect of stent geometry parameters such as strut shape, size and connectivity on its performance mainly in terms of fatigue life, radial stiffness and tissue stress. For instance, Wang et al. [61] investigated a parametric stent design focusing on reducing dogboning during balloon expansion. They altered the strut width and balloon length to achieve this aim. They found out that increasing the strut width at the end rings of a stent and slightly reducing balloon length provided a way to control dogboning effectively,

hence eliminating the risk of arterial injury. Timmins et al. [63] went further to develop an algorithm to optimise stent design for by using strut spacing, radius of curvature and amplitude of the rings as design parameters. By assigning weighing coefficients to the competing solid mechanical concerns, such as arterial stress and lumen gain into their design algorithm, a unique set of parameters was identified to maximise lumen gain while simultaneously minimising arterial wall stress. The accuracy of the method was evaluated using FEA in a non-diseased artery. This study provides a general guideline for stent design that could treat different types of lesions. In other words, it enables to produce stiff or less stiff stent designs for a balanced stenting outcome. Wu et al. [109] used topology optimisation to increase the stiffness of a repeating stent strut unit while retaining the drug holding capacity. Li et al. [91] utilised a shape optimisation approach to maximise radial gain and minimise recoil and dogboning by employing a single objective function. Another study by Wu et al. [88] achieved lower principal stresses in a balloon expandable magnesium alloy stent using shape optimisation of a repeating strut unit for improved safety properties.

In terms of investigating the effect of stenting on realistic arteries, a very limited number of studies [97,98,134–136] have simulated stent deployment. These studies have used patient derived 3D reconstructed arterial models for their analyses and mainly focused on evaluating stent-artery stresses due to balloon expansion, strut coverage and vessel deformation. Although it is a step towards stent customisation, it does not consider actual lesion material properties, their corresponding

compressive forces and stent design optimisation. Guimarães et al. [110] utilised topology optimisation to generate a strut cell design for flexibility and stiffness separately to mimic the implant procedure. In another optimisation study Pant et al. [132] used a multi-objective function incorporating recoil, volume average stress in the arterial tissue, flow index, drug distribution and stent flexibility to advance the design with parameters such as strut width and height. It was demonstrated that change in one parameter leads to improvement in one objective while compromising one or more of the other.

Although attempts have been made rarely to assess the effects of stent deployment in varying plaque material environments [64,65,103,111], none of the mentioned design optimisation studies have explored stent geometry optimisation in varying plaque shape and stiffness conditions. From the literature, regarding design optimisation, the following conclusions could be made:

- The great majority of stent design studies only consider size and shape optimisation
- To the best of authors' knowledge, only four stent topology optimisation studies, publicly available, have been carried out mainly focusing on single strut optimisation
- The topology optimisation studies do not consider the effect of varying plaque geometry and stiffness
- The topology optimisation studies do not investigate the full-length stent problem

It is envisaged that patient-specific stent design in true sense would not just involve simulating patient derived arterial models alone. Considering the realistic solid mechanical effects of plaque composition in each case will be a necessary step. The studies mentioned previously, lack this approach of linking actual patient specific arterial information to the design process. One of the reasons for this is the absence of the technology in the current procedures to carry out this accurately. The next section describes a unique approach taken by the current research to tackle this lack of personalisation.

3.4 Research Novelty

Design studies in the current literature do not consider accurately assessing and mapping the forces acting on stents exerted by complex lesions for stent customisation. Arterial assessment, current procedure for involve intravascular ultrasound (IVUS) that mainly relies on acoustic reflections to determine plaque composition [137], other methods include computed tomography (CT) scanning [138], cardiac magnetic resonance (CMR) [139,140] and optical coherence tomography (OCT) [141]. However, advancements in arterial imaging and sensing technologies, and the conversion from images to *in silico* models will be necessary in order to benefit from customisation. Researchers have developed stretchable polymer-electronic balloon catheters from novel materials containing dense arrays of sensors and therapeutic modules [142,143]. These catheters could be used to provide high sensitivity accurate information about the local arterial microenvironment such as temperature, material type and force exerted by lesions. In the current

study, this concept has been taken further by exploiting finite element analysis (FEA) and implanting a cylinder *in silico* into a set of stenotic arteries to extract the exact forces applied by the arteries to tailor stent designs using topology optimisation. The proposed future solution will take the following form to achieve this aim:

- Extract patient-specific arterial composition, shape and loading using advanced catheters (simulated using FEA in the current research)
- Utilising contact FEA and TO assess and generate customised designs

With regard to material, recent studies [49,144] have suggested bioresorbable stents, commonly referred to as scaffolds, as a possible future for coronary intervention. Based on this assumption, polylactic acid (PLA) was chosen as the material during the design process. Bioresorbable stents have the advantage of natural absorption by the body after functioning for the required period of time. No longer being present in the body as a permanent implant, the risk of restenosis is reduced as well as allowing the artery to resume its beneficial natural vasomotion.

Various approaches have been proposed for TO [82,145–152], which is gaining attention in a wide variety of applications. TO based contact analysis of stent and diseased artery is a novel approach to take into account the accurate loading conditions of different plaque types to customise stent architectures according to specific lesions while

maintaining vessel lumen area. Although many groups have researched the biomechanical performance of stents using finite element methods [65,68,103,129,130,153], including very limited stent TO studies [109,110,154], topological optimisation has not been explored in the plaque-specific stent design fields. This study aims to demonstrate that TO can be used to generate designs that enable recoil to be minimised even in conditions where there are strong variations in material property and surface topology of the lumen side of an artery, particularly in the axial direction.

3.5 Aim and Objectives of Current Research

The aim of this research is to improve lesion-specific stent designs by linking assumed patient data (achieved through contact FEA) to the design process, using finite element analysis (FEA) and optimisation techniques, which reduce the risk of restenosis. The main objectives in order to achieve this aim are:

1. To identify and investigate the key features of stents that minimise adverse effects such as recoil and restenosis.
2. To investigate stent-artery contact analyses in complex lesions and extract the compressive forces involved.
3. To develop new and optimal lesion-specific stents using topology optimisation.
4. Experimental validation of finite element analysis (FEA) stent-artery simulations using mock silicone artery and additively manufactured stent.

5. To compare the performance of optimised designs with a conventional stent design in terms of post-implantation recoil.

4. Methodology: Finite Element Analysis and Lesion-Specific Optimisation

4.1 Introduction

This chapter describes the approach taken for lesion-specific optimisation of stents. It introduces the steps taken for creation of a range of stenotic arteries and deployment of a force extracting cylinder in each case, which provides the basis for topology optimisation.

To generate these numerical simulations, the finite element method requires a number of inputs; the model geometry of the arterial vessels, the material properties of the plaque, artery and stents and the application of appropriate loading and boundary conditions. Similarly, for the optimisation step, the objective function and constraints along with other control parameters are described in detail.

The current work methodology involves three main steps, i.e. initial exploration of topology optimisation of a cylinder under arbitrary loading scenarios (e.g. implantation in a healthy artery), topology optimisation of stents in a range of stenotic arteries and finally, experimental validation of the computational approach taken. These steps are outlined in Figure

4-1. The experimental methodology is explained in detail in the subsequent chapter.

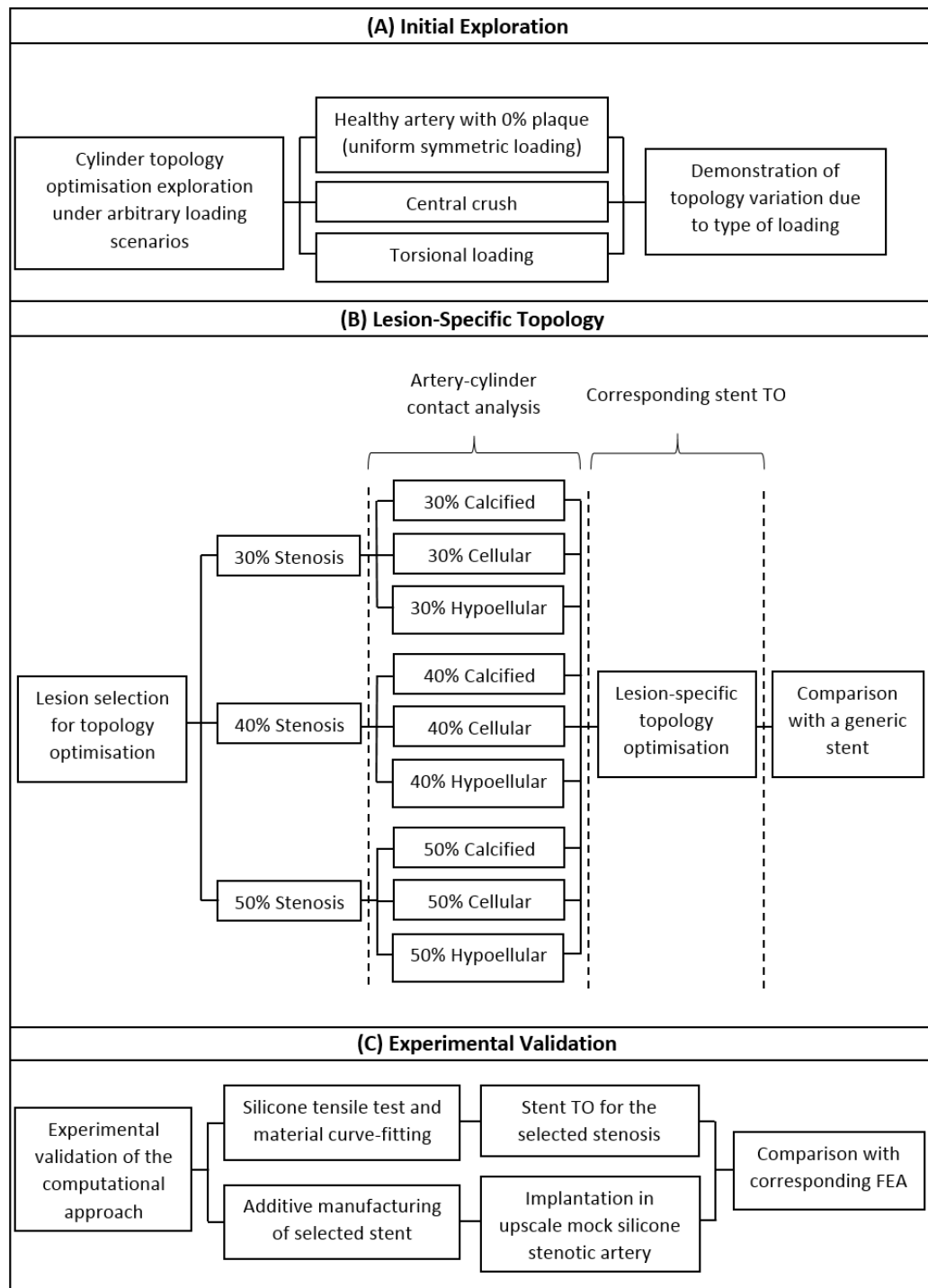


Figure 4-1: Methodology of the current work showing three steps: (A) Initial exploration, (B) lesion-specific stent optimisation and (C) experimental validation.

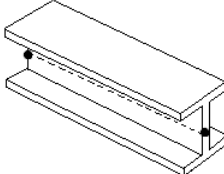
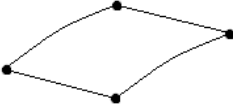
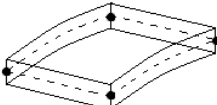
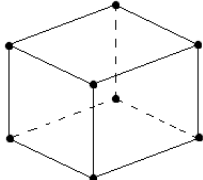
4.2 Selection of Element Types and Solution Methods

Before describing the details of FEA parameters, this section briefly discusses the elements types and solution methods used for the current study. The force-extracting cylinder, generic stent and design domain for topology optimisation were meshed with shell elements while 8 node hex elements were used for the stenotic artery, details of which are described in subsequent sections. This approach of mixing full 3D model and reduced-order model has been validated by Avdeev et al. [155]. Choosing appropriate elements to represent a structure is an important consideration in FEA. As FEA is an approximation technique, with an increase in the number and complexity of elements, the accuracy of the solution increases and converges towards that which would be expected from an analytical solution. However, this will also increase the computational cost and so it is important to develop a model that is able to represent the actual system to the required degree of accuracy without unnecessary computational expense.

There is a wide range of elements types available in commercial software packages that provide flexibility in modelling different geometries and structures. The structure to be analysed is also known as a field or domain and the dependent variables to be found out are known as field variables. Elements selected for a problem should accurately represent a field variable in reality. For a field variable nonlinear by nature, there could be two possibilities of element types: linear interpolation and higher order elements. Using linear elements, the element size should be small enough such that the nonlinear field variable can be approximated in a

piecewise manner. Compared to higher order elements, such as quadratic or cubic polynomial, linear elements are quicker to solve. Higher order elements will usually yield more accurate results but at the cost of a significant increase in complexity and computational time. A suitable mesh, from a numerical accuracy standpoint, is one that yields no significant differences between results when the mesh is further refined. Some of the common elements used for stent-artery analyses are illustrated in Table 4-1. The elements used for the current work for arteries were 8 node hexahedral elements, and 2D shell elements for stent models.

Table 4-1: Commonly used elements for stent systems and arterial tissues.

Used For	Element Types
<ul style="list-style-type: none"> • Wire stents 	 <p data-bbox="1059 1249 1222 1272">Beam elements</p>
<ul style="list-style-type: none"> • Stent expansion balloons • Stent crimping tools 	 <p data-bbox="978 1424 1302 1451">Membrane/surface elements</p>
<ul style="list-style-type: none"> • Stents • Residing vessels 	 <p data-bbox="1054 1617 1206 1644">Shell elements</p>
<ul style="list-style-type: none"> • Wire stents • Residing vessels • Laser-cut stents 	 <p data-bbox="1019 1868 1270 1895">Continuum (solid) elements</p>

Shell elements are usually used for a thin structure where it is in presence of membrane stresses combined with bending stresses. Shell elements

approximate a 3D continuum with a surface model and can model in-plane deformations and bending efficiently. To determine the appropriateness of using shell elements for a structure, a common rule of thumb is if the thickness is less than $1/10^{\text{th}}$ of a typical global structural dimension, then the use of shells are deemed to be appropriate.

Moreover, shell elements allow curvature in space, and are sometimes known as $2\frac{1}{2}\text{D}$ elements i.e. surface elements in 3D space. However, the curvature must not be too great to ensure validity. The ratio of curvature to thickness should not exceed 5 to produce reasonable results in most cases. The thickness of shell elements is represented using an analytical model which improves the efficiency significantly compared to solid elements. Thin or thick shells may be used depending on the problem requirements. The thin shell formulation follows Kirchoff theory where transverse shear deformation is neglected. The thick shell formulation follows Mindlin theory which does account for shear behaviour [156]. Shell elements normally have three displacement degrees of freedom per node and two rotation degrees of freedom. A thin shell can be very strong if the membrane action dominates, which is similar to an arch when subjected to compression.

Solid elements are three-dimensional finite elements that can model solid bodies and are commonly used when modelling arteries. The boundary conditions acting on solid elements are treated more realistically compared to beam or shell elements. A solid hexahedral element is also known as a hex or brick in the finite element literature and is topologically

equivalent to a cube. Due to the bending properties of hexahedral elements, stents and arteries can be modelled effectively.

2D thin shell elements support 6 degrees of freedom, but all solid elements have only 3 translational degrees of freedom and no rotational degrees of freedom. Regarding hex meshing, it is generally recommended to use a minimum of 2 elements across any thickness. It should also be noted that with hex meshing, more effort is needed to prepare an appropriate mesh, and the processing time also increases significantly.

In this work, the two types of aforementioned elements, hex and shell, were used for the diseased arteries and stents respectively. MSC Marc allows contact between these two element types and appropriate model loading conditions.

4.2.1 Introduction to MSC Patran & Marc Mentat

In this research, commercial packages from MSC Software Corporation (MSC Software, Santa Ana, CA), Patran, Marc Mentat and Nastran are employed. Patran and Mentat were used as pre and post processors while Marc as a non-linear solver and Nastran for topology optimisation. Other commercial software commonly used for structural optimisation include Ansys (ANSYS Inc., Canonsburg, PA), Tosca (FE-DESIGN, Karlsruhe, Haid-und-Neu-Strabe), Optistruct (Altair, Troy, MI) etc.

MSC Patran and Marc Mentat enable interactive pre and post processing of data for solving models using the finite element method. Contact is a complex behaviour because of the requirement to accurately track the

motion of involved bodies and their interaction after contact occurs. MSC Marc was used to simulate deformable-deformable contact. Marc enables contact analyses automatically without the use of these special elements. Both pre and post processors (MSC Patran, Mentat) could be used with Marc and has the ability to process large problems in parallel using domain decomposition technique.

A nonlinear analysis usually utilises incremental load (or displacement) steps. At the end of each increment the structure geometry changes and possibly the material is nonlinear or the material has yielded. Each of these things, geometry change or material change, may then need to be considered as the stiffness matrix is updated for the next increment in the analysis.

An explicit or implicit incremental procedure can be implemented. An explicit FEM analysis updates the stiffness matrix based on geometry changes/material changes (at the end of each increment). Then a new stiffness matrix is constructed and the next increment of load or displacement is applied to the system. In this type of analysis the hope is that if the increments are small enough the results will be sufficiently accurate. One problem with this method is that it needs many small increments for accuracy and thus is computationally time consuming. On the other hand, if the number of increments is not sufficient, the solution tends to drift away from the correct solution. Additionally, this method does not enforce equilibrium of the internal structure forces with the externally applied loads.

An implicit FEM analysis differs from an explicit analysis with the addition that after each increment the analysis carries out Newton-Raphson iterations to enforce equilibrium of the internal structure forces with the externally applied loads. The implicit type of analysis tends to be more accurate and can take somewhat bigger incremental steps. If carried out correctly, the Newton-Raphson iterations have a quadratic rate of convergence which is very desirable. Therefore, the implicit method is used in the current work.

Because of the complexity of nonlinear analyses, the solution of most nonlinear problems requires an incremental solution schemes and several iterations within each load/time step to achieve convergence. In MSC Marc, an adaptive multi-criteria scheme is available for contact analysis and was used to specify the load step procedure in this work. Table 4-2 describes the adaptive stepping criteria. Automatic time step cut back was used to adjust the increment size as necessary while relative displacement was specified as the criteria for the convergence testing.

Table 4-2: Adaptive stepping criteria details used for contact analyses.

Adaptive Stepping Multi-Criteria	
Initial fraction of loading time	0.01
Minimum fraction of loading time	10^{-7}
Maximum fraction of loading time	0.5
Maximum number of steps	1000

4.2.2 Treatment of Contact in MSC Marc

Contact in Marc is detected by tracking nodes belonging to a contact body with a contact boundary condition. Contact occurs when two nodes are within a user set tolerance distance, which is by default equal to 5% of the smallest element edge length of the contacting bodies. Contact analysis results are mesh-dependent and finer mesh in the area of contact yields more accurate outcome.

For contact problems that involve structures with large strains, two procedures exist in Marc, the total Lagrange and the updated Lagrange formulation. Since, the total Lagrange formulation is not recommended for material behaviour that experiences large strains and plasticity, in the current study, the updated Lagrange formulation was used for modelling stent-artery interaction. Marc automatically detects contacting bodies and adjusts the load step automatically to satisfy the contact condition.

During contact analysis, a constraint minimisation problem is being solved where the constraint is to have “no penetration”. In Marc, mathematical constraints are applied to the system by using Lagrange multipliers for standard contact problems or by the penalty stiffness method for explicit dynamic problems such as impact simulation. In the current work, the default procedure of constraint, Lagrange multiplier, is used.

4.3 Diseased Artery Selection and Analysis Steps

As described in chapter 2, in order to create customised stents, it was necessary to accurately measure and map the forces acting on stents

exerted by complex lesions. In that pursuit, the initial step of the investigation was to analyse a cylinder with a set of arteries having different plaque types in terms of stenosis levels and materials. The cylinder and diseased artery contact simulates the implantation of a stretchable polymer-electronic balloon catheter developed by researchers [142,143]. These catheters aim to provide high sensitivity accurate information about the arterial local microenvironment such as temperature, material type and force exerted by lesions-which we assumed and gathered using contact FEA. This information is beneficial for the design customisation of implants, as illustrated in Figure 4-2.

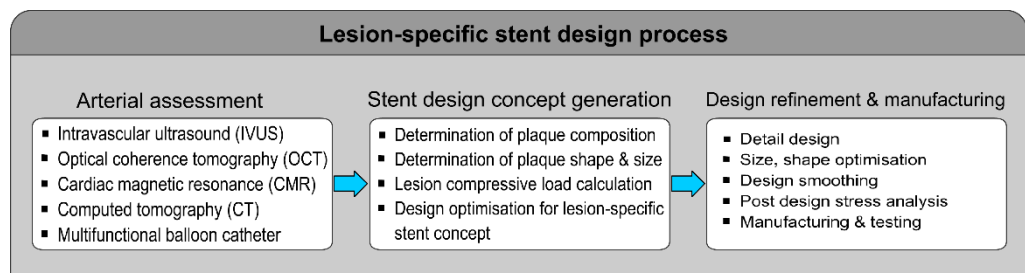


Figure 4-2: A complete design process for customised stents, with step 1 simulated using FEA before carrying out steps 2 and 3.

In the current study, the cylinder acts as a force-extracting balloon catheter, similar to the mentioned concept by exploiting FE and measuring the exact forces applied by the arteries to tailor stent designs using topology optimisation. In terms of plaque morphology, based on clinical practice, a residual stenosis lower than 30% is considered acceptable [112,113], whereas a stenosis value of $\geq 50\%$ is classified as potentially significant [157]. In addition to these geometrical features, it has also been reported that coronary lesions are found to be more eccentric or crescent-shaped [101,158]. Keeping these clinical

incidences in view, arteries with 30%, 50% and a median value were considered for the current work. Coupled with three different plaque stiffnesses for each, an analyses of 9 different types of diseased artery models was carried out. Figure 4-3 illustrates the analyses steps.

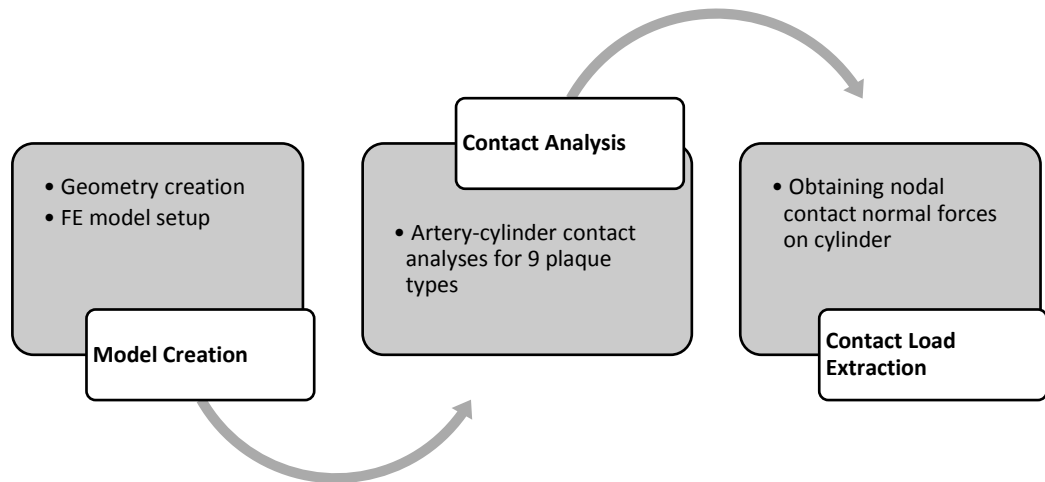


Figure 4-3: Contact analysis steps.

In MSC Marc Mentat, the motion of contacting bodies can be defined in the following four ways:

- Prescribed velocity
- Prescribed position
- Prescribed load
- Prescribed scaling

Since the analysis involved arterial inflation and deflation around the cylinder only, face pressure was used as prescribed loading to inflate the artery so that the cylinder could be 'implanted'. The detailed model setup is explained in the following sections. The forces resulting from cylinder-artery contacts were used as the inputs to the stent topology optimisation discussed latter in the chapter.

4.4 Artery-Cylinder Model Creation

Each stenosed artery was defined by two different parameters: stenosis level and plaque material type (Table 4-3). With 3 stenosis levels: 30%, 40%, 50% and 3 plaque material types: calcified, cellular and hypocellular (with have clinically proven different stiffness as discussed in section 2.10), 9 different diseased artery models and their contacting cylinder were created with MSC Patran. MSC Marc was employed for contact analysis as the non-linear solver (MSC Software, Santa Ana, CA).

Each simulation model was composed of two bodies, a diseased artery and a cylinder acting as a force sensing catheter (or the generic stent in place of the cylinder for comparison). The cylinder used had an outer radius of 2.47 mm (10% greater than the artery accounting for a stent-to-artery ratio of 1.1:1), a length of 15mm and a thickness of 0.2mm. These geometric values are in line with manufacturer's recommendations and common stenting practice [159,160]. Each stenotic artery was modelled as an asymmetrical diseased vessel with a length of 20mm. The thickness of atherosclerotic human coronary arteries range from 0.5 to 1.2 mm, depending on the location of the arteries on the surface of the heart [161]; in our study a thickness of 0.5 mm similar to a previous study [109], was chosen. The artery was modelled as a straight vessel with a localised plaque with maximum plaque tip radius of 1.56mm for 30%, 1.22mm for 40% and 0.972mm for 50% stenosis as illustrated in Figure 4-4. Figure 4-5 shows the generic stent used for comparison purposes.

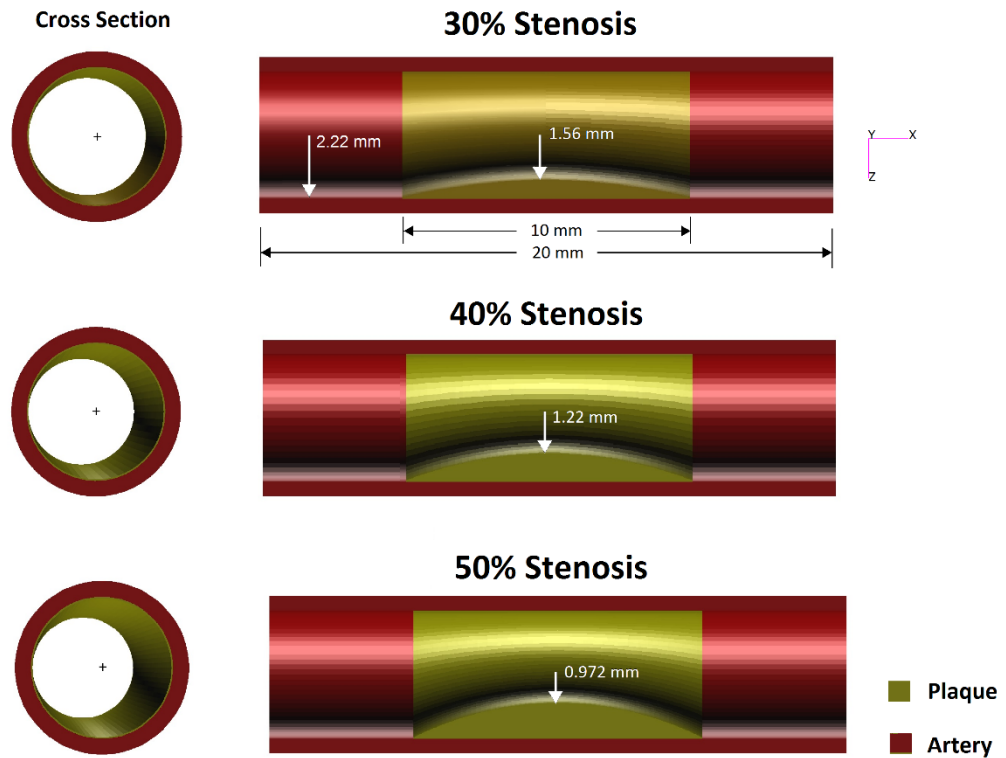


Figure 4-4: Artery models with plaque types used for the analyses (XY plane cut view).

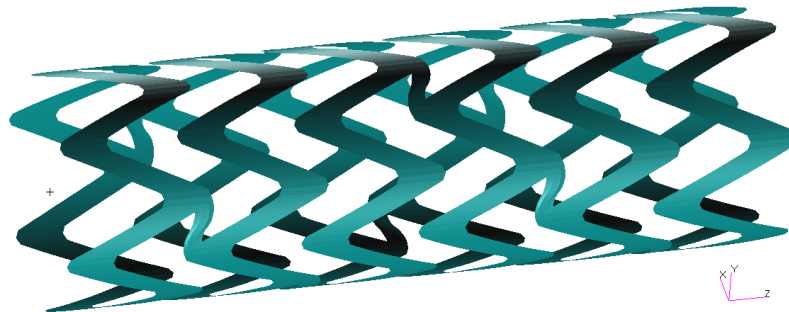


Figure 4-5: Generic stent, 15mm in length, selected for comparison with optimised stents of the same size.

4.5 Selection of Material Model

The material used for the generic stent and the force extracting cylinder was modelled as an elasto-plastic polylactic acid (PLA) polymer blend, having elastic modulus, $E = 3.5$ GPa, yield stress $\sigma_y = 60$ MPa with 0.1% linear strain hardening and Poisson's ratio, $\nu = 0.36$, based on data in the literature [162–164]. The artery and 3 plaque types were modelled with

third-order non-linear hyperelastic mechanical properties suitable for an incompressible isotropic material based on previous studies [64,165] and has the form given in Eq (4.2). This has been found to adequately describe the non-linear stress-strain relationship of elastic arterial tissue [166].

$$W= C_{10}(I_1-3) + C_{01}(I_2-3) + C_{20}(I_1-3)^2 + C_{11}(I_1-3)(I_2-3) + C_{30}(I_1-3)^3 \quad (4.2)$$

where W is the strain-energy density function of the hyperelastic material, I_1 , I_2 and I_3 are the strain invariants and C_{10} , C_{01} , C_{20} , C_{11} , C_{30} are the hyperelastic constants. Table 4-3 summarises the constants used for the hyperelastic constitutive equations to define the 4 material types.

Table 4-3: Hyperelastic constants to describe plaque and arterial tissue [64,165].

Constants	Arterial Tissue (kPa)	Calcified Plaque (kPa)	Cellular Plaque (kPa)	Hypocellular Plaque (kPa)
C_{10}	708.416	-495.96	-802.723	165.111
C_{01}	-620.042	506.61	831.636	16.966
C_{20}	2827.33	3637.80		
C_{11}		1193.53	1157.68	955.388
C_{30}		4737.25		

4.6 Meshing and Boundary Conditions

After selecting appropriate element types, it is important to identify a suitable mesh size. The finer the mesh, the more accurate the result, although the computational time increases. Therefore, to find a suitable accuracy and computational time, a mesh convergence study was carried out.

There are two main methods of mesh refinement: (i) *h*-refinement and (ii) *p*-refinement. *h* mesh refinement refers to the process of increasing the number of elements used to model a given domain, consequently, reducing individual element size. In the second method, *p*-refinement, element size is unchanged but the order of the polynomials used as interpolation functions is increased. *h*-refinement method was used in the current study. Eight node hex, full integration elements were used to mesh all the atherosclerotic artery models (Figure 4-8). Mesh convergence studies shown in Figure 4-6 were carried out for one of the artery models to select an adequate mesh size. The results demonstrate that 41760 elements in the artery and plaque were reasonable due to minimal difference in the outcome due to mesh refinement as seen in Figure 4-6. The cylinder to be implanted for contact normal force sensing was modelled as a shell mesh of 6804 quad 4 elements, which would later act as the design domain for stent optimisation.

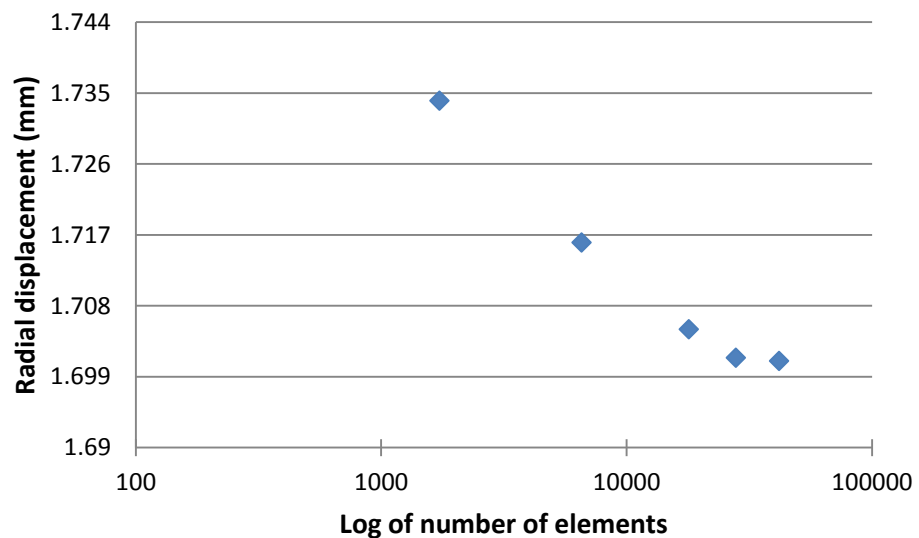


Figure 4-6: Maximum radial displacement of plaque tip in the artery with five different meshes.

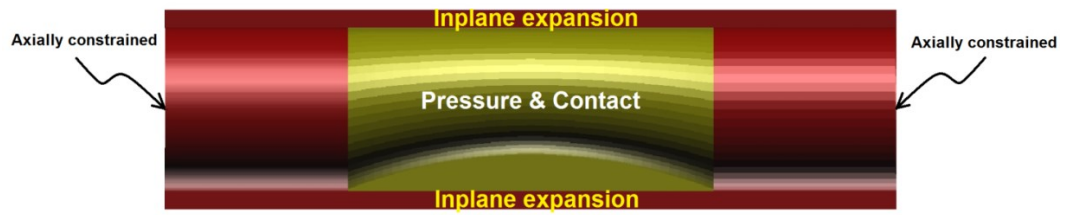


Figure 4-7: Graphical representation of the application of boundary conditions for the artery with internal pressure and axial constraints on both ends.

The boundary conditions applied to the boundary value problem included pressure, displacement boundary conditions and contact (Figure 4-7). Both ends of the artery and cylinder were constrained axially and allowed to expand and contract radially. The cylinder in each case was positioned inside the artery with elements de-activated in the first load case as depicted in Figure 4-9.

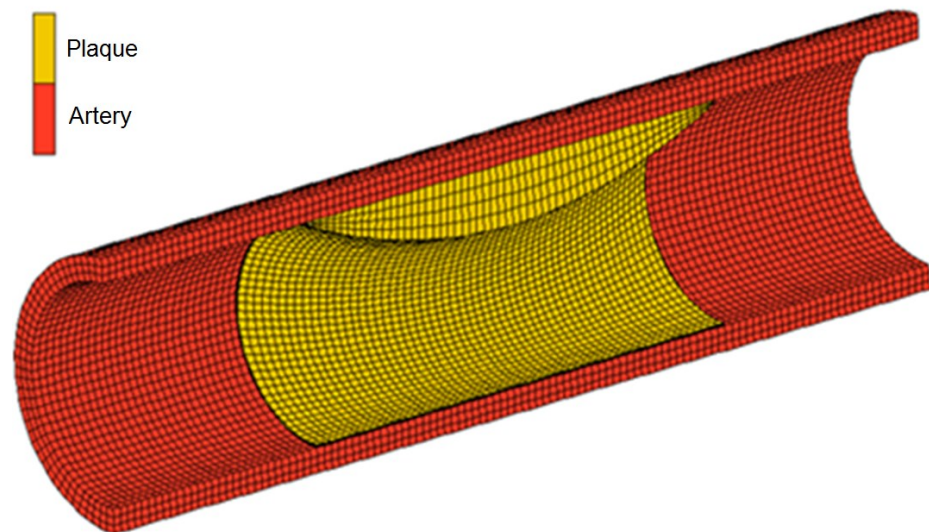


Figure 4-8: Hex-meshed model of 50% stenotic artery for contact analysis with cylinder (XZ cut view).

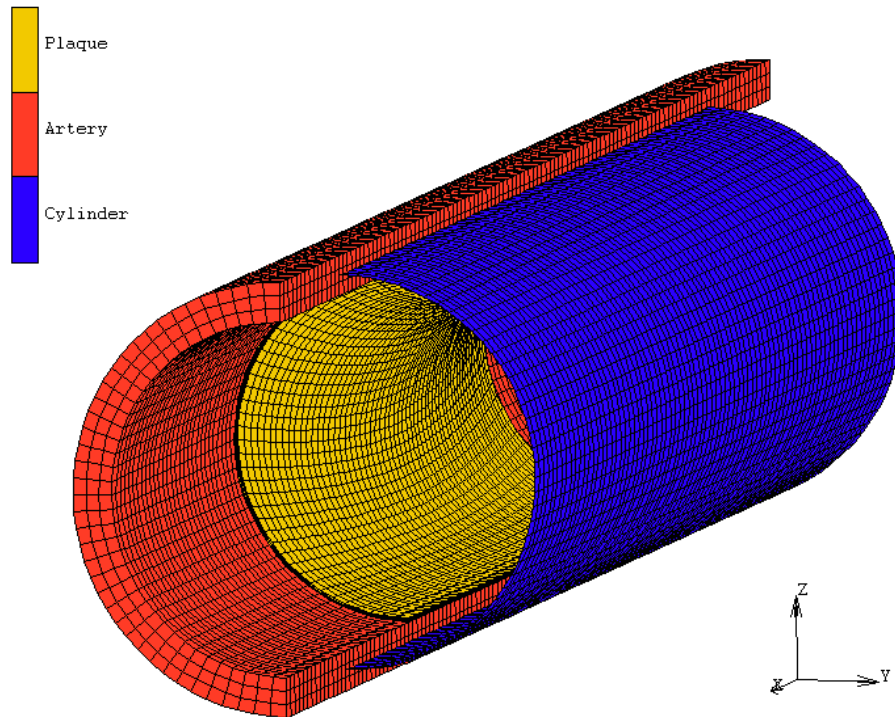


Figure 4-9: Relative position of cylinder and 40% stenotic artery before contact (artery sliced for illustration purpose).

The vessel was then inflated by applying a pressure of 32.5 MPa for 30% and 40% stenosis and 65.05MPa for 50% stenosis. This pressure expanded the artery enough such that the 10% oversized cylinder could be positioned inside or “implanted.” This process was carried out in two load case steps; first, the cylinder elements were deactivated from the contact table such that the artery could expand freely. In the second step, cylinder elements were activated in the contact table, pressure was then reduced to diastole (0.013MPa) such that the artery wrapped around the cylinder. Contact between artery models and the cylinder was defined as deformable-deformable ‘touch’ contact. The size of contact tolerance can have significant impact on the computational cost and solution accuracy. For example, a small contact tolerance can lead to a high computational cost while a large contact tolerance can affect the solution accuracy. All

the artery models were solved for contact analysis separately in the same manner.

For the analysis involving a generic stent, an internal pressure of 0.52 MPa was applied to the stent initially to expand and plastically deform it while stenotic artery elements were deactivated. The pressure was then removed to allow the stent to recoil and achieve its final diameter of 5.15 mm (10% bigger than the artery). Detailed results of the contact analyses, optimised stents generation and comparisons are described in chapter 6.

4.7 Lesion-Specific Stent Topology Optimisation

The analysis carried out initially involved 3 arbitrary scenarios of loading conditions, to explore and demonstrate topology variation, i.e. uniform loading on cylinder (to mimic 0% plaque), point crush load at the centre and torsion at one end. The analysis was then taken further to optimise stent design with respect to its stiffness for different plaque types. This forms the second stage in the investigation for creating lesion-specific stents and uses the output from the contact analyses, of different types of arteries with cylinder, as discussed in the preceding sections. This section explains the steps taken for model creation and optimisation setup in detail. The optimisation results and their analysis are presented in chapter 6. Mesh dependency and the effect minimum member size (MMS) control parameters for the initial loading scenarios can be found in Appendix D.

As the aim was to optimise the stent design for different artery stenosis conditions such that the radial recoil after implantation is minimised, the

objective, therefore, was set to minimise the structural compliance of the stent or in other terms, to maximise the stiffness.

The first stage in the design process was to extract the loading applied by a set of diseased arteries on a cylinder in terms of the radial contact normal force as described earlier. The second step was to apply the obtained loads to a cylindrical design domain to perform TO. In the final step, the optimisation results were transformed to clear, manufacturable design concepts and their performance was evaluated by implanting them in their respective stenosed artery types. The results were compared with a generic stent in similar arteries. The generic stent design was inspired by the Igaki-Tamai biodegradable stent [167], which is one of the few commercially produced bioresorbable stents.

The steps taken are summarised as follows, with step (i) already discussed in detail in the previous section:

- (i) A contact analysis between 30%, 40% and 50% asymmetrically stenotic arteries by area, having three types of plaque each, with a cylindrical tube considered as contact force extractor or a design domain for stent topology optimisation. The extracted force acts as a loading boundary condition for step (ii).
- (ii) Topology optimisation of stents using SIMP, based on extracted contact normal forces on a cylinder obtained from analysis in step (i) for each plaque shape and material.

- (iii) Contact analysis of the generic and optimised stents with the mentioned diseased vessels for performance comparison in terms of radial deformation.

Figure 4-10 illustrates the steps taken to optimise and compare the stent designs obtained. Details of the optimisation process are explained in subsequent sections.

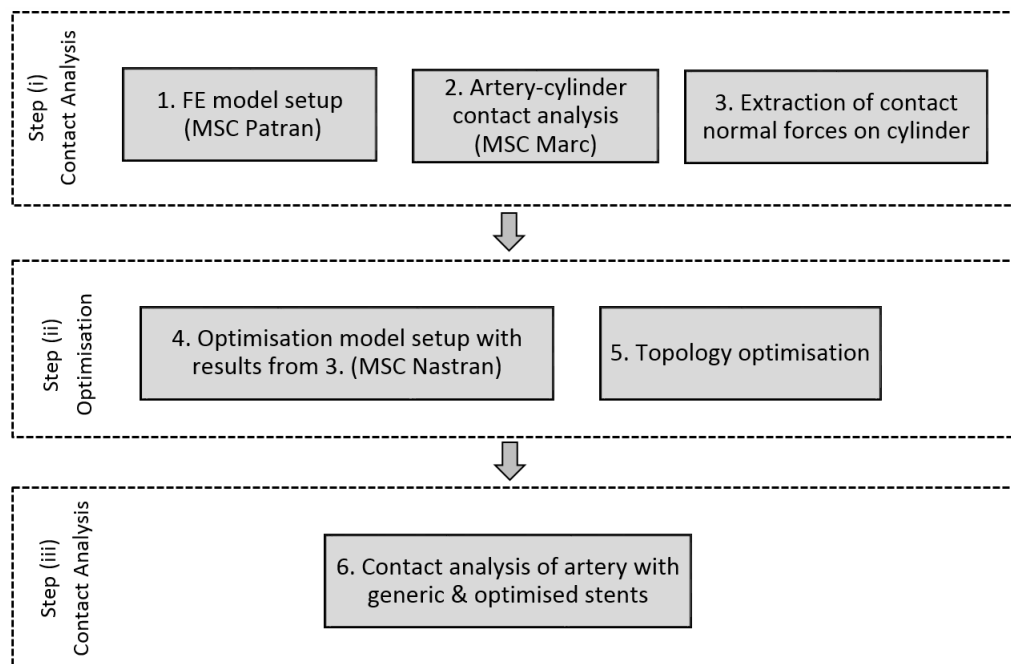


Figure 4-10: Analysis steps for lesion-specific stent optimisation.

Figure 4-11 demonstrates the proposed method of creating lesion-specific stent using SIMP topology optimisation while highlighting the focus of the current work. The process begins with arterial assessment of a patients' diseased artery using imaging and sensing methods to extract lesion compressive forces that would act if it was pushed against the arterial wall. A subsequent process of optimisation would follow to generate optimal designs for the specific conditions.

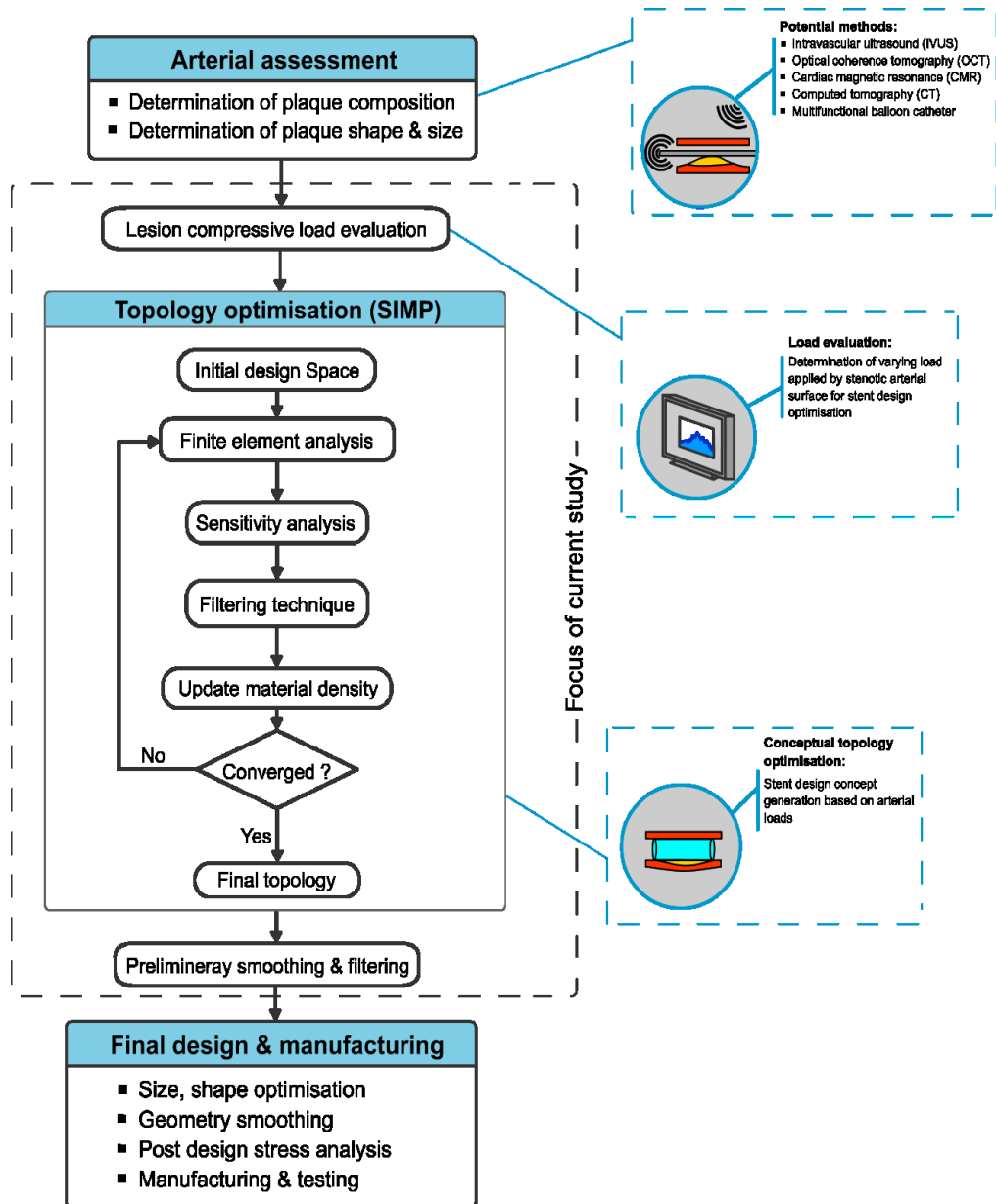


Figure 4-11: Proposed approach to design lesion-specific stents.

4.7.1 Model setup and initial exploration

In order to explore and demonstrate the variation of topology with changing load cases, an optimisation study of three different arbitrary loads was carried out. The first consisted of a uniform compressive pressure mimicking loading from a healthy artery with 0% plaque, then radial crush loading at the centre of the cylinder by two opposing point loads and the third with pure torsion applied to one end while keeping the

other fixed. For the first load case scenario, to allow both ends of the structure to have unconstrained nodal motion (expansion in this case) in the radial direction, rigid body elements (RBE3) supported by Nastran were used as shown in Figure 4-12 and Figure 4-13. The central node at one end was fixed in all six degrees of freedom. Three nodes along the periphery were allowed in-plane motion (UY, UZ) while the rest in the periphery were allowed translation in UX, UY and UZ. For the second load case both ends were fixed in all six degrees of freedom while radially inward forces were applied as depicted in Figure 4-15. In the third scenario, with pure torsion, RBE2 elements were used on both ends with one end fixed in all translations and rotation while the other central node at the end was subjected to torsion as shown in Figure 4-16. A uniform loading of 0.03 MPa was chosen for the first case based on contact analysis of healthy artery, whereas 7N was selected for crush and torsion to explore topology variation.

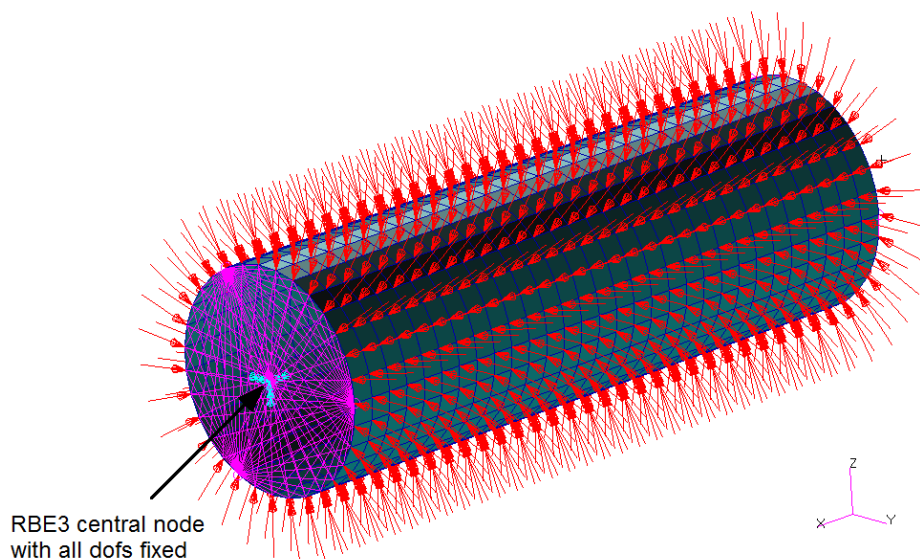


Figure 4-12: Load case 1: Uniform inward radial load distribution representing healthy artery compressive pressure on cylinder (coarse mesh used for illustration purpose).

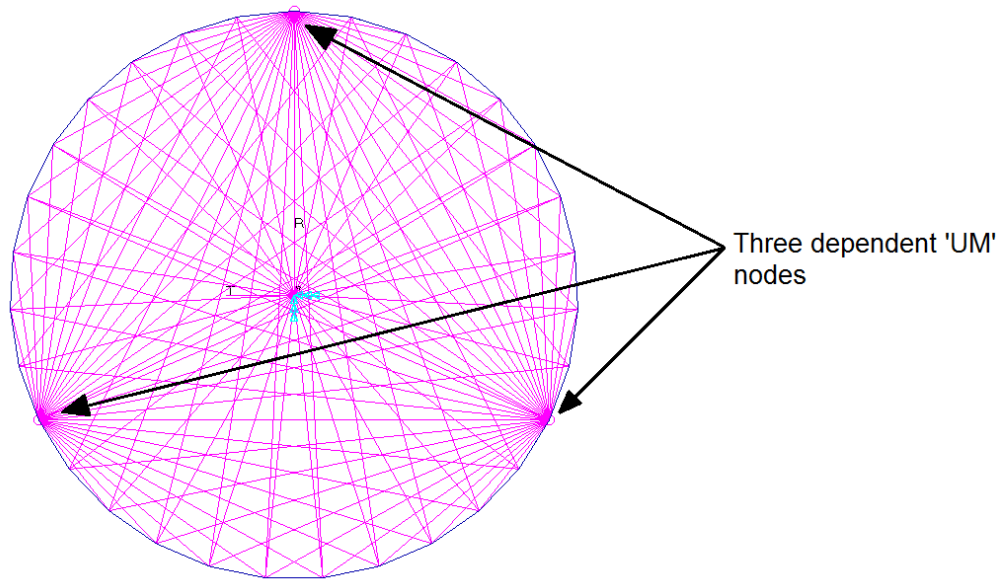


Figure 4-13: RBE3 elements connecting end nodes at one end of the cylinder for unconstrained compression. Note the three dependent nodes with free in-plane dof forming a triangle for best numerical conditioning while the central dependent node being fixed in all dofs (coarse mesh used for illustration purpose).

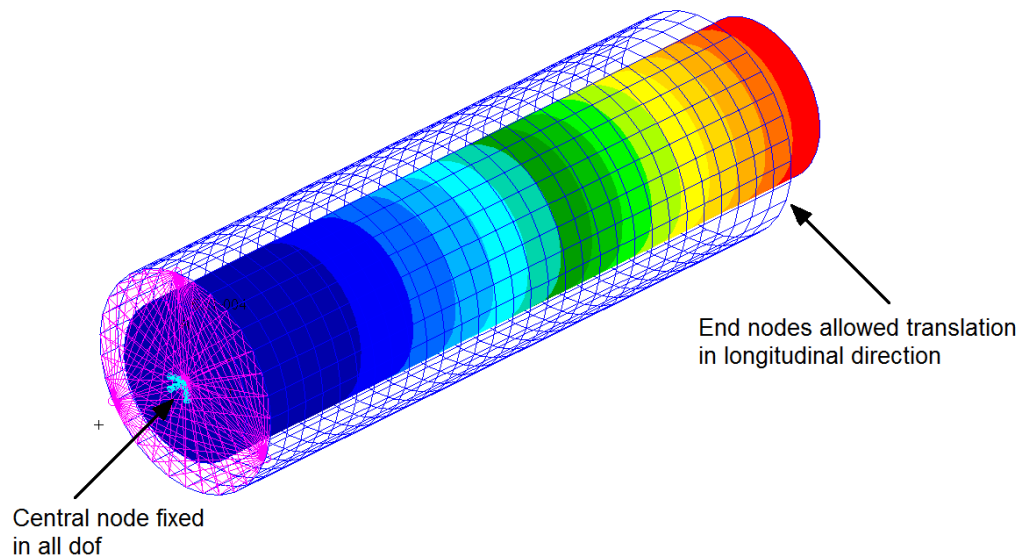


Figure 4-14: Demonstration of unconstrained uniform compression due to external pressure using RBE3 elements. Note the Poisson effect shortening (coarse mesh used for illustration purpose).

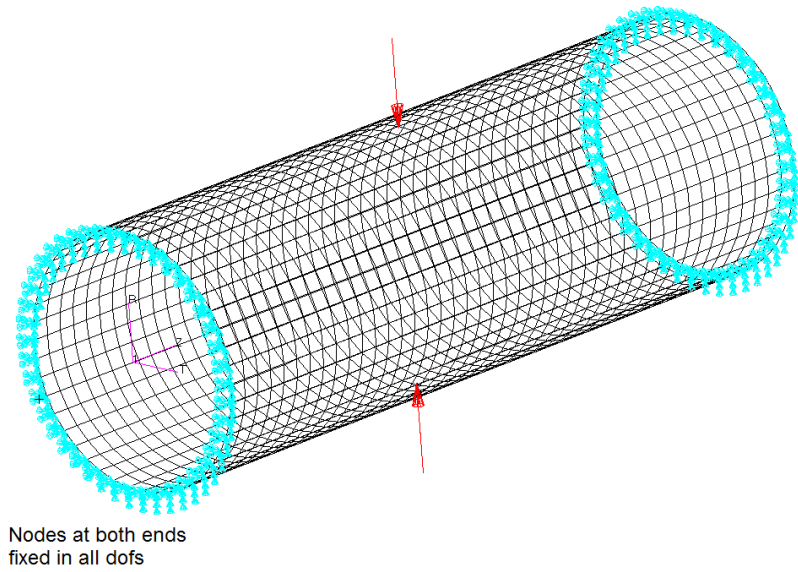


Figure 4-15: Load case 2: Radial compressive force application at centre top and bottom (coarse mesh used for illustration purpose).

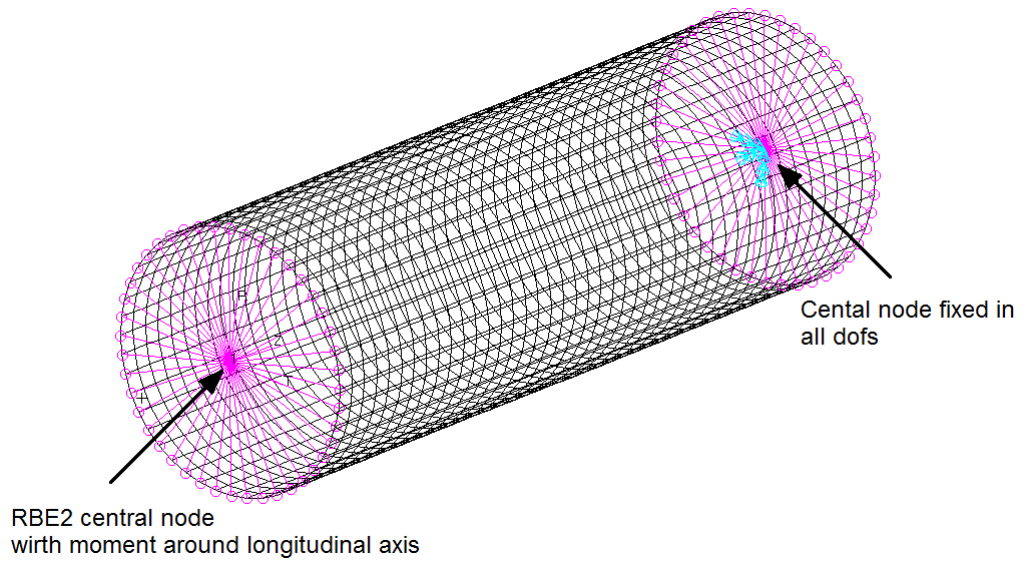


Figure 4-16: Load case 3: Torsional load application using RBE2 elements at both ends of the cylinder (coarse mesh used for illustration purpose).

Figure 4-17 illustrate the varying radial compressive force extracted from one of the contact analyses and applied to the design domain for optimisation.

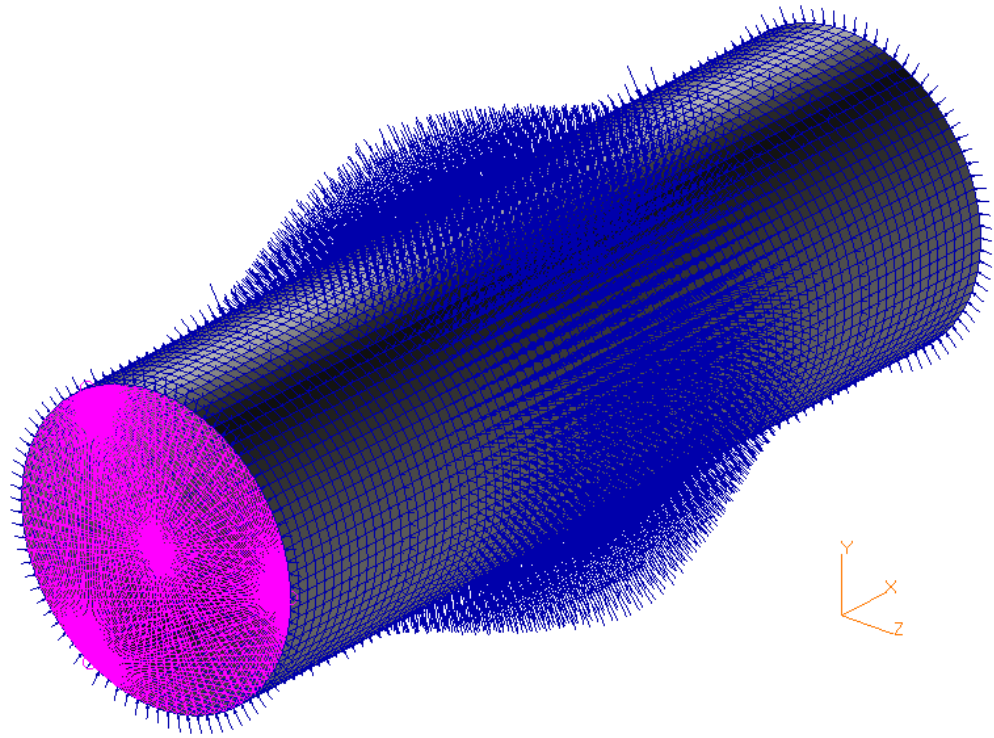


Figure 4-17: Varying radial force on one of the stent design domains obtained from contact analysis with 40% stenosis with calcified plaque for TO. Central node at one end of the cylinder is allowed to expand/contract using RBE3 elements. Note higher forces in the middle due to peak plaque thickness.

For the lesion-specific scenarios, the design domain for stent optimisation was the same as the cylinder used for contact analysis to extract contact forces from the arterial contact. The contact analyses were performed as a first step as described earlier in this chapter, thereby providing the loading for the optimisation problem. Figure 4-18 illustrates the expected load variation acting on the stent design domain resulting from its contact with stenotic artery.

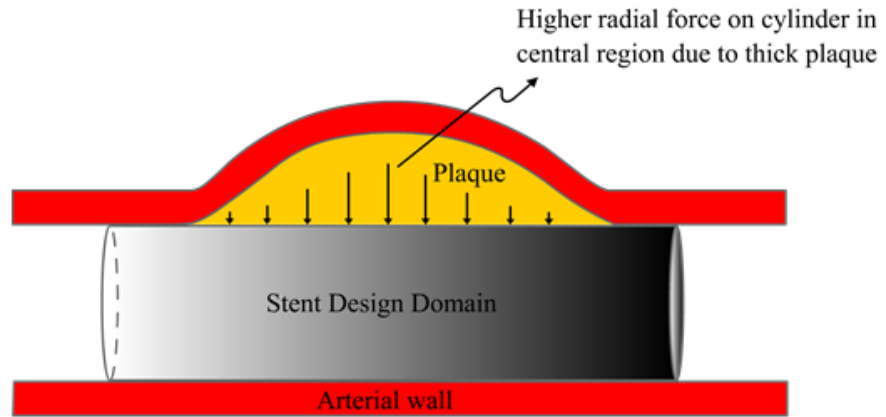


Figure 4-18: Illustration of diseased artery section with cylinder implanted for force extraction showing expected higher compressive forces from stenotic region.

The material used for the design domain was modelled as linear elastic polylactic acid (PLA), having elastic modulus $E = 3.5$ GPa and Poisson's ratio $\nu = 0.36$, based on data in the previous literature [162]. It took the form of a cylindrical shell mesh of 6804 quad 4 elements.

4.7.2 Optimisation parameters

After performing contact analysis of the cylinder with each type of diseased artery, the contact normal forces on the cylinder imposed by the vessel in each case were applied as loads on the same sized cylindrical stent design domain for topology optimisation. The objective was to minimise the compliance C^* of the structure (where C^* is the reciprocal of stiffness) or strain energy, while satisfying the constraints of volume removal (to meet the acceptable stent-artery coverage ratio) under contact loading conditions of the stenotic artery. The compliance of a structure is defined as

$$C^* = \mathbf{U}^T \mathbf{F} \quad 5.8$$

where \mathbf{U} is the global displacement vector and \mathbf{F} is the global force vector applied to the structure. The strain energy S of the structure is defined as

$$\mathbf{S} = \frac{1}{2} \mathbf{U}^T \mathbf{F} \quad 5.9$$

Assuming constant \mathbf{F} , minimising compliance would mean minimising strain energy or the deformation \mathbf{U} , in an elastic regime. Thereafter the SIMP method was applied for stent topology optimisation [77,168,169]. As discussed in section 2.9, this method assigns density x^i to each element, which was the design variable of the optimisation. The SIMP method then minimises compliance as follows

Objective: $\min C^* = \mathbf{U}^T \mathbf{F} \quad 5.10$

$$\begin{aligned} C^* &= \mathbf{U}^T \mathbf{K} \mathbf{U} = \sum_{i=1}^N u^i k^i u^i \\ &= \sum_{i=1}^N (x^i)^p u^i k_0 u^i \end{aligned}$$

Subject to: $V = \sum_{i=1}^N x^i v^i \leq V_0 - V^* \quad 5.11$

$$\mathbf{F} = \mathbf{K} \mathbf{U}$$

$$k^i = (x^i)^p k_0$$

$$0 < x_{min} \leq x^i \leq x_{max} < 1$$

where \mathbf{K} is the stiffness matrix of the stent structure, u^i is the displacement vector of the nodes, N is the total number of elements, k_0

and k^i are the element's initial stiffness and the stiffness matrix after optimisation, respectively. In the constraints, V is the volume of the structure after optimisation which in this case was set to 0.3 (30%) based on being in the range (25%-65%) of currently available polymer stents [170]. V_0 is the initial volume, V^* the amount of material to be removed, v^i is the element volume after optimisation.

The density design variable x^i of each element has a value ranging between 0 (void) and 1 (solid). Closeness to 0 or 1 determined if an element is to be removed or kept, respectively with x_{min} the lower bound of element density and x_{max} the upper bound of element density. The reason for keeping a lower bound for the density instead of restricting it to zero is to avoid singularity of the stiffness matrix. As mentioned earlier, a penalty factor p is introduced to enforce the design variable to be close to 0-1 solution when $p > 1.0$. A value of $p= 2$ was used for this problem. A tolerance of convergence of 0.0001 was selected for the optimisation runs. Table 4-4 shows the parameters used for the optimisation. The Nastran input deck with all the optimisation parameters is given in appendix B.

Table 4-4: Optimisation parameters.

Parameter	Value
Initial design variable value (XINIT)	0.5
Lower bounds (XLB)	0.001
Maximum design cycle (DESMAX)	250
Penalty factor (Power)	2
Move limit (DELXV)	0.2
Tolerance of convergence	10^{-4}
Checkerboard free pattern	Yes
Symmetry constraints	XY, ZX

4.7.3 Complications in topology optimisation method

The two main complications with topology optimisation solutions are its dependency on mesh size and the appearance of checkerboard pattern.

The Checkerboard problem

The issue of checkerboarding mainly emerges from the discretisation error of the FE method. This refers to the checkerboard pattern that forms due to the arrangement of elements with density of 0 and 1 connected only at corners (Figure 4-19).

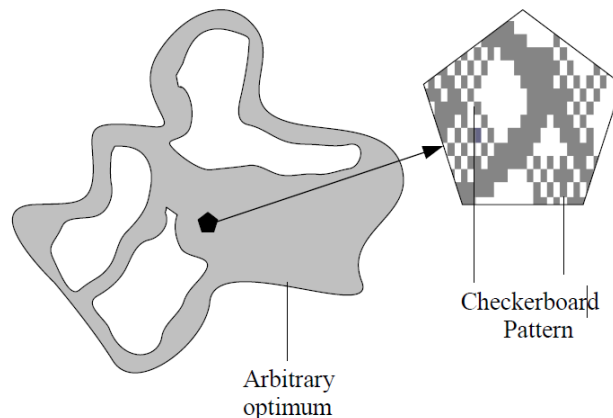


Figure 4-19: Checkerboard pattern in an arbitrary optimum [171].

The stiffness for elements just connected by the corners is over estimated [172] and in SIMP the use of one variable per element and the penalising of intermediate densities causes checkerboard patterns to arise. There are a few different ways to tackle this issue, for instance, using higher order elements, which reduces the effect, adding filters that smooth the element densities close to each other or by the introduction of a restricted value for the local gradient of element densities [86,173]. MSC Nastran provides an option for avoiding the checkerboarding problem and has been utilised in this work.

Mesh-dependency of solutions

Results from SIMP TO are mesh dependent in that different structures are obtained when the mesh is refined without altering other parameters of the optimisation. Structures with finer meshes lead to different topologies rather than the anticipated better structural boundaries. To address mesh-dependency issues, there are a few techniques used such as perimeter control, relaxation and reduction of the admissible design space by adding a local or global constraint on the variation of the density variable, which eliminates the possibility of finer microstructure [86]. The filtering technique has been the most successful method to date and is similar to the filtering technique used for checkerboarding. It filters the design sensitivities and is computationally inexpensive due to not requiring extra constraints. Before selecting the final mesh size for the stent optimisation problem, several coarse meshes were analysed and a mesh convergence study was performed. The current mesh was selected

due to its compatibility with the artery contact model in-terms of mesh size, and computational time efficiency.

4.7.4 Post processing

The first phase in analysing and investigating the newly obtained optimised stents was to post process the resulting structures, where they were transformed into analysable and practical geometries. TO results using SIMP consists of elements with intermediate densities along with the solid elements in the structure. In order to proceed with this process the following steps were carried out:

- Unwrapping the TO stent results
- Filtering intermediate densities using MATLAB
- Repairing and manual amendment using image editing software
- Smoothing using MSC Patran's built-in FEM smooth option
- Wrapping the final structure back to cylindrical mesh using MATLAB for further investigation and comparison with a generic stent.

Post-processing was also necessary to remove unwanted geometrical artefacts of the optimisation (such as suspended elements) in the optimised stent topologies that could hinder further analysis. This involved reducing the number of sharp corners and detached elements. This is important to avoid issues during the contact analysis of the optimised stents with the stenotic arteries. A MATLAB code was written to perform wrapping/unwrapping and smoothing of the resulting stent structures. The code is provided in appendix B. Figure 4-20 depicts

Patran's FEM smooth option that was used for preliminary smoothing. The process was completed using MATLAB and image editing software.

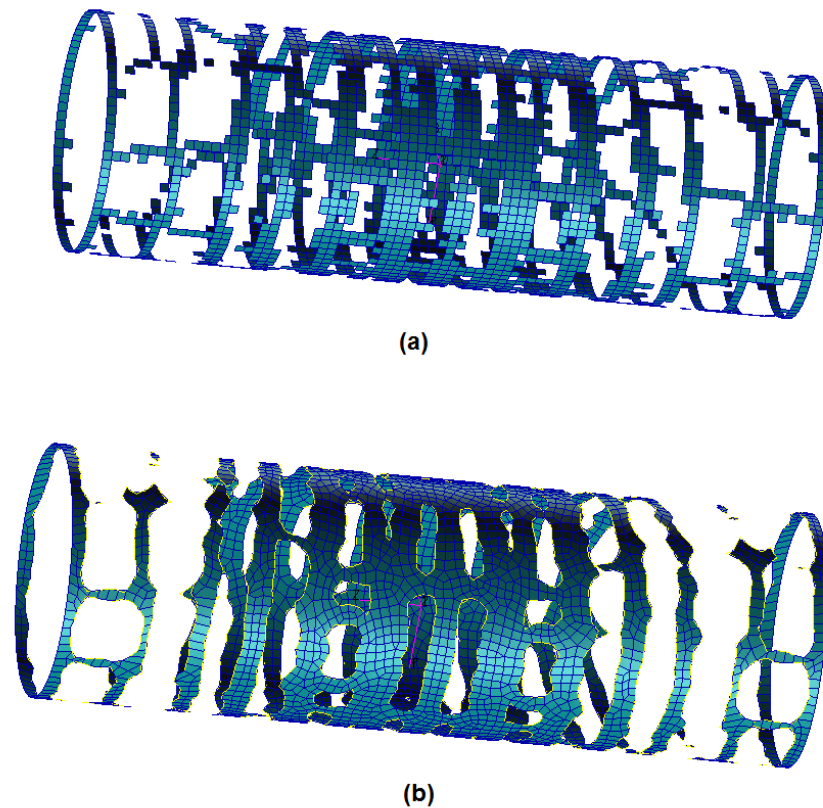


Figure 4-20: Patran FEM smooth option with image (b) showing smoothed elements.

4.8 Comparison with generic stent

The main aim of stent implantation is to keep the artery open by pushing the plaque against the arterial wall. Therefore a stent should have enough radial stiffness to deal with different types of plaques in terms of their shape and stiffness. In this study a set of plaque types with different size and stiffness were used, hence focus was on the stent performance in terms of radial recoil after implantation. After performing contact analysis of the optimised stents with their respective stenotic artery types, the final step of the study was to simulate a typical generic stent and compare its radial deformation to the topologically optimised stents.

For the analysis involving a generic stent, an internal pressure of 0.52 MPa was applied to the stent initially to expand and plastically deform it while stenotic artery elements were deactivated. The pressure was then removed to allow the stent to recoil and achieve its final diameter of 5.15 mm. The stenotic artery in each case was then inflated and deflated in the last load case to wrap around the stent as performed in previous analyses. The generic stent selected was inspired by the bioabsorbable Igaki-Tamai stent [167]. The material used for the generic stent was the same as that for the optimised stents and consisted of 6849 Quad 4 shell elements. The volumes of the generic and optimised stents were kept similar for comparison purposes. The axial motion of the stent was fixed and 4 nodes on both ends of the stent were constrained in a manner to allow radial expansion and compression.

4.9 Summary

This chapter explained in detail the procedures and methods used for the contact analyses and topology optimisation for stent design. It started with an introduction to the finite element method and then described the process of element selection and contact analysis setup. The chapter also explained the SIMP method with the description of the parameters used for lesion-specific stent optimisation for the selected stenotic arteries. Initial exploration of topology variation under three arbitrary loading scenarios was also described followed by optimisation steps for selected lesions. Results of the force-extracting cylinder-artery contact analyses and optimisation process along with comparison of generic stent are detailed in the results chapter.

The next chapter will look at the methodology used for creating the experimental setup for validation of the FEA. It will explain the test rig manufacture and stent placement in mock silicone arteries for comparison with FEA models.

5. Experimental Validation of the Numerical Methods

5.1 Introduction

Computational tools are less expensive and a faster way of testing new devices but they lack the certainty as no model can completely emulate the physics of the real world. Therefore experiments are used to validate parts of the computational study. Furthermore, in terms of experiments, *in vivo* studies of arterial stents in animal models carry ethical and financial concerns whereas *in vitro* testing on the other hand can provide reasonable pre-clinical results in order to develop stent designs and identify any mechanical complications.

This chapter provides details about the experimental validation of the computational approach used in this thesis. This was achieved by inflating and deflating a silicone mock artery representing a coronary artery in a specially designed rig along with the implantation of an optimised stent acquired from the preceding chapter. Two different scales, both self-consistent, were used in the current work. The models used in this chapter were scaled up 1.9 times to match the commercially available silicone tube. The stent and the test rig were made using additive manufacturing (AM) techniques. FEA simulations were generated by inputting the mock artery and stent geometry and material

properties. The radial displacements acquired from the experiments were measured and compared against their corresponding FEA models.

5.2 Methods

The goal in the experimental methodology was to visually examine the behaviour of stent and silicone mock artery in terms of their radial deformation due to internal pressure variation and stent implantation. Silicone NGP 60 is a biocompatible elastomer and has been previously used for mock artery applications. A test rig was designed for the experiments. Material response of silicone mock artery was also evaluated using simple tensile tests for FEA simulations. In order to deploy a stent in a mock artery, three separate experiments were performed as listed below:

- (a) Silicone tube inflation with given pressures
- (b) Silicone tube inflation and stent deployment followed by tube deflation
- (c) Stent deployment along with simulated silicone lesion

5.3 Experimental test rig setup

A rig was designed and developed that could adequately support the mock artery at both ends while allowing inflation and stent deployment through hollow hose connectors. One end of the rig was connected to a pressure line via a hose and pressure regulator while the other end consisted of a metal stent plunger. The rig was then clamped to a sturdy workbench to restrict any unwanted movements during tube inflation. A commercially available silicone tube with an inner diameter of 8.6 mm

and wall thickness of 1.6 mm was selected for the experiments. This would allow placement of a 10% bigger stent in terms of diameter, based on common stenting practice and the FEA carried out in this thesis. The size selected for the silicone tube matched with the size of stents that were 'printable' due to their thin struts with SLS technique, as described in the latter section. The mock artery was connected to the rig with the help of hose connections at both ends. The hose connection on the plunger side of the rig was created to house a stent before insertion into the tube. Figure 5-1 presents a schematic diagram of the test rig.

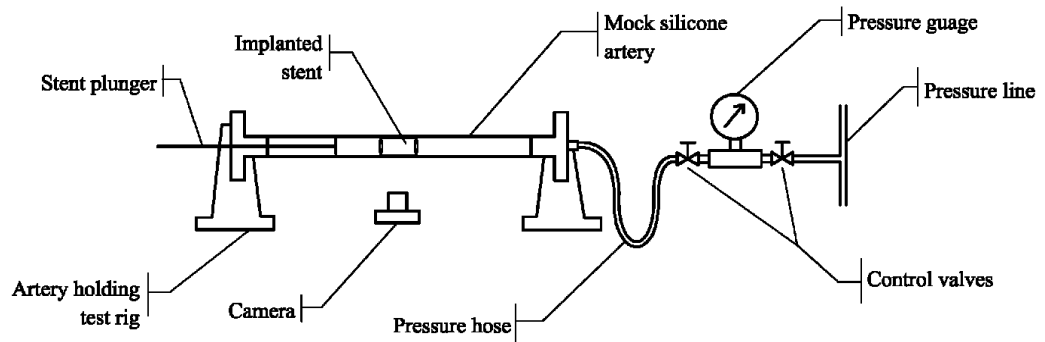


Figure 5-1: Schematic diagram of the experimental test rig.

For capturing arterial deformation images due to inflation pressure and stent performance evaluation, a camera was positioned close to the mock artery. The translucency of silicone tube enabled visualisation of the stent for positioning inside with the help of a specially designed plunger. Ample length was kept between the fixed ends of the tube to avoid any measurement error due to the influence of fixtures. The final test rig setup is illustrated in Figure 5-2, Figure 5-3 shows a close up view of stent delivery plunger and transparent stent housing before implantation.

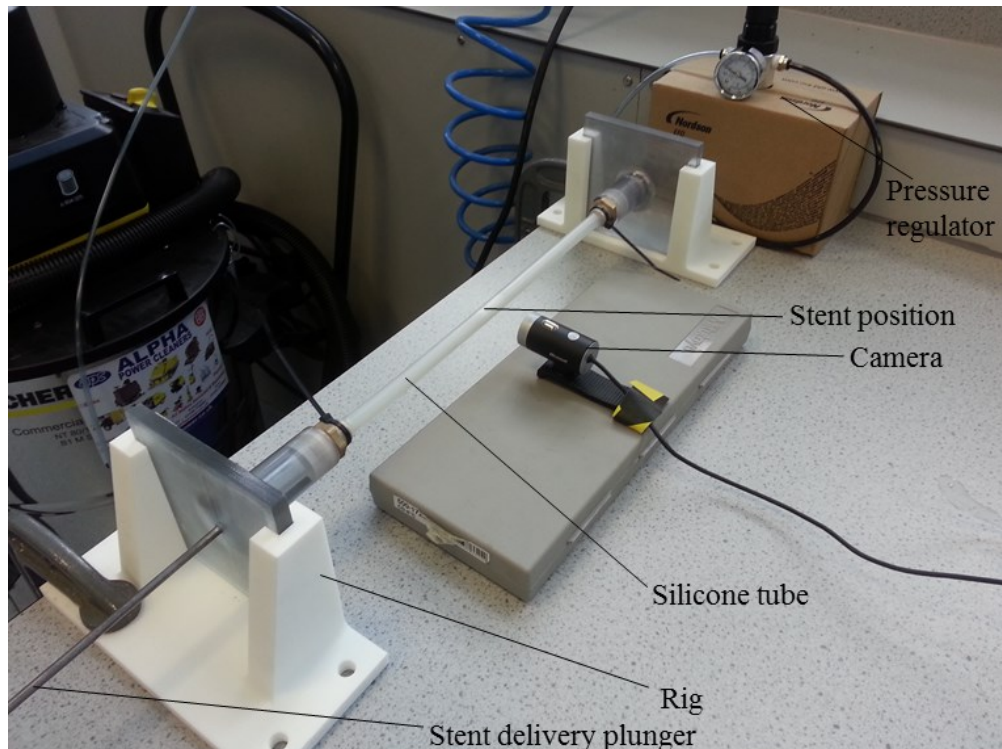


Figure 5-2: Image showing experimental setup used for mock artery inflation and stent deployment.

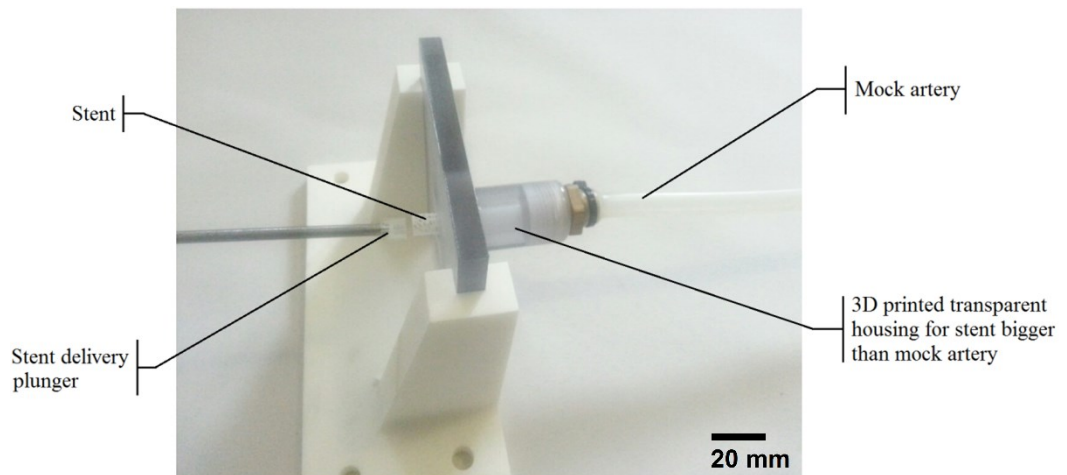


Figure 5-3: A close-up image of stent delivery mechanism showing transparent stent housing for orientation before insertion into the inflated tube.

5.4 Additive Manufacturing of stents

One of the stent topologies obtained, by the process described in section 4.7, was selected for manufacture and testing. Before manufacture, it was necessary to transform the stent geometry to STL file format after smoothing the topology design, which was needed to manufacture the

part using AM. The STL model was then converted into slices or two-dimensional layers using Magics® (Materialise, Leuven) software, which can be then used as a direct input for the machine to manufacture. Further requirements depend upon the individual process from CAD to the manufacturing process for example, the need for repairing, cutting or scaling of the models. Assistance in this process was provided by Mark Hardy. Although the stent material used for the optimisation process was PLA, the methodology adopted for the validation process was selective laser sintering (SLS) technique with nylon as the material. Nylon 12 is the most common material used in SLS process. Also SLS process has the ability to create intricate design overhangs without support material. Figure 5-4 shows the stent CAD model used for additive manufacturing.

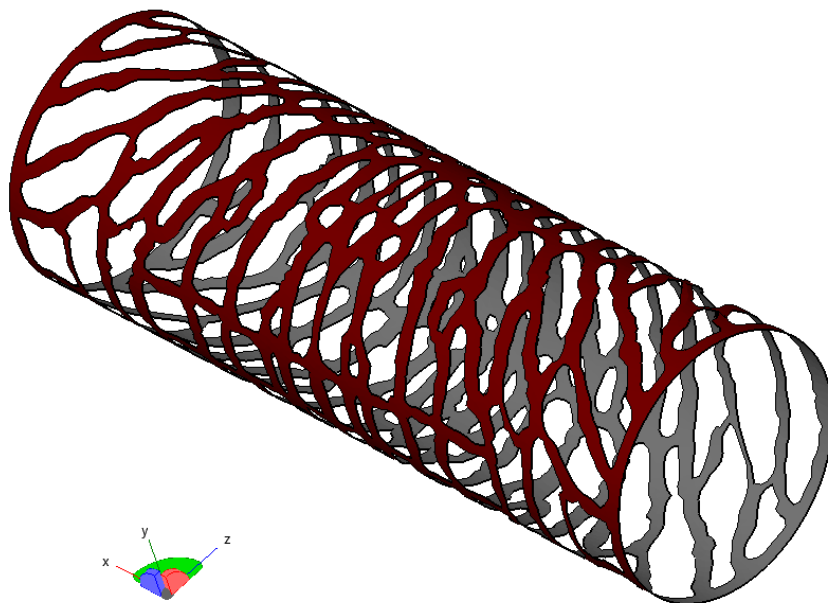


Figure 5-4: Stent model used for additive manufacturing and testing.

Selective laser sintering is a powder bed fusion technique which involves sequentially fusing together powder particles layer by layer with a laser to build a part [122]. The EOS Formiga P110, which is a polymer powder

bed instrument that uses a 30W CO₂ laser, was used for producing the stents. This machine has a build envelope of 200 mm x 250 mm x 330 mm. The stent samples were successfully produced without any support material required. Other processes such as selective laser melting (SLM), material jetting, stereolithography (SLA) and fused deposition modelling (FDM) do require support structures if there is a certain degree of overhang in the design of a component. Polyamide PA2200 commonly known as Nylon 12 was used for stent manufacture. The material was also supplied by EOS in powdered form. Laser sintered PA2200 has a Young's modulus of 1700+/-150N/mm² [174], Poisson's ratio of 0.204 [175] and density varying between 0.90g/cm³ to 0.95g/cm³. The stent model was scaled up 1.93 times to match the commercially available silicone tube and also to avoid manufacturing defects (Figure 5-5) due to very thin struts- which depends upon the layer resolution of the machine. Stent used for the experiments had inner radius of 9.55mm, strut thickness 0.38mm and a length of 29 mm (Figure 5-6).

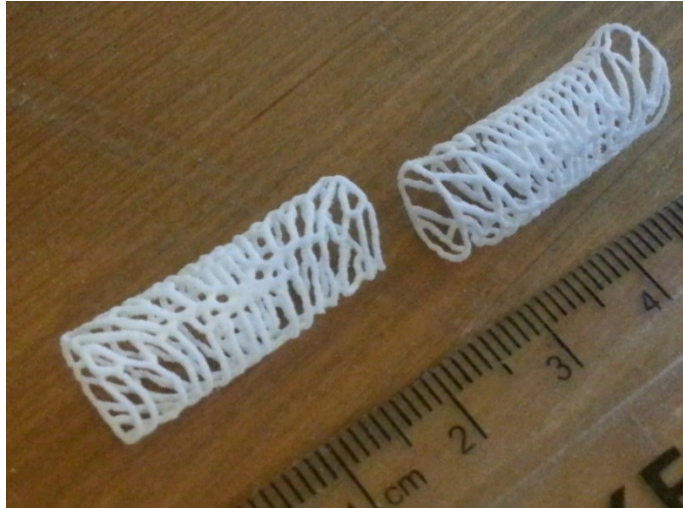


Figure 5-5: Manufacturing defects: Struts at stent ends distorted due to being too thin.

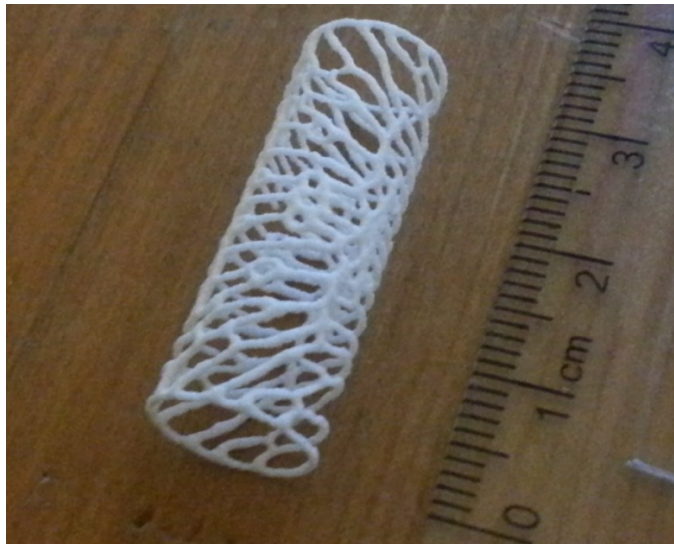


Figure 5-6: Scaled up optimised stent made using SLS used for the experiments.

Using polyamide rather than PLA to make stents did not compromise the aim of the experimental validation since in the FEA portion for validation same material properties were used and it was considered appropriate for the proof of stent design concept. Nylon 12 and PLA have similar tensile properties, while human artery and the selected silicone tube both exhibit hyperelastic non-linear behaviour. In terms of laser sintering nylon 12, a uniform mechanical performance was assumed throughout the build volume of the SLS machine.

5.5 Silicone tensile tests

The material behaviour of silicone was obtained from the uniaxial tensile testing carried out following BS ISO 37:2017 [176] standard for elastomers. Silicone rubbers are hyperelastic in nature and have shown similar results to human vascular behaviour in tension at low stretch [177]. An Instron 5969 tensile test machine was used with a load cell capacity of 50 KN as shown in Figure 5-7. Dumb-bell specimens were cut according to the standard shape (Figure 5-8).

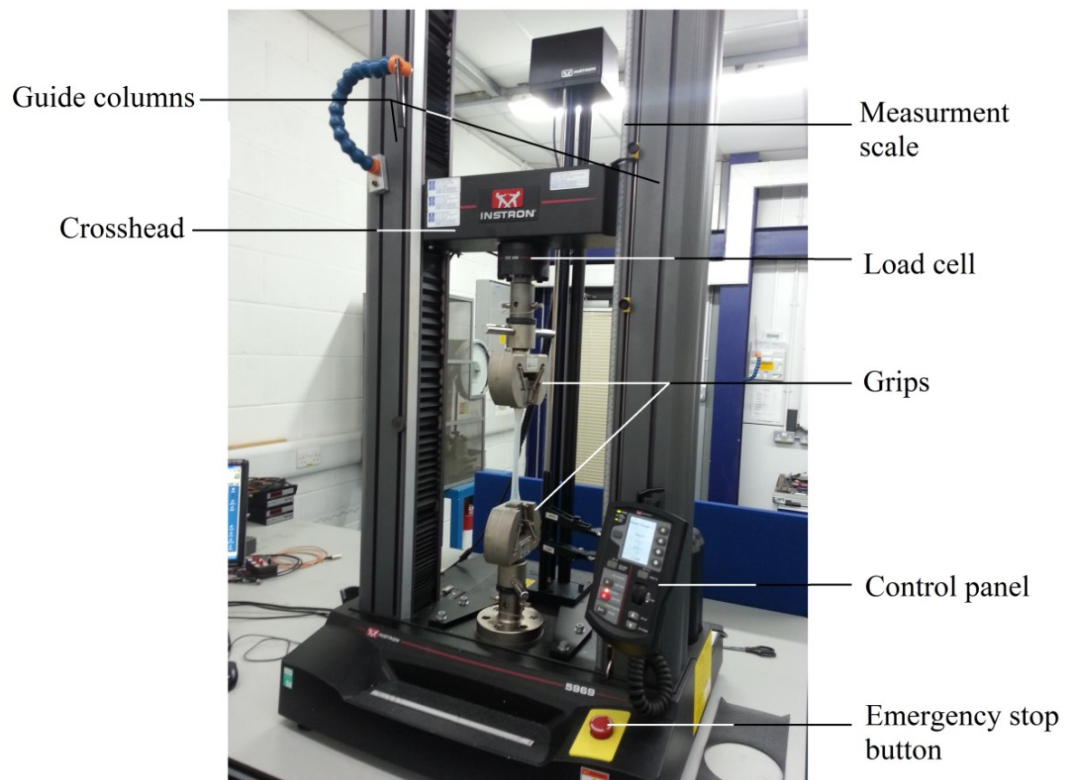
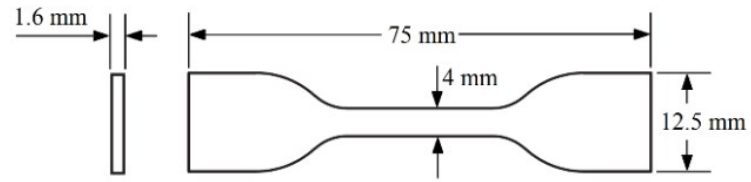


Figure 5-7: Instron tensile test machine used for tensile tests.



(a)



(b)

Figure 5-8: Silicone dumb-bell specimen (a) dimensions and (b) samples cut from tube for tensile tests with die according to BS ISO 37:2017 .

The silicone specimen data used was as follows:

- Wall thickness- 1.6 mm
- Gauge width- 4.0 mm
- Grip separation rate- 500 mm/min

The stress vs strain data obtained from 4 tensile specimen is plotted in Figure 5-9. Isotropic behaviour was assumed for the selected silicone tube.

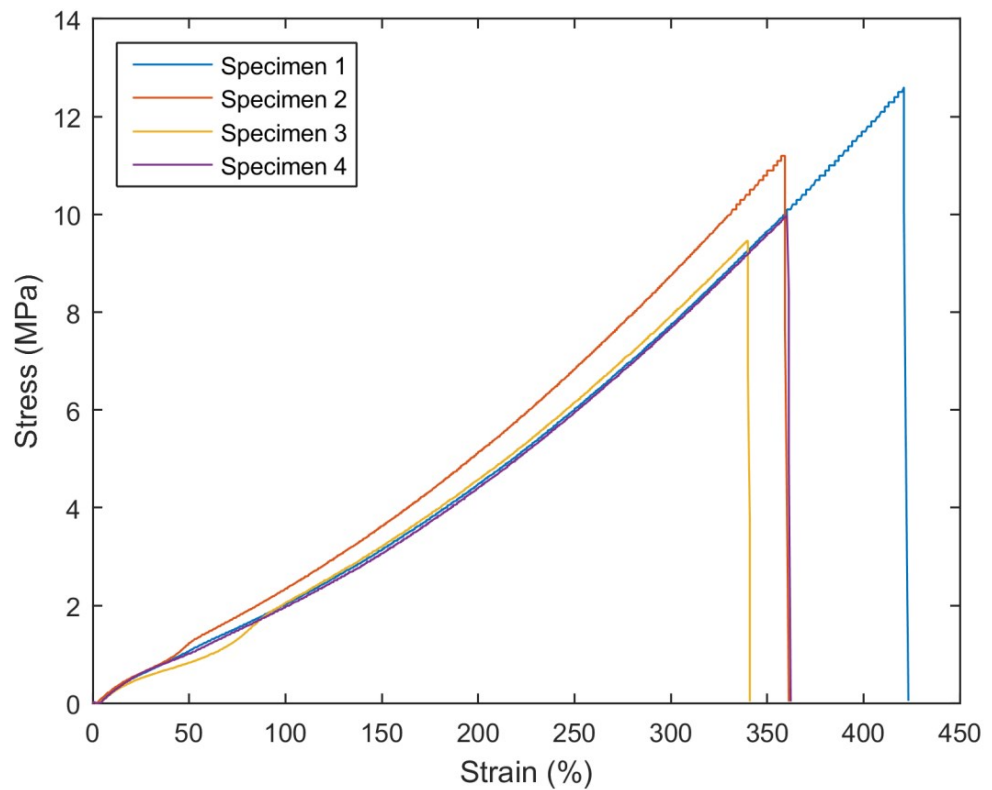


Figure 5-9: Stress vs strain curves of dumb-bell samples.

5.6 Experimental procedure

The first experiment, consisting of a tube inflation without a stent was carried out with a tube sealed by closing the open end of the rig. Following steps were carried out:

1. The silicone mock artery was anchored at both ends to the hose connections in the rig and the camera placed at approximately 30 mm away from the centre of the vessel.
2. An image was captured with the camera of tube with zero gauge pressure.
3. Pressure was then introduced to inflate the tube and gradually raised to 0.15 MPa using a pressure regulator.

4. A second image of the tube was captured at 0.17MPa before deflation for image analysis.

The steps to deploy the optimised stent were as follows:

1. The tube was removed from the connections allow placement of the stent inside one of the hose connections (the stent diameter being 10% larger than the vessel) as shown in Figure 5-10.
2. Image was captured of the tube without a stent zero gauge pressure.
3. Pressure was then increased gradually until the 10% bigger stent could be inserted in to the inflated mock artery (Figure 5-11).
4. The stent, which was placed in the tube connector, was then gradually inserted in to the tube with the help of a plunger and positioned in the middle of the tube. The stent was oriented in such a way that the symmetrical half was facing the camera.
5. After stent insertion, pressure was then reduced to zero such that the mock artery wrapped around the stent (Figure 5-12).
6. A second image of the final shape of the vessel was captured with the stent deployed for image analysis.

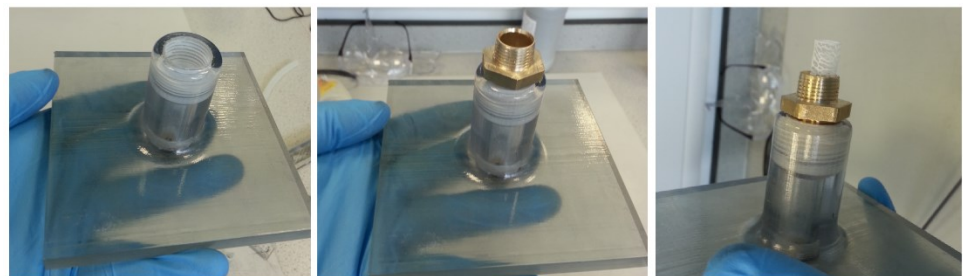


Figure 5-10: Insertion of optimised stent in the hose connector before tube attachment.

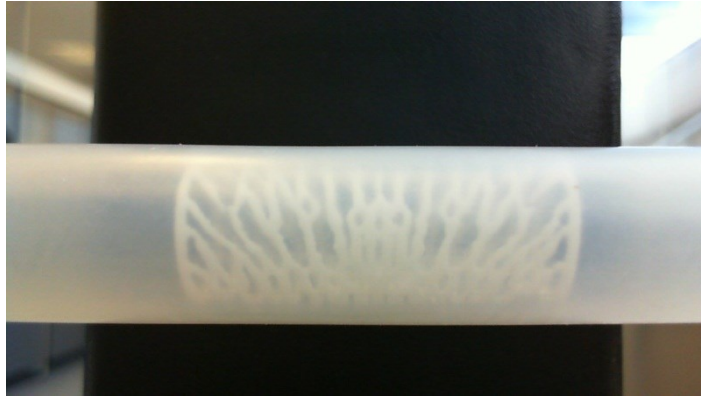


Figure 5-11: Stent inserted in to the inflated artery.



Figure 5-12: Stent deployment after reducing the gauge pressure to zero.

During the experiments camera and tube movements were restricted to avoid any errors in measurements. Similar steps were carried out for the third experiment where the aim was to implant the selected stent in the mock artery with 40% simulated stenosis added at the centre as shown in Figure 5-14 and Figure 5-13. The simulated plaque was cut using a scalpel and measured using a Vernier calliper for dimensional accuracy. Figure 5-15 and Figure 5-16 depict plaque placed at the centre of the tube and then after stent implantation. Another method of obtaining a precise shape of the plaque would be to use a 3D printed trimming jig.

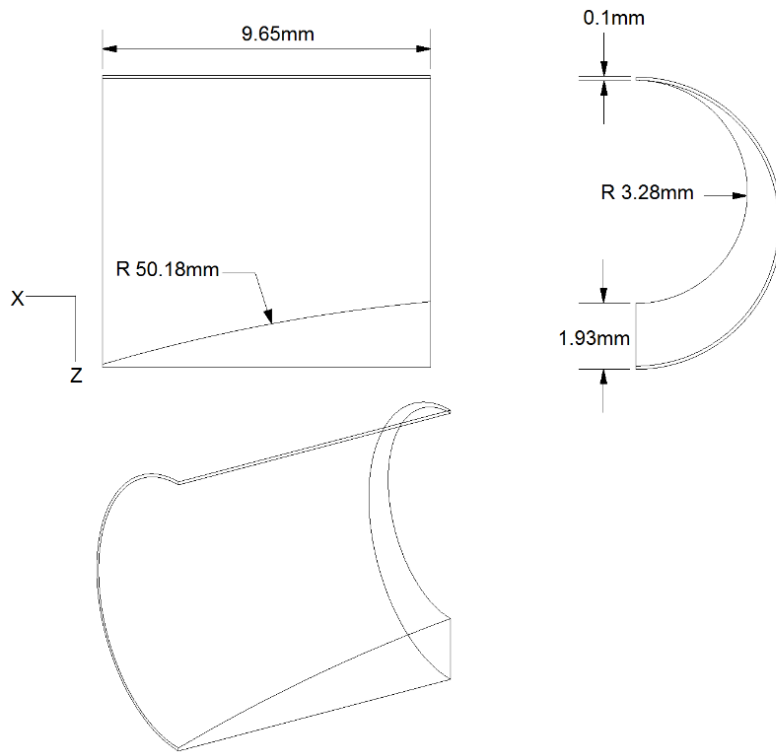


Figure 5-13: Scaled quarter model plaque with dimensions used for experimental observation.

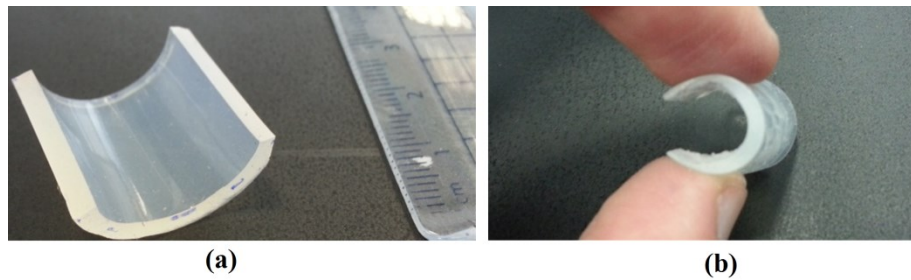


Figure 5-14: 40% simulated plaque made of the same material as the silicone mock artery, initial shape (a), cut to size (b).



Figure 5-15: Simulated plaque added to the mock artery with the thickest part at the bottom.

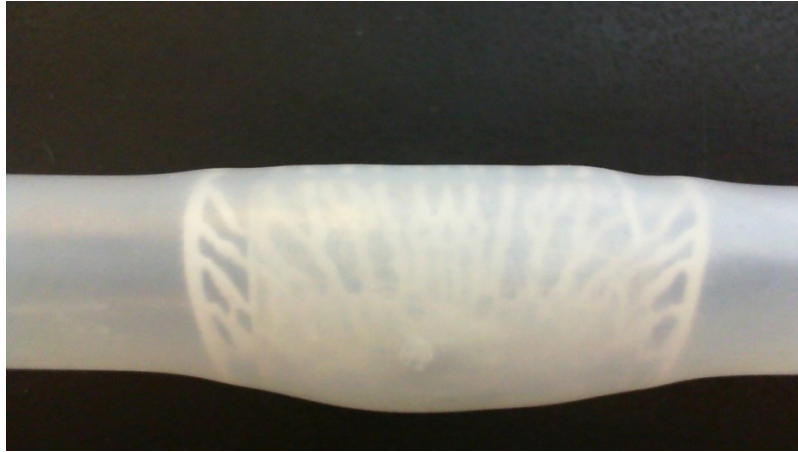


Figure 5-16: Stent implantation in artery with 40% simulated stenosis.

5.7 Image analysis

X-ray micro-tomography, intra-vascular (IVUS) ultrasound and image processing methods have been used previously for the analysis of *in-vivo* and *ex-vivo* arterial strain measurements [178–183]. In the last two decades, with significant development of low-cost cameras and image processing algorithms, non-contact measurement techniques have become more and more common in the experimental mechanics community [182]. The important benefit of non-contact measurement techniques is that touching the sample being examined is avoided and it often saves cost and time. As for the current experiments it was only intended to capture the exterior vessel deformations, and as a consequence a USB camera (Microsoft LifeCam Cinema HD) which could capture images of size 1280 x 720 pixels, was deemed appropriate. The camera was aligned with the centre of the tube where a stent was finally to be positioned. A MATLAB code was used to process the images off-line, by capturing changes in the vessel external boundaries during the experiments. The code is given in appendix C.

5.8 FE Analysis

FE analysis of a simple cylindrical tube simulating the mock silicone artery was carried out for validation purposes. The analysis steps were the same as described in section 4.4 to 4.6, apart from the fact that the units were consistent with the experiment. Dimensions of the tube were chosen to be the same as the silicone tube i.e. 8.6 mm inner diameter with 1.6 mm wall thickness. The model used with stent initial position is shown in Figure 5-17.

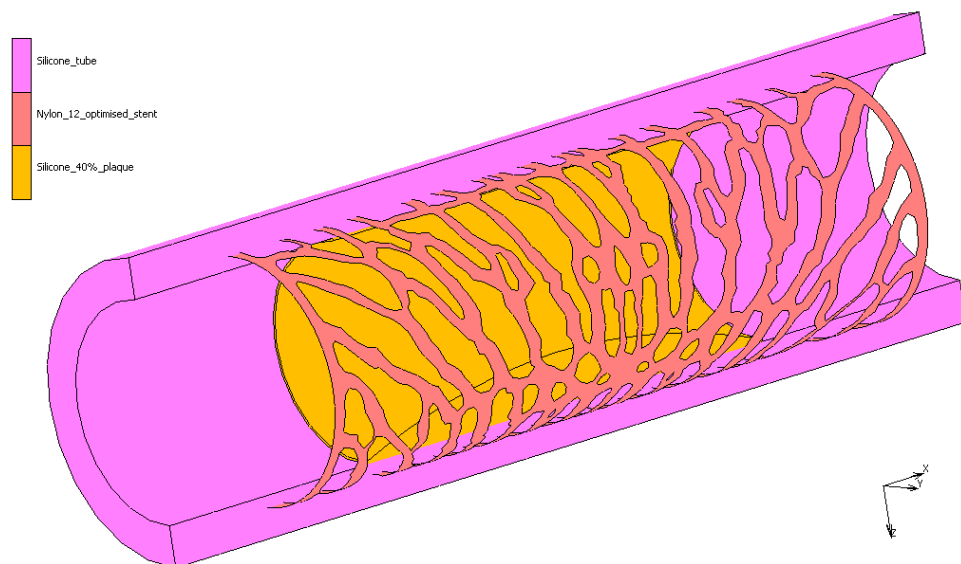


Figure 5-17: FEA model of 40% stenotic silicone mock artery and nylon 12 stent.

Since the analysis consisted of tube inflation and deflation, experimental data of only uniaxial tensile tests was deemed appropriate to be used for the material selection and curve fitting process in MSC Marc Mentat. Arteries and silicone both are non-linear hyperelastic in nature and tensile data has been used previously to mimic arterial behaviour [177].

5.9 Summary

This chapter described the experimental procedure carried out to validate the computational approach used in this thesis. This was achieved by measuring the variation in tube diameter due to inflation and stent placement using a silicone mock artery. The experimental test rig design and steps were discussed in detail along with the additive manufacturing of the optimised stent used. For FE analysis, the material input for silicone mock artery was evaluated by uniaxial tensile tests. Results of the procedures discussed are detailed in the next chapter.

6. Results and Discussion

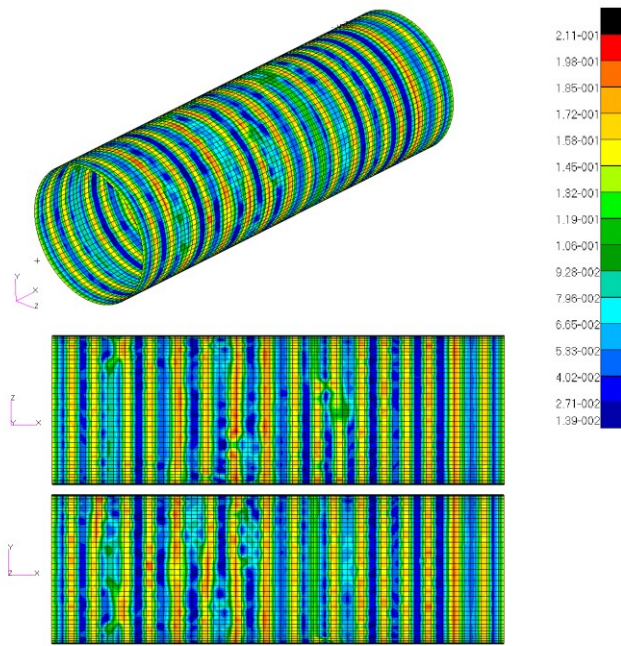
6.1 Introduction

This chapter presents the results and analysis from finite element analysis, optimisation and experimental work. Results arising from the contact analyses between the artery and force extracting cylinder are described which forms the basis of lesion-specific stent TO. The new TO stent designs were filtered, smoothed then analysed by implanting them in corresponding stenotic arteries and a comparison is then made against a generic stent design in terms of immediate post implantation recoil. Results from the experimental analysis of stent implantation are also presented that validate a portion of the FEA. Having found a suitable material model to represent the hyperelastic behaviour of silicone mock artery, one of the optimised stents was implanted with simulated stenosis both experimentally and numerically. Focus was kept on the arterial radial dimensions to analyse stent recoil.

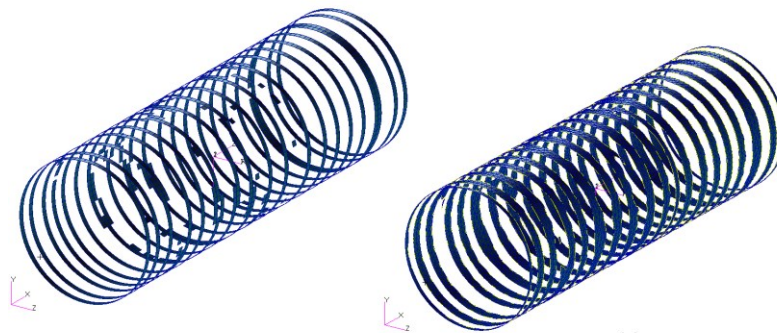
6.2 Investigation of initial load case scenarios

The analysis carried out initially involved 3 different scenarios of loading conditions i.e. uniform loading on cylinder, point crush load at the centre and torsion at one end to show the effect on resulting topologies from the chosen arbitrary loading conditions. It is evident from TO of these load

cases that the geometry reacts and exhibits changes to compensate the applied forces. A uniform loading of 0.1MPa produces 'stiffener rings' type outcome which is consistent with conventional use of rings in pressure related cylindrical structures. A pair of point load simulating crush at the centre of the cylinder results in struts emanating from the centre and for torsion the design results in a helical pattern. While the objective function remains the same, volume fraction constraint of 0.3 has been explored with 3 different meshes including one with varying minimum member size (MMS). The results presented here are from cylindrical mesh containing 6804 elements (mesh 1). Further refined meshes with 13685 (mesh 2) and 47507 elements (mesh 3) for the initial load case scenarios are presented in Appendix D, which demonstrate mesh-dependent changes in topology and strut width alteration resulting from change in MMS. It should also be noted that in the case of uniform (Figure 6-1) and pure torsional loading (Figure 6-4), the topologies do not vary significantly between the different mesh sizes. In the load case of central crush, MMS of 0.3mm, 0.4mm and 0.5mm allow a slight geometry change with changing strut width. Figure 6-5 shows the element density distribution in one of the cases (crush load) during different design cycles.



(a)



(b)

(c)

Figure 6-1: Mesh 1 (6804 elements) with uniform loading: (a) element density distribution, ρ , representing material densities between 0-1 (b) threshold 0.3 for element filtering and (c) FEM smoothing of the filtered elements.

The resulting density was filtered by specifying a threshold (0.25-0.3) in order to obtain structures that are free from isolated or free suspended elements. Further smoothing option which is built-in Patran enhances the structure by producing a smooth transition of elements by removing jagged edges. Figure 6-2 illustrates the FEM smoothing results in the uniform loading case.

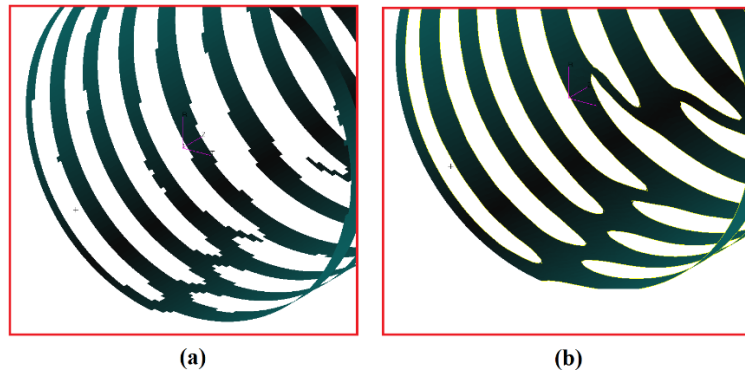


Figure 6-2: FEM option allowing smooth transition of elements and threshold control for enhancing member connectivity (a) before and (b) after applying element smoothing.

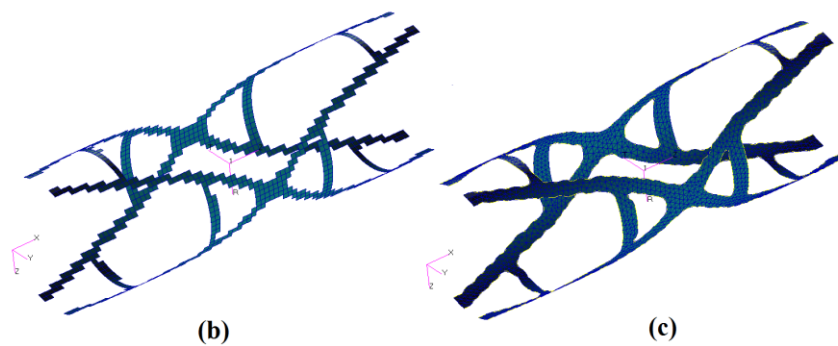
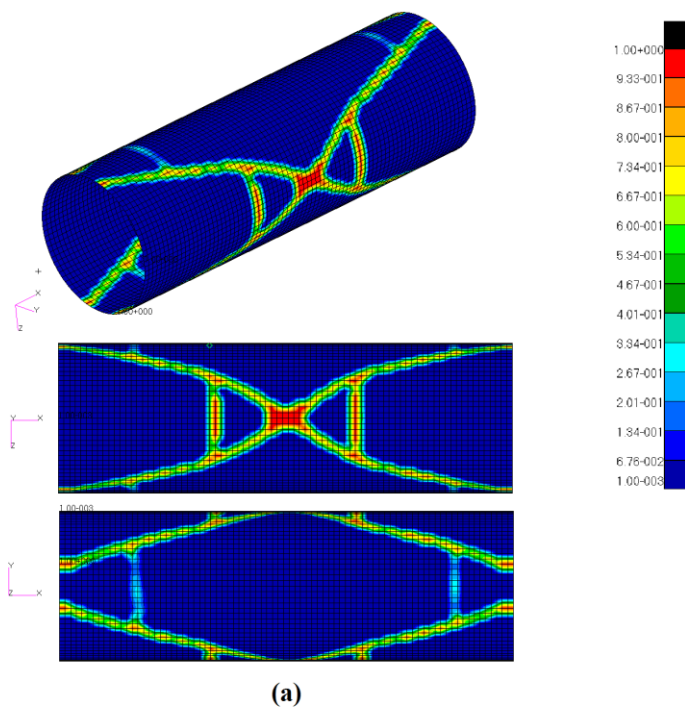
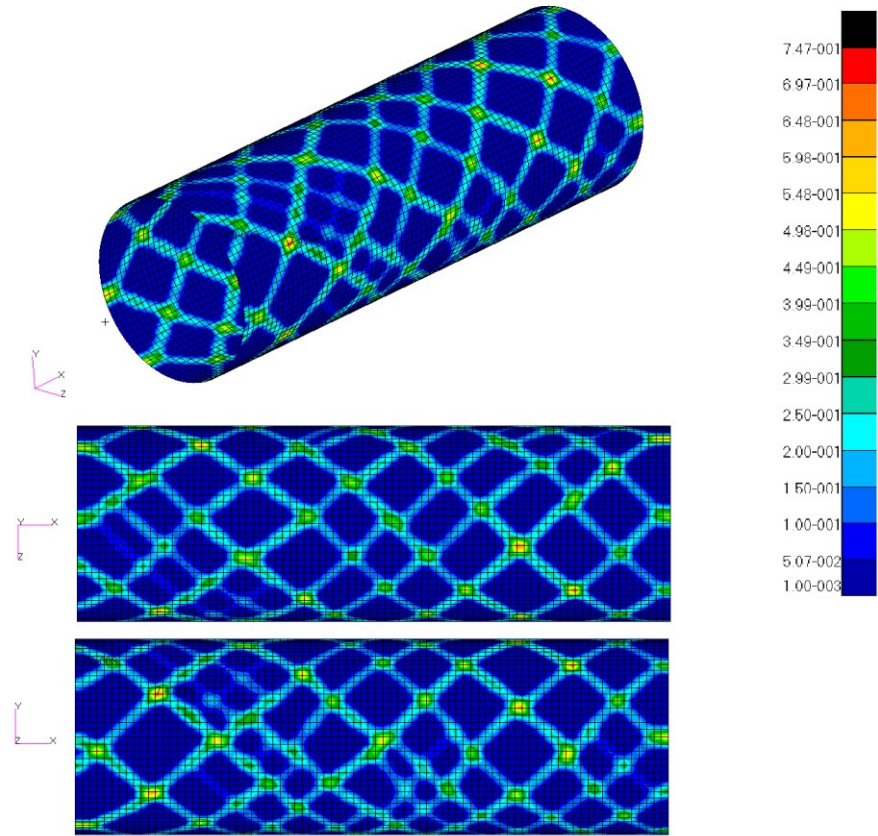


Figure 6-3: Mesh 1 (6804 elements) with crush loading: (a) element density distribution, ρ , representing material densities between 0-1 (b) threshold 0.3 for element filtering and (c) FEM smoothing of the filtered elements.



(a)

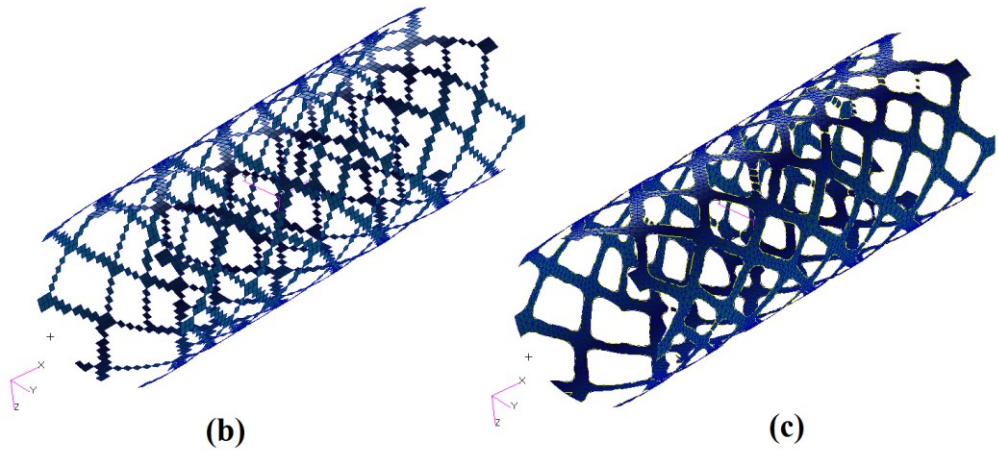


Figure 6-4: Mesh 1 (6804 elements) with torsional loading: (a) element density distribution, ρ , representing material densities between 0-1 (b) threshold 0.3 for element filtering and (c) FEM smoothing of the filtered elements.

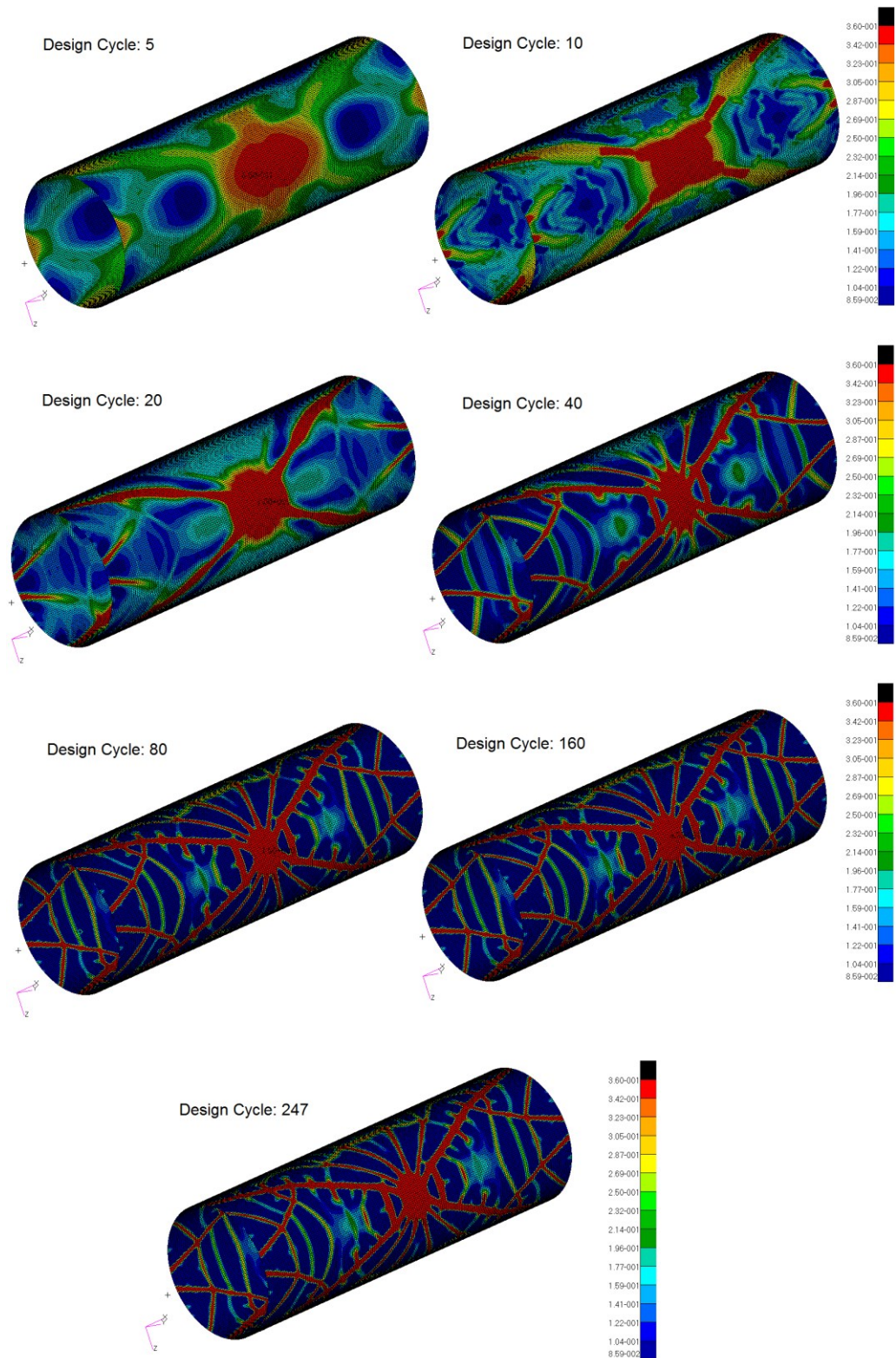


Figure 6-5: Mesh 3 (47507 elements) density distribution, ρ , with central crush loading and MMS 0.3 during different iteration cycles. Note the minimal difference between design cycles 80 through 247.

The results from torsion applied to one end of the cylinder were very similar to a previous study by Taggart et al. [184], which attempts to

validate topology optimised results to known theoretical solutions, an example of which is shown in Figure 6-6.

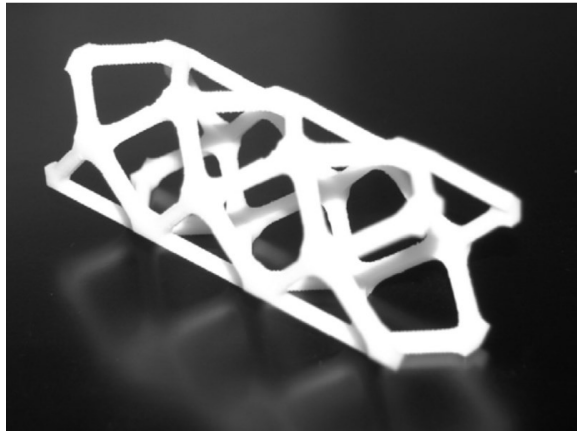


Figure 6-6: Topology of a cylindrical structure resulting from pure torsion [184].

6.3 Assessment of stent-artery contact analysis

The initial contact analyses involving the artery models with the cylinder were used to generate a set of contact normal forces acting radially inward on the cylinder for each case, to be used as the input load for the topology optimisation. The resultant radial force from a contact analysis of all 3 types of plaque materials and 3 stenosis levels is shown in Figure 6-7, Figure 6-8 and Figure 6-9. These results were also unwrapped from a cylindrical shape for illustration purposes and depict the contour plot of the radially inward nodal forces on the cylinder. It can be noted that highest load is acting in the top-left edge (-ve Z-axis) due to plaque peak thickness.

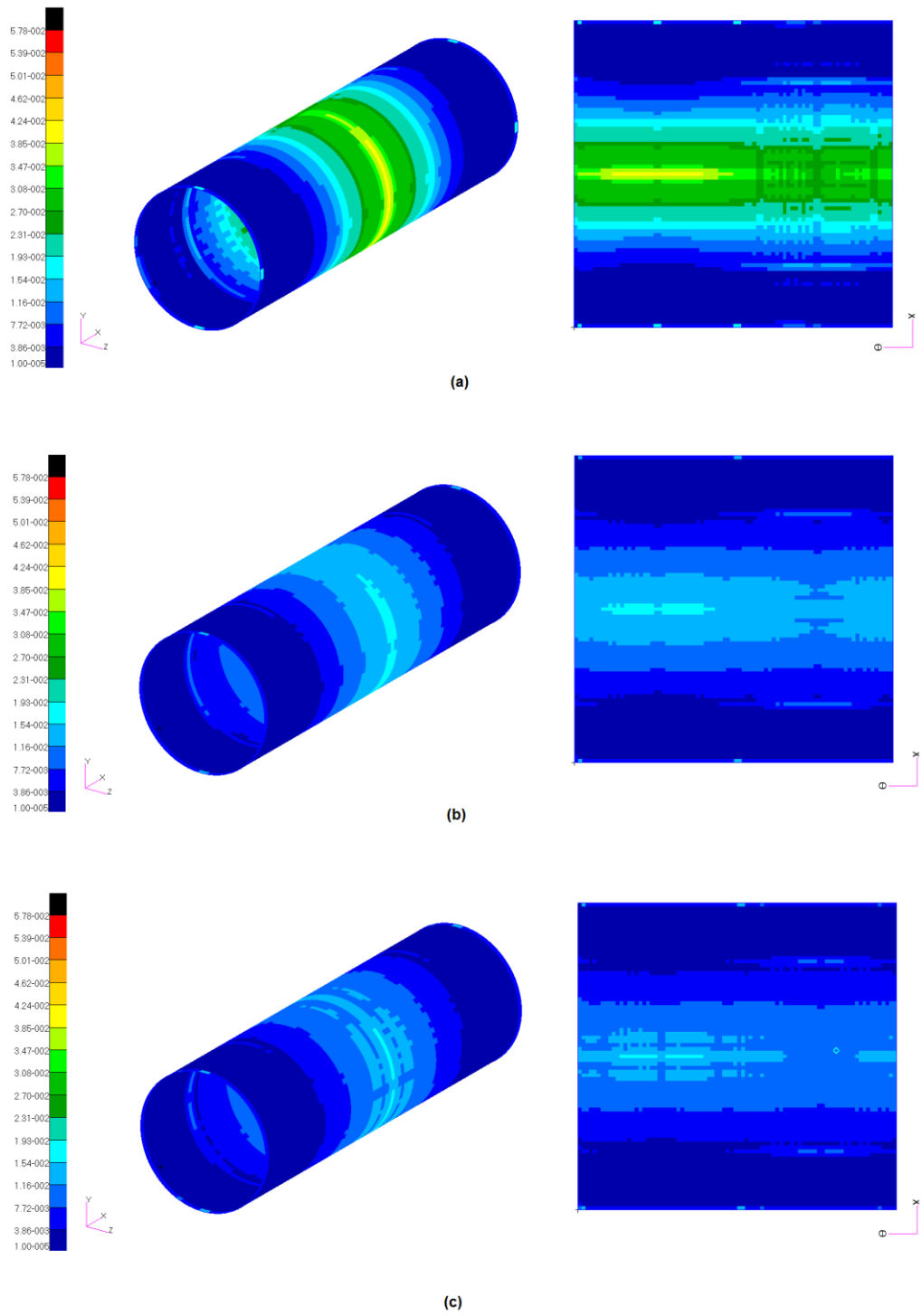


Figure 6-7: Contour plot showing radially inward nodal load (N) variation on the design space for stent topology optimisation based on cylinder-artery contact with 30% calcified (a) hypocellular (b) and cellular plaques (c) along with unwrapped versions from cylindrical shape for illustration purpose.

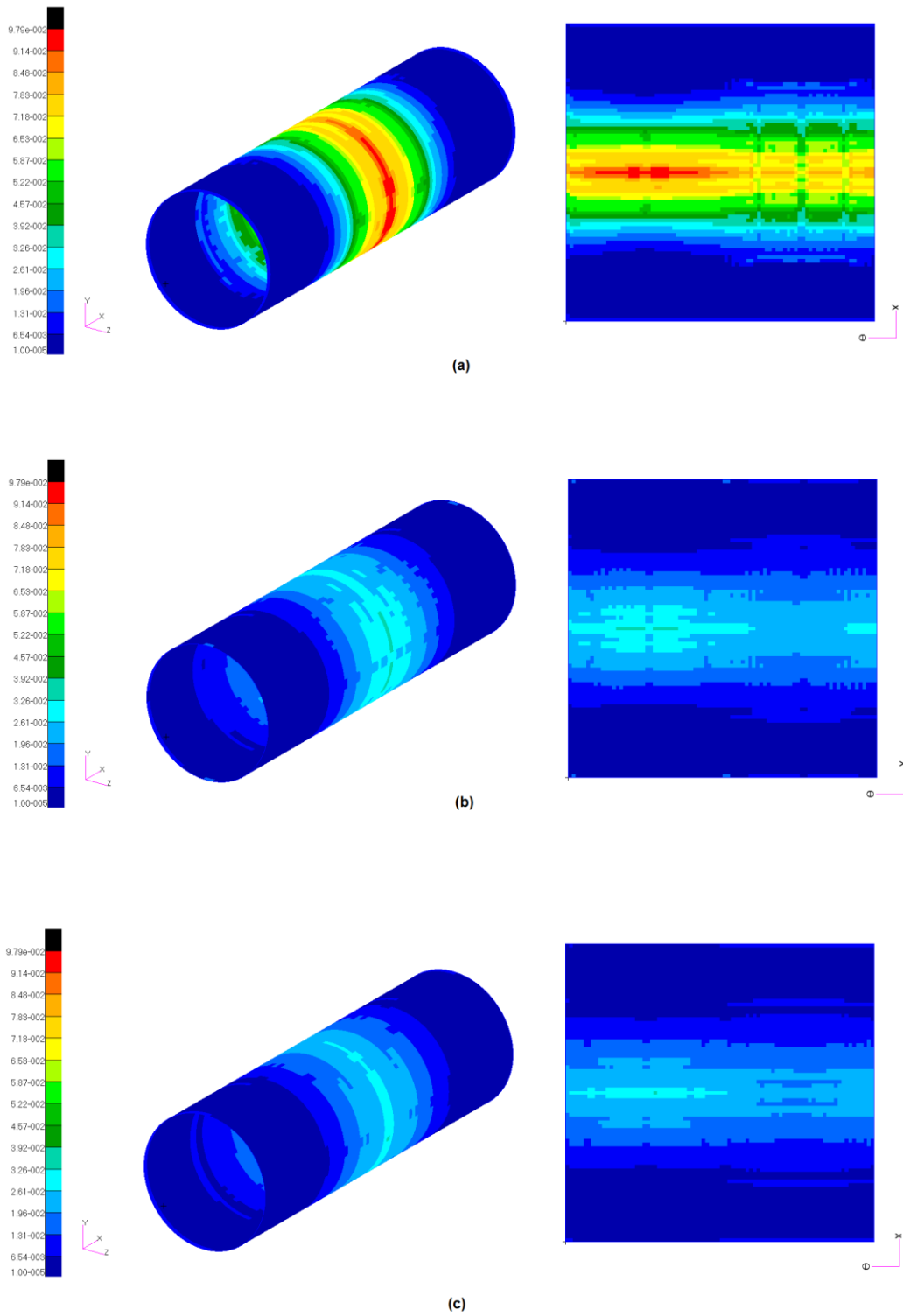
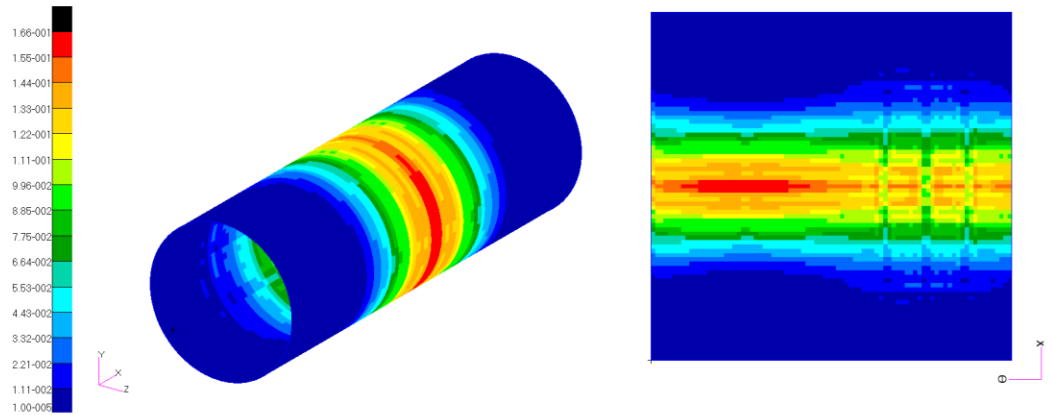
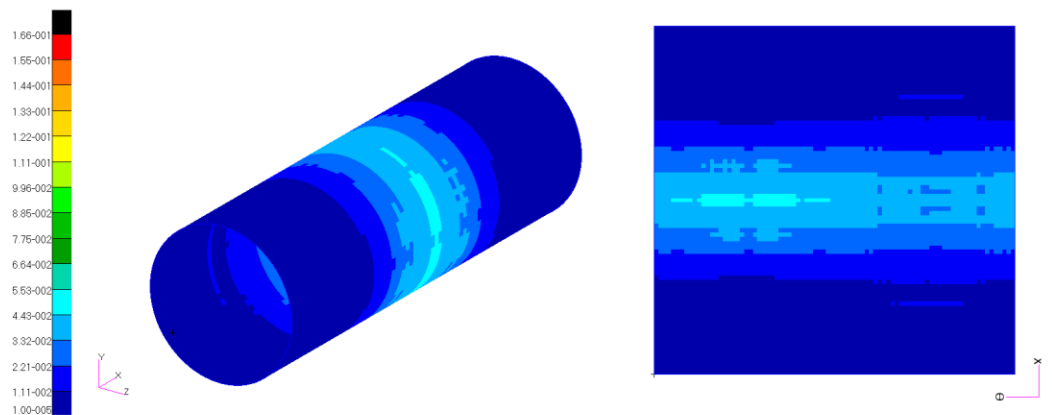


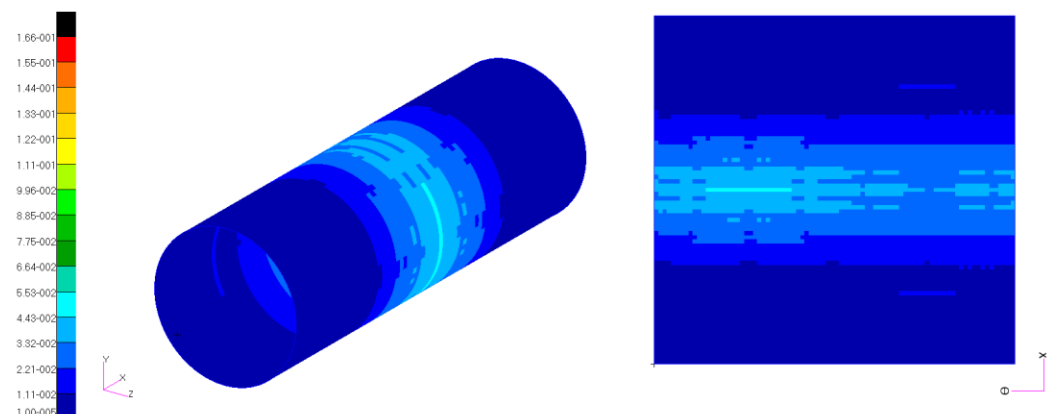
Figure 6-8: Contour plot showing radially inward nodal load (N) variation on the design space for stent topology optimisation based on cylinder-artery contact with 40% calcified (a) hypocellular (b) and cellular plaques (c) along with unwrapped versions from cylindrical shape for illustration purpose.



(a)



(b)



(c)

Figure 6-9: Contour plot showing radially inward nodal load (N) variation on the design space for stent topology optimisation based on cylinder-artery contact with 50% calcified (a) hypocellular (b) and cellular plaques (c) along with unwrapped versions from cylindrical shape for illustration purpose.

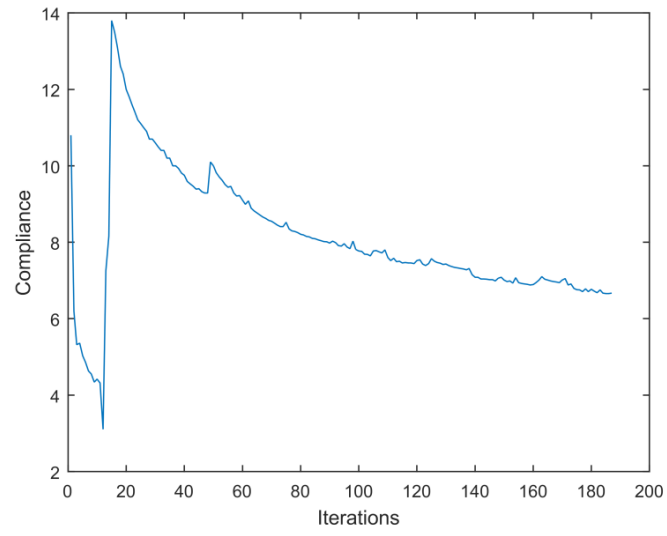
It is evident from these contact analyses of different plaques with the cylinder that calcified plaque exerts the highest peak compressive force followed by hypocellular plaque with the lowest peak force from cellular plaque. This is in agreement with their stiffness level. These peak values are summarised in the table below.

Table 6-1: Peak compressive force exerted by stenotic arteries on cylinder after deflation to diastole.

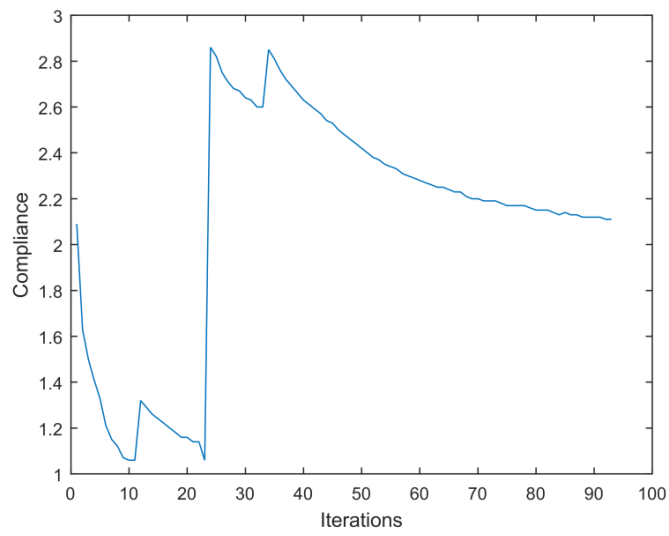
Peak Compressive Force (N)			
Stenosis (%)	Calcified	Cellular	Hypocellular
30	0.057	0.034	0.044
40	0.097	0.033	0.043
50	0.166	0.050	0.052

6.4 Lesion-specific stent topology optimisation results

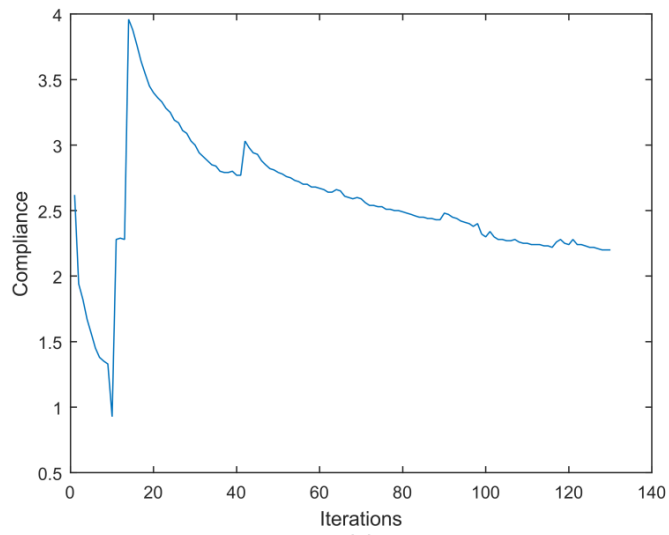
Topology optimisation using the force distribution from the contact analysis was used to generate the optimal material distribution of material for the 9 different plaque loading conditions. Figure 6-10, Figure 6-11 and Figure 6-12 show the optimisation solution convergence of compliance against the number of iterations of stents under stenosis load of 30% (6.67, 2.11 and 2.20 Nmm), 40% (25.40, 7.54 and 4.76 Nmm) and 50% (66.10, 8.75 and 9.35 Nmm) for calcified (a), cellular (b) and hypocellular (c) plaque scenarios respectively. Hard convergence criteria was achieved (compares the results of this most recent finite element analysis with those from the previous design cycle) based on convergence tolerance 0.0001.



(a)

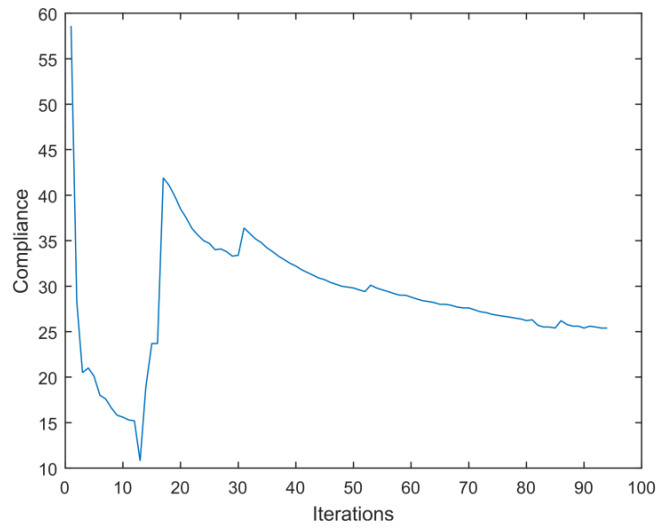


(b)

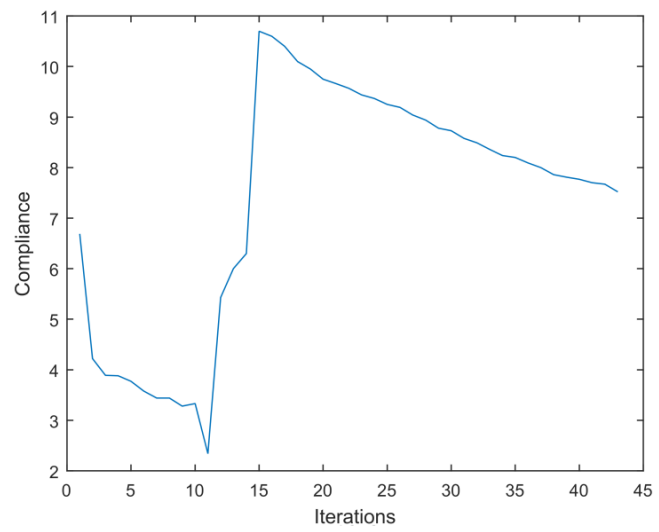


(c)

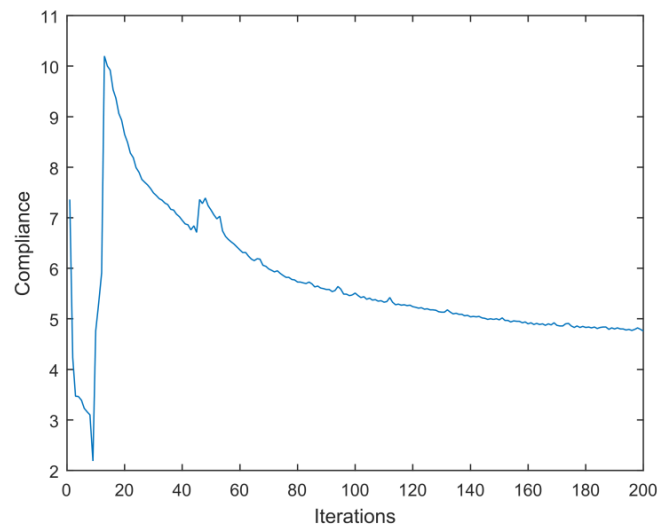
Figure 6-10: Stent topology optimisation convergence plots: compliance (Nmm) with respect to design iterations for 30% stenosis for: (a) calcified, (b) cellular and (c) hypocellular plaque types respectively.



(a)

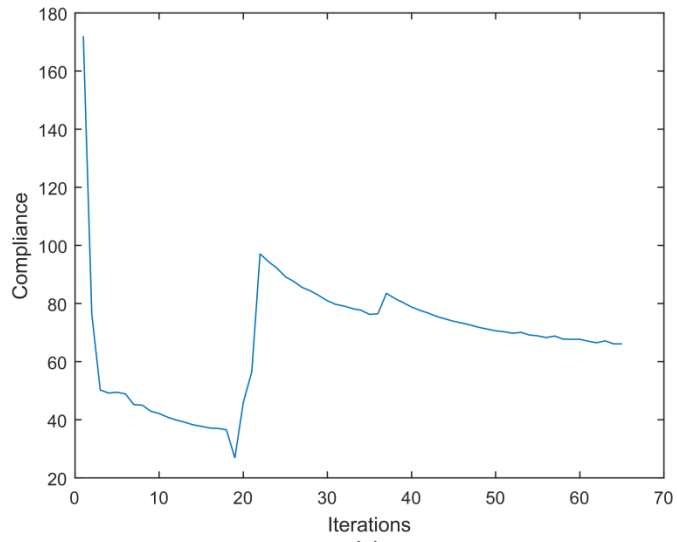


(b)

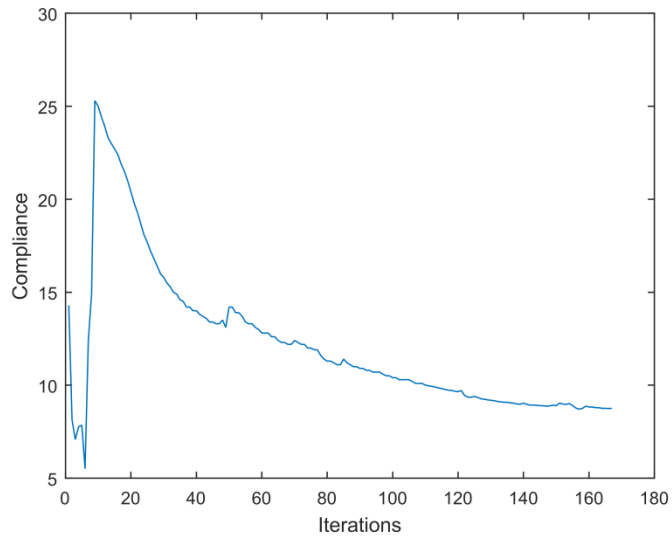


(c)

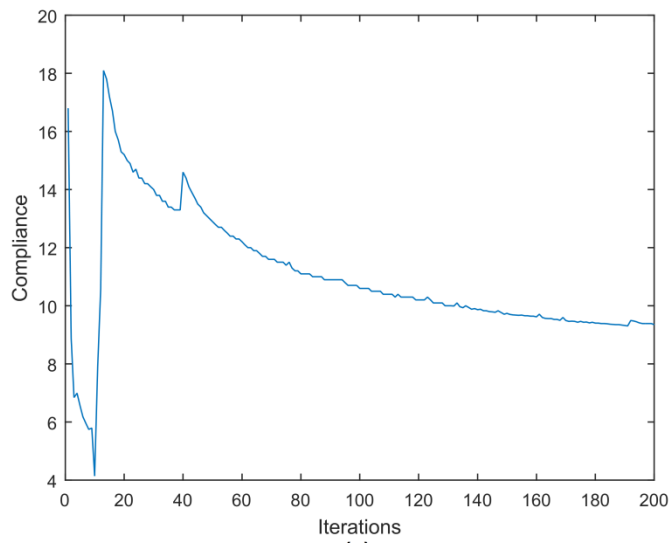
Figure 6-11: Stent topology optimisation convergence plots: compliance (Nmm) with respect to design iterations for 40% stenosis for: (a) calcified, (b) cellular and (c) hypocellular plaque types respectively.



(a)



(b)



(c)

Figure 6-12: Stent topology optimisation convergence plots: compliance (Nmm) with respect to design iterations for 50% stenosis for: (a) calcified, (b) cellular and (c) hypocellular plaque types respectively.

Figure 6-13 shows the normalised material density distribution, from TO with a 0.3 volume fraction constraint. The resulting amount of material in each optimised stent was similar to the generic stent (varying less than 5%). The results were unwrapped using MATLAB to form a flat 2D plot for illustration purposes. It can be seen that there is a higher material concentration in the central part of the stent, as a consequence of the plaque induced higher forces here as previously shown in Figure 6-14, especially in the centre of the lower half of each stent where it comes into contact with the thickest part of the plaque in each case.

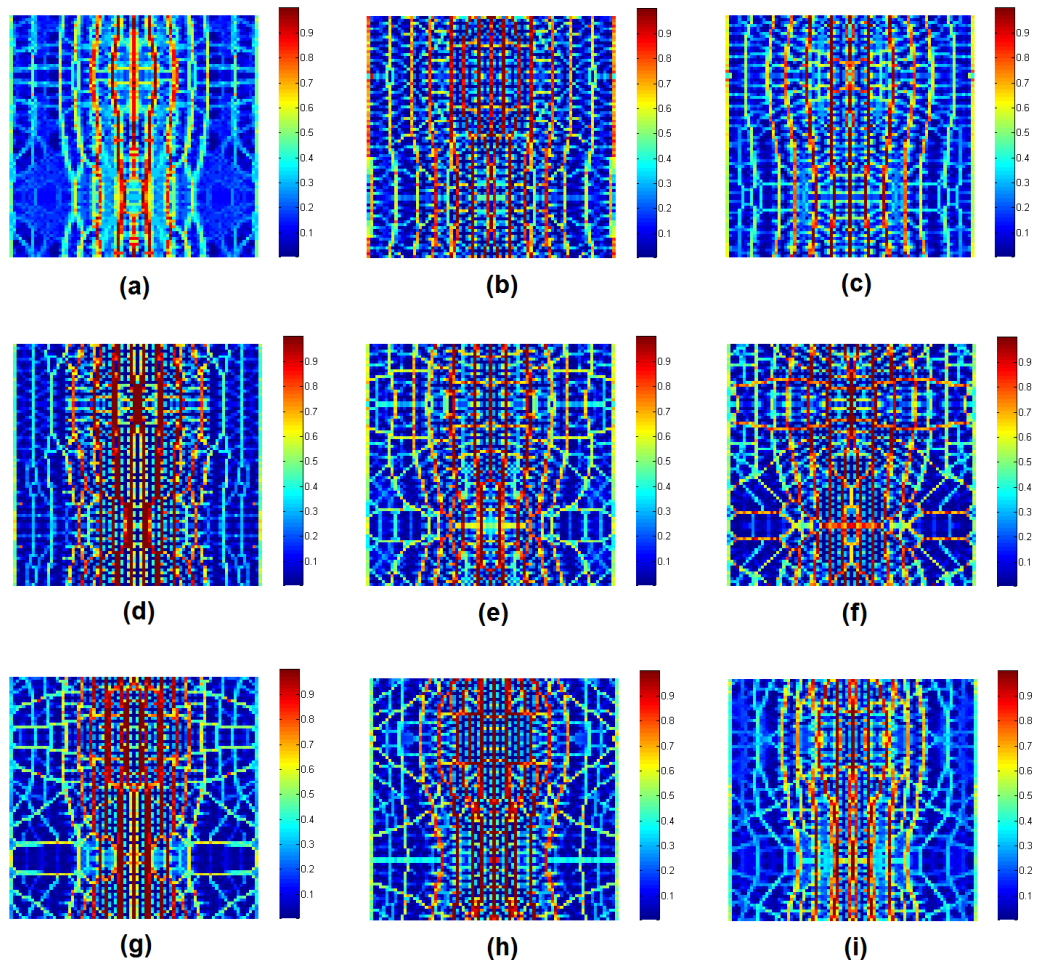


Figure 6-13: Stent topology optimisation density distribution results for (a-c) 30%, (d-f) 40% and (g-i) 50% stenosis for calcified, cellular and hypocellular plaque types respectively (results of axial-stent-half unwrapped from cylindrical shape for illustration purposes).

MATLAB and image editing software were used to unwrap, construct and smooth the optimisation geometry in order to transform it into an analysable stent structure, as illustrated in Figure 6-14. This modification led to an additional 5-10% volume increase of the stent but the overall volume remained in the range of current stents in practice.

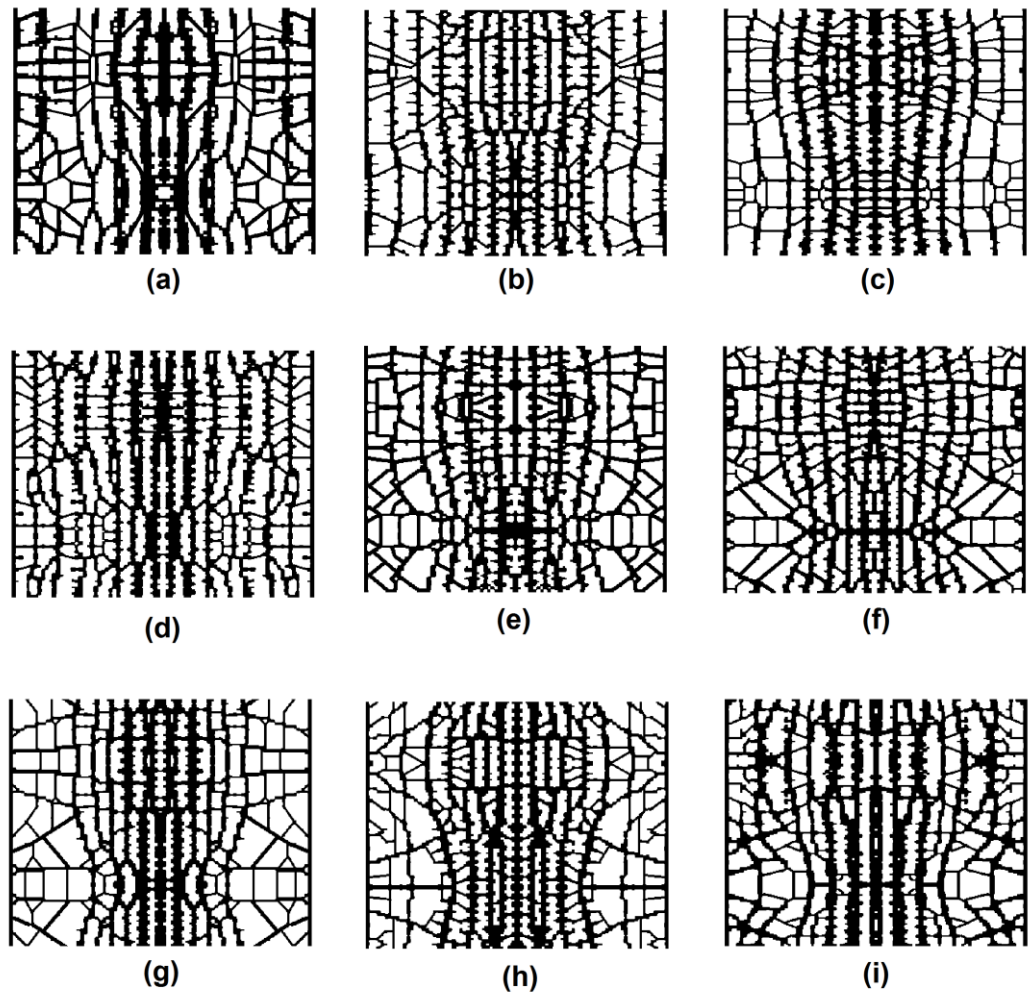


Figure 6-14: Stent topologies for (a-c) 30%, (d-f) 40% and (g-i) 50% for calcified, cellular and hypocellular plaque types respectively, (results unwrapped from cylindrical shape for illustration purpose).

The smoothed optimised stent results were then wrapped to form cylindrical shapes and solved for contact analysis with their respective arteries in the same manner as the contact FEA with the force extracting cylinder. The final lumen radial deformation of 20 equidistant points in

each of the diseased arteries along the thickest part of the plaque were recorded to provide a comparative measure of the ability of the stent to maintain an arterial opening.

6.5 Assessment of radial displacement

For comparison, the first step was to evaluate recoil of a generic stent in stenotic arteries with different plaque materials for 30, 40 and 50% stenosis levels. Plaque peak thickness in the 30% stenosis protruding inside the artery had a minimum unstented radius 1.56 mm. After implantation of optimised stents, this increased to 2.43 mm, 2.54 mm and 2.54 mm, representing 2%, 0.5% and 1% residual stenosis, for calcified, cellular and hypocellular plaques respectively with the corresponding optimised stent. This difference in the narrowest lumen radius is shown in Figure 6-15 as 0.87mm, 0.98mm and 0.98mm. In the same scenario, lumen position values after generic stent implantation were 2.17 mm, 2.29 mm and 2.24 mm for calcified, cellular and hypocellular plaques respectively (Figure 6-18). In the 40% stenotic artery, the unstented minimum position from central axis was, as expected, even less than with the 30% plaque, at 1.22mm. After stenting with the optimised designs, lumen gain was achieved, with the minimum radius increasing to 2.24 mm, 2.51 mm and 2.34 mm representing 2%, 0.5% and 2% residual stenosis, for calcified, cellular and hypocellular plaques respectively, with the corresponding optimised stent. This amounted to a difference of 1.02mm, 1.29mm and 1.12mm as illustrated in Figure 6-16. Results in the same environment with a generic stent were 1.68 mm, 2.13 mm and 2.0 mm for calcified, cellular and hypocellular plaques respectively

(Figure 6-19). Similarly for 50% artery stenosis, plaque peak thickness had an unstented position of 0.972 mm in the Z direction. After stenting this increased to 2.06 mm, 2.49 mm and 2.50 mm, representing 6%, 4% and 3% residual stenosis, for calcified, cellular and hypocellular respectively, with the corresponding optimised stent. This amounted to a difference of 1.08mm, 1.51mm and 1.52mm as illustrated in Figure 6-17. In similar conditions, lumen positions with a generic stent were 1.54 mm, 1.97 mm and 1.78 mm for calcified, cellular and hypocellular plaques respectively (Figure 6-20). Increase in the lumen diameter post-stenting with generic and optimised designs are summarised in Table 6-2, measured at the plaque peak position.

Table 6-2: Post-stenting lumen gain in the generic and optimised designs due to peak plaque radius change.

Stenosis (%)	Post-stenting lumen radius gain (mm)					
	Calcified		Cellular		Hypocellular	
	Generic	Optimised	Generic	Optimised	Generic	Optimised
30	0.61	0.87	0.73	0.98	0.68	0.98
40	0.46	1.02	0.91	1.29	0.78	1.12
50	0.56	1.08	0.99	1.51	0.80	1.52

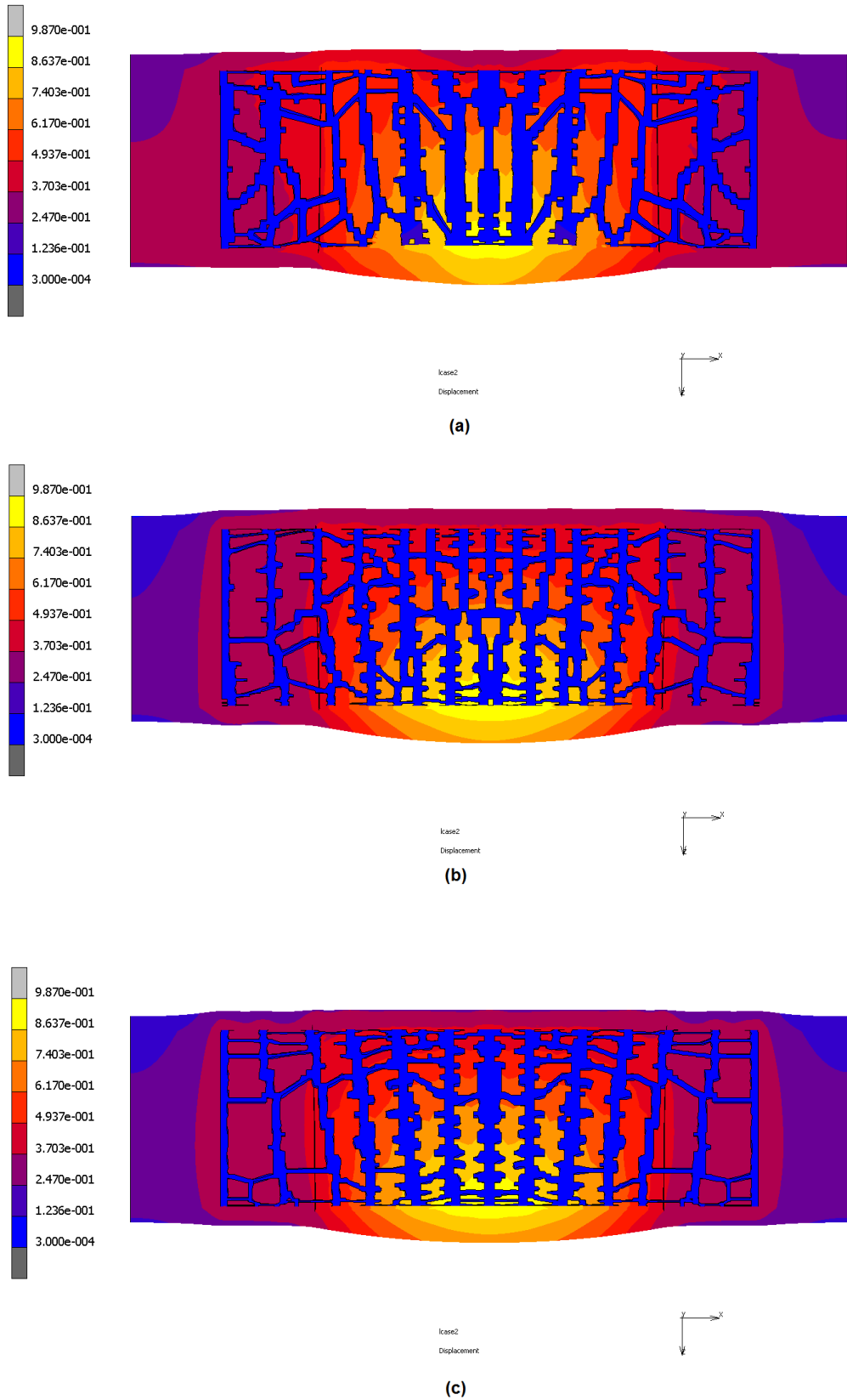


Figure 6-15: Deformation plot (mm) showing contact of optimised stents with their respective stenotic arteries having 30% calcified (a) cellular (b) and hypocellular plaques (c).

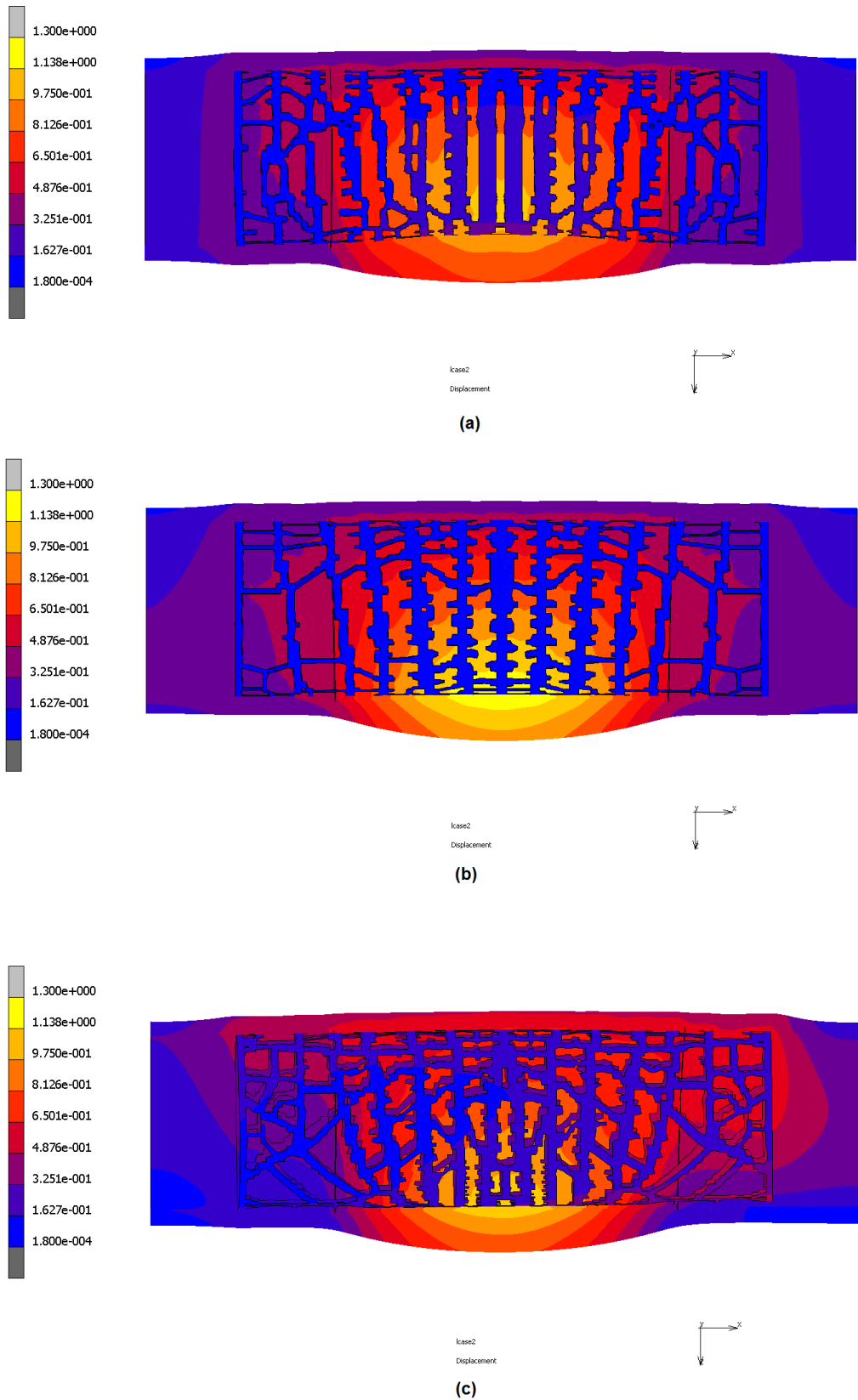


Figure 6-16: Deformation plot (mm) showing contact of optimised stents with their respective stenotic arteries having 40% calcified (a) cellular (b) and hypocellular plaques (c).

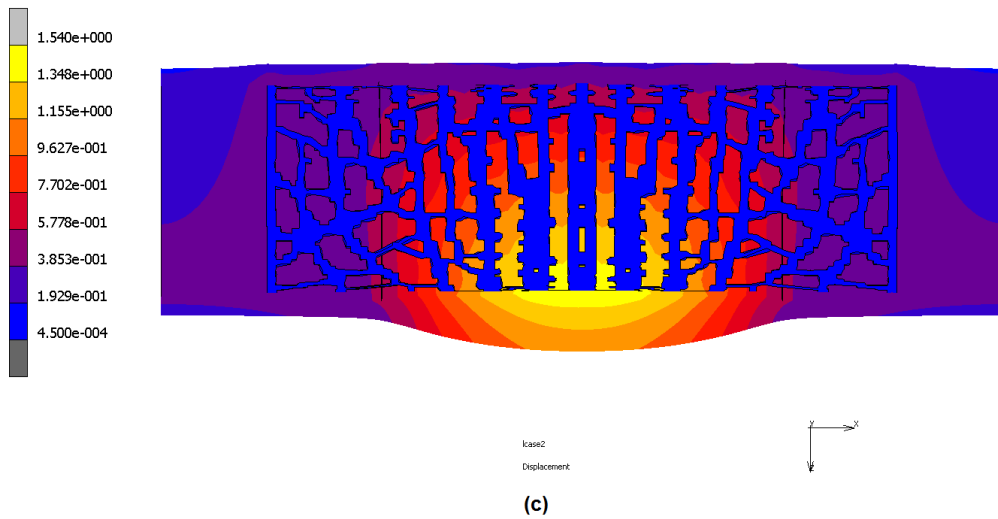
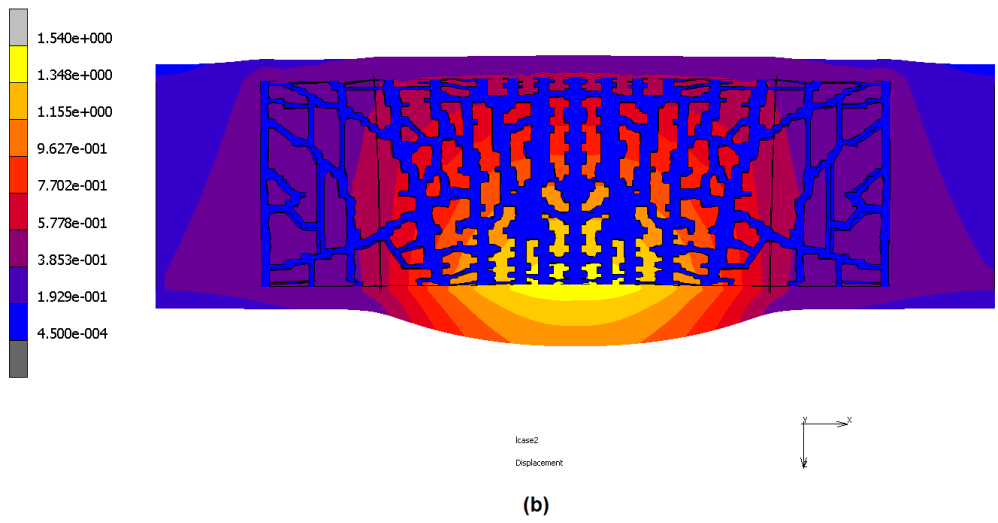
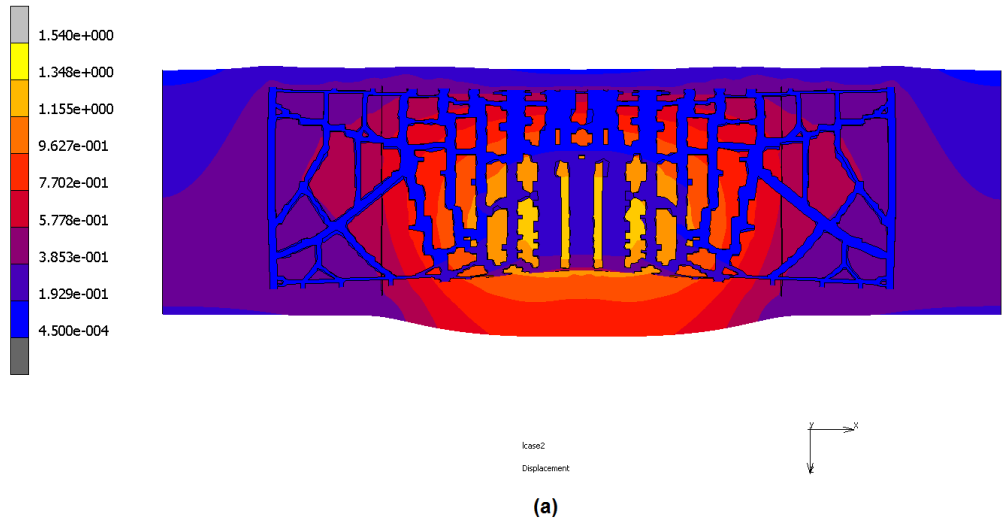
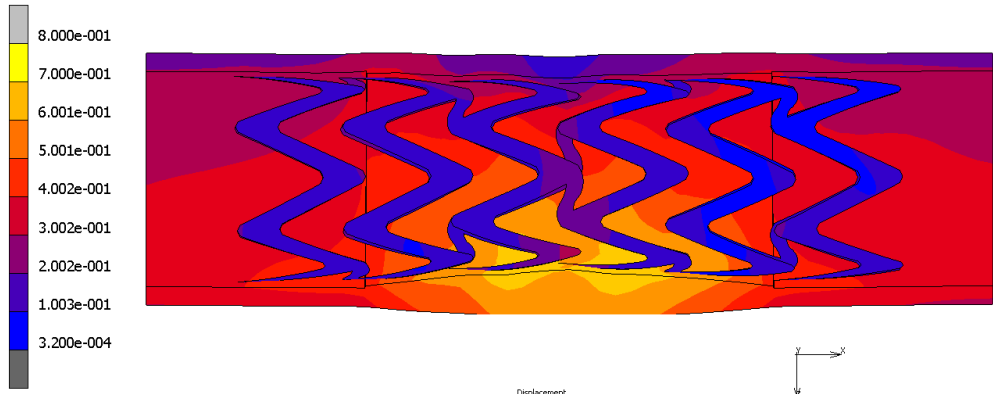
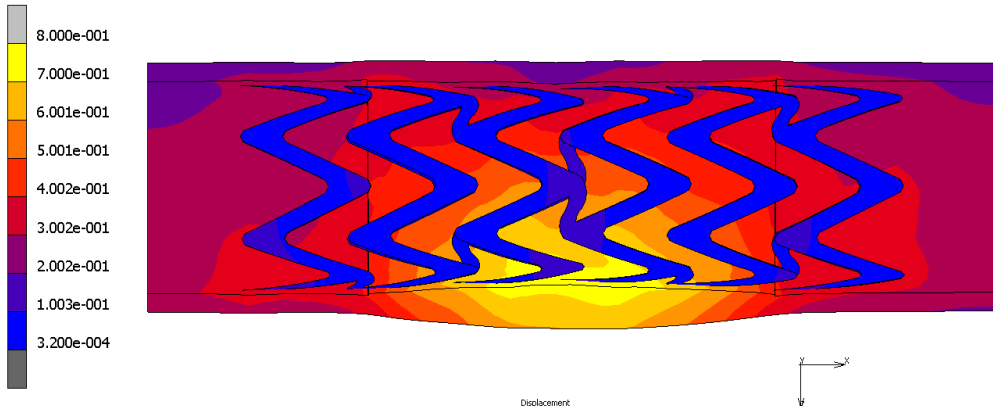


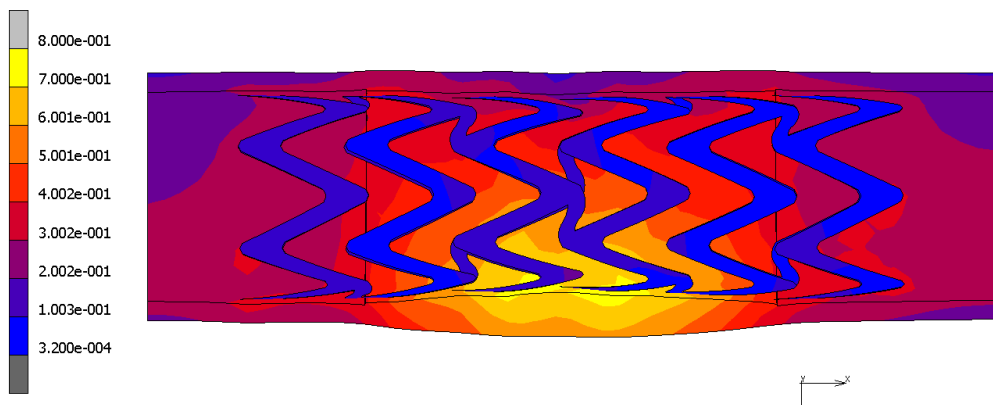
Figure 6-17: Deformation plot (mm) showing contact of optimised stents with their respective stenotic arteries having 50% calcified (a) cellular (b) and hypocellular plaques (c).



(a)



(b)



(c)

Figure 6-18: Deformation plot (mm) showing contact of a generic stent with stenotic arteries having 30% calcified (a) cellular (b) and hypocellular plaques (c).

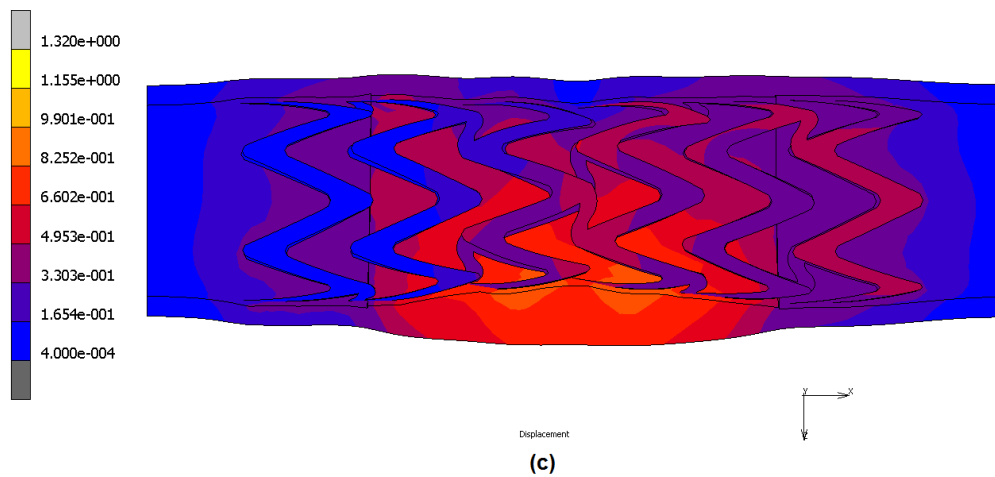
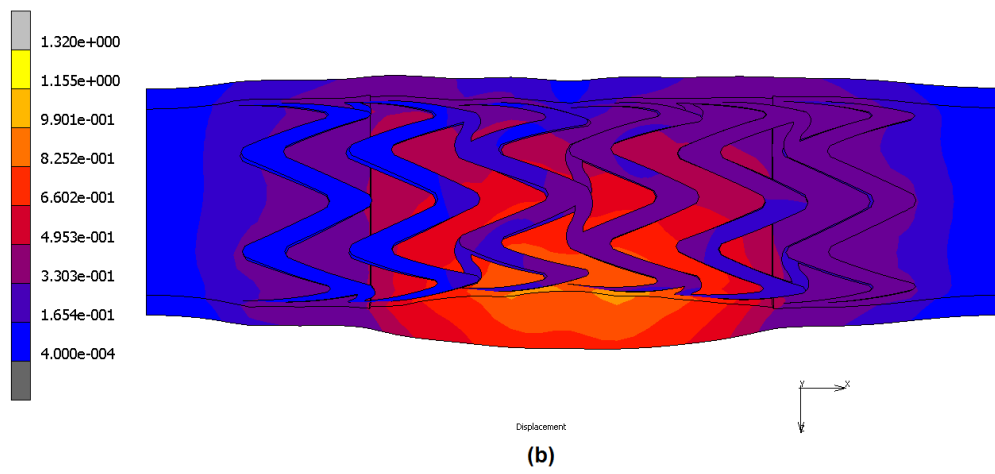
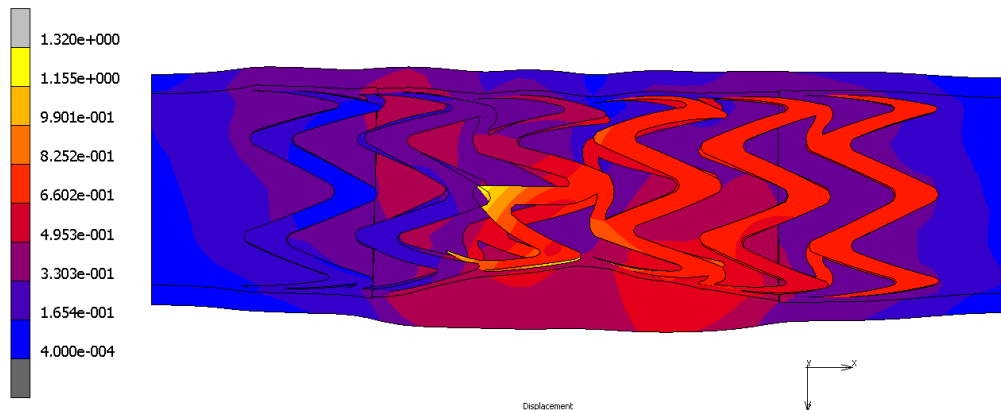


Figure 6-19: Deformation plot (mm) showing contact of generic stent with stenotic arteries having 40% calcified (a) cellular (b) and hypocellular plaques (c).

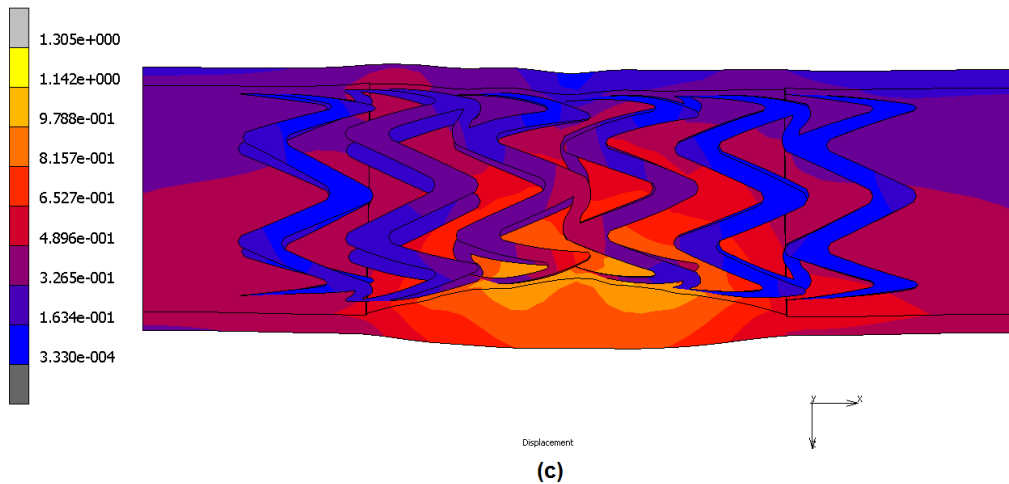
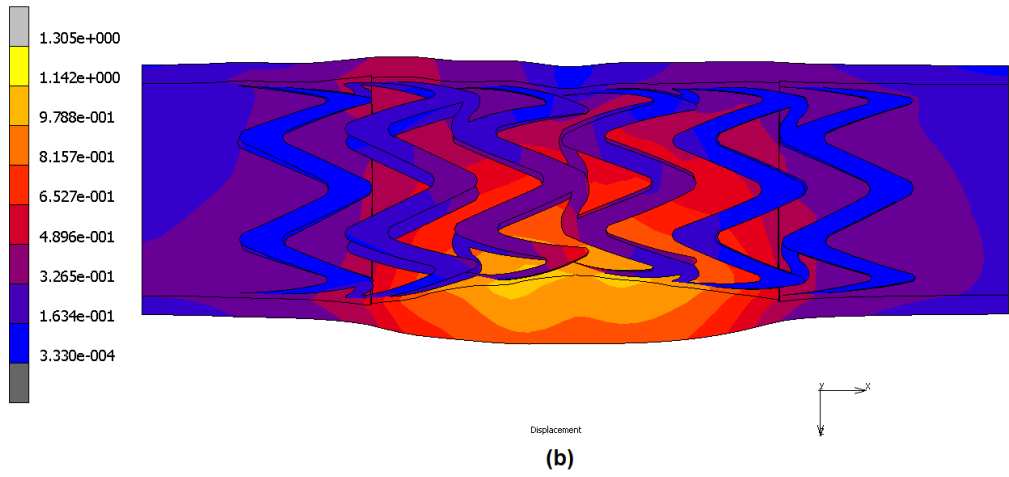
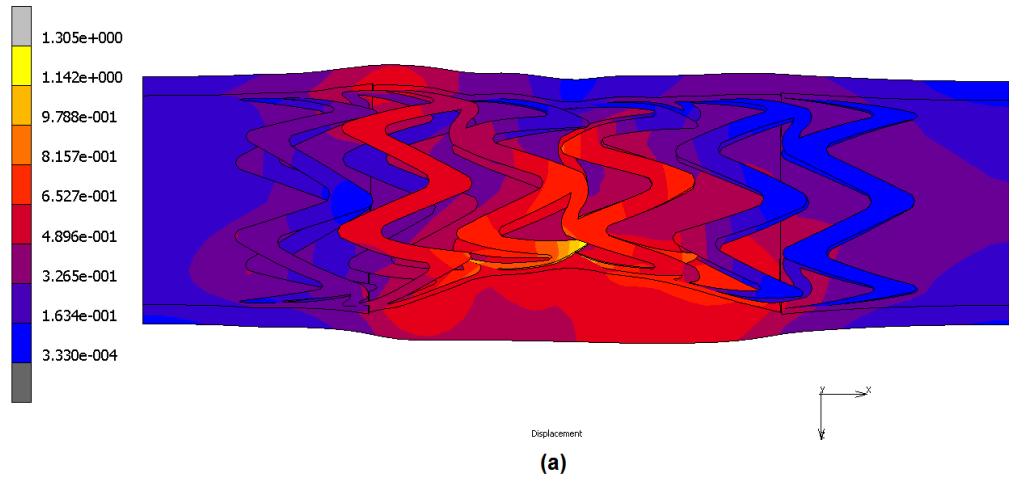


Figure 6-20: Deformation plot (mm) showing contact of generic stent with stenotic arteries having 50% calcified (a) cellular (b) and hypocellular plaques (c).

For the optimisation study carried out, the issue of structural integrity was not explored in detail as the aim of this work was to show geometry dependency and its relative performance in a given loading scenario. However, structural integrity of mechanical components is crucial in service and can be measured using maximum stresses. TO normally offers the first phase of a design optimisation process. The next phase would commonly consist of shape or size optimisation to ensure the structural integrity of the optimal designs and its manufacturability. For demonstrating the usefulness of the new designs, maximum principal and shear stress results of the generic and optimised designs of 30% stenosis in calcified, cellular and hypocellular plaques are presented in Figure 6-21 to Figure 6-24. As expected these stress contours reveal higher stresses in the central region on stents implanted in calcified plaques compared to hypocellular and cellular plaques. Furthermore, peak maximum stress value in generic stents (beyond intended plastic deformation to strain harden) was found to be 65.5 MPa compared to peak value in the optimised design of 45.0 MPa, which thus satisfies the structural integrity as the designs were not intended for expansion/plastic deformation. As the maximum principal results represent the compressive hoop stress exerted by the lesion, they are shown as a negative value. Maximum shear stress on the other hand was also higher in generic stent in all three plaque cases i.e. 32.9 MPa compared to optimised designs where they peaked at 22.5 MPa. It is also expected that modification of these optimised stent structures could further lower

the peak stresses by automated size or shape optimisation or manually adjusting a parametric CAD geometry.

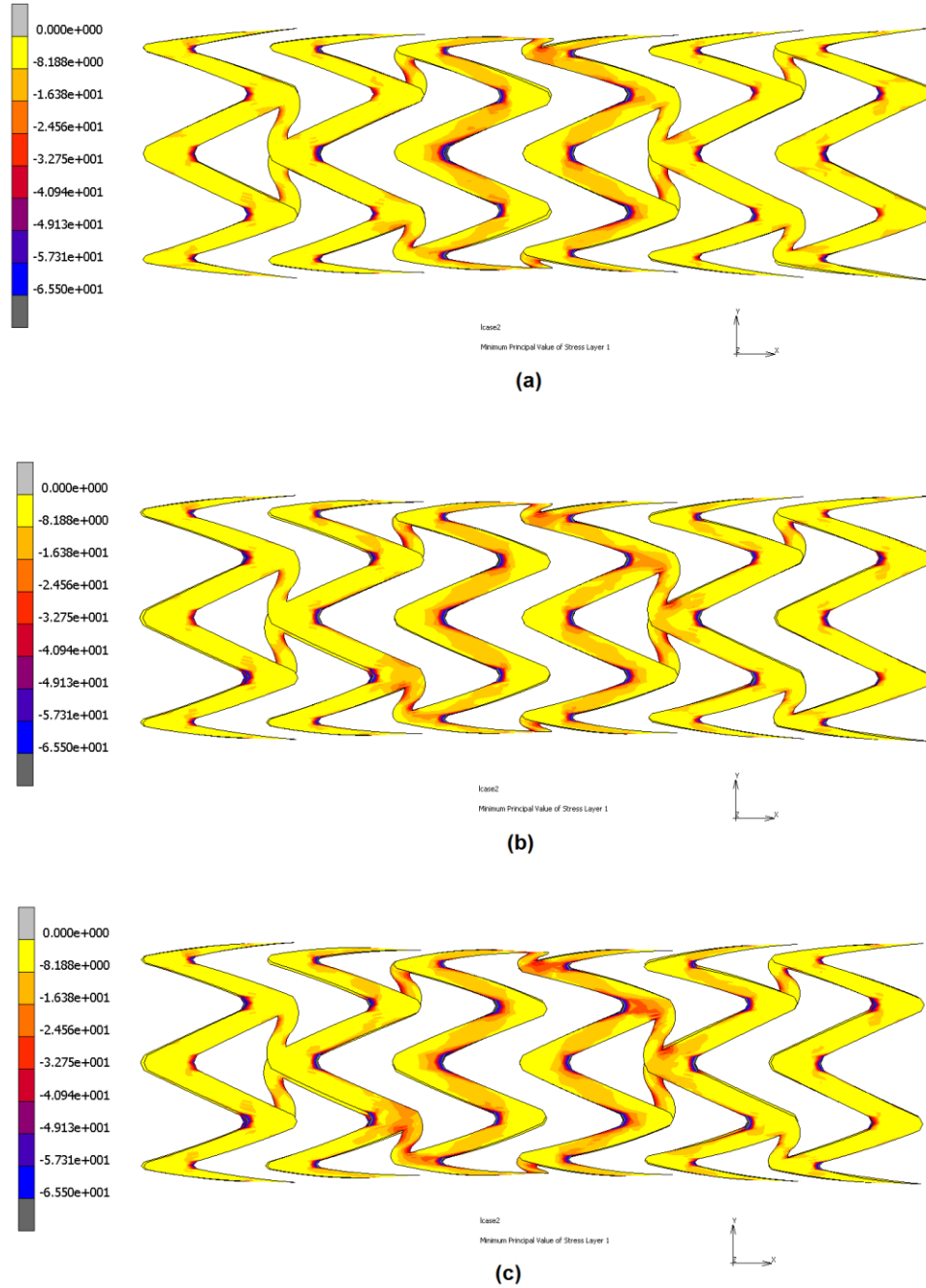


Figure 6-21: Stress plots (MPa) for calcified 30% (a-c), cellular (d-f) and hypocellular (g-i) representing compressive principal stress.

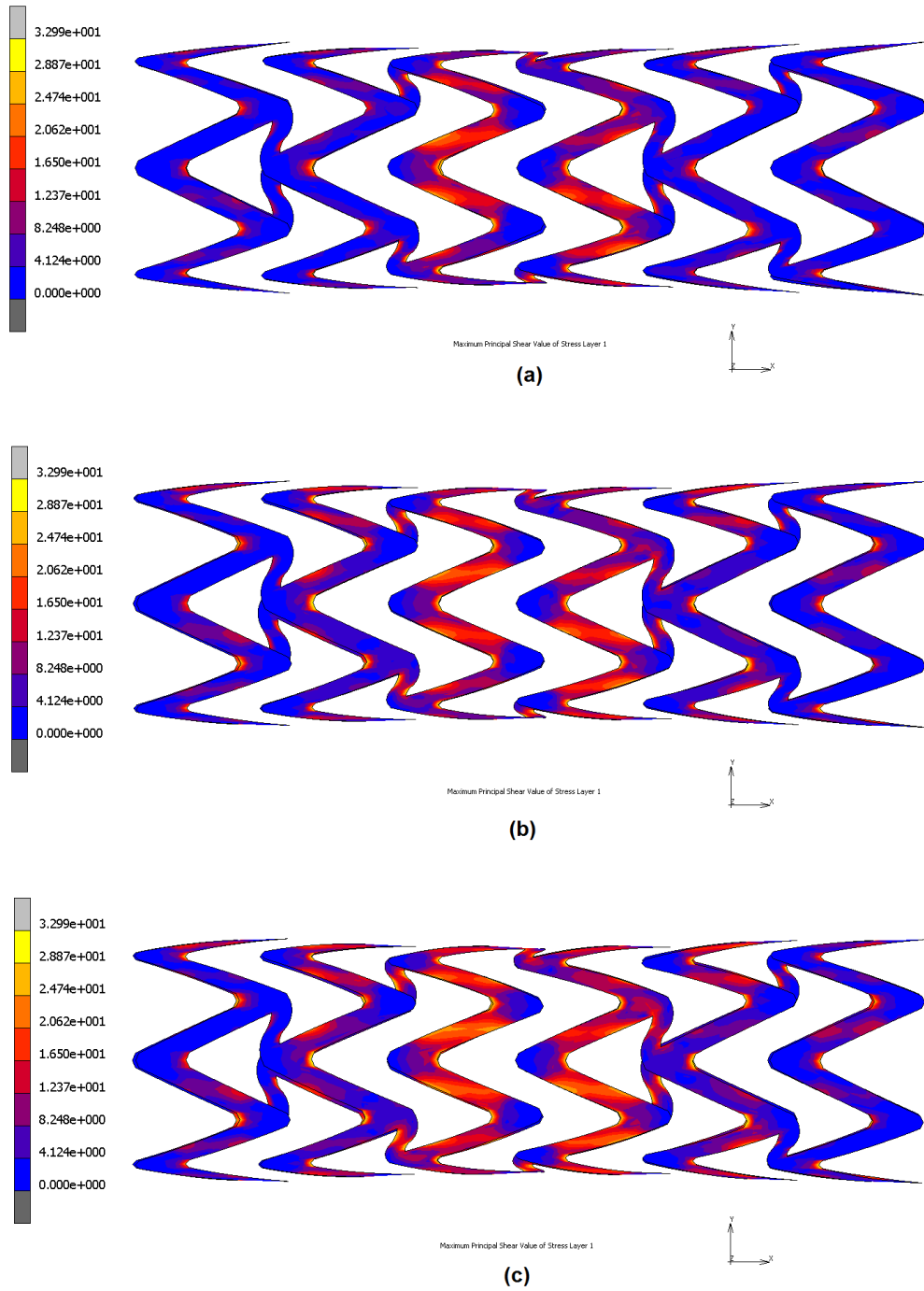


Figure 6-22: Stress plots (MPa) for calcified 30% (a), cellular (b) and hypocellular (c) representing maximum shear stress.

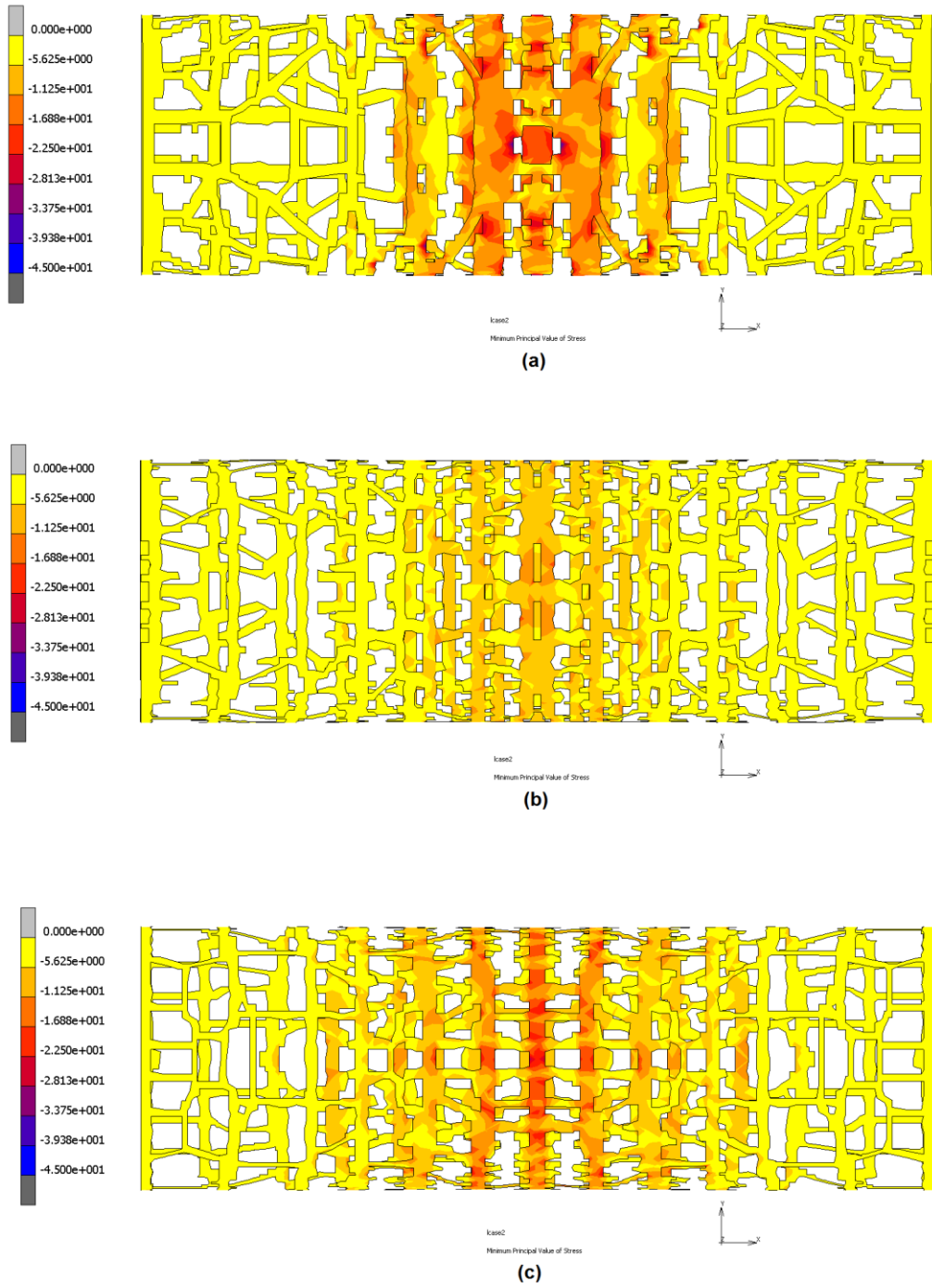


Figure 6-23: Stress plots (MPa) for optimized stents placed in arteries with calcified 30% (a), cellular (b) and hypocellular (c) plaques representing compressive principal stress.

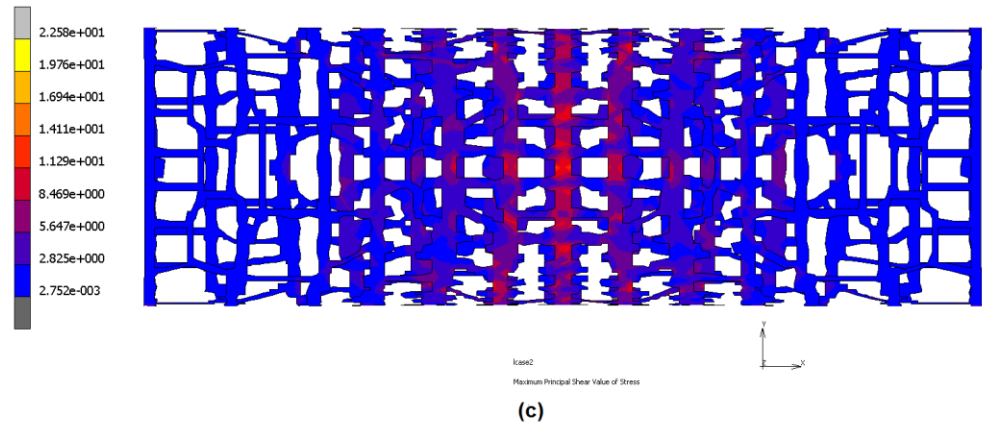
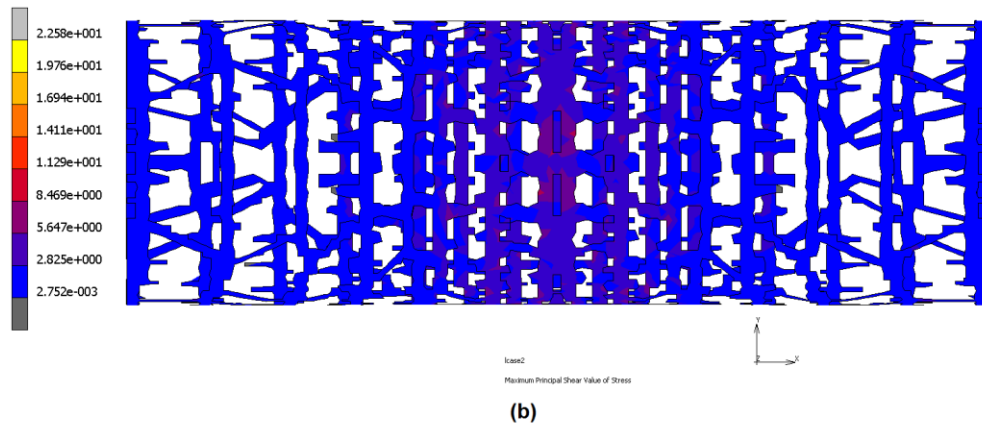
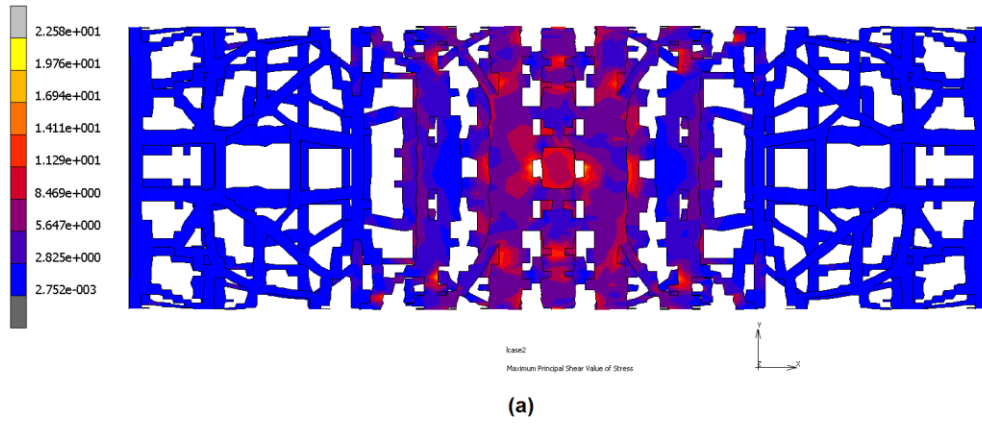


Figure 6-24: Stress plots (MPa) for optimised stents placed in arteries with calcified 30% (a), cellular (b) and hypocellular (c) plaques representing maximum principal shear stress.

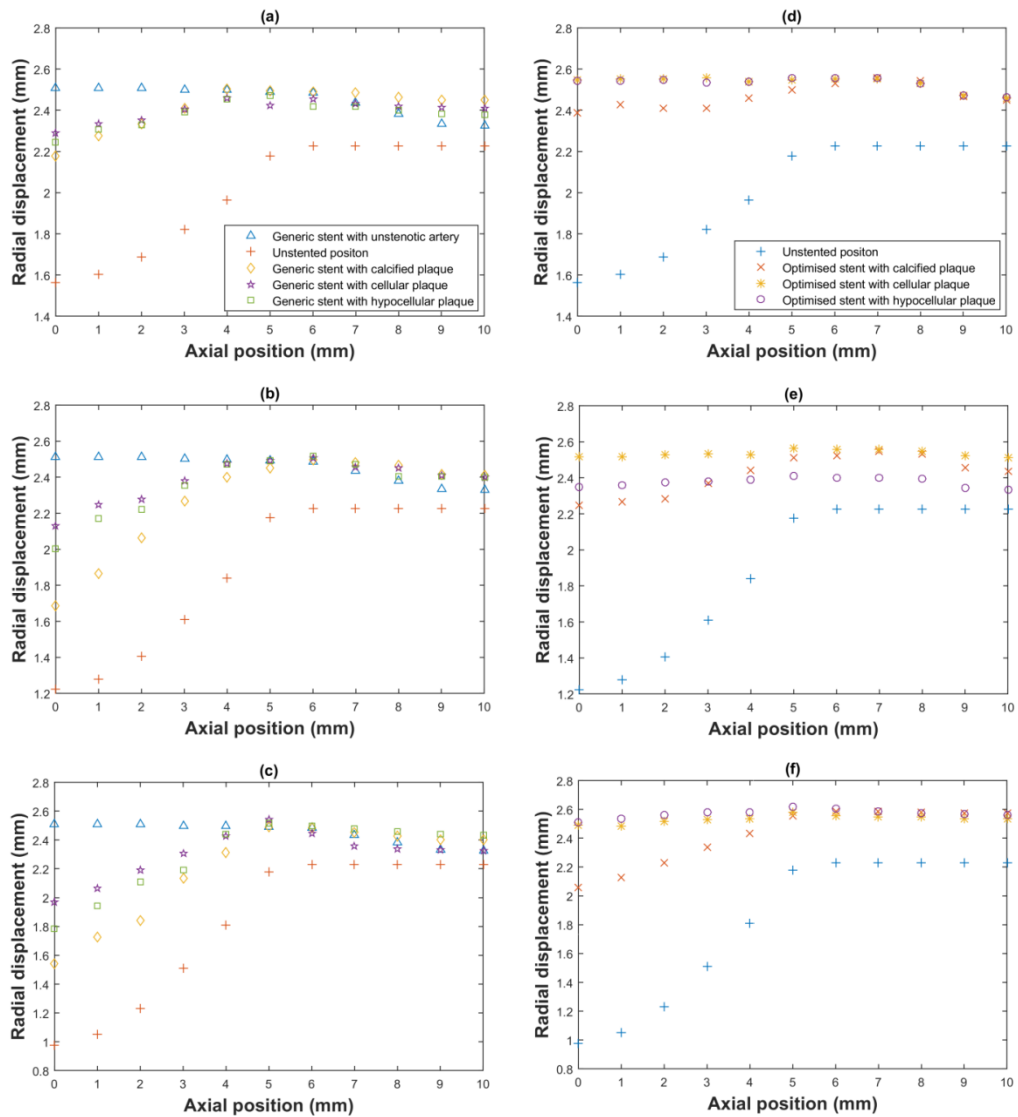


Figure 6-25: Final lumen radial deformation with a generic stent (a-c) and optimised stents (d-f) for 30, 40 and 50% stenotic arteries respectively with different plaque types based on 11 equally distant points longitudinally along thickest part of plaque, relative to central axis (one half of the stenotic artery deformations illustrated).

Analysis of the generic stent studied shows that severe calcification could lead to immediate lumen gain after the implantation of the stent as illustrated in Figure 6-20. The generic stent deployed in the calcified 30%, 40% and 50% diseased vessel, recoiled significantly more than the optimised stents in the central region leading to 10%, 29% and 35% residual stenosis respectively (Figure 6-25 & Figure 6-26). This was in agreement with a previous study [111].

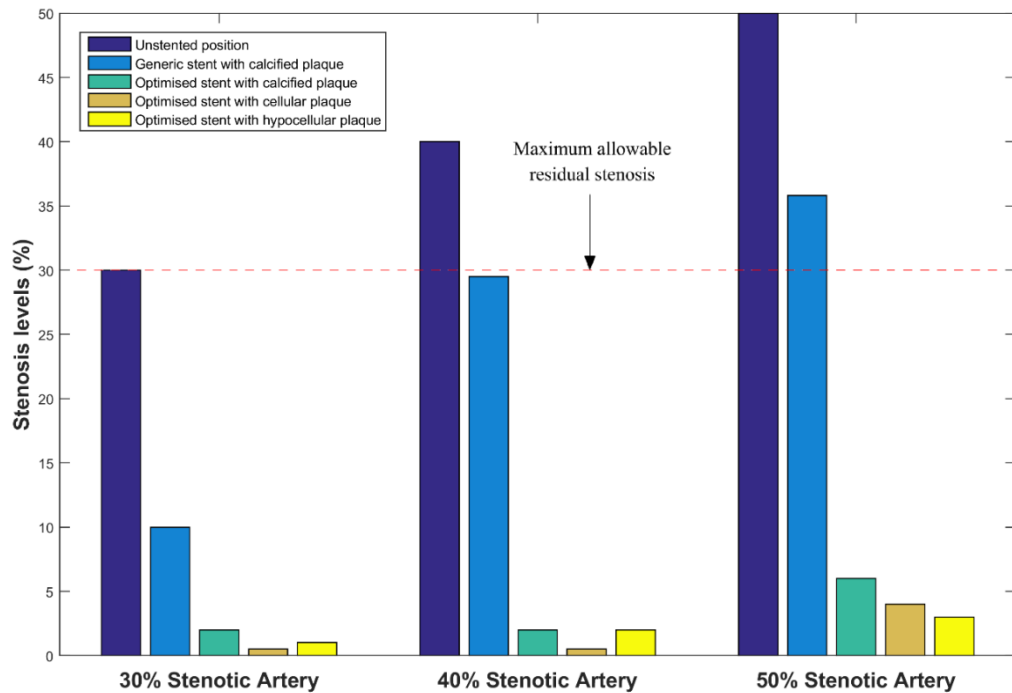


Figure 6-26: Post implantation stenosis levels in the remodelled artery due to optimised and generic stents recoil.

In other words, in spite of having similar volume of material, the stent showed less efficacy in supporting the disease and the displacement could not meet the limits of standard stenting effectiveness of 30% or lower allowable immediate post-implantation residual stenosis [112,113].

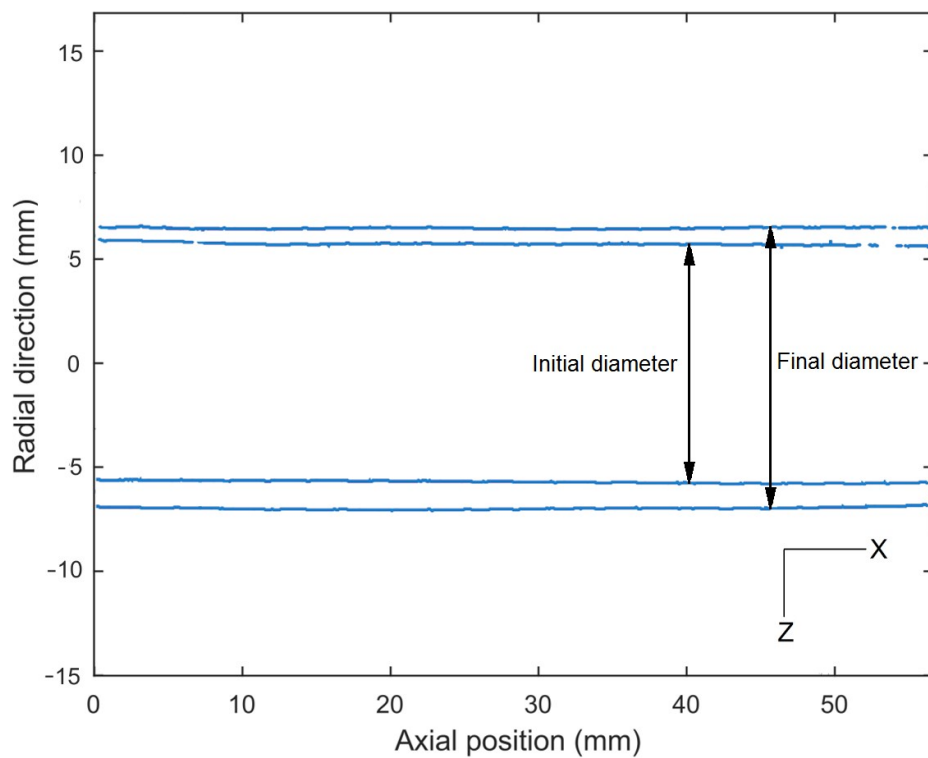
6.6 Experimental validation results

Three separate experiments were performed to extract the mock silicone artery's external diameter in XZ view with the help of a digital camera. In the first experiment, which involved only inflation and deflation of the artery with air pressure, the initial diameter was 11.8 mm at zero gauge pressure. With the application of 0.15 MPa, it increased to 13.9 mm as shown in Figure 6-27. This pressure was enough to implant a 10% bigger size stent in the mock artery, which was the second experiment (Figure

6-28). Several trials were carried out with pressure variations to get consistent results against a black background.

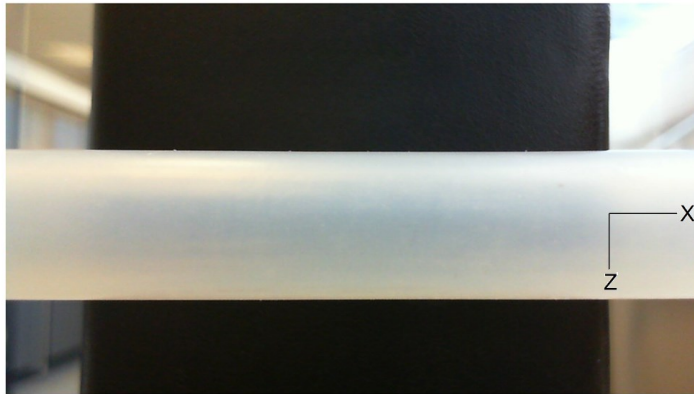


(a)

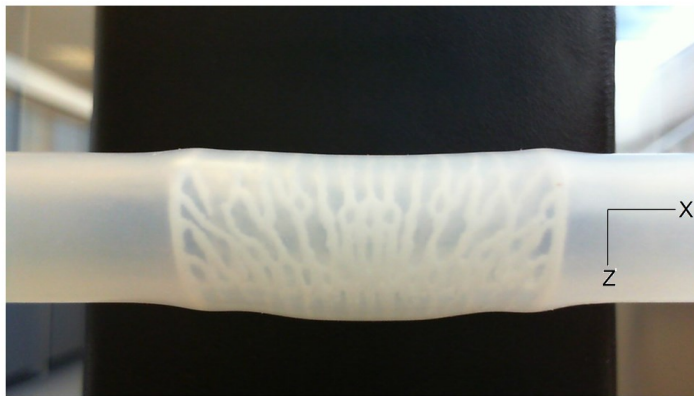


(b)

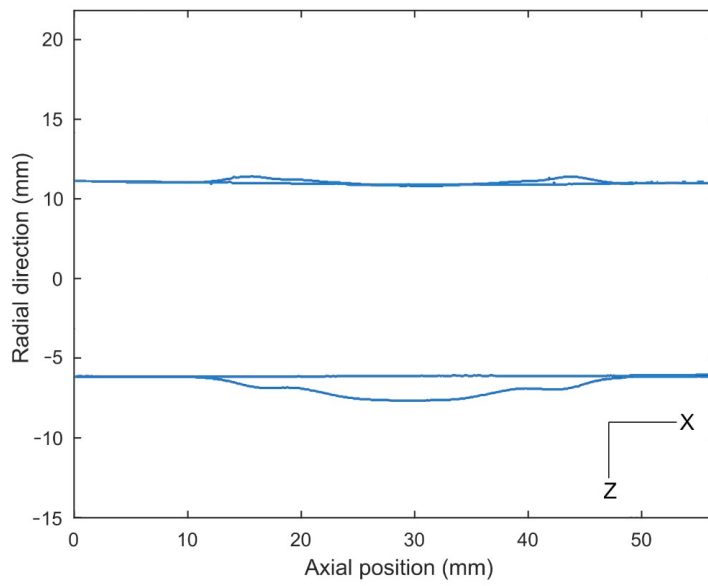
Figure 6-27: Image of mock silicone artery (XZ view) before inflation (a) and superimposed image of after inflation showing boundaries using MATLAB.



(a)



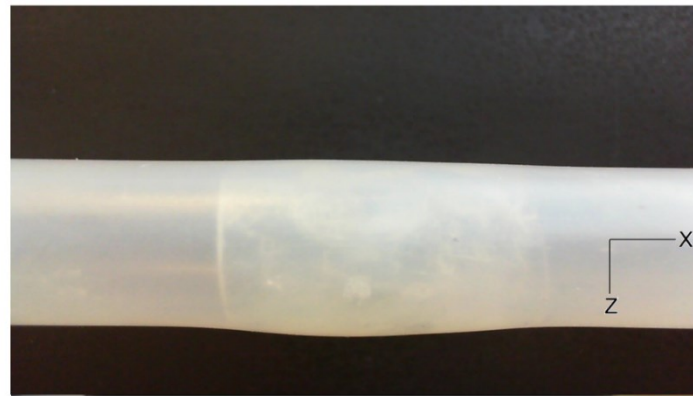
(b)



(c)

Figure 6-28: Mock silicone artery (XZ view) before (a) and after (b) stent implantation. Both images superimposed in MATLAB showing external tube boundaries (c).

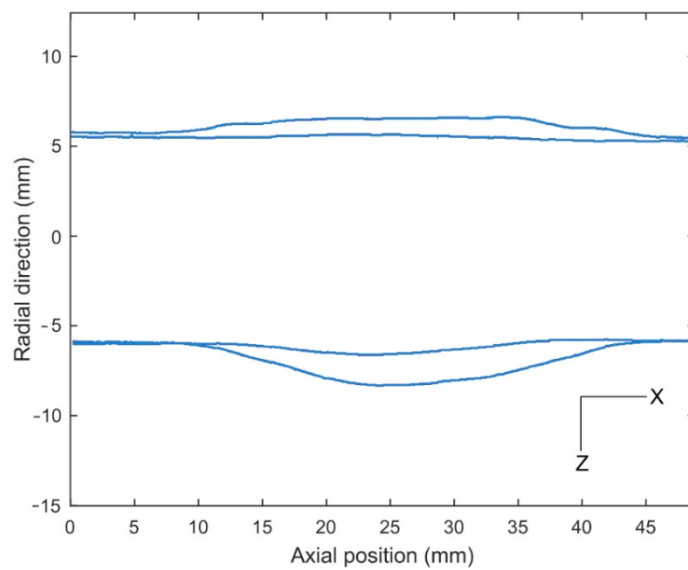
The third experiment consisted of placement of a 40% stenosis inducing plaque at the centre of the tube before implantation of the additively manufactured nylon 12 optimised stent (Figure 6-29).



(a)



(b)



(c)

Figure 6-29: Mock silicone artery (XZ view) with 40% stenosis before (a) and after (b) stent implantation. Both images superimposed in MATLAB showing external tube boundaries (c).

It is demonstrated that the optimised stent owing to its greater material distribution at the centre exhibits an ability to withstand the higher compressive forces from plaque, hence keeping the lumen wider. The images clearly show a bulge in the exterior dimensions (XZ), which is an indication of plaque being pushed by the stent. The uniaxial tensile testing of silicone dumbbell samples stress vs strain data followed Mooney-Rivlin hyperelastic material model closely in MSC Marc Mentat in the curve fitting process to the curves of uniaxial tensile, biaxial and planar shear modes, especially at low strain, as illustrated in Figure 6-30.

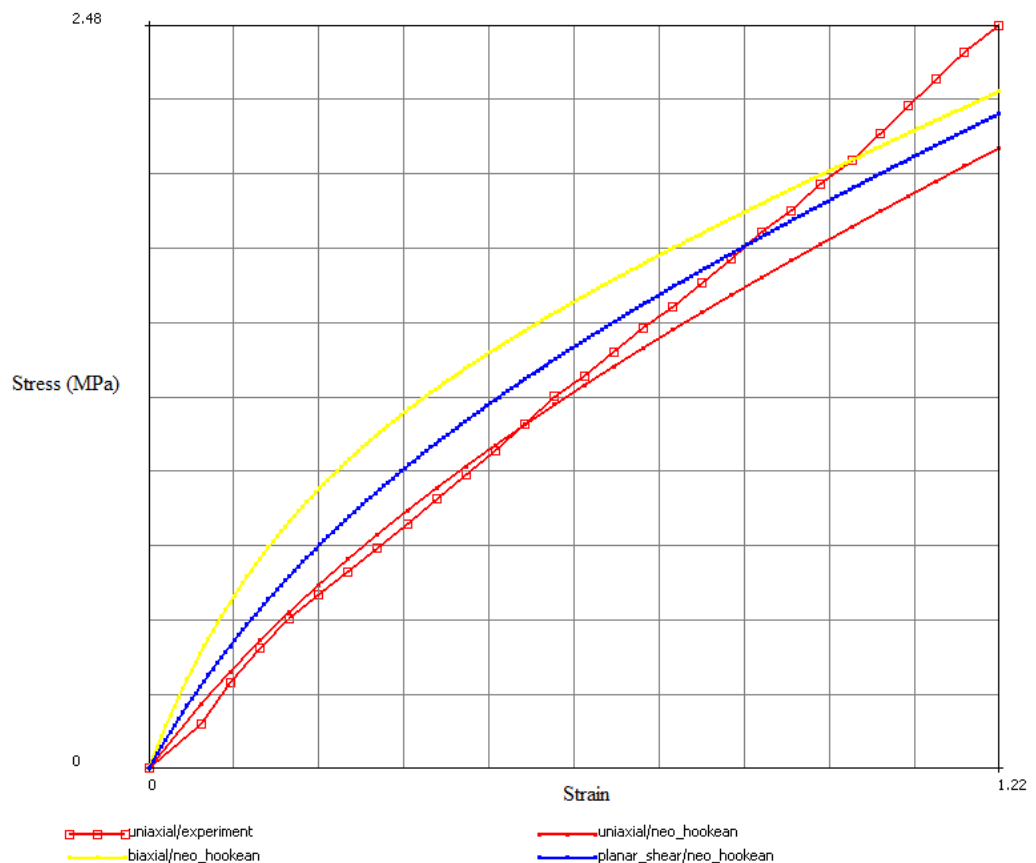


Figure 6-30: Experimental uniaxial tensile data curve fit of silicone NGP60 with Neo-Hookean model in MSC Marc Mentat.

Subsequent FEA of optimised stent implantation in mock 40% stenotic silicone artery also demonstrated a reasonable correlation with the experimental analysis. The radial position of artery exterior from XZ view,

which showed the plaques thickest part, was evaluated and compared with the arterial boundary extracted from experiment using MATLAB image analysis. The external diameter of the tube at mid length before pressure inflation was 11.8 mm, which after stent implantation increased to 13.9 mm as depicted in Figure 6-31, Figure 6-32 and Figure 6-33. The corresponding final diameter of the experimental analysis was found to be 14.9mm.

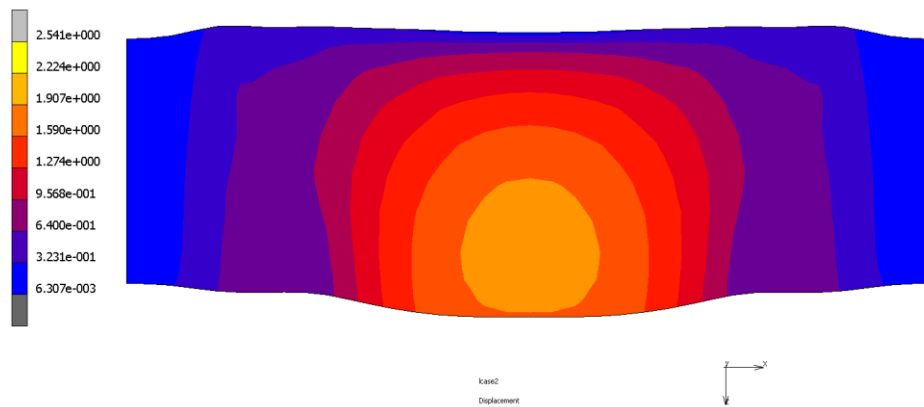


Figure 6-31: FEA model of stenotic mock silicone artery with stent: Deformation plot showing radial displacement (mm).

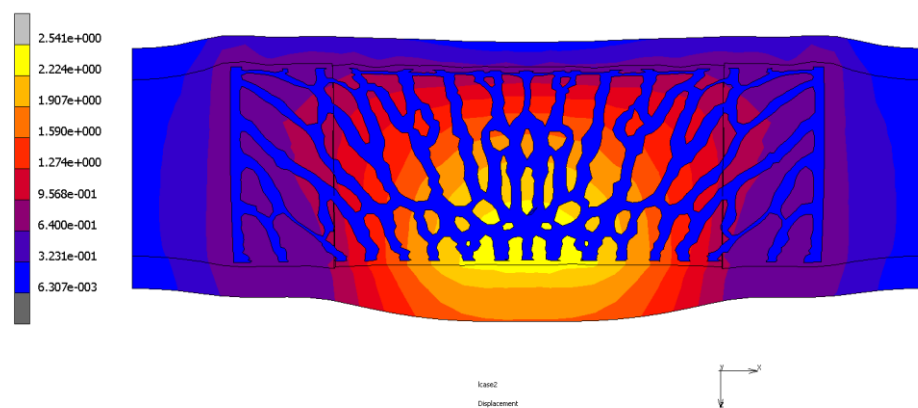


Figure 6-32: Deformation plot illustrating radial displacement (mm) in mock artery cross-section with stent implanted.

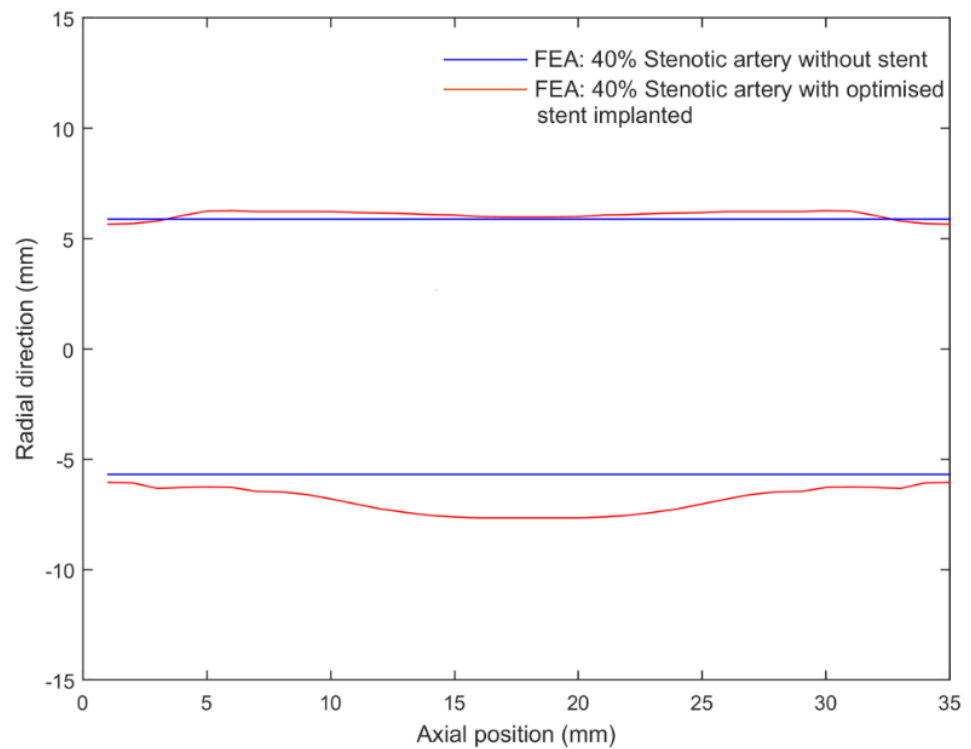


Figure 6-33: Radial displacement plot of arterial external boundary (XZ view) with 40% stenosis before and after stent implantation in FEA.

Displacements gathered from the experiment involving stenting of the 40% stenotic artery were then compared with FEA analysis results. 21 equidistant points were selected on the boundary of axially symmetrical half of the model for diameter calculation. The change in pre and post stenting diameters was calculated for both, the simulation and the experiment, and is illustrated in Figure 6-34. The root mean squared difference between them was found to be 0.626 mm which accounts for a 4% error.

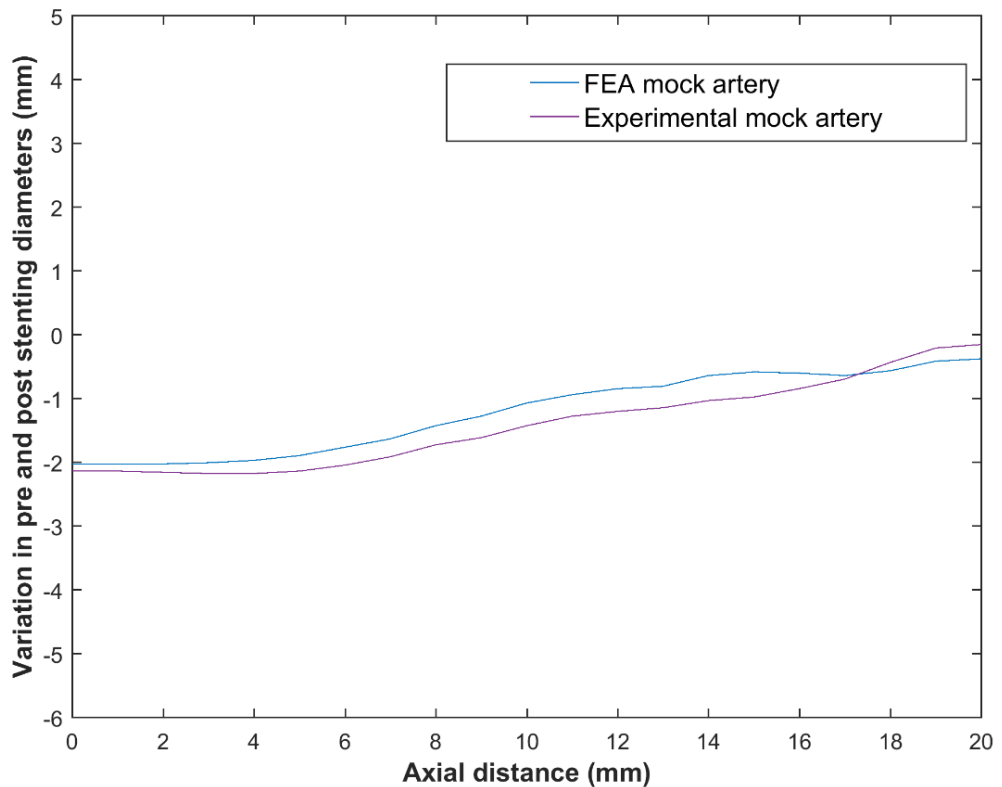


Figure 6-34: Diameter variation resulting from pre and post optimised stent placement in FEA and experimental models (plot showing axial half).

These results reveal the ability of the proposed design method, utilising contact FEA and topology optimisation, to generate optimised stents able to restore the lumen area for given plaque types to an acceptable level, i.e. resulting lower recoil than 30% residual stenosis, whilst retaining the beneficial features of the standard stent, such as lower stent volume. It could be noted that the calcified lesion (Figure 6-25 & Figure 6-26), owing to its greater stiffness, led to slightly lower stented lumen area compared to the other plaque types in all types of stenosis, as expected, however, with the optimised stent, performance post stenting is still acceptable.

The results also show that a 50% stenosis lead to an increased post stenting radius of 2.50 mm compared to 2.34 mm for a hypocellular 40 percent stenosis (Figure 6-25). This slight variation in post-implantation reduction in radius was expected and is believed to be attributed to the

change in structure resulting from post-processing of raw stent topologies. The variation was deemed acceptable as the post-implantation stenosis levels were well below 30%.

The results obtained from the topology optimisation give a concept design and demonstrate that stents could be tailored according to the accurate loading conditions in specific-plaques geometries as opposed to the current 'off-the-shelf' stenting practice. Post-processing of the stent designs obtained from the topology optimisation (Figure 6-13) is an important step as changing the geometry could lead to altered stiffness, if not performed carefully.

In terms of implantability, it is also important to note that the designs derived from topology optimisation (Figure 6-14) are anisotropic in nature and are only optimised if the stents can be placed such that the regions with higher strut densities are placed in the artery at a specific angle with respect to the lesion. Another important clinical implication of the current work, when combined with an appropriate expanding mechanism (e.g. ratchet expansion), is that the issues arising from overexpansion of stents could be eliminated which has been found to be one of the reasons for ISR [32]. Another beneficial aspect of the new geometries is that the stent design criteria of withstanding 400 million fatigue cycles required by FDA [114] will not be needed due to their bioresorbable nature as some studies suggest that the presence of stents benefits the affected site only for a number of weeks [49].

The method proposed in chapter 4 for arterial load assessment using FEA could be realised by the use of a multi-functional balloon catheter [143] that can potentially capture patient-specific lesion compressive forces. This data will also represent the level and severity of the plaque condition. These loads could then be translated to FEA for stent topology optimisation.

The experimental method described, provided information about the varying radial stiffness of the stent in a simulated mock stenotic artery which was able to maintain lumen patency. These results exhibited a reasonable agreement with the FE model. This highlights that while computational tools are helpful in developing new stent designs, experimental prototypes are necessary to physically validate those concepts in reality and formulate hypothesis for further *in vivo* study.

6.7 Summary

This chapter presented the results of cylinder-artery contact analysis and the generation of optimised stent designs for specific lesions with varying plaque size and materials. The obtained designs were then filtered before simulating them in their respective stenotic arteries and comparison against a generic stent. It was evident from the results that the new customised designs showed lower recoil in varying plaque conditions. This chapter also described the results acquired from experimental validation of the FEA approach. One of the optimised stents was additively manufactured and implanted in a mock silicone artery with 40%

stenosis. The results achieved from FEA analysis showed a close correlation with the corresponding experiment.

7. Conclusions & future work

7.1 Conclusions

A topology optimisation method has been applied to obtain optimal stent geometries for a set of specific lesion sizes and types. Nine different possible scenarios were analysed with varying plaque morphology i.e. 30%, 40%, 50% and composition i.e. calcified, cellular and hypocellular. In each of the scenario, compressive contact pressure was evaluated and then used to optimise stents in order to minimise recoil for the corresponding case.

After transforming the TO results to clear design concepts, it has been demonstrated that such designs are able to maintain lumen area to a greater degree than a generic stent. Through mechanical design the stent recoil was reduced, even under conditions of significant stenosis and strong variations in the material solid rheology.

The designs achieved look unconventional but they make engineering sense. They are also anisotropic in nature hence they will require implantation in the artery at a specific angle with respect to the lesion. That could be achieved through an approach similar to that of Hong et al. [185], for example, incorporating multiple radio-opaque markers in to the new designs possibly on proximal and distal ends. Hong et al. used this technique (*in vitro*) to avoid side branch jailing in bifurcation lesions whereas in designs generated in the current study, it could be used to

manipulate angular positioning with respect to the lesion. In regard to material for markers, gold or bioabsorbable radio-opaque materials (e.g. impregnation with iodine as used in REVA stent [170,186]) could be considered.

Balloon pre and post-dilation is commonly performed in procedures to modify an uneven plaque distribution to create a more uniform lesion to be stented [187]. Due to the customised nature of the new designs, the proposed method also has an additional potential benefit to eliminate the need for this additional procedure. Direct stenting with the optimised designs will also make the procedures faster, easier, economical and reduce the cost and procedural risks associated with the pre and post-dilation. The generic stent selected for comparison purposes represents the vast majority of stents with 'links' and 'rings' design having almost constant radial stiffness along its length. Development of the new designs illustrate that a stent could be tailored having variable radial stiffness, using topology optimisation, in contrast to generic stents.

The findings can be summarised as follows:

1. The contact analysis of the different plaque scenarios revealed that peak contact normal force on 'implanted' force-extraction cylinders in calcified lesions was the highest as expected due to higher stiffness of the plaque i.e. 1.3 and 1.6 times higher than in hypocellular and cellular plaques respectively in 30% stenosis. Similarly it was 2.2 and 2.9 times higher in 40% stenosis while in 50%, it was 3.1 and 3.2 times higher.

2. The new topology optimised stent designs were able to achieve higher lumen gain and lower residual stenosis compared to the generic stent. In artery with 30% stenosis, the residual value was reduced to 2%, 1% and 0.5% in calcified, hypocellular and cellular lesions respectively. Similarly, in the 40% scenario it was reduced to 2%, 2% and 0.5% while in the 50% case, 6%, 3% and 4% residual area stenosis levels were achieved. For the generic stent on the other hand, residual stenosis values for 30%, 40% and 50% occlusions were 10%, 29% and 35% respectively showing higher recoil.
3. Each topology optimised stent design showed higher density of material distribution and strut concentration in areas where plaque was thickest, which is a result of higher compressive stress paths generated by lesion contact and hence contributed to lower recoil in each case. This allows design adaptation of different lesion types, for instance, the resulting stents are stiffer in the central region to push the plaque and less stiff at the ends-hence exerting lower force on the healthy part of the artery.
4. The experimental validation of the computational approach with additively manufactured nylon 12 optimised stent implanted in 40% simulated stenotic silicone mock artery showed close correlation between its corresponding FEA analysis of the same scale, which demonstrates a proof of concept for the current methodology.

7.2 Limitations and Future Work

Topology optimisation results are normally mesh-dependent and therefore could be further investigated by employing different methods to refine the desired solution. One such recently developed method [152] is the use of extended finite element method (X-FEM), which is an evolutionary optimisation method and allows to obtain smooth and clearly defined structural boundaries and would potentially reduce the need to modify the TO results to obtain a manufacturable design. Another emerging computational mechanics approach known as isogeometric analysis (IGA), has been developed relatively recently and is gaining further attention. This technique, the key concept of which was outlined by Hughes et al. [188], can be considered as an alternate to standard FE analysis and offers a possibility of integrating analysis and CAD (Computer Aided Design). It utilises the predominant CAD technology NURBS (Non-Uniform Rational B-Spline), which is used to represent complex geometries, not only as geometry discretisation but also as a discretisation tool for analysis [189]. This can reduce the time it takes to design and analyse significantly leading to greater efficiency while allowing exact CAD depiction and simplified mesh-refinement. In stent design context, this technique could provide effective representation of complex lesion shapes and potentially efficient computational cost.

The current work does not consider stent crimping and expansion process in the design approach and is focused on early-stage topology optimisation to achieve geometries at a conceptual stage. A complete, but challenging solution is to use a topology optimisation method to

create a compliant mechanism [190] and simulate implantation. However, one is not always dependent on plastic deformation to fix a stent, for example, another one potential route is to incorporate a ratchet-like mechanism to the designs similar to the REVA stent and a recoil prevention device [170,186,191], which upon balloon expansion has struts that slide and lock without plastic deformation of the stent. In the future, a more complete study will involve the examination of curved and bifurcating systems, as well as the importance of advanced material models including anisotropic, plastic, failure modes [192,193] and stent fatigue. Further studies should also consider other materials such as stronger bioresorbable polymers and biocompatible super-elastic alloys such as nitinol.

This approach to design of stents will likely realise complex topologies that will be difficult to manufacture with traditional techniques. Whilst these could be manufactured using, for example, laser cutting methods common for stent production, a technology for the future is additive manufacturing. This technology could also potentially be utilised to custom design bioresorbable polymer scaffolds, as suggested, with micro mechanisms for expansion- studies in which have been carried out [194–196]. That could be achieved by determining full 3D patient specific arterial geometries and properties prior to stenting to optimise the outcome of stenting procedures. Production and modification of metallic stents has already been demonstrated and printable polymeric biomaterials for drug release and implants are becoming more widely available [197–204]. Medical applications for additive manufacturing and

3D printing are rapidly rising and could potentially revolutionise healthcare with many benefits such as customisation, cost-effectiveness and increased productivity [205]. Unlike the current stents, which mostly have repeating cellular strut structure, the new designs will likely be cost-effective in lesions with significant asymmetric plaque morphology due to their varying radial stiffness properties. In addition to that, customisation of designs have the potential to offer tailored solutions in conjunction with improved quality of life as shown in other implants for example, cranial reconstruction [206]. However it should be noted that in spite of the exciting applications there still remain notable regulatory challenges.

The workflow presented here has potential benefit not only for the personalised treatment of CVD; the scalability and freedom of design based AM offers a benefit for other intravascular applications. The combination of design, additive manufacturing and identification of patient specific arterial geometries and properties offers considerable patient benefit.

The custom stent test rig designed and developed in this work using additive manufacturing and 3D printing techniques has the potential to provide a base for further investigation of experimentally analysing and testing numerous stent designs and plaque conditions in order to customise the treatment. However, it does not provide three dimensional local strain. The set up if used in conjunction with optical surface strain measurement system, as utilised by Steinert et al. [181], could provide more information about surface variation in complex asymmetrical lesions.

References

- [1] NHS, 2012, "Cardiovascular disease," Natl. Heal. Serv. Choices [Online]. Available: <http://www.nhs.uk/conditions/cardiovascular-disease/Pages/Introduction.aspx>. [Accessed: 27-Mar-2013].
- [2] Sigwart, U., Puel, J., Mirkovitch, V., Joffre, F., and Kappenberger, L., 1987, "Intravascular stents to prevent occlusion and restenosis after transluminal angioplasty.," *N. Engl. J. Med.*, **316**(12), pp. 701–6.
- [3] Van Beusekom, H. M., and Serruys, P. W., 2010, "Drug-eluting stent endothelium: presence or dysfunction.," *JACC. Cardiovasc. Interv.*, **3**(1), pp. 76–7.
- [4] "Coronary heart disease | Introduction | Health Library | NHS Inform" [Online]. Available: <http://www.nhsinform.co.uk/health-library/articles/c/coronary-heart-disease/introduction>. [Accessed: 24-Sep-2014].
- [5] Kastrati, A., Mehilli, J., Dirschinger, J., Pache, J., Ulm, K., Schühlen, H., Seyfarth, M., Schmitt, C., Blasini, R., Neumann, F. J., and Schömig, A., 2001, "Restenosis after coronary placement of various stent types.," *Am. J. Cardiol.*, **87**(1), pp. 34–9.
- [6] Mortier, P., 2010, "Computer Modelling of Coronary Bifurcation Stenting," Ph.D. dissertation, Ghent University.
- [7] Kumar, V., Abbas, A. K., and Aster, J. C., 2015, *Robbins & Cotran Pathologic Basis of Disease*, Elsevier Saunders, Philadelphia.
- [8] Hansson, G., 2005, "Inflammation, atherosclerosis, and coronary artery disease," *Engl. J. Med.*, **352**, pp. 1685–1695.
- [9] Esper, R. A., Nordaby, J. O., Vilari, C., Paragano, J. L., and Machado, R. A., 2006, "Endothelial dysfunction: a comprehensive appraisal," *Cardiovasc Diabetol*, p. 5:4.
- [10] Chisolm, G. M., and Steinberg, D., 2000, "The oxidative modification hypothesis of atherogenesis: an overview," *Free Radic. Biol. Med.*, (28), pp. 1815–1405.
- [11] Berkely-Heart-Lab, 2015, "Atherosclerosis progression" [Online]. Available: <http://larryalmonste.com/wp-content/gallery/>.
- [12] National Institute of Health, 2011, "Stents" [Online]. Available: <https://www.nhlbi.nih.gov/health-topics/stents>. [Accessed: 10-Mar-2018].
- [13] Gruentzig, A., 1978, "Transluminal dilatation of coronary artery stenosis," **1**, p. 263.
- [14] Colombo, A., Stankovic, G., and Moses, J. W., 2002, "Selection

- of coronary stents.," J. Am. Coll. Cardiol., **40**(6), pp. 1021–33.
- [15] Kurnik, R., and Martens, K., 2003, Clinical Group - MIT students report at Biotechnology and Engineering lecture.
- [16] Hoffmann, R., Mintz, G., Dussailant, G., Popma, J., Pichard, A., Satler, L., Kent, K., Griffin, J., and Leon, M., 1996, "Patterns and mechanisms of in-stent restenosis. A serial intravascular ultrasound study," *Circulation*, (94), pp. 1247–1254.
- [17] Yoon, H.-J., and Hur, S.-H., 2012, "Optimization of Stent Deployment by Intravascular Ultrasound," *Korean J. Intern. Med.*, **27**(1), pp. 30–38.
- [18] Zahedmanesh, H., Cahill, P. A., and Lally, C., 2010, "Vascular Stent Design Optimisation Using Numerical Modelling Techniques."
- [19] Holmes, D. R., Kereiakes, D. J., Garg, S., Serruys, P. W., Dehmer, G. J., Ellis, S. G., Williams, D. O., Kimura, T., and Moliterno, D. J., 2010, "Stent thrombosis.," *J. Am. Coll. Cardiol.*, **56**(17), pp. 1357–65.
- [20] Serruys, P., De, J. P., Kiemeneij, F., Macaya, C., Rutsch, W., Heyndrickx, G., Emanuelsson, H., Marco, J., Legrand, V., Materne, P., Belard, i J., Sigwart, U., Colombo, A., Goy, J., Van, den H. P., Delcan, J., and Morel, M., 1994, "A comparison of balloon-expandable-stent implantation with balloon angioplasty in patients with coronary artery disease," *N Engl J Med.*, **331**, pp. 489–495.
- [21] Fischman, D., Leon, M., Baim, D., Schatz, R., Savage, M., Penn, I., Detre, K., Veltri, L., Ricci, D., Nobuyoshi, M., Cleman, M., Heuser, R., Almond, D., Teirstein, P., Fish, R., Colombo, A., Brinker, J., Moses, J., Shaknovich, A., Hirshfeld, J., Bailey, S., Ellis, S., Rake, R., and Goldberg, S., 1994, "A randomized comparison of coronary-stent placement and balloon angioplasty in the treatment of coronary artery disease," *N Engl J Med.*, (331), pp. 496–501.
- [22] Betriu, A., Masotti, M., Serra, A., Alonso, J., Fernandez-Aviles, F., Gimeno, F., Colman, T., Zueco, J., Delcan, J. L., Garcia, E., and Calabuig, J., 1999, "the treatment of de novo coronary artery lesions (START): a four-year follow-up," *J. Am. Coll. Cardiol*, **34**, pp. 1498–1506.
- [23] Eisenberg, M., and Konnyu, K., 2006, "Review of randomized clinical trails of drug-eluting stents for the prevention of in-stent restenosis," *Am J Cardiol*, (98), pp. 375–382.
- [24] Joner, M., Finn, A. ., Farb, A., Mont, E. ., Kolodgie, F. ., and Ladich, E., 2006, "Pathology of drug-eluting stents in humans. Delayed healing and late thrombotic risk," *J. Am. Coll. Cardiol*, **48**, pp. 193–202.
- [25] Bult, H., 2000, "Restenosis: a challenge for pharmacology," *Trends Pharmacol. Sci.*, **21**(7), pp. 274–279.

- [26] Farb, A., Sangiorgi, G., Carter, A., Walley, V., Edwards, W., Schwartz, R., and Virmani, R., 1999, "Pathology of acute and chronic coronary stenting in humans," *Circulation*, (99), pp. 44–52.
- [27] Schwartz, R., Huber, K., Murphy, W J Gand Edwards, Camrud, A., Vlietstra, R., and Holmes, D., 1992, "Restenosis and the proportional neointimal response to coronary artery injury: results in a porcine model," *J Am Coll Cardiol*, **19**, pp. 267–274.
- [28] Carter, A., Laird, J., Farb, A., Kufs, W., Wortham, D., and Virmani, R., 1994, "Morphologic characteristics of lesion formation and time course of smooth muscle cell proliferation in a porcine proliferative restenosis model," *J Am Coll Cardiol*, **24**, pp. 1398–1405.
- [29] Knig, A., Schiele, T., Rieber, J., Theisen, K., Mudra, H., and Klauss, V., 2002, "Influence of stent design and deployment technique on neointima formation and vascular remodeling," *Z Kardiol*, **91**, pp. 98–102.
- [30] Hoffmann, R., Mintz, G., Mehran, R., Kent, K., Pichard, A., Satler, L., and Leon, M., 1999, "Tissue proliferation within and surrounding palmaz-schatz stents is dependent on the aggressiveness of stent implanation technique," *Am J Cardiol*, (83), pp. 1170–1174.
- [31] Kornowski, R., Hong, M. K., Tio, F. O., Bramwell, O., Wu, H., and Leon, M. B., 1998, "In-stent restenosis: contributions of inflammatory responses and arterial injury to neointimal hyperplasia.," *J. Am. Coll. Cardiol.*, **31**(1), pp. 224–30.
- [32] Rogers, C., and Edelman, E. R., 1995, "Endovascular stent design dictates experimental restenosis and thrombosis," *Circulation*, (91), pp. 2995–3001.
- [33] Pache, J. ürge., Kastrati, A., Mehilli, J., Schühlen, H., Dotzer, F., Hausleiter, J. ör., Fleckenstein, M., Neumann, F.-J., Sattelberger, U., Schmitt, C., Müller, M., Dirschinger, J., and Schömig, A., 2003, "Intracoronary stenting and angiographic results: strut thickness effect on restenosis outcome (ISAR-STEREO-2) trial," *J. Am. Coll. Cardiol.*, **41**(8), pp. 1283–1288.
- [34] Morton, A. C., Crossman, D., and Gunn, J., 2004, "The influence of physical stent parameters upon restenosis.," *Pathol. Biol. (Paris)*, **52**(4), pp. 196–205.
- [35] Rittersma, S. Z. H., de Winter, R. J., Koch, K. T., Bax, M., Schotborgh, C. E., Mulder, K. J., Tijssen, J. G. P., Piek, J. J., and Rittersma, Z. H. S., 2004, "Impact of strut thickness on late luminal loss after coronary artery stent placement.," *Am. J. Cardiol.*, **93**(4), pp. 477–80.
- [36] Sommer, C. M., Grenacher, L., Stampfl, U., Arnegger, F. U., Rehnitz, C., Thierjung, H., Stampfl, S., Berger, I., Richter, G. M., Kauczor, H. U., and Radeleff, B. a, 2010, "Impact of stent design on in-stent stenosis in a rabbit iliac artery model.," *Cardiovasc.*

- Intervent. Radiol., **33**(3), pp. 565–75.
- [37] Ku, D., 1997, “Blood flow in arteries,” *Annu Rev Fluid Mech*, **29**, pp. 399–434.
- [38] Ku, D., Zarins, C., Giddens, D., and Glagov, S., 1985, “Pulsatile flow and atherosclerosis in the human carotid bifurcation: positive correlation between plaque localization and low and oscillating shear stress,” *Arteriosclerosis*, **5**, pp. 292–302.
- [39] Moore, J. J., Xu, C., Glagov, S., Zarins, C., and Ku, D., 1994, “Fluid wall shear stress measurements in a model of the human abdominal aorta: oscillatory behavior and relationship to atherosclerosis,” *Atherosclerosis*, **110**(2), pp. 225–40.
- [40] Wentzel, J., Krams, R., Schuurbiers, J., Oomen, J., Kloet, J., Giessen, W., Serruys, P., and Slager, C., 2001, “Relationship between neointimal thickness and shear stress after wallstent implantation in human coronary arteries,” *Circulation*, **103**, pp. 1740–1745.
- [41] Stoeckel, D., Ther, M. I., Technol, A., Bonsignore, C., and Duda, S., 2002, “A survey of stent designs.,” *Minim. invasive Ther. allied Technol.*, **11**(4), pp. 137–47.
- [42] Schatz, R. A., 1989, “A view of vascular stents.,” *Circ.* , **79**(2), pp. 445–457.
- [43] Rundback, J., Leonardo, R., and Rozenbilt, G., 2000, “Peripheral vascular stents,” *Stent-grafts current clinical practice*, B. Dolmatch, and U. Blum, eds., Thieme, New York, pp. 1–22.
- [44] Wong, S., and Schatz, R., 1993, “Clinical use of the Palmaz-Schatz intracoronary stent,” *Developmental background and design of the Palmaz-Schatz coronary stents*, H. Herrmann Jr, and J. Hirshfeld, eds., Futura Publishing Company, Inc., New York, pp. 3–19.
- [45] Karanasiou, G. S., Papafaklis, M. I., Conway, C., Michalis, L. K., Tzafriri, R., Edelman, E. R., and Fotiadis, D. I., 2017, “Stents: Biomechanics, Biomaterials, and Insights from Computational Modeling,” *Ann. Biomed. Eng.*, **45**(4), pp. 853–872.
- [46] Mani, G., Feldman, M. D., Patel, D., and Agrawal, C. M., 2007, “Coronary stents: a materials perspective.,” *Biomaterials*, **28**(9), pp. 1689–710.
- [47] Garg, S., and Serruys, P. ., 2010, “Coronary stents: current status,” *J. Am. Coll. Cardiol.*, (56), pp. S1-42.
- [48] Lim, I. A. L., 2004, “Biocompatibility of Stent Materials,” **11**, pp. 33–37.
- [49] Iqbal, J., Onuma, Y., Ormiston, J., Abizaid, A., Waksman, R., and Serruys, P., 2014, “Bioresorbable scaffolds: rationale, current status, challenges, and future,” *Eur. Heart J.*, **35**(12), pp. 765–76.
- [50] Peuster, M., Hesse, C., Schloo, T., Fink, C., Beerbaum, P., and Schnakenburg, C., 2006, “Long-term biocompatibility of a

corrodible peripheral iron stent in the porcine descending aorta," *Biomaterials*, **27**(28), pp. 4955–62.

- [51] Peuster, M., Wohlsein, P., Brugmann, M., Ehlerding, M., Seidler, K., and Fink, C., 2001, "A novel approach to temporary stenting: degradable cardiovascular stents produced from corrodible metal—results 6-18 months after implantation into new zealand white rabbits," *Heart*, **86**(5), pp. 563–9.
- [52] Mueller, P., May, T., Perz, A., Hauser, H., and Peuster, M., 2006, "Control of smooth muscle cell proliferation by ferrous iron," *Biomaterials*, **27**(10), p. 2193–200.
- [53] Stack, R., Califf, R., and Phillips, H., 1988, "Interventional cardiac catheterization at Duke Medical Center," *Am J Cardiol*, **62**, p. 3F–24F.
- [54] Cooper, S., Visser, S., Hergenrother, R., Ratner, B., Hoffman, A., Schoen, F., and Lemons, J., 2004, "Biomaterials science an introduction to materials in medicine," Elsevier Academic Press, pp. 67–69.
- [55] Kathuria, Y. P., 2005, "Laser microprocessing of metallic stent for medical therapy," *J. Mater. Process. Technol.*, **170**(3), pp. 545–550.
- [56] Allen, D. M., Esho, G., and Almond, H., 2012, "Design and novel fabrication of cylindrical magnesium stents," *Proceedings of the 1st International Conference on Design and Processes for Medical Devices*, pp. 1–6.
- [57] Russel, S. M., and Pelton, A. R., 2000, "Nitinol Melting and Fabrication," *SMST-2000: Proceedings of the International Conference on Shape Memory and Superelastic Technologies*, SMST, The International Organization on Shape Memory and Superelastic Technology, California, pp. 1–9.
- [58] Bjoern, P., Peter, E., and Felix, B., 2009, "The role of stents in the treatment of congenital heart disease: Current status and future perspectives," *Ann. Pediatr. Cardiol.*, **2**(1), pp. 3–23.
- [59] Vaithilingam, J., Goodridge, R. D., Hague, R. J., and Christie, S. D., 2012, "Additive Manufacturing and Surface Modification of Tracheobronchial Stents Using Self-assembled Monolayers," *9th World Biomaterials Conference*, Chengdu, China.
- [60] Migliavacca, F., Petrini, L., Colombo, M., Auricchio, F., and Pietrabissa, R., 2002, "Mechanical behavior of coronary stents investigated through the finite element method.," *J. Biomech.*, **35**(6), pp. 803–11.
- [61] Wang, W.-Q., Liang, D.-K., Yang, D.-Z., and Qi, M., 2006, "Analysis of the transient expansion behavior and design optimization of coronary stents by finite element method.," *J. Biomech.*, **39**(1), pp. 21–32.
- [62] Zahedmanesh, H., and Lally, C., 2009, "Determination of the influence of stent strut thickness using the finite element method:

- implications for vascular injury and in-stent restenosis.," *Med. Biol. Eng. Comput.*, **47**(4), pp. 385–93.
- [63] Timmins, L. H., Moreno, M. R., Meyer, C. A., Criscione, J. C., Rachev, A., and Moore, J. E., 2007, "Stented artery biomechanics and device design optimization.," *Med. Biol. Eng. Comput.*, **45**(5), pp. 505–13.
- [64] Pericevic, I., Lally, C., Toner, D., and Kelly, D. J., 2009, "The influence of plaque composition on underlying arterial wall stress during stent expansion: the case for lesion-specific stents.," *Med. Eng. Phys.*, **31**(4), pp. 428–33.
- [65] Timmins, L. H., Meyer, C. a, Moreno, M. R., and Moore, J. E., 2008, "Effects of stent design and atherosclerotic plaque composition on arterial wall biomechanics.," *J. Endovasc. Ther.*, **15**(6), pp. 643–54.
- [66] Holzapfel, G. A., Stadler, M., and Gasser, T. C., 2005, "Changes in the Mechanical Environment of Stenotic Arteries During Interaction With Stents: Computational Assessment of Parametric Stent Designs," *J. Biomech. Eng.*, **127**(1), pp. 166–180.
- [67] Lally, C., Dolan, F., and Prendergast, P. J., 2005, "Cardiovascular stent design and vessel stresses: a finite element analysis.," *J. Biomech.*, **38**(8), pp. 1574–81.
- [68] Bedoya, J., Meyer, C. A., Timmins, L. H., Moreno, M. R., and Moore, J. E., 2006, "Effects of stent design parameters on normal artery wall mechanics.," *ASME J. Biomech. Eng.*, **128**(5), pp. 757–65.
- [69] Rogers, C., Tseng, D. Y., Squire, J. C., and Edelman, E. R., 1999, "Balloon-Artery Interactions During Stent Placement: A Finite Element Analysis Approach to Pressure, Compliance, and Stent Design as Contributors to Vascular Injury," *Circulation*, **84**(4), pp. 378–383.
- [70] Mortier, P., De Beule, M., Carlier, S. G., Van Impe, R., Verheghe, B., and Verdonck, P., 2008, "Numerical study of the uniformity of balloon-expandable stent deployment.," *J. Biomech. Eng.*, **130**(2), p. 21018.
- [71] David Chua, S. N., MacDonald, B. J., and Hashmi, M. S. J., 2004, "Effects of varying slotted tube (stent) geometry on its expansion behaviour using finite element method," *J. Mater. Process. Technol.*, **155–156**, pp. 1764–1771.
- [72] Bhatti, A., 2000, *Practical optimization methods: with mathematica applications*, Springer.
- [73] Nocedal, J., and Wright, S., 1999, *Numerical Optimization*, Springer.
- [74] Huang, X., and Xie, Y. M., 2010, *Evolutionary topology optimization of continuum structures: methods and applications*, Wiley, Chichester.
- [75] MSC Software Corporation, 2012, "MSC Nastran 2012 Design

Sensitivity and Optimization User ' s Guide.”

- [76] Park, G., 2007, Analytic methods for design practice, Springer-Verlag, London.
- [77] Bendsoe, M., and Sigmund, O., 1999, “Material interpolation schemes in topology optimization,” *Arch Appl Mech*, (69), p. 635–54.
- [78] Negm, H. M., and Maalawi, K. Y., 2002, “Structural Design Optimization of Wind Turbine Towers,” *Comput. Struct.*, **74**, pp. 649–666.
- [79] Rispler, A. R., Tong, L., Steven, G. P., and Wisnom, M. R., 2000, “Shape Optimisation of Adhesive Fillets,” *Int. J. Adhes. Adhes.*, **20**, pp. 221–231.
- [80] Waldman, W., Heller, M., and Chen, G., 2001, “Optimal Free-form Shapes for Shoulder Fillets in Flat Plates Under Torsion and Bending,” *Int. J. Fatigue*, **23**, pp. 509–523.
- [81] Jones, R., Chaperon, P., and Heller, M., 2002, “Structural Optimisation with Fracture Strength Constraints,” *Eng. Fract. Mech.*, **69**(13), pp. 1403–1423.
- [82] Bendsøe, M. P., and Kikuchi, N., 1988, “Generating optimal topologies in structural design using a homogenization method,” *Comput. Methods Appl. Mech. Eng.*, **71**(2), pp. 197–224.
- [83] Bendsoe, M. P., and Sigmund, O., 2003, *Topology Optimization. Theory, Methods and Applications*, Springer-Verlag, Berlin Heidelberg.
- [84] Xie, Y. M., and Steven, G. P., 1997, *Evolutionary Structural Optimization*, Springer-Verlag, London.
- [85] Chu, D. N., Xie, Y. M., and Steven, G. P., 1996, “Evolutionary structural optimization for problems with stiffness constraints,” *Finite Elem. Des.*, **21**, p. 13.
- [86] Bendsoe, M. P., and Sigmund, O., 2003, *Topology Optimization. Theory, Methods and Applications*, Springer-Verlag, Berlin Heidelberg.
- [87] Lee, E., 2011, “A strain based topology optimization method,” PhD dissertation, Rutgers, The State University of New Jersey.
- [88] Wu, W., Petrini, L., Gastaldi, D., Villa, T., Vedani, M., Lesma, E., Previtali, B., and Migliavacca, F., 2010, “Finite element shape optimization for biodegradable magnesium alloy stents.,” *Ann. Biomed. Eng.*, **38**(9), pp. 2829–40.
- [89] Abad, E. M. K., Pasini, D., and Cecere, R., 2012, “Shape optimization of stress concentration-free lattice for self-expandable Nitinol stent-grafts.,” *J. Biomech.*, **45**(6), pp. 1028–35.
- [90] De Beule, M., Van Cauter, S., Mortier, P., Van Loo, D., Van Impe, R., Verdonck, P., and Verheghe, B., 2009, “Virtual optimization of self-expandable braided wire stents.,” *Med. Eng. Phys.*, **31**(4), pp. 448–53.

- [91] Li, N., Zhang, H., and Ouyang, H., 2009, "Shape optimization of coronary artery stent based on a parametric model," *Finite Elem. Anal. Des.*, **45**(6–7), pp. 468–475.
- [92] Li, N., and Gu, Y., 2005, "Parametric Design Analysis and Shape Optimization of Coronary Arteries Stent Structure *," (10421002).
- [93] Pant, S., Limbert, G., Curzen, N. P., and Bressloff, N. W., 2011, "Multiobjective design optimisation of coronary stents.," *Biomaterials*, **32**(31), pp. 7755–73.
- [94] Pant, S., Bressloff, N. W., and Limbert, G., 2010, "Geometry Parameterization and Multidisciplinary Constrained Optimisation of Coronary Stents," *Biomechanics*.
- [95] Clune, R., Kelliher, D., Robinson, J. C., and Campbell, J. S., 2014, "NURBS modeling and structural shape optimization of cardiovascular stents," *Struct. Multidiscip. Optim.*, **50**(1), pp. 159–168.
- [96] Li, H., Liu, T., Wang, M., Zhao, D., Qiao, A., Wang, X., Gu, J., Li, Z., and Zhu, B., 2017, "Design optimization of stent and its dilatation balloon using kriging surrogate model," *Biomed. Eng. Online*, **16**(1), pp. 1–17.
- [97] Puértolas, S., Navallas, D., Herrera, A., López, E., Millastre, J., Ibarz, E., Gabarre, S., Puértolas, J. A., and Gracia, L., 2017, "A methodology for the customized design of colonic stents based on a parametric model," *J. Mech. Behav. Biomed. Mater.*, **71**(May 2016), pp. 250–261.
- [98] Amirjani, A., Yousefi, M., and Cheshmaroo, M., 2014, "Parametrical optimization of stent design; A numerical-based approach," *Comput. Mater. Sci.*, **90**, pp. 210–220.
- [99] Schwartz, R. S., Chronos, N. A., and Virmani, R., 2004, "Preclinical restenosis models and drug-eluting stents: still important, still much to learn.," *J. Am. Coll. Cardiol.*, **44**(7), pp. 1373–1385.
- [100] MedMovie.com, "Atherosclerosis" [Online]. Available: https://medmovie.com/library_id/3255/topic/ahaw_0070a/.
- [101] Yin, D., Matsumura, M., Rundback, J., Yoho, J. A., Witzenbichler, B., Stone, G. W., Mintz, G. S., and Maehara, A., 2017, "Comparison of plaque morphology between peripheral and coronary artery disease (from the CLARITY and ADAPT-DES IVUS substudies).," *Coron. Artery Dis.*, **28**(5), pp. 369–375.
- [102] Gu, L., Zhao, S., Muttyam, A. K., and Hammel, J. M., 2010, "The Relation Between the Arterial Stress and Restenosis Rate After Coronary Stenting," *J. Med. Device.*, **4**(3), p. 31005.
- [103] García, A., Peña, E., and Martínez, M. A., 2012, "Influence of geometrical parameters on radial force during self-expanding stent deployment. Application for a variable radial stiffness stent.," *J. Mech. Behav. Biomed. Mater.*, **10**, pp. 166–75.
- [104] Lansky, A. J., Ng, V. G., Maehara, A., Weisz, G., Lerman, A.,

- Mintz, G. S., De Bruyne, B., Farhat, N., Niess, G., Jankovic, I., Lazar, D., Xu, K., Fahy, M., Serruys, P. W., and Stone, G. W., 2012, "Gender and the extent of coronary atherosclerosis, plaque composition, and clinical outcomes in acute coronary syndromes," *JACC Cardiovasc. Imaging*, **5**(3 SUPPL.), pp. 62–72.
- [105] Sheifer, S. E., Canos, M. R., Weinfurt, K. P., Arora, U. K., Mendelsohn, F. O., Gersh, B. J., and Weissman, N. J., 2000, "Sex differences in coronary artery size assessed by intravascular ultrasound," *Am. Heart J.*, **139**(4), pp. 649–652.
- [106] Hiteshi, A. K., Li, D., Gao, Y., Chen, A., Flores, F., Mao, S. S., and Budoff, M. J., 2014, "Gender differences in coronary artery diameter are not related to body habitus or left ventricular mass," *Clin. Cardiol.*, **37**(10), pp. 605–609.
- [107] Trejo, M. C., Medina, H., and Rojas, C. A., 2018, "Utilidad del puntaje de calcio coronario en mujeres," *Rev. Colomb. Cardiol.*, **25**, pp. 73–83.
- [108] Timmins, L. H., Meyer, C. A., Moreno, M. R., and Jr, J. E. M., 2009, "NIH Public Access," *Biomed. Eng. (NY)*, **36**(12), pp. 2042–2050.
- [109] Wu, W., Yang, D.-Z., Huang, Y.-Y., Qi, M., and Wang, W.-Q., 2008, "Topology optimization of a novel stent platform with drug reservoirs.," *Med. Eng. Phys.*, **30**(9), pp. 1177–85.
- [110] Guimarães, T. a., Oliveira, S. a. G., and Duarte, M. a., 2008, "Application of the topological optimization technique to the stents cells design for angioplasty," *J. Brazilian Soc. Mech. Sci. Eng.*, **30**(3), pp. 261–268.
- [111] Zhao, S., Gu, L., and Froemming, S. R., 2012, "Finite Element Analysis of the Implantation of a Self-Expanding Stent: Impact of Lesion Calcification," *ASME J. Med. Devices*, **6**(2), p. 21001.
- [112] Elezi, S., Kastrati, a., Neumann, F.-J., Hadamitzky, M., Dirschinger, J., and Schomig, a., 1998, "Vessel Size and Long-Term Outcome After Coronary Stent Placement," *Circulation*, **98**(18), pp. 1875–1880.
- [113] Krankenberg, H., Schlüter, M., Steinkamp, H. J., Bürgelin, K., Scheinert, D., Schulte, K.-L., Minar, E., Peeters, P., Bosiers, M., Tepe, G., Reimers, B., Mahler, F., Tübler, T., and Zeller, T., 2007, "Nitinol stent implantation versus percutaneous transluminal angioplasty in superficial femoral artery lesions up to 10 cm in length: the femoral artery stenting trial (FAST).," *Circulation*, **116**(3), pp. 285–92.
- [114] Food and Drug Administration, 2010, *Guidance for Industry and FDA Staff Non-Clinical Engineering Tests and Recommended Labeling for Intravascular Stents and Associated Delivery Systems*, US Department of Health and Human Services. Food and Drug Administration, Center for Devices and Radiological Health.

- [115] Nair, R. N., and Quadros, K., 2011, "Coronary Stent Fracture: A Review of the Literature," *Card. Cath Lab Dir.*, **1**(1), pp. 32–38.
- [116] Santos, H. A. F. A., Auricchio, F., and Conti, M., 2013, "Numerical fatigue life assessment of cardiovascular stents: A two-scale plasticity-damage model," *J. Phys. Conf. Ser.*, **451**(1).
- [117] Ang, H. Y., Bulluck, H., Wong, P., Venkatraman, S. S., Huang, Y., and Foin, N., 2017, "Bioresorbable stents: Current and upcoming bioresorbable technologies," *Int. J. Cardiol.*, **228**, pp. 931–939.
- [118] Tiwari, M., and Harding, J. A., 2011, *Evolutionary Computing in Advanced Manufacturing*, John Wiley and Son, New Jersey.
- [119] Boothroyd, G., Dewhurst, P., and Knight, W. A., 2011, *Product Design for Manufacture and Assembly*, CRC Press, New York.
- [120] Chu, C., Graf, G., and Rosen, D. W., 2008, "Design for additive manufacture of cellular structure," *Comput. Aided Des. Appl.*, p. 11.
- [121] Khan, M. F., Brackett, D. J., Ashcroft, I. A., Tuck, C. J., and Wildman, R. D., 2016, "A Novel Approach to Design Lesion-Specific Stents for Minimum Recoil," *J. Med. Device*.
- [122] Deckard, C., 1988, "Selective Laser Sintering. PhD dissertation," University of Texas at Austin.
- [123] Holzapfel, G. a., Stadler, M., and Schulze-Bauer, C. a. J., 2002, "A Layer-Specific Three-Dimensional Model for the Simulation of Balloon Angioplasty using Magnetic Resonance Imaging and Mechanical Testing," *Ann. Biomed. Eng.*, **30**(6), pp. 753–767.
- [124] Gervaso, F., Capelli, C., Petrini, L., Lattanzio, S., Di Virgilio, L., and Migliavacca, F., 2008, "On the effects of different strategies in modelling balloon-expandable stenting by means of finite element method.," *J. Biomech.*, **41**(6), pp. 1206–12.
- [125] Migliavacca, F., Petrini, L., Montanari, V., Quagliana, I., Auricchio, F., and Dubini, G., 2005, "A predictive study of the mechanical behaviour of coronary stents by computer modelling.," *Med. Eng. Phys.*, **27**(1), pp. 13–8.
- [126] McClean, D. R., Eiger, N. L., and Eigler, N. L., 2001, "Stent Design : Implications for Restenosis," *Rev. Cardiovasc. Med.*, **3**, pp. S16-22.
- [127] Hara, H., Nakamura, M., Palmaz, J. C., and Schwartz, R. S., 2006, "Role of stent design and coatings on restenosis and thrombosis.," *Adv. Drug Deliv. Rev.*, **58**(3), pp. 377–86.
- [128] Poncin, P., and Proft, J., 2003, "Stent Tubing : Understanding the Desired Attributes," *Medical Device Materials: Proceedings of the Materials & Processes for Medical Devices Conference*. Materials Park, OH: ASM International, pp. 253–259.
- [129] Etave, F., Finet, G., Boivin, M., Boyer, J. C., Rioufol, G., and Thollet, G., 2001, "Mechanical properties of coronary stents

determined by using finite element analysis.," J. Biomech., **34**(8), pp. 1065–75.

- [130] Petrini, L., Migliavacca, F., Auricchio, F., and Dubini, G., 2004, "Numerical investigation of the intravascular coronary stent flexibility.," J. Biomech., **37**(4), pp. 495–501.
- [131] Lee, R. T., Grodzinsky, A. J., Frank, E. H., Kamm, R. D., and Schoen, F. J., 1991, "Structure-dependent dynamic mechanical behavior of fibrous caps from human atherosclerotic plaques.," *Circulation*, **83**(5), pp. 1764–1770.
- [132] Pant, S., Limbert, G., Curzen, N. P., and Bressloff, N. W., 2011, "Multiobjective design optimisation of coronary stents.," *Biomaterials*, **32**(31), pp. 7755–73.
- [133] James, K. a., and Waisman, H., 2016, "Layout design of a bi-stable cardiovascular stent using topology optimization," *Comput. Methods Appl. Mech. Eng.*, **305**, pp. 869–890.
- [134] Gijssen, F. J. H., Migliavacca, F., Schievano, S., Socci, L., Petrini, L., Thury, A., Wentzel, J. J., van der Steen, A. F. W., Serruys, P. W. S., and Dubini, G., 2008, "Simulation of stent deployment in a realistic human coronary artery.," *Biomed. Eng. Online*, **7**(23).
- [135] Zahedmanesh, H., John Kelly, D., and Lally, C., 2010, "Simulation of a balloon expandable stent in a realistic coronary artery-Determination of the optimum modelling strategy.," *J. Biomech.*, **43**(11), pp. 2126–32.
- [136] De Bock, S., Iannaccone, F., De Santis, G., De Beule, M., Mortier, P., Verheghe, B., and Segers, P., 2012, "Our capricious vessels: The influence of stent design and vessel geometry on the mechanics of intracranial aneurysm stent deployment.," *J. Biomech.*, **45**(8), pp. 1353–9.
- [137] Nissen, S. E., and Yock, P., 2001, "Intravascular Ultrasound: Novel Pathophysiological Insights and Current Clinical Applications," *Circulation*, **103**(4), pp. 604–616.
- [138] Budoff, M. J., Achenbach, S., Blumenthal, R. S., Carr, J. J., Goldin, J. G., Greenland, P., Guerci, A. D., Lima, J. A. C., Rader, D. J., Rubin, G. D., Shaw, L. J., and Wiegers, S. E., 2006, "Assessment of coronary artery disease by cardiac computed tomography: a scientific statement from the American Heart Association Committee on Cardiovascular Imaging and Intervention, Council on Cardiovascular Radiology and Intervention, and Committee on C," *Circulation*, **114**(16), pp. 1761–91.
- [139] Dweck, M. R., Puntmann, V. O., Vesey, A. T., Fayad, Z. A., and Nagel, E., 2016, "MR Imaging of Coronary Arteries and Plaques," *JACC Cardiovasc. Imaging*, **9**(3), pp. 306–316.
- [140] Makowski, M. R., Henningsson, M., Spuentrup, E., Kim, W. Y., Maintz, D., Manning, W. J., and Botnar, R. M., 2013, "Characterization of Coronary Atherosclerosis by Magnetic

- Resonance Imaging,” *Circulation*, **128**(11), pp. 1244–1255.
- [141] Pulido, M. A., Angiolillo, D. J., and Costa, M. A., 2004, “Imaging of atherosclerotic plaque,” *Int. J. Cardiovasc. Imaging*, **20**(6), pp. 553–559.
- [142] Kim, D. H., Lu, N., Ghaffari, R., Kim, Y. S., Lee, S. P., Xu, L., Wu, J., Kim, R.-H., Song, J., Liu, Z., Viventi, J., de Graff, B., Elolampi, B., Mansour, M., Slepian, M. J., Hwang, S., Moss, J. D., Won, S.-M., Huang, Y., Litt, B., and Rogers, J. A., 2011, “Materials for multifunctional balloon catheters with capabilities in cardiac electrophysiological mapping and ablation therapy,” *Nat Mater*, **10**(4), pp. 316–323.
- [143] Slepian, M. J., Ghaffari, R., and Rogers, J. A., 2011, “Multifunctional balloon catheters of the future,” *Interv. Cardiol.*, **3**(4), pp. 417–419.
- [144] Moore, J. E., Soares, J. S., and Rajagopal, K. R., 2010, “Biodegradable Stents: Biomechanical Modeling Challenges and Opportunities,” *Cardiovasc. Eng. Technol.*, **1**(1), pp. 52–65.
- [145] Bendsøe, M. P., 1989, “Optimal shape design as a material distribution problem,” *Struct. Optim.*, **1**(4), pp. 193–202.
- [146] Zhou, M., and Rozvany, G. I. N., 1991, “The COC algorithm, Part II: Topological, geometrical and generalized shape optimization,” *Comput. Methods Appl. Mech. Eng.*, **89**(1–3), pp. 309–336.
- [147] Wang, M. Y., Wang, X., and Guo, D., 2003, “A level set method for structural topology optimization,” *Comput. Methods Appl. Mech. Eng.*, **192**(1–2), pp. 227–246.
- [148] Allaire, G., Jouve, F., and Toader, A.-M., 2004, “Structural optimization using sensitivity analysis and a level-set method,” *J. Comput. Phys.*, **194**(1), pp. 363–393.
- [149] Xie, Y. M., and Steven, G. P., 1993, “A simple evolutionary procedure for structural optimization,” *Comput. Struct.*, **49**(5), pp. 885–896.
- [150] Querin, O. M., Steven, G. P., and Xie, Y. M., 1998, “Evolutionary structural optimisation (ESO) using a bidirectional algorithm,” *Eng. Comput.*, **15**(8), pp. 1031–1048.
- [151] Yang, X. Y., Xie, Y. M., Steven, G. P., and Querin, O. M., 1999, “Bidirectional Evolutionary Method for Stiffness Optimization,” *AIAA J.*, **37**(11), pp. 1483–1488.
- [152] Abdi, M., Wildman, R., and Ashcroft, I., 2013, “Evolutionary topology optimization using the extended finite element method and isolines,” *Eng. Optim.*, **46**(5), pp. 628–647.
- [153] Migliavacca, F., Petrini, L., Montanari, V., Quagliana, I., Auricchio, F., and Dubini, G., 2005, “A predictive study of the mechanical behaviour of coronary stents by computer modelling,” *Med. Eng. Phys.*, (27), pp. 13–18.
- [154] Liu, Q., 2014, “Concept Design of Cardiovascular Stents Based

- on Load Identification,” J. Inst. Eng. Ser. C, **96**(2), pp. 99–105.
- [155] Avdeev, I., and Shams, M., 2010, “Vascular stents: Coupling full 3-D with reduced-order structural models,” IOP Conf. Ser. Mater. Sci. Eng., **10**, p. 12133.
- [156] Hellen, T., 2007, How to use beam, plate and shell elements, NAFEMS (National Agency for Finite Element Methods and Standards) Limited.
- [157] Mollet, N. R., Cademartiri, F., van Mieghem, C. A. G., Runza, G., McFadden, E. P., Baks, T., Serruys, P. W., Krestin, G. P., and de Feyter, P. J., 2005, “High-Resolution Spiral Computed Tomography Coronary Angiography in Patients Referred for Diagnostic Conventional Coronary Angiography,” *Circulation*, **112**(15), p. 2318 LP-2323.
- [158] Waller, B. F., 1989, “The eccentric coronary atherosclerotic plaque: Morphologic observations and clinical relevance,” *Clin. Cardiol.*, **12**(1), pp. 14–20.
- [159] Van Ditzhuijzen, N. S., Kurata, M., Van Den Heuvel, M., Sorop, O., Van Duin, R. W. B., Krabbendam-Peters, I., Ligthart, J., Witberg, K., Murawska, M., Bouma, B., Villiger, M., Garcia-Garcia, H. M., Serruys, P. W., Zijlstra, F., Van Soest, G., Duncker, D. J., Regar, E., and Van Beusekom, H. M. M., 2017, “Neoatherosclerosis development following bioresorbable vascular scaffold implantation in diabetic and non-diabetic swine,” *PLoS One*.
- [160] Higashida, R. T., Meyers, P. M., Phatouros, C. C., Connors, J. J., Barr, J. D., and Sacks, D., 2004, “Reporting Standards for Carotid Artery Angioplasty and Stent Placement,” *Stroke*, **35**(5), p. e112 LP-e134.
- [161] Van Andel, C. J., Pistecky, P. V, and Borst, C., 2003, “Mechanical properties of porcine and human arteries: implications for coronary anastomotic connectors,” *Ann. Thorac. Surg.*, **76**(1), pp. 58-64-65.
- [162] Jamshidian, M., Tehrany, E. A., Imran, M., Jacquot, M., and Desobry, S., 2010, “Poly-Lactic Acid: Production, Applications, Nanocomposites, and Release Studies,” *Compr. Rev. Food Sci. Food Saf.*, **9**(5), pp. 552–571.
- [163] Vroman, I., and Tighzert, L., 2009, “Biodegradable polymers,” *Materials (Basel)*, **2**(2), pp. 307–344.
- [164] Nishida, M., Yamaguchi, M., Todo, M., Takayama, T., Häggblad, H. Å., and Jonsén, P., 2009, “Evaluation of dynamic compressive properties of PLA polymer blends using split Hopkinson pressure bar,” *DYMAT 2009 - 9th International Conferences on the Mechanical and Physical Behaviour of Materials under Dynamic Loading*, Brussels, Belgium, pp. 909–915.
- [165] Loree, H. M., Grodzinsky, A. J., Park, S. Y., Gibson, L. J., and Lee, R. T., 1994, “Static circumferential tangential modulus of

- human atherosclerotic tissue,” *J. Biomech.*, **27**(2), pp. 195–204.
- [166] Lally, C., Reid, A. J., and Prendergast, P. J., 2004, “Elastic Behavior of Porcine Coronary Artery Tissue Under Uniaxial and Equibiaxial Tension,” *Ann. Biomed. Eng.*, **32**(10), pp. 1355–1364.
- [167] Tamai, H., Igaki, K., Tsuji, T., Kyo, E., Kosuga, K., Kawashima, A., Matsui, S., Komori, H., Motohara, S., Uehata, H., and Takeuchi, E., 1999, “A Biodegradable Poly-L-lactic Acid Coronary Stent in the Porcine Coronary Artery,” *J. Interv. Cardiol.*, **12**(6), pp. 443–450.
- [168] Kiziltas, G., Kikuchi, N., Volakis, J., and Halloran, J., 2004, “Topology optimization of dielectric substrates for filters and antennas using SIMP,” *Arch Comput Methods Eng.*, (11), p. 355–88.
- [169] Zuo, K., Chen, L., Zhang, Y., and Yang, J., 2007, “Study of key algorithms in topology optimization,” *Int J Adv Manufact Technol.*, (32), p. 787–96.
- [170] Ormiston, J. A., and Serruys, P. W. S., 2009, “Bioabsorbable coronary stents,” *Circulation*, **2**(3), pp. 255–60.
- [171] Adedeji, A., 2013, “Topology Optimization for Additive Manufacture,” Loughborough University.
- [172] Rozvany, G. I. N., 2009, “A critical review of established methods of structural topology optimization,” *Struct. Multidiscip. Optim.*, **37**(3), pp. 217–237.
- [173] Sigmund, O., and Petersson, J., 1998, “Numerical instabilities in topology optimization: A survey on procedures dealing with checkerboards, mesh-dependencies and local minima,” *Struct. Optim.*, **16**(1), pp. 68–75.
- [174] Electro Optical Systems, 2009, “Product Information EOSINT P/PA220-Pulver” [Online]. Available: <http://eos.materialdatacenter.com/eo/en>. [Accessed: 16-Jun-2014].
- [175] Vesenjaka, M., Krstulovic-Oparab, L., Rena, Z., and Domazetb, Z., 2010, “Cell shape effect evaluation of polyamide cellular structures,” *Polym. Test.*, **29**, pp. 991–994.
- [176] BS ISO 37, 2017, “Rubber, vulcanized or thermoplastic — Determination of tensile stress-strain properties.”
- [177] Chueh, J. Y., Wakhloo, A. K., and Gounis, M. J., 2009, “Neurovascular modeling: Small-batch manufacturing of silicone vascular replicas,” *Am. J. Neuroradiol.*, **30**(6), pp. 1159–1164.
- [178] Connolley, T., Nash, D., Buffière, J.-Y., Sharif, F., and McHugh, P. E., 2007, “X-ray micro-tomography of a coronary stent deployed in a model artery,” *Med. Eng. Phys.*, **29**(10), pp. 1132–41.
- [179] Herzog, C., Grebe, C., Mahnken, A., Balzer, J., Mack, M., and Zangos, S., 2005, “Peripheral artery stent visualization and in-

stent stenosis analysis in 16-row computed tomography: an in-vitro evaluation,” *Eur Radiol*, **15**, pp. 2276–83.

- [180] Veress, A. I., Weiss, J. a., Gullberg, G. T., Vince, D. G., and Rabbitt, R. D., 2002, “Strain Measurement in Coronary Arteries Using Intravascular Ultrasound and Deformable Images,” *J. Biomech. Eng.*, **124**(6), p. 734.
- [181] Steinert, B. D., Zhao, S., and Gu, L., 2012, “Monitoring the Wall Mechanics During Stent Deployment in a Vessel,” *J. Vis. Exp.*, (63), p. e3945.
- [182] Rajesh, R., Conti, J. C., and Strobe, E. R., 2007, “Linear elastic mechanics of mock arteries: empirical versus theoretically predicted pulsatile stent deflection,” *Biomed. Sci. Instrum.*, **43**, pp. 54–62.
- [183] Rajesh, R., Conti, J. C., and Strobe, E. R., 2007, “Mock artery distension: comparison of optical, mechanical and theoretical results,” *Biomed. Sci. Instrum.*, **43**, pp. 46–53.
- [184] Taggart, D. G., and Dewhurst, P., 2010, “Development and validation of a numerical topology optimization scheme for two and three dimensional structures,” *Adv. Eng. Softw.*, **41**(7), pp. 910–915.
- [185] Hong, M.-K., Kim, J.-S., Kim, B.-K., Ko, Y.-G., Choi, D., and Jang, Y., 2011, “A new stent design with multiple radio-opaque markers for protection of side-branch vessels in bifurcation lesions: HJ stents,” *Cardiovasc. Revasc. Med.*, **12**(5), pp. 323–8.
- [186] Ramcharitar, S., and Serruys, P., 2008, “Fully Biodegradable Coronary Stents,” *Am. J. Cardiovasc. Drugs*, **8**(5), pp. 305–314.
- [187] Martinez-Elbal, L., Ruiz-Nodar, J. M., Zueco, J., Lopez-Minguez, J. R., Moreu, J., Calvo, I., Ramirez, J. A., Alonso, M., Vazquez, N., Lezaun, R., and Rodriguez, C., 2002, “Direct coronary stenting versus stenting with balloon pre-dilation: immediate and follow-up results of a multicentre, prospective, randomized study. The DISCO trial. Direct Stenting of COronary Arteries,” *Eur. Heart J.*, **23**(8), pp. 633–640.
- [188] Hughes, T. J. R., Cottrell, J. A., and Bazilevs, Y., 2005, “Isogeometric analysis: CAD, finite elements, NURBS, exact geometry and mesh refinement,” *Comput. Methods Appl. Mech. Eng.*, **194**(39), pp. 4135–4195.
- [189] Nguyen, V. P., Anitescu, C., Bordas, S. P. A., and Rabczuk, T., 2015, “Isogeometric analysis: An overview and computer implementation aspects,” *Math. Comput. Simul.*, **117**, pp. 89–116.
- [190] Yin, L., and Ananthasuresh, G. K., 2001, “Topology optimization of compliant mechanisms with multiple materials using a peak function material interpolation scheme,” *Struct. Multidiscip. Optim.*, **23**(1), pp. 49–62.
- [191] Mehdizadeh, A., Ali, M. S. M., Takahata, K., Al-Sarawi, S., and Abbott, D., 2013, “A recoil resilient lumen support, design,

- fabrication and mechanical evaluation,” *J. Micromechanics Microengineering*, **23**(6), p. 65001.
- [192] Gamero, L. G., Armentano, R. L., and Levenson, J., 2002, “Arterial wall diameter and viscoelasticity variability,” *IEEE Computers in Cardiology*, Memphis, Tennessee, USA, pp. 513–516.
- [193] Moore, J. J., and Berry, J. L., 2002, “Fluid and solid mechanical implications of vascular stenting,” *Ann. Biomed. Eng.*, **30**(4), pp. 498–508.
- [194] Zopf, D., Hollister, S., Nelson, M., Ohye, R., and Green, G., 2013, “Bioresorbable Airway Splint Created with a Three-Dimensional Printer,” *N. Engl. J. Med.*, **368**(21), pp. 2043–45.
- [195] He, Y., Kilsby, S., Tuck, C., Wildman, R., Christie, S., Edmondson, S., and Yang, H., 2013, “Processing biodegradable polycaprolactone through 3D printing,” 24th International SFF Symposium - An Additive Manufacturing Conference, SFF 2013, pp. 200–214.
- [196] He, Y., Kilsby, S., Tuck, C., Wildman, R., Christie, S., Yang, H., and Edmondson, S., 2014, “A biodegradable polycaprolactone based ink developed for 3D inkjet printing,” International SAMPE Technical Conference.
- [197] Vaithilingam, J., Kilsby, S., Goodridge, R. D., Christie, S. D. R., Edmondson, S., and Hague, R. J. M., 2015, “Functionalisation of Ti6Al4V components fabricated using selective laser melting with a bioactive compound,” *Mater. Sci. Eng. C*, **46**, pp. 52–61.
- [198] Vaithilingam, J., Kilsby, S., Goodridge, R. D., Christie, S. D. R., Edmondson, S., and Hague, R. J. M., 2014, “Immobilisation of an antibacterial drug to Ti6Al4V components fabricated using selective laser melting,” *Appl. Surf. Sci.*, **314**, pp. 642–654.
- [199] He, Y., Wildman, R. D., Tuck, C. J., Christie, S. D. R., and Edmondson, S., 2016, “An Investigation of the Behavior of Solvent based Polycaprolactone ink for Material Jetting,” *Sci. Rep.*, **6**, p. 20852.
- [200] Gunasekera, D. H. A. T., Kuek, S., Hasanaj, D., He, Y., Tuck, C., Croft, A., and Wildman, R. D., 2016, “Three dimensional ink-jet printing of biomaterials using ionic liquids and co-solvents,” *Faraday Discuss.*, **190**, pp. 509–523.
- [201] He, Y., Tuck, C. J., Prina, E., Kilsby, S., Christie, S. D. R., Edmondson, S., Hague, R. J. M., Rose, F. R. A. J., and Wildman, R. D., 2016, “A new photocrosslinkable polycaprolactone-based ink for three-dimensional inkjet printing,” *J. Biomed. Mater. Res. B. Appl. Biomater.*, **00B**(0).
- [202] Begines, B., Hook, A. L., Alexander, M. R., Tuck, C. J., and Wildman, R. D., 2016, “Development, printability and post-curing studies of formulations of materials resistant to microbial attachment for use in inkjet based 3D printing,” *Rapid Prototyp. J.*,

22(5), pp. 835–841.

- [203] Seyednejad, H., Gawlitta, D., Dhert, W. J. A., van Nostrum, C. F., Vermonden, T., and Hennink, W. E., 2011, "Preparation and characterization of a three-dimensional printed scaffold based on a functionalized polyester for bone tissue engineering applications.," *Acta Biomater.*, **7**(5), pp. 1999–2006.
- [204] Williams, J. M., Adewunmi, A., Schek, R. M., Flanagan, C. L., Krebsbach, P. H., Feinberg, S. E., Hollister, S. J., and Das, S., 2005, "Bone tissue engineering using polycaprolactone scaffolds fabricated via selective laser sintering.," *Biomaterials*, **26**(23), pp. 4817–4827.
- [205] Ventola, C. L., 2014, "Medical Applications for 3D Printing: Current and Projected Uses," *Pharm. Ther.*, **39**(10), pp. 704–711.
- [206] Jardini, A. L., Larosa, M. A., Filho, R. M., Zavaglia, C. A. de C., Bernardes, L. F., Lambert, C. S., Calderoni, D. R., and Kharmandayan, P., 2014, "Cranial reconstruction: 3D biomodel and custom-built implant created using additive manufacturing," *J. Cranio-Maxillo-Facial Surg.*, **42**(8), pp. 1877–1884.
- [207] Garasic, J. M., Edelman, E. R., Squire, J. C., Seifert, P., Williams, M. S., and Rogers, C., 2000, "Stent and artery geometry determine intimal thickening independent of arterial injury.," *Circulation*, **101**(7), pp. 812–8.
- [208] Gunn, J., and Cumberland, D., 1999, "Does stent design influence restenosis?," *Eur. Heart J.*, **20**(14), pp. 1009–1013.
- [209] Takebayashi, H., Mintz, G. S., Carlier, S. G., Kobayashi, Y., Fujii, K., Yasuda, T., Costa, R. A., Moussa, I., Dangas, G. D., Mehran, R., Lansky, A. J., Kreps, E., Collins, M. B., Colombo, A., Stone, G. W., Leon, M. B., and Moses, J. W., 2004, "Nonuniform strut distribution correlates with more neointimal hyperplasia after sirolimus-eluting stent implantation.," *Circulation*, **110**(22), pp. 3430–3434.
- [210] Garcia, A., Pena, E., and Martinez, M. A., 2012, "Influence of geometrical parameters on radial force during self-expanding stent deployment. Application for a variable radial stiffness stent.," *J. Mech. Behav. Biomed. Mater.*, **10**, pp. 166–175.
- [211] Hoffmann, R., Jansen, C., König, a, Haager, P. K., Kerckhoff, G., vom Dahl, J., Klauss, V., Hanrath, P., and Mudra, H., 2001, "Stent design related neointimal tissue proliferation in human coronary arteries; an intravascular ultrasound study.," *Eur. Heart J.*, **22**(21), pp. 2007–14.

APPENDICES

Appendix A

Overview of Selected Clinical and FE Stent Studies

	Stent studies focus	Conclusion	Study type	Study by	New designs made
Dogboning & Foreshortening Studies	Dogboning & Balloon Expansion studies	Increased strut width at distal ends and eliminate dogboning	FEA	Wang et al., 2004 [61]	Yes
	Expansion & Recoil	The ideal stent possesses a low profile, uniform expansion, good flexibility to navigate tortuous vessels, adequate radiopacity, low recoil, sufficient radial strength, a low metal surface area and high scaffolding ability.	Clinical	McClellan et al., 2002 [126]	No
	Expansion & Dogboning study	Asymmetric design decreases dogboning from 27% to less than 10%	FEA	De Beule et al., 2008 [70]	Yes
	Dogboning, Foreshortening & Contact Study	Vascular Injury is caused by dogboning, foreshortening and excessive balloon contact	Clinical	Garasic et al., 2000 [207]	No
	Review on stent expansion, dogboning and strut distribution	Forces of expansion should be distributed evenly to facilitate uniform expansion	Clinical	Gunn et al., 1999 [208]	No
	Dogboning results investigation	Non-uniform expansion increases vascular injury	Clinical	Farb et al., 1999 [26]	No
	Dogboning and recoil study	A stent with a low metal-to-artery surface ratio has a higher radial and longitudinal recoil, but a lower dogboning.	FEA	Migliavacca et al., 2002 [60]	Yes

	Shape Optimisation for minimum dogboning, recoil & radial loss	Changes in wave lengths at the distal ends alleviate dogboning	FEA	Li et al., 2009 [91]	Yes
Flexibility	Stent Flexibility of two commercial designs	A methodology to evaluate stent flexibility	FEA	Petrini et al., 2004 [130]	No
Strut Shape and Distribution Studies	Comparison of two commercial designs for arterial stresses	Larger strut spacing causes less arterial stresses & subsequently less arterial injury	FEA	Gu et al., 2010 [102]	No
	Review on stent strut thickness, cross-section and cell design	Thin struts and round cross-sections are preferable	Clinical	Morton et al., 2004 [34]	No
	Strut distribution	Non- uniform and less strut distribution causes more Intimal Hyperplasia (IH) after SES (Sirolimus Eluting Stent) implantation	Clinical	Takebayashi et al., 2004 [209]	No
	Corrugated stent design Vs coil or meshwire	Tubular or corrugated designs have better results than coil or meshwire stents	Clinical	Hara et al., 2006 [127]	No
	Variable radial force on artery and plaque induced by changing strut thickness in the mid portion	Improved forces on artery and plaque resulted in change in thickness.(manually by selecting two designs)	FEA	Garcia et al., 2012 [210]	Yes
Open Cell Vs Closed	Comparison of two commercial designs	Results show 29% less strut-strut links reduces arterial injury by 42%, thrombosis by 69% & hyperplasia by 38%	Clinical		No

				Rogers et al., 1995 [32]	
	Comaprison of two commercial designs for their stress impact	Open cell design(less links) causes less arterial stresses	FEA	Lally et al., 2005 [67]	No
Geometry parameterisation for arterial stress	Stent geometry parameterization	Increased crown radii and strut distance causes less hoop stresses	FEA	Bedoya et al., 2006 [68]	Yes
	Geometry multiobjective optimisation	Shape and size of links & circumferencial rings change radial stiffness & flexibility. Large strut width & smaller amplitude of circumferencial rings are optimal interms of average stress & drug delivery	FEA	Pant et al., 2010,2011 [94,132]	Yes

Strut Studies for radial force and arterial injury	Strut thickness study	Thicker struts cause more arterial injury	Clinical	Rittersma et al., 2004 [35]	No
	Strut thickness	Strut thickness confirmed vessel injury	Clinical	Hoffman et al., 2001 [211]	No
	Comparison of two stents with different struts per cross-section	Less struts per cross-section causes more arterial injury	Clinical	Garasic et al., 2000 [207]	No
	Topology optimisation of stent struts to create drug reservoirs	Effective topology with stiffer and less volume struts developed for same amount of drug as commercially available initial design	FEA	Wu et al., 2008 [109]	Yes
	Parametric model of colonic stents	Variable stent diameters achieved for colonic stent in order to be obstruction-specific.	FEA	Puertolas et al., 2017 [97]	Yes
	Parametric stent design for coronary arteries	Stent strut size optimisation for lower von-mises stresses and better fatigue life.	FEA	Amirjani et al., 2014 [98]	Yes.
	Size optimisation of stent design	Study achieved better fatigue life by employing kriging surrogate model.	FEA	Li et al., 2017 [96]	Yes

Appendix B

Code for unwrapping Nastran stent model and stent topology optimisation input deck

This appendix contains the code written in MATLAB for unwrapping, smoothing and wrapping 3D cylindrical stent TO results from MSC Nastran model files for smoothing and illustration purposes. Model input deck is also presented at the end for Nastran optimisation.

```
%% Transformation to the points
fid2 = fopen([file_path 'input.txt']);
node_inp = textscan(fid2, '%s', 'delimiter', '\n');
fclose(fid2);

no_nodes_in_cyl_cut = 84;
node_data = node_inp{1};

x = zeros(no_nodes_in_cyl_cut,1);
y = x;
z = zeros(size(node_data, 1), 1);
node_ids = z;

for(i=1:no_nodes_in_cyl_cut)
    y(i) = str2num(node_data{i}(33:40));
    x(i) = str2num(node_data{i}(41:end));
end

for i=1:size(node_data, 1)
    node_ids(i) = str2num(node_data{i}(9:17));
    z(i) = str2num(node_data{i}(25:32));
end

R = 2.475;
```

```

theta = abs(atan(x./y));

only_y_negative = false(size(theta));
only_x_negative = only_y_negative;
x_y_negative = only_y_negative;

only_y_negative(y<0) = 1; only_y_negative(x<0) = 0;
only_x_negative(x<0) = 1; only_x_negative(y<0) = 0;
x_y_negative(y<0) = 1; x_y_negative(x>0) = 0;

case_1 = find(only_y_negative==1);
case_2 = find(only_x_negative==1);
case_3 = find(x_y_negative==1);

theta(case_1) = pi-theta(case_1);
theta(case_2) = 2*pi-theta(case_2);
theta(case_3) = pi+theta(case_3);

% theta(end+1) = theta(1)+2*pi;
x_new = R*(theta);

times = floor(size(node_data,1)/no_nodes_in_cyl_cut);
node_zyx = zeros(size(node_data,1),4);

for(i=1:times)
    node_zyx(no_nodes_in_cyl_cut*(i-
1)+1:no_nodes_in_cyl_cut*i,4) = x_new;
end

node_zyx(:,2) = z;
node_zyx(:,1) = node_ids;
node_start_max_old = max(node_ids);

add_node_zyx = zeros(times,4);
add_node_zyx(1:times,1) =
[node_start_max_old+1:node_start_max_old+times];
add_node_zyx(1:times,2) =
node_zyx(1:no_nodes_in_cyl_cut:no_nodes_in_cyl_cut*times,
2);
add_node_zyx(1:times,3) =
node_zyx(1:no_nodes_in_cyl_cut:no_nodes_in_cyl_cut*times,
3);
add_node_zyx(1:times,4) =
node_zyx(1:no_nodes_in_cyl_cut:no_nodes_in_cyl_cut*times,
4)+2*pi*R;

replace_nodes = zeros(times,3);
replace_nodes(:,1) =
node_zyx(1:no_nodes_in_cyl_cut:no_nodes_in_cyl_cut*times,
1);
replace_nodes(:,2) =
node_zyx(no_nodes_in_cyl_cut:no_nodes_in_cyl_cut:no_nodes
_in_cyl_cut*times,1);

```

```

replace_nodes(:,3) =
[node_start_max_old+1:node_start_max_old+times];

final_node_zyx = [node_zyx; add_node_zyx];

%% element arrangement addressing
fid2 = fopen([file_path 'faces.txt']);
element_inp = textscan(fid2, '%s', 'delimiter', '\n');
fclose(fid2);

faces = zeros(size(element_inp{1}, 1), 4);
for i = 1:size(element_inp{1}, 1)
    line = element_inp{1}{i};
    faces(i, :) = [str2num(line(25:32)),
str2num(line(33:40)), str2num(line(41:48)),
str2num(line(49:end))];
end

faces_old = faces;
for(j = 1:size(element_inp{1}, 1)/no_nodes_in_cyl_cut)

    temp_vec_1 = faces(no_nodes_in_cyl_cut*j,:);
    ind = find(replace_nodes(:,2)'==temp_vec_1(1));
    ind2 = find(temp_vec_1(:)==replace_nodes(ind,1));
    ind3 = find(temp_vec_1(:)==replace_nodes(ind+1,1));

    faces(no_nodes_in_cyl_cut*j,ind2) =
replace_nodes(ind,3);
    faces(no_nodes_in_cyl_cut*j,ind3) =
replace_nodes(ind+1,3);
end

%% read in density results for each element and plot as
patches
fid2 = fopen([file_path
'30_calcified_dof_zero_removed.des']);
dens_inp = textscan(fid2, '%s', 'delimiter',
'\n','headerlines', 4);
fclose(fid2);

ids = dens_inp{1}(1:2:end);
dens = str2num(cell2mat((dens_inp{1}(2:2:end))));
ids2 = zeros(size(ids, 1),1);
for i = 1:size(ids, 1)
ids2(i) = str2num(ids{i}(1:8));
end

% code for addition of empty rows so that consistent row
numbers for vertices for patch
vertices = zeros(max(final_node_zyx(:, 1)), 4);
for i = 1:size(final_node_zyx, 1)
    vertices(final_node_zyx(i), :) = final_node_zyx(i,
:);

```

```

end

% plot
figure;
p=patch('faces',faces,'vertices',vertices(:, 2:end),
'facecolor', 'flat', 'FaceVertexCData', dens,
'edgecolor', 'none','facealpha', 1);
view([0 1 0]); axis off; colormap(flipud(gray))

```

Code for smoothing intermediate densities in unwrapped stent topology results

```

% reading image
a =
double(rgb2gray(imread('flash_traced_30_calci.png')))/255
;

figure;imshow(a)

% smooth
f = fspecial('average', 3);
smoothed = imfilter(a,f,'replicate');
figure;imshow(smoothed)

% threshold
isoval = 0.15;
b = 1-smoothed;
b(b>isoval) = 1;
b(b<=isoval) = 0;
figure;imshow(~b)

```

Code for wrapping the smoothed optimised stent topologies

```

%% analysing image
z_max = 15;
R = 2.475;
x_temp = ~logical(rgb2gray(imread([file_path
'final_30_calci.png']))) );
img = x_temp;
nely = size(img,1); nelx = size(img,2);

connectivity=zeros(nelx*nely,4);
for ii=1:nelx*nely
    rw=mod(ii,nely);
    cl=fix((ii-1)/nely)+1;
    connectivity(ii,1)=cl-1+ii;
end

```



```

        connectivity(ii,2)=connectivity(ii,1)+1;
        connectivity(ii,3)=connectivity(ii,1)+nely+1+1;
        connectivity(ii,4)=connectivity(ii,3)-1;
end

prop_id_max = max(img(:));
prop = double(img(:));
prop(img==0) = prop_id_max+1;

mat = [[1:nelx*nely]' prop connectivity];
fid5 = fopen([file_path 'elem_ori.txt'], 'w');
fprintf(fid5, 'CQUAD4,%d,%d,%d,%d,%d,%d\n',mat. ');
fclose(fid5);

%% Processing - Elements
fid2 = fopen([file_path 'elem_ori.txt']);
elem = textscan(fid2, '%s %d %d %d %d %d %d',
'delimiter', ', ');
fclose(fid2);

length_elem_list = size(elem{1},1);
no_elem_in_cyl_cut = nely;

no_nodes_in_cyl_cut = no_elem_in_cyl_cut+1;

for(i=no_elem_in_cyl_cut:no_elem_in_cyl_cut:length_elem_list)
    elem{4}(i) = elem{4}(i);
    elem{5}(i) = elem{5}(i) - no_elem_in_cyl_cut;
    elem{6}(i) = elem{6}(i) - no_elem_in_cyl_cut;
    elem{7}(i) = elem{7}(i);
end

fid4 = fopen([file_path 'elem.txt'], 'w');
mat = [elem{2}'; elem{3}'; elem{4}'; elem{5}'; elem{6}';
elem{7}'];
fprintf(fid4, 'CQUAD4,%d,%d,%d,%d,%d,%d\n',mat);
fclose(fid4);

%% Nodes
theta = 2*pi/no_elem_in_cyl_cut*[0:no_elem_in_cyl_cut-1];
x = R*cos(theta)';
y = R*sin(theta)';
times = (length_elem_list/no_elem_in_cyl_cut);

z = [0:z_max/times:z_max]';

nodes = zeros(no_nodes_in_cyl_cut*(length(z)),4);
for(j = 1:length(z))
    k = (j-1)*no_nodes_in_cyl_cut;
    nodes(k+1:k+no_nodes_in_cyl_cut,1) =
[k+1:k+no_nodes_in_cyl_cut];
    nodes(k+1:k+no_nodes_in_cyl_cut-1,2) = x;
    nodes(k+1:k+no_nodes_in_cyl_cut-1,3) = y;

```

```
        nodes(k+1:k+no_nodes_in_cyl_cut-1,4) = z(j);
end

fid3 = fopen([file_path 'node.txt'], 'w');
fprintf(fid3, 'GRID,%d,,%f,%f,%f\n', nodes.);
fclose(fid3);
```

Nastran input deck for compliance minimisation

The following input deck represents the optimisation model and parameters for stent optimisation based on 30% calcified artery plaque, to be analysed by Nastran. Other set of input decks are similar except the radial varying loading.

```
$ Design Sensitivity and Optimization Analysis
SOL 200 $ Specifies Design Sensitivity and Optimization Analysis solution
sequence
TIME 600
CEND $ Designates the end of the Executive Control section
$ Direct Text Input for Global Case Control Data
ECHO = NONE $ Neither sorted nor unsorted Bulk Data will be printed
MAXLINES = 999999999 $ Sets the maximum number of output lines
DESOBJ = 1 $ Selects the DRESP entry to be used as the design objective.
DESGLB = 1 $ Selects the design constraints to be applied.

ANALYSIS = STATICS
SUBCASE 1
$ Subcase name : Default
  SUBTITLE=Default
  SPC = 2 $ Selects a single point constraint set (DOF BCs) to be applied.
  LOAD = 2 $ Selects a load to be applied.
  DISPLACEMENT(SORT1,REAL)=ALL $ Specifies the form and type of
displacement vector output.
  SPCFORCES(SORT1,REAL)=ALL $ Specifies the SPC forces output.
  STRESS(SORT1,REAL,VONMISES,BILIN)=ALL $ Specifies stress output.
BEGIN BULK $ Designates the end of the Case Control Section and/or the
beginning of a Bulk Data Section.
$ Direct Text Input for Bulk Data
PARAM,AUTOMSET,YES
PARAM  POST  -1 $ Specifies the output form.
PARAM  PRTMAXIM YES $ Specifies the output of maximums of applied
loads, single-point forces of constraint, multi-point forces of constraint, and
displacements.
$ Elements and Element Properties for region: stent
$ Defines the membrane, bending, transverse shear, and coupling properties
of thin shell elements. The real value in the entry is
the shell thickness.
PSHELL 1 1 .2 1 1
$ Pset: "stent" will be imported as: "pshell.1"
$ Defines a curved quadrilateral shell or plane strain element with 4 grid
points.
CQUAD4 1 1 1 2 87 86
CQUAD4 2 1 2 3 88 87
$...etc. for all the elements
$ Referenced Material Records
```

\$ Material Record : PLA
 \$ Description of Material : PLA
 MAT1 1 3500. .36 1.3-9
 \$ Multipoint Constraints of the Entire Model
 \$ ID conflict : the PATRAN MPC ID was 1
 \$Describes the connectivity of RBE3 elements to nodes on both ends of stent
 for free expansion and compression

```

RBE3 6805      6970 123456 1. 123 1 2
      3 4 5 6 7 8 9 10
      11 12 13 14 15 16 17 18
      19 20 21 22 23 24 25 26
      27 28 29 30 31 32 33 34
      35 36 37 38 39 40 41 42
      43 44 45 46 47 48 49 50
      51 52 53 54 55 56 57 58
      59 60 61 62 63 64 65 66
      67 68 69 70 71 72 73 74
      75 76 77 78 79 80 81 82
      83 84
      UM 22 23 78 23 50 23
  
```

\$ Nodes of the Entire Model
 \$ Defines the location of a geometric grid point (node), the directions of its
 displacement, and its permanent single-point
 constraints of the entire model.

```

GRID* 1          2.5          2.47499990463257
* 0.
GRID* 2          2.5          2.46808052062988
* .18494039773941
  
```

\$...etc. for all the grid points
 \$ Loads for Load Case : Default

```

SPCADD 2 1
LOAD 2 1. 1. 1
  
```

\$ Displacement Constraints of Load Set : fix_x_y
 \$ Defines a set of single-point constraints (DOF BCs)

```

SPC1 1 123456 6970
  
```

\$ Nodal Forces of Load Set : force

\$ Defines a static concentrated force at a grid point by specifying a vector.

```

FORCE 1 1 1 0.00799 -1. 0. 0.
FORCE 1 2 1 0.01158 -1. 0. 0.
  
```

\$...etc. for all the nodal force

\$ Optimisation Parameters :

\$...OPTIMISATION CONTROL

\$ Overrides default values of parameters using in design optimisation

\$Tcheck for avoiding checkerboard pattern.

```

DOPTPRM DESMAX 250 CONV1 1.-4 TCHECK 1
  
```

\$ Design Variables for TOPOLOGY Optimisation :

\$ Topology variable and symmetry manufacturing constraints.

```

TOPVAR 1 PSHELL PSHELL .4 .001 .2 3. 1
      2 XY ZX
  
```

\$ TDMIN .1

\$ Global Target Constraints : MASS FRACTION

```

DCONSTR 1 10001 0.3000
  
```

```
DRESP1 10001 FRM FRMASS
$ Objective Responses : Minimize Compliance
DRESP1 1 COMPL COMP
$ Referenced Coordinate Frames
CORD2C 1 10. 0. 0. 20. 0. 0.
      10. 0. 10.
CORD2R 2 10. 0. 0. 20. 0. 0.
      10. 0. 10.
ENDDATA ded0dc75 $ Designates the end of the Bulk Data Section
```

Appendix C

Code for image analysis

```
%reading first image
image1=imread('1a.png');
figure;imshow(image1);

%convert image1 to grey scale
image2=rgb2gray(image1);
figure;imshow(image2)

%edge detection
BW = edge(image2,'sobel',5e-2);
figure;imshow(BW);
figure;imshow(image2);
imshow(BW);
BW(BW==0)=nan;

%reading second image
image3=imread('1b.png');

%convert image3 to grey scale
image4=rgb2gray(image3);
figure;imshow(image4)

%edge detection of image 4
BW2 = edge(image4,'sobel',5e-2);
figure;imshow(BW2);

figure;imshow(image4);
imshow(BW2);
```

```

BW2 (BW2==0)=nan;

%imfuse two images and place reference markers
C=imfuse(BW,BW2,'blend','Scaling','joint');
imwrite(C,'fused_image.png');
imshow(C)
figure(99);imshow(C);
x_center_line=[640;640];
y_center_line=[0;1280];
hold on; plot(x_center_line,y_center_line,'--y');
x_limleft=transpose(640:72:1000);
x_limright=transpose(640:-72:280);

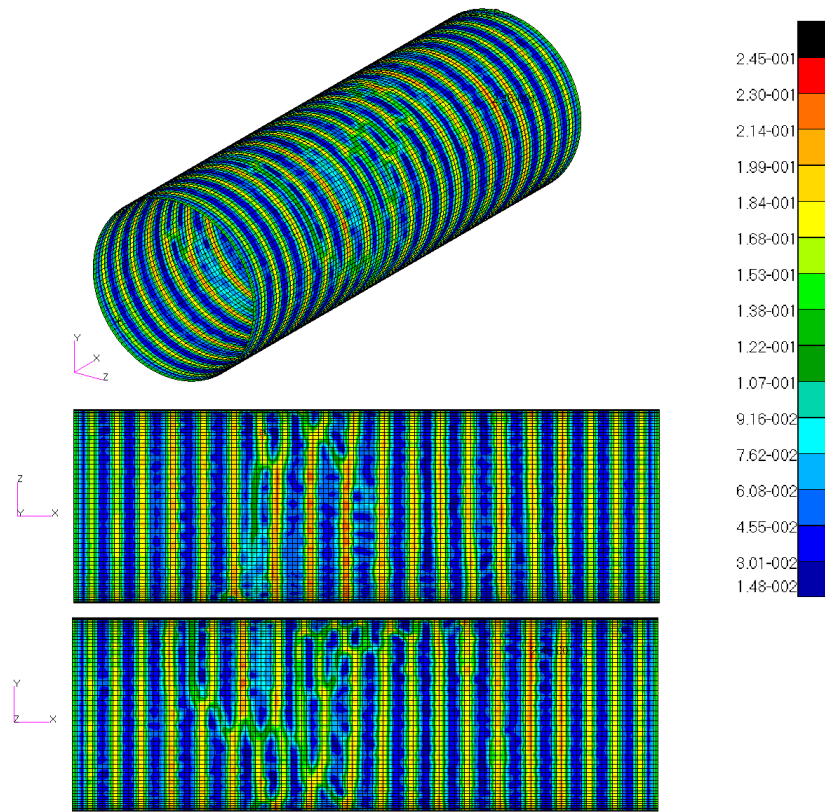
y_limup=transpose(1280*ones(1,6));
y_limdown=transpose(0*ones(1,6));
up_left=[x_limleft,y_limup];
down_left=[x_limleft,y_limdown];
hold on;plot(down_left,up_left,'--c');
xb_limleft=transpose(210:72:640);
for i=2:6
    hold
    on;plot([x_limleft(i);x_limleft(i)],[y_limdown(i);y_limup
(i)], '--c');
end
for i=2:6
    hold
    on;plot([xb_limleft(i);xb_limleft(i)],[y_limdown(i);y_lim
up(i)], '--c');
end

```

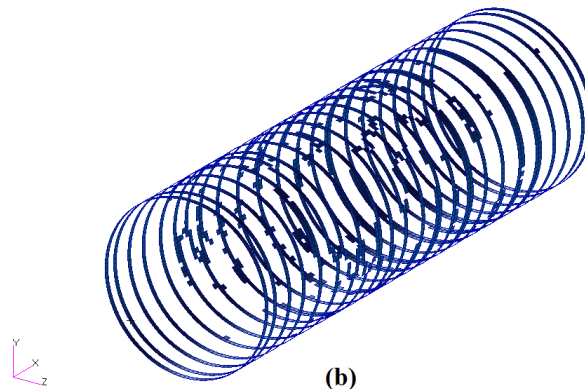
Appendix D

Mesh refinement and minimum member size (MMS) study of the preliminary load case scenarios

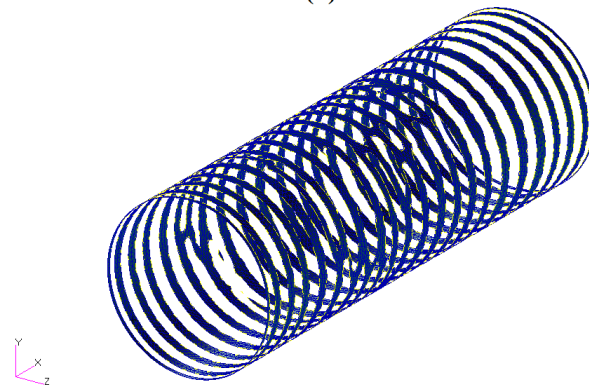
The following figures present topology optimisation results of higher mesh densities and the variation due to the minimum member size control (MMS) option in Nastran topology optimisation of cylinder under different initial loading scenarios.



(a)

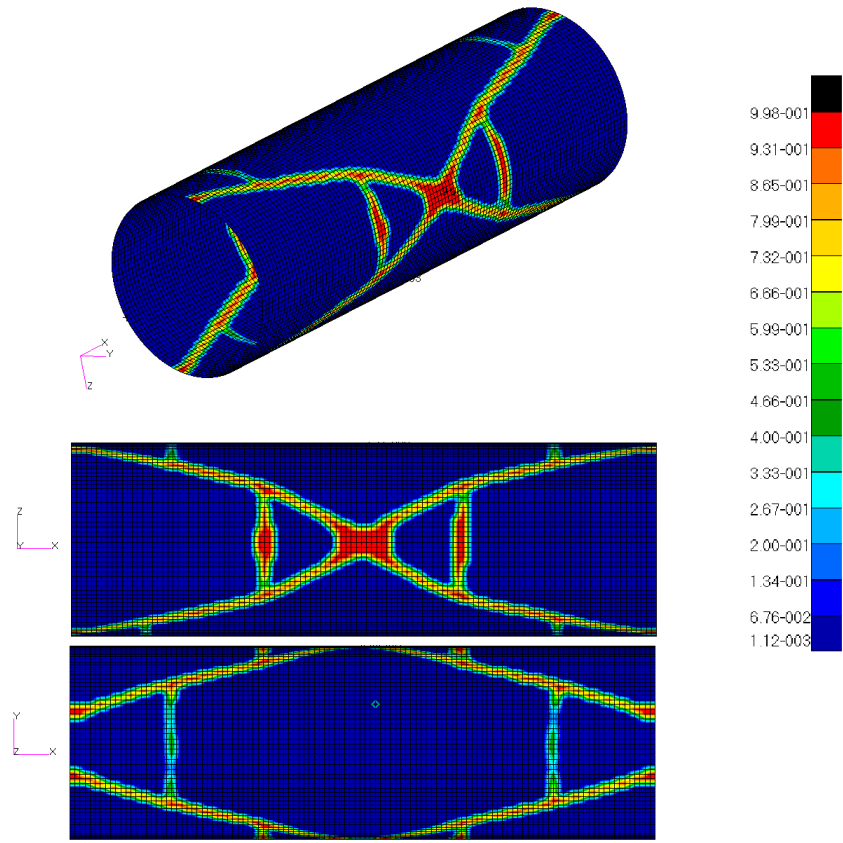


(b)

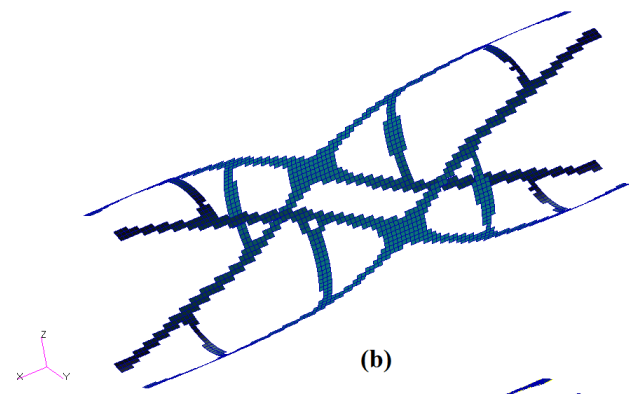


(c)

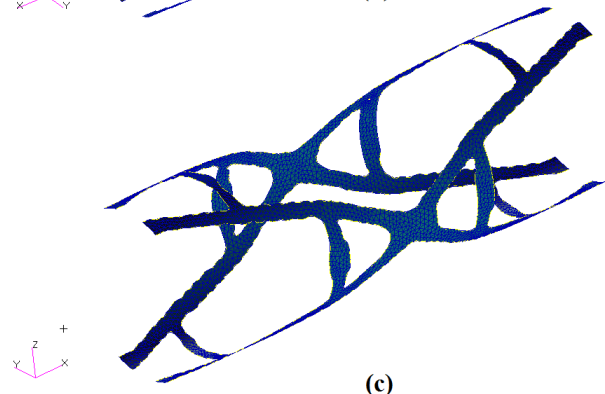
Figure 7-1: Mesh 2 (13685 elements) with uniform loading: (a) element density distribution, ρ , representing material densities between 0-1 (b) threshold 0.3 for element filtering and (c) FEM smoothing of the filtered elements.



(a)

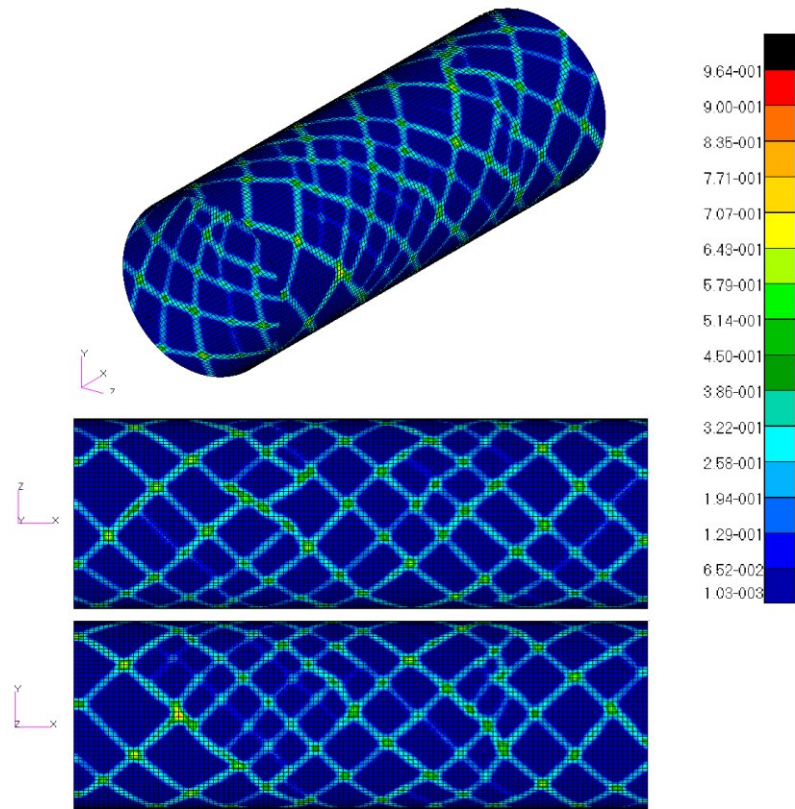


(b)

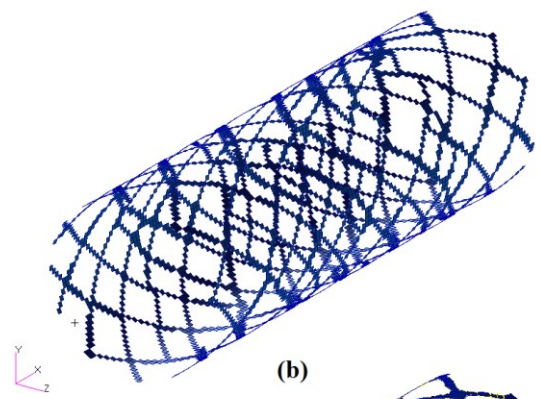


(c)

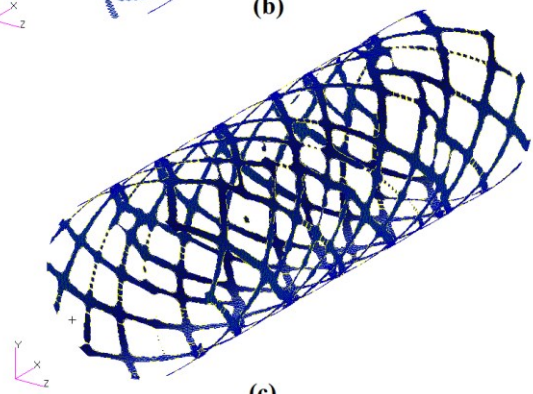
Figure 7-2: Mesh 2 (13685 elements) with central crush loading: (a) element density distribution, ρ , representing material densities between 0-1 (b) threshold 0.3 for element filtering and (c) FEM smoothing of the filtered elements.



(a)

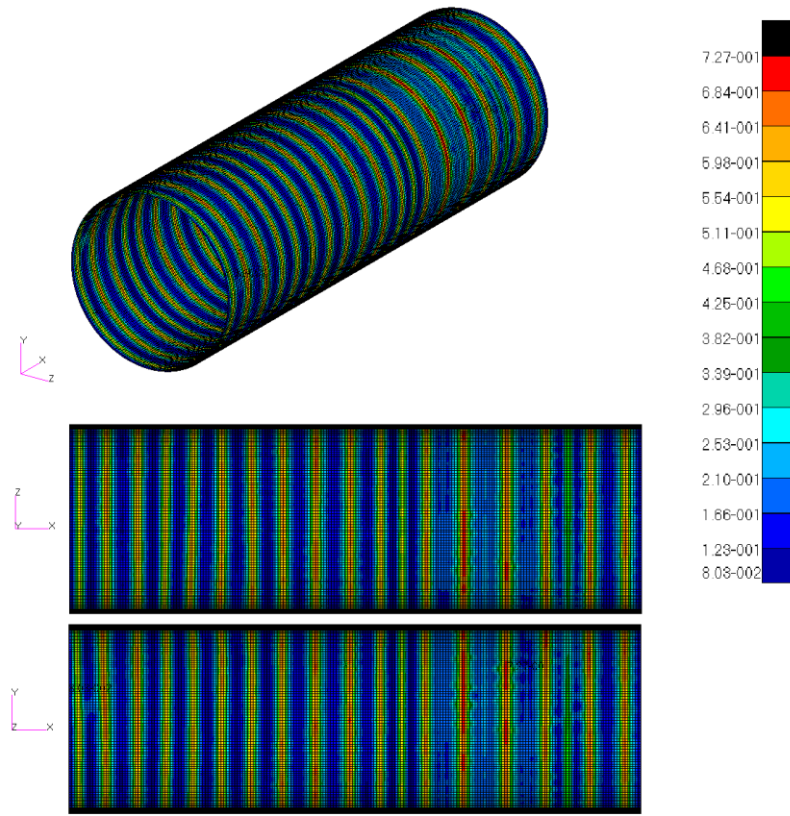


(b)

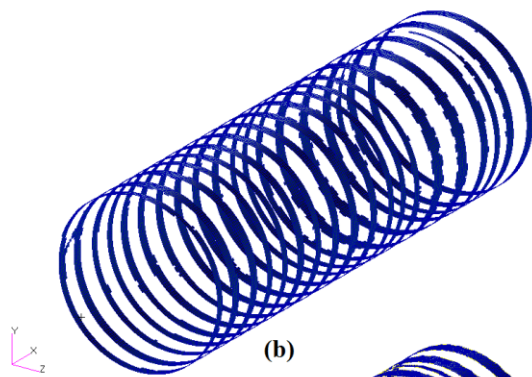


(c)

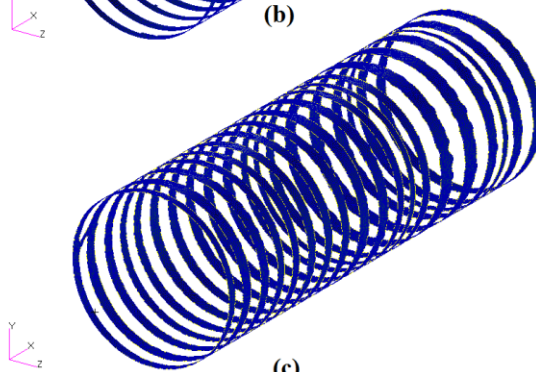
Figure 7-3: Mesh 2 (13685 elements) with torsional loading: (a) element density distribution, ρ , representing material densities between 0-1 (b) threshold 0.3 for element filtering and (c) FEM smoothing of the filtered elements.



(a)

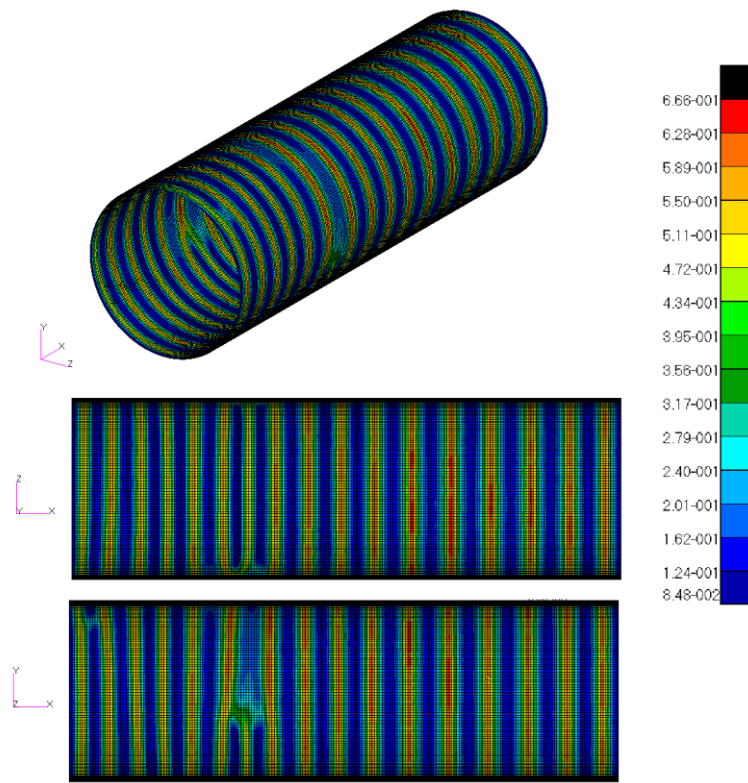


(b)

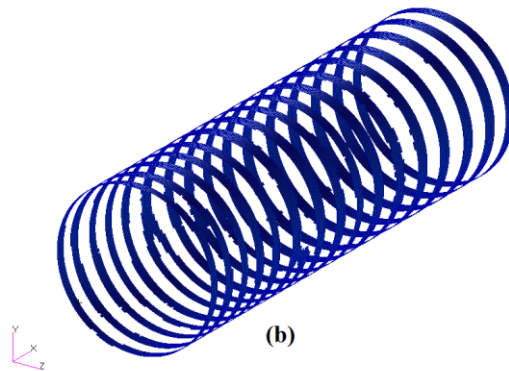


(c)

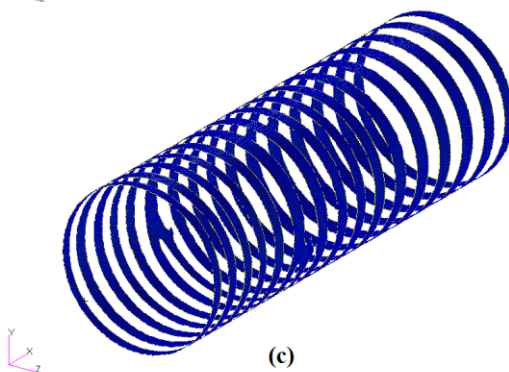
Figure 7-4: Mesh 3 (47507 elements) with uniform loading and MMS 0.3: (a) element density distribution, ρ , representing material densities between 0-1 (b) threshold 0.25 for element filtering and (c) FEM smoothing of the filtered elements.



(a)

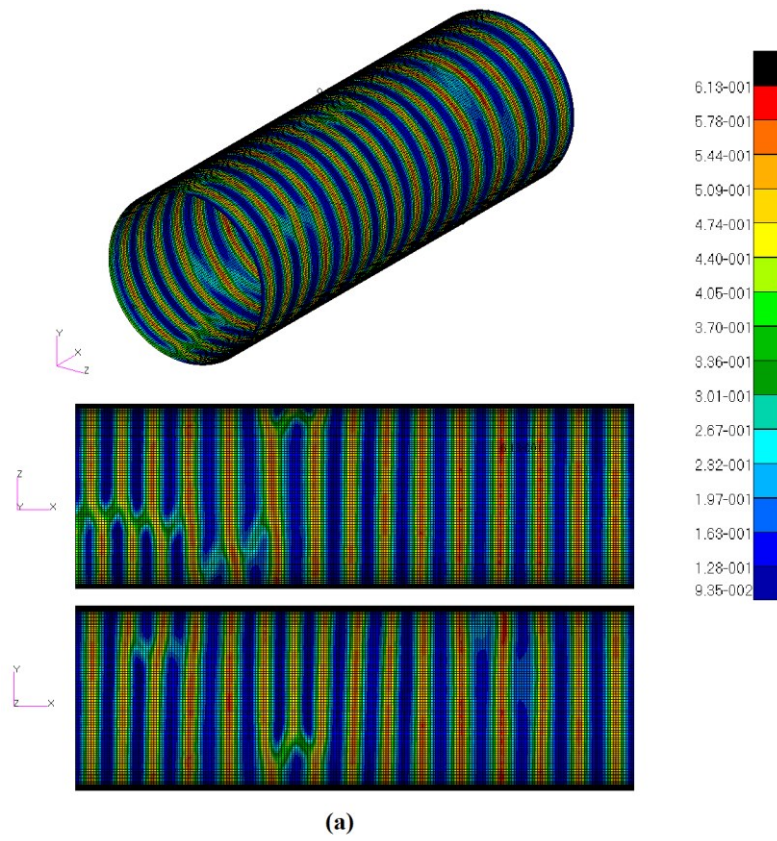


(b)

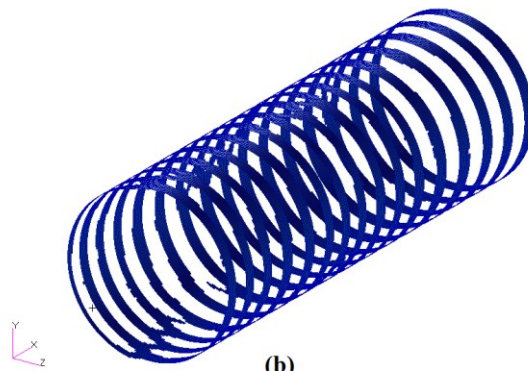


(c)

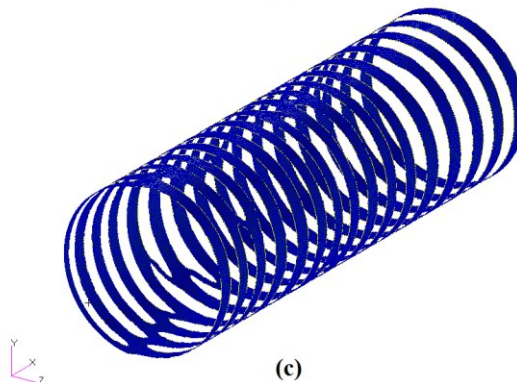
Figure 7-5: Mesh 3 (47507 elements) with uniform loading and MMS 0.4: (a) element density distribution, ρ , representing material densities between 0-1 (b) threshold 0.25 for element filtering and (c) FEM smoothing of the filtered elements.



(a)

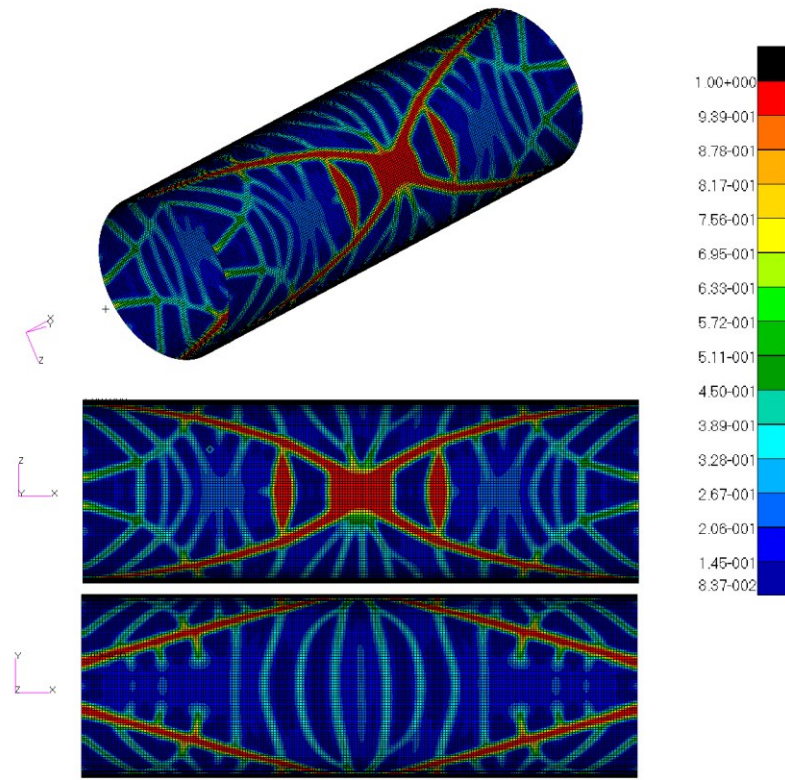


(b)

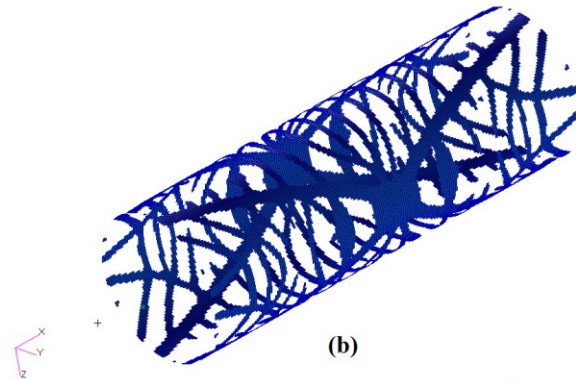


(c)

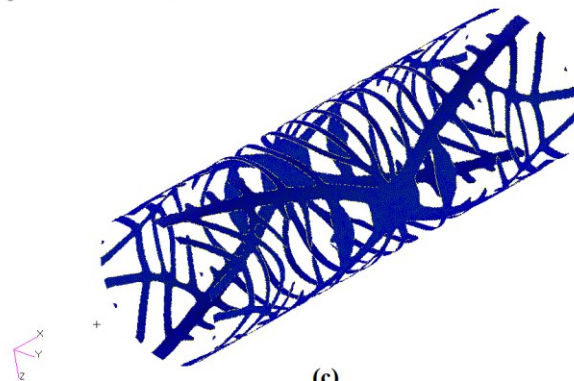
Figure 7-6: Mesh 3 (47507 elements) with uniform loading and MMS 0.5: (a) element density distribution, ρ , representing material densities between 0-1 (b) threshold 0.25 for element filtering and (c) FEM smoothing of the filtered elements.



(a)

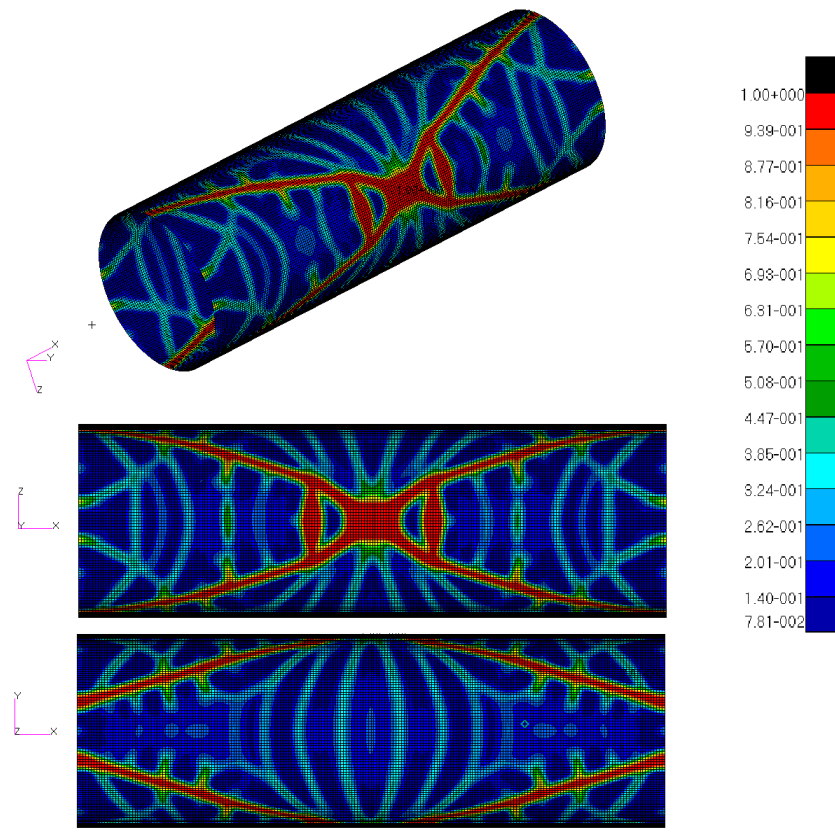


(b)

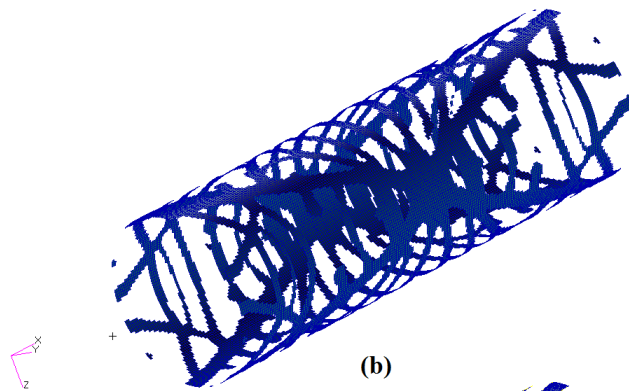


(c)

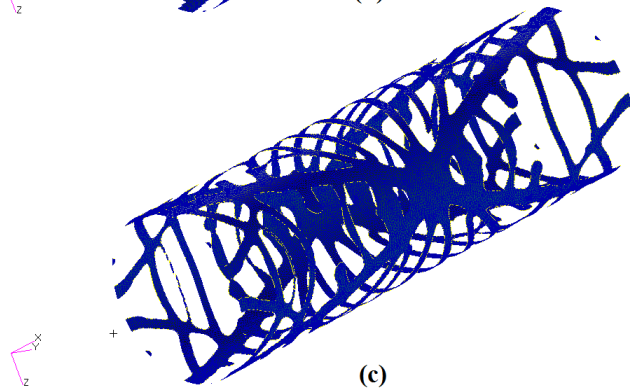
Figure 7-7: Mesh 3 (47507 elements) with central crush loading and MMS 0.3: (a) element density distribution, ρ , representing material densities between 0-1 (b) threshold 0.25 for element filtering and (c) FEM smoothing of the filtered elements.



(a)

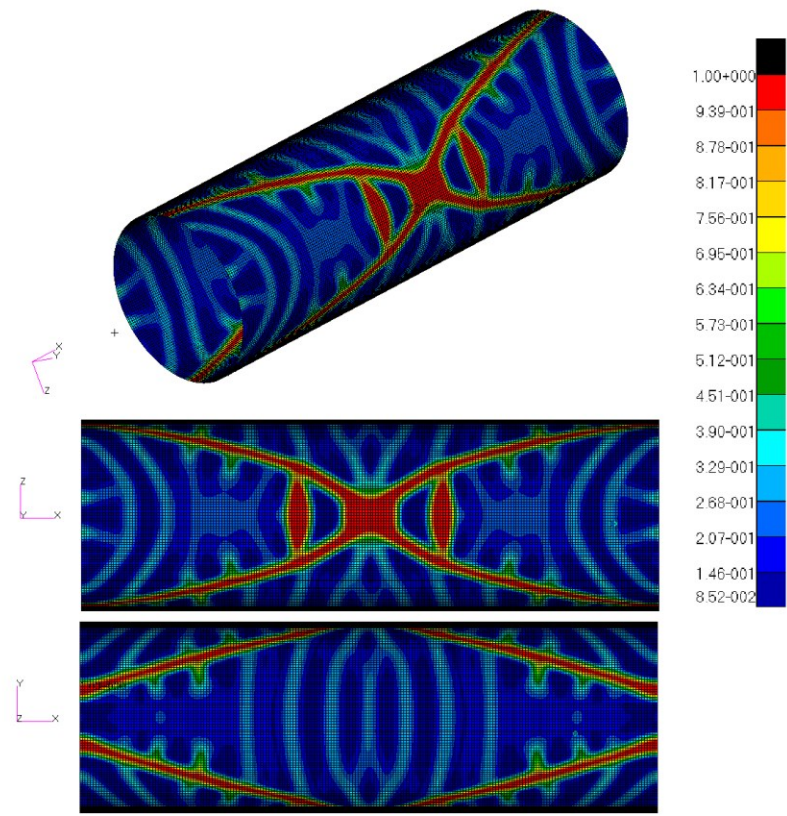


(b)

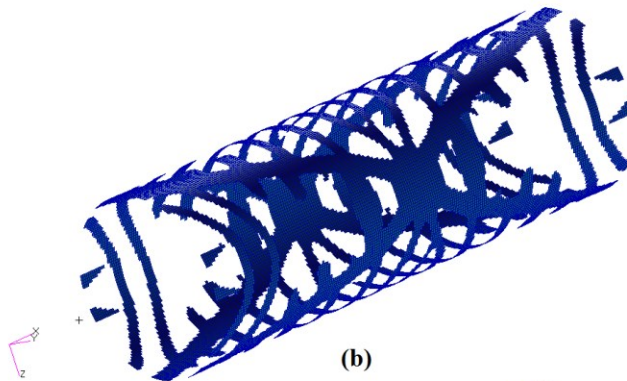


(c)

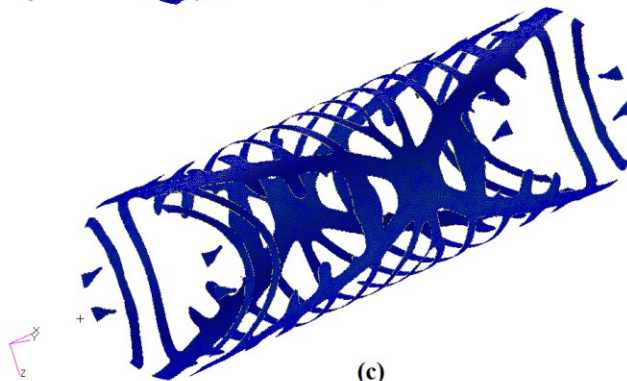
Figure 7-8: Mesh 3 (47507 elements) with central crush loading and MMS 0.4: (a) element density distribution, ρ , representing material densities between 0-1 (b) threshold 0.25 for element filtering and (c) FEM smoothing of the filtered elements.



(a)

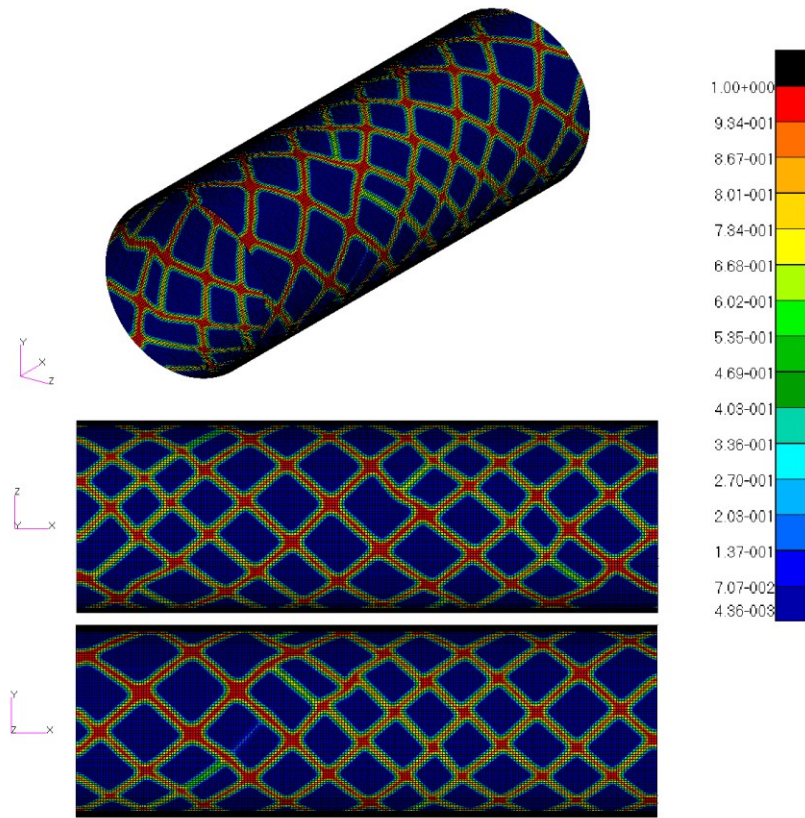


(b)

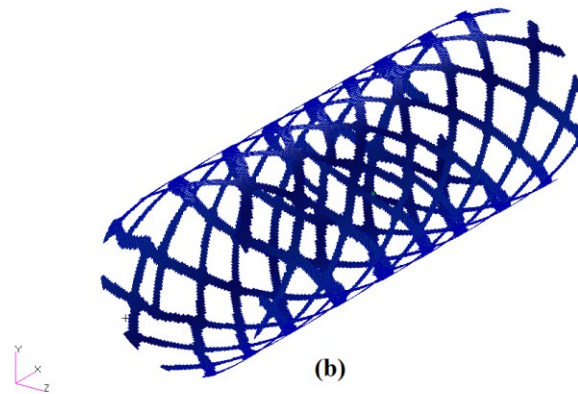


(c)

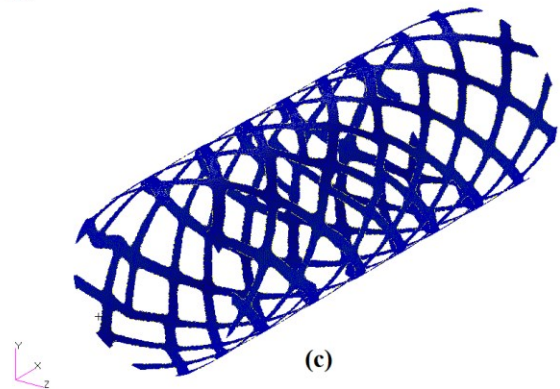
Figure 7-9: Mesh 3 (47507 elements) with central crush loading and MMS 0.5: (a) element density distribution, ρ , representing material densities between 0-1 (b) threshold 0.25 for element filtering and (c) FEM smoothing of the filtered elements.



(a)

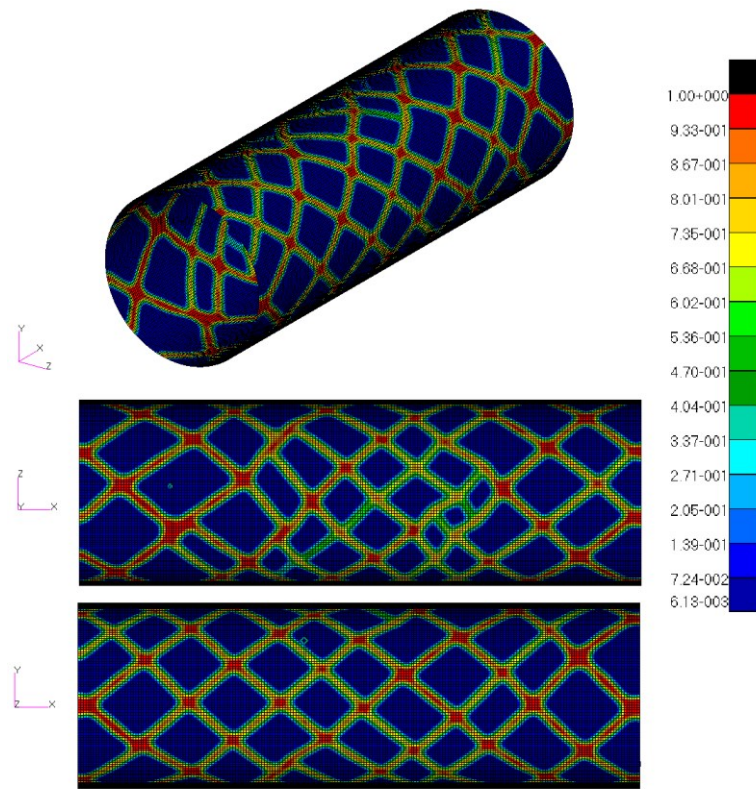


(b)

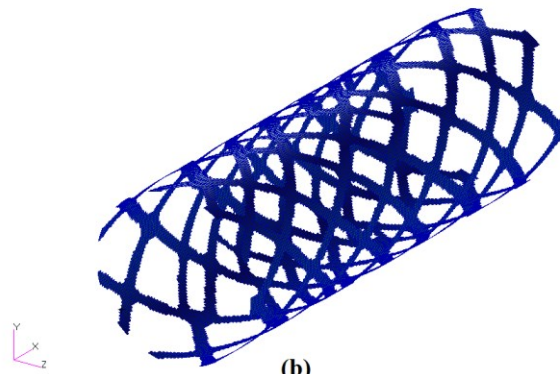


(c)

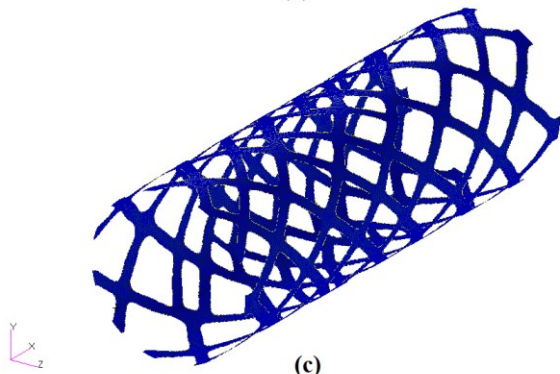
Figure 7-10: Mesh 3 (47507 elements) with torsional loading and MMS 0.3: (a) element density distribution, ρ , representing material densities between 0-1 (b) threshold 0.25 for element filtering and (c) FEM smoothing of the filtered elements.



(a)

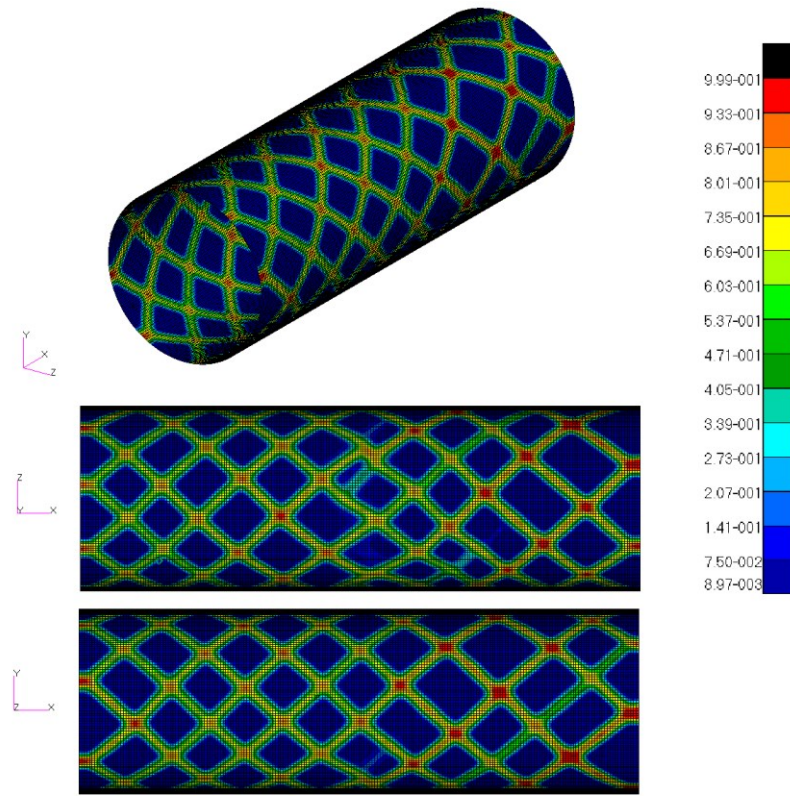


(b)

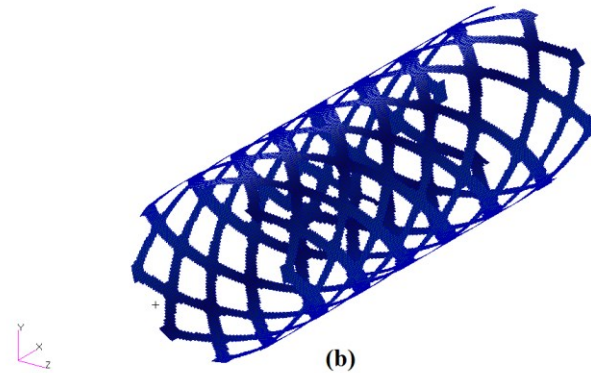


(c)

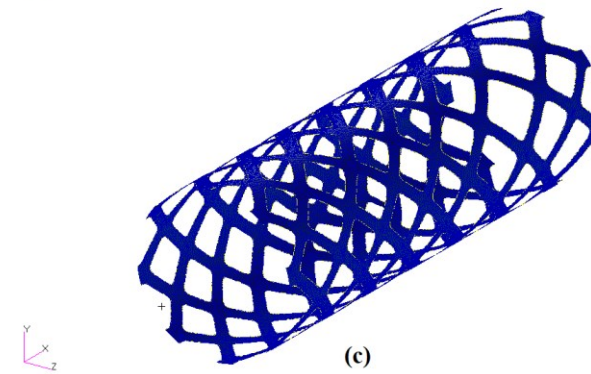
Figure 7-11: Mesh 3 (47507 elements) with torsional loading and MMS 0.4: (a) element density distribution, ρ , representing material densities between 0-1 (b) threshold 0.25 for element filtering and (c) FEM smoothing of the filtered elements.



(a)



(b)



(c)

Figure 7-12: Mesh 3 (47507 elements) with torsional loading and MMS 0.5: (a) element density distribution, ρ , representing material densities between 0-1 (b) threshold 0.25 for element filtering and (c) FEM smoothing of the filtered elements.